



HAL
open science

The Hanbury Brown and Twiss Effect for Cold Atoms

Martijn Schellekens

► **To cite this version:**

Martijn Schellekens. The Hanbury Brown and Twiss Effect for Cold Atoms. Atomic Physics [physics.atom-ph]. Université Paris Sud - Paris XI, 2007. English. NNT: . tel-00168946

HAL Id: tel-00168946

<https://pastel.hal.science/tel-00168946v1>

Submitted on 30 Aug 2007

HAL is a multi-disciplinary open access archive for the deposit and dissemination of scientific research documents, whether they are published or not. The documents may come from teaching and research institutions in France or abroad, or from public or private research centers.

L'archive ouverte pluridisciplinaire **HAL**, est destinée au dépôt et à la diffusion de documents scientifiques de niveau recherche, publiés ou non, émanant des établissements d'enseignement et de recherche français ou étrangers, des laboratoires publics ou privés.

**INSTITUT D'OPTIQUE GRADUATE SCHOOL
LABORATOIRE CHARLES FABRY**

**UNIVERSITÉ PARIS XI
U.F.R. SCIENTIFIQUE D'ORSAY**

THÈSE

présentée pour obtenir

le GRADE de DOCTEUR EN SCIENCES
DE L'UNIVERSITÉ PARIS XI ORSAY

par

Martijn SCHELLEKENS

Sujet :

**L'EFFET HANBURY BROWN ET TWISS POUR LES
ATOMES FROIDS**

Thèse soutenu le 10 mai 2007 devant le jury composé de :

| | | |
|-----|---------------------|--------------------|
| M. | Christoph WESTBROOK | Directeur de thèse |
| Mme | Michèle LEDUC | Rapporteur |
| M. | Jean-François ROCH | Rapporteur |
| Mme | Danielle DOWEK | Examinatrice |
| M. | Alain ASPECT | Membre invité |

Remerciements

Les travaux de thèse présentés dans ce manuscrit ont été effectués au laboratoire Charles Fabry de l'Institut d'Optique. Je remercie son directeur, Pierre Chavel, pour m'avoir accueilli dans ce laboratoire, ainsi que pour l'intérêt qu'il a porté à nos travaux.

Les travaux ont été effectués dans le groupe d'Optique Atomique, dirigé par Alain Aspect. Je voudrais le remercier particulièrement, et pas seulement pour m'avoir accueilli dans son groupe. Il a été responsable de mon apprentissage en optique quantique, et ses grandes qualités de pédagogue ont fortement conditionné mon désir d'approfondir ce domaine. Il a par ailleurs fortement contribué dans mon choix à poursuivre mon cursus à l'École Supérieure d'Optique; choix que je n'ai pas eu à regretter. Je n'ai pas eu grand mal à accepter sa proposition d'étudier les corrélations atomiques au sein de son groupe, et je le remercie particulièrement à cet égard. Je veux aussi remercier dans ce sens Christoph Westbrook, responsable de l'expérience de l'hélium métastable, qui m'a accueilli, avec tout l'enthousiasme qui est le sien, sur son expérience et qui a bien voulu diriger mes travaux de thèse.

Je tiens à remercier Michèle Leduc, Jean-François Roch et Danielle Doweck pour l'intérêt manifeste qu'ils ont montré pour ces travaux en participant au jury. Plus particulièrement je voudrais remercier Michèle Leduc et Jean-François Roch pour avoir bien voulu rapporter ce manuscrit.

Le travail présenté est naturellement celui d'une équipe que je remercie chaleureusement. L'ambiance a été très positive, et cela malgré des périodes difficiles dues aux caprices de l'expérience. Les travaux présentés n'auraient pas pu se réaliser sans les multiples compétences et caractères des uns et des autres.

L'équipe est encadrée par Christoph Westbrook, et les travaux effectués lui sont en grande partie dus. L'expérience de Hanbury Brown avec des atomes a en effet été le moteur de son intégration au CNRS, et ses travaux dans cette direction avaient commencé bien avant mon arrivée dans le groupe. Ceci a contribué indiscutablement à sa grande motivation et son enthousiasme constante par rapport aux progrès de l'expérience. Cet enthousiasme a été pour moi un moteur puissant, en particulier dans les périodes difficiles. Cet enthousiasme a été une véritable récompense quand les premiers résultats sont tombés. J'ai éprouvé par ailleurs un grand plaisir à discuter la physique de l'expérience avec lui, autant que des choix technologiques à faire. Je le remercie donc chaleureusement pour cet enthousiasme partagée pour cet expérience, ainsi que pour la direction qu'il a donné à ma thèse, de même que pour la grande confiance et autonomie qu'il m'a accordées dans ces travaux.

L'autre pilier de l'expérience est indiscutablement Denis Boiron. Ses connaissances approfondies du dispositif expérimental, sa rigueur scientifique inébranlable, ainsi que sa bonne humeur perpétuelle ont complété les points qui ont pu me faire défaut. Ses grandes qualités pédagogiques m'ont permis d'appréhender

l'expérience dans sa complexité, sa culture des formulations mathématiques a permis de quantifier grand nombre d'intuitions physiques. Il est pour moi la démonstration même que la multiplicité des compétences et des points de vue conduit à des résultats plus riches. Son apport à ce travail a été inestimable, et je le remercie chaleureusement. Par ailleurs, il a fait un grand travail dans la relecture de ce manuscrit: merci.

Malgré ses nombreuses occupations, Alain Aspect a aussi contribué largement à l'aboutissement de ces résultats. Sa grande culture scientifique, et sa passion renommée pour les corrélations quantiques, ont permis d'éclairer largement les résultats obtenus, et ont permis de leur donner une autre dimension. Sa culture s'est avérée particulièrement utile lors de l'analyse des données ainsi que pendant les phases de rédaction. Un grand merci donc pour son enthousiasme manifeste pour cet expérience.

Quand je suis arrivé sur l'expérience, elle était essentiellement aux mains d'Olivier Sirjean, Signe Seidelin et Jose Viana Gomes. Ils m'ont introduit à la prise des données de condensats, et m'ont permis d'entrevoir la perspective des choses à venir. Ce bref recouvrement, et leur expérience accumulée, a été très important dans les choix qui ont suivi: je les en remercie donc ainsi que pour leur sympathie. C'est avec Rodolphe Hoppeler que nous avons entrepris le démontage du dispositif qui fonctionnait, et que nous avons entrepris dans sa longue reconstruction. Les difficultés que nous avons eu à obtenir un condensat ont été nombreuses, et je pense que nous gardons tous les deux des souvenirs par moment pénibles de cette période. Pendant cette période, nous avons été rejoint brièvement par John Obrecht, qui commençait sa thèse dans le Colorado. C'est après l'été 2004 (si rien ne marche, prenez des vacances !) que nous avons réussi à débloquer nos difficultés. Nous avons alors été rejoint par Aurélien Perrin avec qui nous avons finalement réussie début 2005 à recondenser. Je tiens à ce niveau à remercier l'aide et la compassion apportées par Antoine Browaeys, un grand ancien de l'expérience, qui a su nous faire part de son expérience en termes de condensation. C'est alors que nous avons pu commencer la période exaltante de prise de données, et que nous avons pu observer les premières corrélations. L'enthousiasme que nous avons alors pu partager a été à la base d'une grande joie, et cette période a été véritablement exaltante. Je remercie Rodolphe et Aurélien chaleureusement pour ce temps que nous avons partagé dans la salle de manipulation, pour le meilleur et pour le pire, ainsi que pour leur patience autrement plus importante que la mienne.

L'été 2005, Rodolphe est parti et nous avons été rejoint par Hong Chang et Valentina Krachmalnicoff. Pendant que Aurélien et Hong se sont penchés sur la magnifique expérience des paires atomiques, avec Valentina on s'est donné pour mission d'approfondir nos connaissances sur le détecteur, dans un double but de transmission des connaissances et de répondre à des questions encore ouvertes. Valentina a du faire face à mes compétences obscures en termes de détecteur et d'informatique. Ses nombreuses questions m'ont permis d'éclairer de nombreux points même pour moi, et la (relative) clarté du Chapitre 2 lui doit beaucoup. C'est avec un grand regret que je la laisse, et avec encore de nombreuses problèmes à résoudre; mais je soupçonne que sa grande persévérance en viendra au bout. C'est cette persévérance qui s'est en effet montré très bénéfique quand nous nous sommes enthousiasmé pour l'expérience des corrélations fermioniques.

The Fermionic correlation experience has been possible for various reasons. If

the calendar possibilities as well as the mechanical compatibilities for the detector have been essential, the shared enthusiasm between Orsay and Amsterdam has definitely been the key to its realisation. The unequalled enthusiasm of Wim Vassen together with the latest outstanding achievements of his students John McNamara and Tom Jeltens made the collaboration possible, and this collaboration proved extremely efficient. The time we spend in Amsterdam has been fairly tough, for the high work rythme as well as for those un-air-conditioned hotel rooms in the middle of a heat wave. But I keep an excellent memory of that period as well, and I would like to heartily thank Valentina, John, and Tom as well as Wim and Hong for the excellent time we spend in Amsterdam. Je voudrais remercier particulièrement toutefois Valentina, qui a fait preuve ici encore d'une grande persévérance et a fait par ailleurs un excellent travail dans l'analyse de ces données: je lui souhaite indiscutablement bonne chance dans sa poursuite avec l'expérience. Je souhaite par ailleurs bon courage aux nouveaux entrants sur cette expérience dans la poursuite des corrélations atomiques.

Si la collaboration avec ces collègues a été essentielle, elle ne devrait pas cacher pour autant le travail technique apporté par les techniciens. Je pense en particulier à André Villing et Frédéric Moron, dont l'aide et le travail sur nos besoins électroniques ont été inestimables. De nombreuses fois, nous les avons sollicités avec tel ou tel boîtier qui avait subi les foudres de nos incompétences, mais ils ont toujours répondu présent. Ils sont aussi à l'origine d'une très grande partie des dispositifs électroniques qui font tourner l'expérience. Je leur adresse un grand merci.

Un autre technicien qui a eu un rôle prépondérant sur ce travail de thèse, a été Robert Sellem. Son enthousiasme infatigable pour la mesure du temps a été à l'origine de notre compréhension de ces mesures, et le TDC qu'il nous a fourni a été une pièce maîtresse de l'expérience. Il s'est employé en particulier à rendre son TDC compatible au mieux avec nos besoins déments (mesurer des picosecondes sur une durée de centaines millisecondes à des taux du MHz!). Sans son travail et son TDC, l'expérience se serait fait dans bien d'autres conditions. Il s'est employé en particulier à utiliser son enthousiasme pour diffuser ses compétences à l'ensemble des laboratoires intéressés en créant avec Daielle Doweck et Serge Della Negra la plateforme DTPI (Détection Temps, Position et Image). Je les remercie sincèrement pour cet initiative, qui a permis par ailleurs de nous confronter à beaucoup d'autres utilisateurs de détecteurs à base de galettes à micro-canaux.

Il convient ensuite de remercier l'ensemble des services techniques et administratives de l'Institut d'Optique, qui rendent le travail quotidien possible. En particulier je tiens à remercier l'atelier d'optique qui a bien voulu abriter nos bouteilles d'azote tout le long de ces années. Un autre grand merci au service de maintenance, dont les interventions en cas de gros besoins ont toujours montré leur efficacité. Je remercie le service d'achats pour la grande patience dont ils ont toujours su faire part à l'encontre de mes retards multiples. Je remercie aussi Jean-Louis Tutou du service mécanique du laboratoire Aimé Cotton pour son dévouement dans la construction du bâti de l'enceinte principale. Enfin, un grand merci encore au service des TPs, pour les multiples dépannages que leur matériel a apportés.

This period has also been an opportunity to meet different laboratories through the European Graduate College Interference and Quantum Applications. This collaboration between Glasgow, Hanover and Orsay would certainly not be without the enthusiasm of Eberhard Tiemann and Olivier Dulieu. This college has given me

various opportunities to visit Hanover, and I would like to thank all the members for the good yet instructive time we spend in the various workshops, and more in particular the German members for their hospitality. This college has also driven Haikel Jelassi and Thibault Vogt and me to organise such a workshop. I thank them for their precious work on this event.

De la même manière, l'excellente ambiance qui règne parmi les nombreux étudiants Européens travaillant sur l'optique atomique a été à l'origine de notre organisation de la conférence YAO 2006. Je voudrais remercier à ce propos Aurélien Perrin, Andrés Varón, Gaël Varoquaux et Jean-Baptiste Trebbia avec qui nous avons pu mener à bien cet organisation. Nous avons fortement apprécié le travail et soutien de Francesca Arcara dont l'expérience a été fort utile. Mais c'est surtout grâce au travail de Françoise Chavel et le soutien de la Société Française d'Optique qui nous avons pu mener ce travail dans des conditions optimales. Je lui adresse un très grand merci. Je voudrais par ailleurs remercier l'École Polytechnique, et plus particulièrement Philippe Alquier dont la présence, l'aval et l'efficacité ont été essentiels à la réalisation de cette conférence.

La thèse a aussi été l'occasion de dispenser des cours, et j'ai eu en particulier beaucoup de plaisir à assurer les cours de C. La particularité de ce cours a été le fait que deux enseignants assuraient ensemble un cours, ce qui a permis de créer une certaine proximité. Je remercie donc chaleureusement Nouari Kebaïli, Bruno Grioni, Sylvie Lebrun, Frédéric Capmas ainsi que François Goudail et Arnaud Bénére, pour l'enthousiasme avec lequel nous avons pu préparer et assurer ces cours.

Je voudrais ensuite remercier l'ensemble des personnes du groupe, anciens comme nouveaux, pour la très bonne ambiance qui règne dans ce groupe, ambiance qui contribue indiscutablement à la bonne marche des expériences. Je voudrais décerner en ce sens la palme d'or à Isabelle Bouchoule, qui avec tout son enthousiasme a su partager sa passion de la voile en drainant chaque année une équipage à la régata organisée avec grand dévotion et enthousiasme par le club nautique du CAES du CNRS. L'équipe de l'Institut a réussi à passer, au cours des années, de la dernière place à la seconde. J'ai bon espoir pour que l'année prochaine ils soient premiers. J'espère partager encore de nombreuses sorties de voile avec Isabelle: bon vent en tout cas ! J'adresse donc un merci chaleureux à tous ces collègues avec qui nous avons passé du temps agréable, pendant et en dehors des horaires de travail, et parmi lesquels je garderai un bon nombre d'amis.

Je voudrais enfin remercier mes amis, ma famille et celles qui ont vécu avec ma volonté de mener à bien ce projet de recherche. Je les remercie pour leur soutien indéfectible!

Contents

| | |
|-----------------------------------------------------------------------|-----------|
| Remerciements | 3 |
| Introduction | 11 |
| 1 The Hanbury Brown and Twiss Effect | 15 |
| 1.1 Historical Overview | 17 |
| 1.1.1 Michelson Interferometry | 17 |
| 1.1.1.1 Principle | 17 |
| 1.1.1.2 Theory of Spatial Coherence | 19 |
| 1.1.1.3 Theory of Temporal Coherence | 20 |
| 1.1.1.4 Real World Experiment | 21 |
| 1.1.2 Intensity Interferometry | 22 |
| 1.1.2.1 Principle | 22 |
| 1.1.2.2 Theory | 23 |
| 1.1.2.3 Advantages | 23 |
| 1.1.2.4 Real World Experiment | 24 |
| 1.1.3 The Hanbury Brown and Twiss Effect | 24 |
| 1.1.3.1 The Keystone Experiment | 25 |
| 1.1.3.2 The Principle | 25 |
| 1.1.3.3 The Theory | 28 |
| 1.2 Hanbury Brown and Twiss with Cold Atoms | 31 |
| 1.2.1 Cold Atom Optics | 31 |
| 1.2.2 Hanbury Brown and Twiss Experiments with Cold Atoms | 32 |
| 1.2.2.1 Counting Techniques | 32 |
| 1.2.2.2 Absorption Imaging | 36 |
| 1.3 The Orsay Helium Experiment | 41 |
| 1.3.1 Triplet Metastable Helium | 41 |
| 1.3.1.1 $^4\text{He}^*$ | 41 |
| 1.3.1.2 Inelastic Collisions | 42 |
| 1.3.1.3 $^3\text{He}^*$ | 43 |
| 1.3.1.4 Detection | 43 |
| 1.3.2 The Hanbury Brown and Twiss Experiment With He^* . . . | 44 |
| 1.3.2.1 The Sources | 44 |
| 1.3.2.2 The Experiment | 45 |
| 1.3.2.3 The Theory | 47 |
| 1.3.3 Signal to Noise Ratio | 49 |
| 1.3.3.1 The Detector | 49 |
| 1.3.3.2 The Signal to Noise Ratio | 51 |
| Conclusion | 55 |

| | | |
|----------|----------------------------------------------|------------|
| 2 | The Detector | 57 |
| 2.1 | Detectors Overview | 59 |
| 2.1.1 | Phosphor Screens | 59 |
| 2.1.2 | Charge Division Devices | 60 |
| 2.1.3 | Advanced Charge Division Devices | 61 |
| 2.2 | The Delay-Line Detector | 63 |
| 2.2.1 | The micro-channel plates | 63 |
| 2.2.1.1 | Mechanism | 64 |
| 2.2.1.2 | Multiple micro-channel plates | 65 |
| 2.2.1.3 | Gain and pulse-height distribution | 65 |
| 2.2.1.4 | Flux saturation | 66 |
| 2.2.1.5 | Our Choice | 67 |
| 2.2.2 | The Delay-Line Detector | 68 |
| 2.2.2.1 | Mechanism | 70 |
| 2.2.2.2 | Operating voltages | 71 |
| 2.2.3 | The Electronics | 73 |
| 2.2.3.1 | Analog to Logical | 73 |
| 2.2.3.2 | Logical to Digital | 76 |
| 2.2.4 | The Computer Acquisition | 79 |
| 2.2.4.1 | The Platform Root | 79 |
| 2.2.4.2 | The Interface Heevman | 82 |
| 2.2.4.3 | The Computer Setup | 85 |
| 2.3 | Detector Characteristics | 87 |
| 2.3.1 | Detection Efficiency | 87 |
| 2.3.1.1 | Analog Part | 87 |
| 2.3.1.2 | Atomic Reconstruction | 92 |
| 2.3.1.3 | Measurements | 94 |
| 2.3.2 | Detection Rate | 96 |
| 2.3.2.1 | Local Saturation | 96 |
| 2.3.2.2 | Deadtimes | 97 |
| 2.3.2.3 | Global Detection Rates | 100 |
| 2.3.3 | Resolution | 102 |
| 2.3.3.1 | Measurement Methods | 102 |
| 2.3.3.2 | Dynamics | 105 |
| | Conclusion | 109 |
| 3 | The Results | 113 |
| 3.1 | Thermal Cloud of Bosonic Atoms | 115 |
| 3.1.1 | The Acquisition | 115 |
| 3.1.1.1 | Experimental Conditions | 115 |
| 3.1.1.2 | Acquisition Time | 117 |
| 3.1.1.3 | Data Sets | 117 |
| 3.1.2 | The Analysis | 120 |
| 3.1.2.1 | The Correlation | 120 |
| 3.1.2.2 | The Normalisation Procedure | 122 |
| 3.1.3 | The Results | 124 |
| 3.1.3.1 | Reference Data | 124 |
| 3.1.3.2 | Temporal Correlation | 125 |

| | | |
|---------|--------------------------------------------|-----|
| 3.1.3.3 | Spatial Correlation | 125 |
| 3.1.4 | Measurements | 127 |
| 3.1.4.1 | The Resolution Functions | 128 |
| 3.1.4.2 | The Correlation Lengths | 129 |
| 3.1.4.3 | The Bunching Volume | 131 |
| 3.2 | Bose-Einstein Condensate | 133 |
| 3.2.1 | The Condensates | 133 |
| 3.2.1.1 | Finite Size | 133 |
| 3.2.1.2 | Density and Interactions | 134 |
| 3.2.1.3 | Saturation | 134 |
| 3.2.1.4 | The Data | 135 |
| 3.2.2 | The Analysis | 135 |
| 3.2.2.1 | Saturation | 135 |
| 3.2.2.2 | Problematic Normalisation | 136 |
| 3.2.2.3 | Solution | 138 |
| 3.2.3 | The Result | 140 |
| 3.3 | Thermal Cloud of Fermionic Atoms | 141 |
| 3.3.1 | The Acquisition | 141 |
| 3.3.1.1 | Preparation | 141 |
| 3.3.1.2 | The Experimental Setup | 141 |
| 3.3.1.3 | The Data | 144 |
| 3.3.2 | Results | 146 |
| 3.3.2.1 | Temporal Correlation | 146 |
| 3.3.2.2 | Spatial Correlation | 146 |
| 3.3.3 | Measurements | 147 |
| 3.3.3.1 | The Resolution Functions | 147 |
| 3.3.3.2 | The Correlation Lengths | 148 |
| 3.3.3.3 | The Bunching Volume | 149 |

Conclusion **151**

Appendixes **153**

| | | |
|---------|-----------------------------------------------|-----|
| A.1 | The Resolution Measurement | 155 |
| A.1.1 | Some Considerations | 155 |
| A.1.1.1 | Number of Pixels | 156 |
| A.1.1.2 | The Resolution | 156 |
| A.1.1.3 | The Jitter | 157 |
| A.1.2 | The Time Sum | 157 |
| A.1.2.1 | The Plain Distributions | 157 |
| A.1.2.2 | The Link to the Resolution | 158 |
| A.1.2.3 | Discussion | 159 |
| A.1.3 | Real Case Study | 159 |
| A.1.3.1 | The Time Sum Maps | 159 |
| A.1.3.2 | The Time Sums | 161 |
| A.2 | The Atomic Reconstruction Algorithm | 163 |
| A.2.1 | The Time Bulb Algorithm | 163 |
| A.2.1.1 | The Data | 163 |
| A.2.1.2 | The Time Bulbs | 163 |

| | | |
|---------|----------------------------------------|------------|
| A.2.1.3 | Scaling | 164 |
| A.2.2 | The Extrication Procedure | 165 |
| A.2.2.1 | Round 1: the Cleaning | 165 |
| A.2.2.2 | Round 2: the Simple Cases | 165 |
| A.2.2.3 | Round 3: the Disentanglement | 166 |
| A.3 | The Oscilloscope Detection | 169 |
| A.3.1 | The Setup | 169 |
| A.3.2 | The Analysis | 170 |
| A.3.3 | Discussion | 171 |
| | Résumé | 173 |
| | Publications | 187 |

Introduction

The Hanbury Brown and Twiss effect has been first demonstrated in 1956 [1], by Robert Hanbury Brown and Richard Q. Twiss. The initial idea was to overcome the limitations of Michelson interferometry in regard to the measurement of angular sizes of stellar objects. Fluctuations of the atmosphere blur the interference patterns and induce the need for large and expensive telescopes. They consequently invented the principle of intensity interferometry [2]. In their field of radio astronomy, this method opened new possibilities [3]. Yet when they applied a similar technique to a thermal light source [1], the correlations they demonstrated among photons puzzled the scientific community .

They showed that the photons provided by a chaotic light source were correlated. They demonstrated that the probability for photons to be grouped was larger than the probability for the photons to be randomly distributed. This bunching behaviour of independent photons opposed the still classical idea some scientists had about photons. The experiment therefore was a breakthrough in modern physics, and it took Roy J. Glauber up to 1962 [4, 5] in order to build up a complete theoretical description of the photonic quantum phenomena. This experiment, and the theory related, opened the way to modern quantum optics. In 2005 Roy J. Glauber has been awarded a Nobel prize in Physics precisely for his work on the Hanbury Brown and Twiss effect and his quantum field description of light.

Nowadays, the Hanbury Brown and Twiss effect is used in various fields ranging from astronomy to particle physics. The Hanbury Brown and Twiss correlation is a quantum effect applying to all particles. Observations have been made with bosonic photons, as well as fermionic electrons [6, 7, 8]. Its observation on macroscopic atoms was still a landmark to set. Masami Yasuda and Fujio Shimizu realised this exploit in 1996 by observing the correlations between Laser cooled metastable Neon atoms [10].

The field of cold atom physics has since reached much lower temperatures, specifically through the use of evaporative cooling techniques, and Bose-Einstein condensation has eventually been reached in 1995 [11, 13, 12]. The Bose-Einstein condensation of metastable Helium atoms in 2001 [14, 15] opened the way to further investigation, and in particular to the measurement of the fundamental change of the Hanbury Brown and Twiss effect at the condensation threshold. The evaporative cooling of fermionic metastable Helium atoms in 2006 [16] made it further possible to measure the Hanbury Brown and Twiss on fermionic neutral particles.

The realisation of the Hanbury Brown and Twiss experiment with metastable Helium atoms would for sure be an interesting measurement. But more interestingly, the capability of measuring this effect would demonstrate the possibility to perform measurements at the phase-space cell scale. This means that such a realisation would render possible quantum correlation measurements in virtually any quantum system that can be build in modern cold atom physics. That is the larger

motivation behind this present work.

This Thesis

This thesis describes the realisation of those experiments, as carried out over the period 2003-2006. As a member of the metastable Helium setup team of the group of Atomic Optics at the Institut of Optics in Orsay, my work has been supervised by Christoph Westbrook. During those years, we progressively went from the preparation of the setup, which implied a long fight with the atom cooling setup, to the effective realisation of the experiments and analysis of the experimental data. Particular time and energy has been invested in the implementation and understanding of the detection chain.

This thesis has taken particularly care in describing the Hanbury Brown and Twiss effect and our proposed implementation of its measurement. It focuses extensively on the detection method, as the detector is the key to the measurement. Finally it handles the experimental measurements as realised on thermal and Bose condensed ^4He atoms in 2005 at the Institut of Optics in Orsay [17], and on thermal fermionic ^3He atoms as realised in 2006 at, and in collaboration with, the Laser Centrum of the Free University in Amsterdam [18].

Although the author of this thesis has actively participated to the outcome of this research, the results presented undeniably results from a team work. With Rodolphe Hoppeler and Denis Boiron, we underwent the painful unmounting and reconstruction of the experimental setup, necessary to the integration of the detector. We were joined in the summer of 2004 by Aurelien Perrin for the effective Bose-Einstein condensation and the acquisition and analysis of the experimental ^4He data in Orsay. The insight of Alain Aspect and Christoph Westbrook proved particularly useful to the understanding, analysis and publication of the results. The team lost Rodolphe Hoppeler yet was completed by Hong Chang and Valentina Krachmalnicoff during the summer of 2005. With the latter, we have focused on a deeper understanding of the detection deficiencies, and on the upgrade of the detection capacities. The experimental work realised in Amsterdam by John McNamara, Tom Jeldes and Wim Vassen, and their control of their experimental setup, was the key to our collaboration as to the Amsterdam measurements. The theoretical analysis has essentially been performed by Denis Boiron, Jose Viana Gomes and Michael Belsley [19].

The Layout

The layout of this thesis is subdivided in three chapters. The first Chapter deals with the Hanbury Brown and Twiss effect. We give a historical background to its measurement and come to a simple understanding and theory. We then will see the particular interest of the cold atomic optics field as to the Hanbury Brown and Twiss effect, and we will study briefly various other experimental measurements of the Hanbury Brown and Twiss effect in this field, that have been carried out previously or during the presented work. Finally, we will focus on the proposed measurement of the Hanbury Brown and Twiss effect with metastable helium and a micro-channel plate based position sensitive detector, and we will provide a simple, yet complete theoretical understanding.

The second Chapter deals with the detection chain. We briefly discuss the various detector options we had. We then will analyse the entire chain of the micro-channel plate based delay-line detector, the only detector that seemed up to our requirements. We will then concentrate on three crucial characteristics of the detector: the detection efficiency, the detection rate and the resolution.

The third Chapter deals with the acquisition and analysis of the experimental results. We first deal with the thermal ^4He clouds acquired in Orsay, that demonstrate the Hanbury Brown and Twiss effect. We then analyse the acquisition of some Bose-Einstein condensate clouds, whose coherence induces the absence of the Hanbury Brown and Twiss effect. Finally we will deal with the fermionic ^3He clouds acquired in Amsterdam, that demonstrate a negative Hanbury Brown and Twiss effect.

The Hanbury Brown and Twiss Effect

Through this chapter, we will study the Hanbury Brown and Twiss effect. The purpose of the first section is to give an overview of what was historically the Hanbury Brown and Twiss experiment. The idea is to demystify the experiment on one side, yet to show its originality and importance. We will remain in the world of photonic optics as most readers are more familiar with the concepts involved.

The second section will deal with the Hanbury Brown and Twiss effect in cold atom optics. We will briefly describe up to what extent cold atoms are an excellent system for the study of this effect. We will then focus on several experimental measurements that have been performed previously, or during the ongoing of this present study.

The last section of this chapter deals with the proposed measurement with metastable Helium. We will recall briefly why He^* is particularly suitable for a Hanbury Brown and Twiss type measurement. We will then describe the experimental setup, and analyse the theory of the experiment. We will finally conclude on several characteristics required for the detector, by outlining the expected signal to noise ratio.

1.1 Historical Overview

Robert Hanbury Brown (1916-2002) was a physicist and astronomer who pioneered the development of radar and radio astronomy. Having worked during the Second World War on radar systems, Hanbury Brown decided to use his acquired knowledge in radio technology to tackle a century old problem: measuring the angular sizes of stars.

A first such measurement had been performed by Galileo Galilei [20]. Using a fine cord to eclipse Vega, and considering his distance to that cord, he measured the angular diameter to be 5 seconds of arc. Although undertaken in a very precise way, this method gave a result three orders of magnitude off.

A first theoretical estimation was made by Isaac Newton. He considered that if the sun were a stellar object like the stars, and if it were removed to a distance that would make it a first magnitude star, then it would have an angular diameter around $2 \cdot 10^{-3}$ seconds of arc. This result is very close to the latest estimates of Vega.

The third notable attempt was performed by Albert A. Michelson and Francis G. Pease in 1920 [21, 22]. They used a technique called amplitude interferometry, since then often referred to as Michelson Interferometry.

We will have a short overview of this technique and its limits. Then we will study an improved scheme of this technique as proposed by Hanbury Brown and Twiss: the intensity interferometer. Finally we will see how this last technique troubled many physicists who had a photonic vision of light, and led to the so called Hanbury Brown and Twiss effect.

1.1.1 Michelson Interferometry

1.1.1.1 Principle

The idea behind Michelson interferometry is mostly a Young slit experiment as shown in Figure 1.1A

If a pointlike quasi-monochromatic light source of wavelength λ lights a screen through a slit P_1 , a squared sinc-function will show up. The observed figure is the diffraction pattern of the slit. If a second slit P_2 is introduced at a distance a from the first, the sinc-function is modulated by a sinusoid of spatial frequency $L \frac{\lambda}{a}$, where L is the distance from the slits to the screen. This results from the two quantum paths that the photons can follow. Those paths interfere with spatially dependent relative phases, which gives the fringe pattern. In the case of a pointlike light source, the contrast between the fringes is unity. This means that the dark bands receive no light at all.

The position of the central bright band, band that is defined by the relative phase between the two paths being zero, is defined by the geometry. If another pointlike light source is introduced, slightly off in position, the observed interference and diffraction pattern of this second light source is identical, but slightly displaced. If now both sources are mutually incoherent and illuminate the double slit, the resulting intensity pattern is the sum of the independently obtained intensity patterns. This has the effect of blurring out the individual patterns, and as such, reduce the contrast of the fringes.

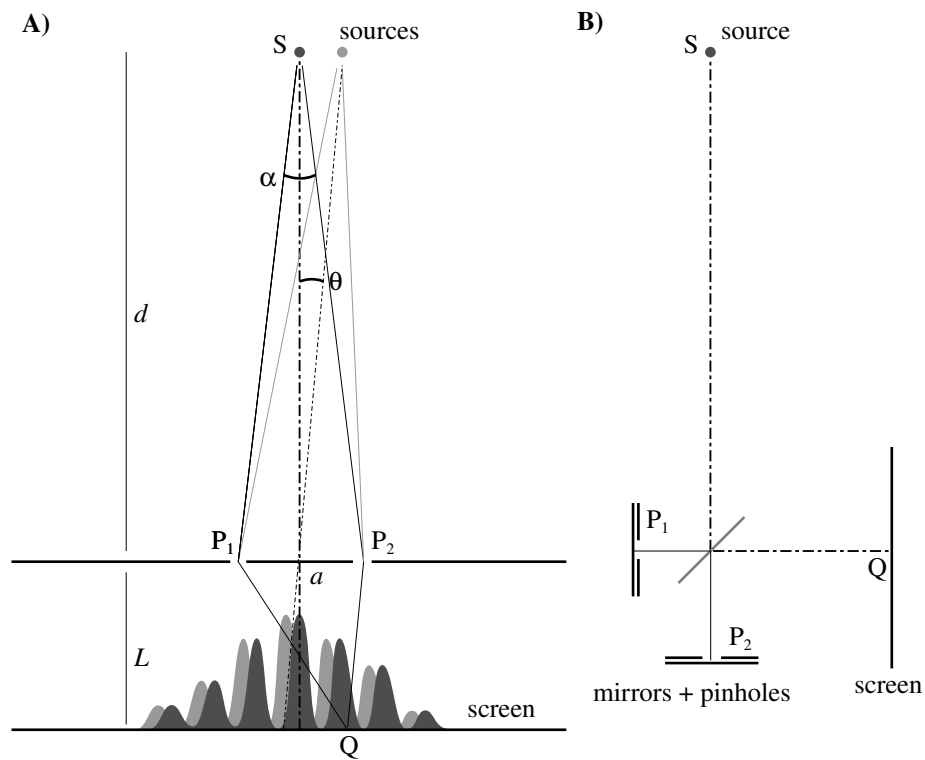


Figure 1.1: In A, the Young slit experiment. The light amplitudes that go through the two slits add up on the screen. The perceived intensity is the square of this amplitude sum. In B, a Michelson interferometer. The light provided by a source s shines on a semi-transparent mirror. The two out-coming fields are retro-reflected on two pinhole mirrors that have a different distance as to the semitransparent mirror where the light fields recombine. The interference is observed on a screen.

In a more general way, if the quasi-monochromatic incoherent light source is non pointlike, but has an angular size as seen from the slits, the contrast of the fringes is reduced. Measuring the contrast of the fringes therefore amounts to measuring the angular size of the source.

Conversely, if one changes the separation of the two slits, the fringes become narrower whereas the separation between fringes pattern does not change. This means we also have a dependence of the contrast on the separation of the pinholes.

1.1.1.2 Theory of Spatial Coherence

In a classical description of light, the light amplitude at a given point in space will be expressed as the real part of an amplitude $A(t)$. The light Amplitude at point Q can then be expressed as:

$$A_Q(t) = t_1 A_1(t) + t_2 A_2(t + \tau) \quad (1.1.1)$$

where t_1 and t_2 are the complex amplitude transmission factors for the two slits, A_1 and A_2 their light amplitudes. The τ translates the time difference for the two beams to reach Q from P_1 and P_2 .

The intensity of the light at Q is the time average of the square of the real part of the amplitude, that can be written:

$$I_Q = \langle A_Q^*(t) A_Q(t) \rangle_t \quad (1.1.2)$$

where the brackets represent the time average. Introducing 1.1.1, we then obtain:

$$I_Q = |t_1|^2 I_1 + |t_2|^2 I_2 + 2 \text{Re}(t_1 t_2 \Gamma_{12}(\tau)) \quad (1.1.3)$$

where $\Gamma_{12}(\tau)$ is the amplitude correlation function at the two slits defined by:

$$\Gamma_{12}(\tau) = \langle A_1^*(t) A_2(t + \tau) \rangle_t \quad (1.1.4)$$

If we consider that those light amplitudes are produced by a distant extended spatially incoherent quasi-monochromatic source σ of wavelength λ , they can then be expressed as the sum of the amplitudes originating from the various source elements:

$$A_i(t) = \int_{\sigma} \frac{A(x, y, t - \|S(x, y)P_i\|/c)}{\|S(x, y)P_i\|} dx dy \quad (1.1.5)$$

where $\|S(x, y)P_i\|$ is the distance from the source element to the Young slit. If we call d the average distance from the slits to the source, and we consider d much larger than the typical source size, we then obtain:

$$\Gamma_{12}(0) = \left\langle \int_{\sigma} \int_{\sigma} A^*(x, y, t - \|S(x, y)P_1\|/c) A(x', y', t - \|S(x', y')P_2\|/c) \frac{dx dy dx' dy'}{d^2} \right\rangle_t \quad (1.1.6)$$

This double integral averages to zero if $(x, y) \neq (x', y')$, whereas for $(x, y) = (x', y')$ the two amplitudes have a spatially defined phase relationship:

$$\Gamma_{12}(0) = \int_{\sigma} \frac{I_{\sigma}(x, y)}{d^2} e^{\frac{2\pi i}{\lambda} (\|S(x, y)P_1\| - \|S(x, y)P_2\|)} dx dy \quad (1.1.7)$$

If we consider the two slits at equal distance from the source, yet with an angular separation α , this expression simplifies to:

$$\Gamma_{12}(0) = \frac{1}{d^2} \int_{\sigma} I_{\sigma}(x, y) e^{-i\frac{2\pi}{\lambda} x \alpha} dx dy \quad (1.1.8)$$

This is a form of the Cittert-Zernike theorem [84]. It tells us that the amplitude correlation at the two pinholes is the Fourier transform of the intensity distribution at the source. We define the normalised correlation γ_{12} function as:

$$\gamma_{12}(\alpha, 0) = \frac{\Gamma_{12}(0)}{\sqrt{I_1 I_2}} = \frac{\int_{\sigma} I_{\sigma}(x, y) e^{-i\frac{2\pi}{\lambda} x \alpha} dx dy}{\int_{\sigma} I_{\sigma}(x, y) dx dy} \quad (1.1.9)$$

We note that $\gamma(0, 0) = 1$ is the maximum value the function can reach. This function describes the spatial coherence of the source. For a non punctual light source, the angular width of $\gamma(\alpha, 0)$ is inversely proportional to the spatial width of the source. We define the coherence angle $\alpha_c = \lambda/D$, with D the diameter of the source. By multiplying with the distance to the source, we get the coherence length:

$$l_c = \lambda/\theta \quad (1.1.10)$$

with θ the angular size of the source as seen from the pinholes.

1.1.1.3 Theory of Temporal Coherence

If we now consider the source being no longer quasi-monochromatic but pointlike, we rather define its frequency components:

$$A(t) = \int_0^{+\infty} a(\omega) e^{i\omega t} d\omega \quad (1.1.11)$$

Furthermore we consider the angle between the pinholes $\alpha = 0$. This means that the pinholes coincident as seen from the source. We increase the distance to the source for pinhole 1, which can be performed through an optical setup as demonstrated in Figure 1.1B. The amplitude correlation function will then be:

$$\Gamma_{12}(\tau) = \langle A_1^*(t) A_2(t + \tau) \rangle_t \quad (1.1.12)$$

where $\tau = \delta d/c$ and δd the displacement of pinhole 1. Using the notation in 1.1.11, this expression changes into:

$$\Gamma_{12}(\tau) = \int_0^{+\infty} a^*(\omega) a(\omega) e^{-i\omega \tau} d\omega \quad (1.1.13)$$

We call $G(\omega) d\omega = a^*(\omega) a(\omega) d\omega$ the spectral density of the light. We obtain the result of the Wiener-Khinchin theorem [85] that tells us that the autocorrelation of a stationary random process is given by the Fourier transform of its power spectrum.

We can again define the normalised amplitude correlation function:

$$\gamma(0, \tau) = \frac{\Gamma_{12}(\tau)}{\sqrt{I_1 I_2}} = \frac{\int_0^{+\infty} G(\omega) e^{-i\omega \tau} d\omega}{\int_0^{+\infty} G(\omega) d\omega} \quad (1.1.14)$$

We note that this function maximises to 1 for $\tau = 0$. It describes the temporal coherence of the source. For a non monochromatic stationary light source, the temporal width of $\gamma(0, \tau)$ is inversely proportional to the spectral width of the source. We define the coherence time:

$$t_c = 2\pi/\Delta\omega = 1/\Delta\nu \quad (1.1.15)$$

with $\Delta\nu$ the spectral width of the source.

1.1.1.4 Real World Experiment

In order to study the angular sizes of stars, Michelson used a telescope as represented in Figure 1.2. They measured with this telescope angular sizes of typically 20ms of arc with visible light. That requires a variable distance between the Young-slit mirrors of a few meters.

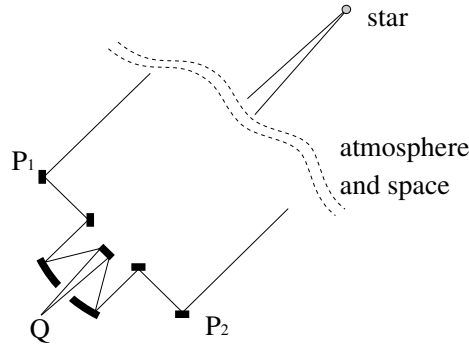


Figure 1.2: The Michelson telescope. Two outer mirrors send the light to a central telescope where they get overlapped. The contrast between the fringes can then be measured at point of observation Q . A stabilised mounting as well as a fast integration time have to compensate for the blurring due to atmospheric fluctuations as well as mechanical vibrations.

The problem lies in the phase dependency between the two paths. If the path difference changes in time, between the source and the slits due to atmospheric perturbations, or between the slits and the observation point Q due to the mechanical instability of the telescope, the temporal integration necessary to observation would blur out the contrast.

Indeed if we introduce a time depending phase difference $\phi(t)$ in formula 1.1.6 it simplifies to the following expression:

$$\Gamma_{12}(0) = \frac{1}{d^2} \int_{\sigma} I_{\sigma}(x, y) \langle e^{-i(\frac{2\pi}{\lambda} x\alpha + \phi(t))} \rangle_t dx dy = 0 \quad (1.1.16)$$

At the time of those measurements in 1920, this observation was done through the trained eye of Michelson, who had to estimate instantaneously the contrast. Even the best trained eye still needs a 10 ms integration time. Consequently, the two arms of the telescope had to be severely stabilised.

Michelson worked with the full spectral range of the stars. Besides the fact that the spatial coherence length of 1.1.10 still had to be convoluted with the effect

of this spectral width, the temporal distances from the slits to the source had to be within the coherence time of the source. That translates to a spatial control of the mirrors of 400 nm. With the required mechanical stability, such a telescope is already a master piece.

Furthermore, the polishing of the mirrors had to be within wavelength control, else the fringes figure would blur out. This has certainly limited the sizes of the mirrors. Consequently, the luminosity at the observation point was limited, and the observation time limited by millisecond fluctuations of the atmosphere. In order to see anything, full spectral range was required.

The measurements made by Michelson in 1920 were made with a 6m telescope. Further attempts with a 15m telescope did not give reproduceable results. Consequently, this technique was limited to only a very small range of large angular first magnitude stars.

1.1.2 Intensity Interferometry

Hanbury Brown initially wanted to measure the angular size of two radio sources: Cygnus A and Cassiopeia A. Theories ranges those sizes from minutes to milliseconds of arc. At the frequency of 125 MHz at which they worked, this would need the slit separation in the worst case as large as the earth. That experiment required two coherent independent oscillators as time references, a technique that was not under control in 1949. In order to circumvent this necessity, Hanbury Brown and Twiss thought of doing intensity interferometry [2, 3].

After the study of what intensity interferometry is, we will outline the advantages it has over Michelson interferometry, whereafter we will have a short outlook at some real life experiments produced by Hanbury Brown and Twiss.

1.1.2.1 Principle

An intensity interferometer is essentially a speckle measurement apparatus. A non-punctual incoherent light sources, seen from a screen with an angular size θ , produces a speckle pattern on this screen, as shown in figure 1.3.

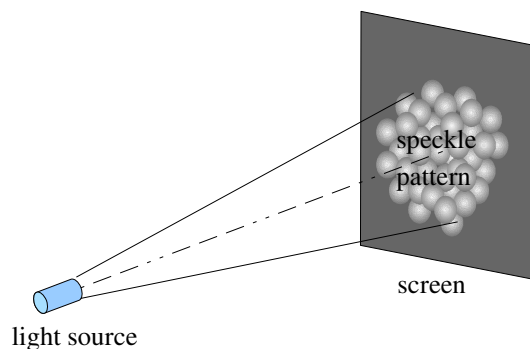


Figure 1.3: The speckle pattern produced by a spatially incoherent light source.

The characteristic size of the spatial dependence is of the order of the spatial coherence l_c . The characteristic time at which this pattern evolves is of the order of

the time coherence t_c . For most sources, this evolution is sufficiently quick compared to the detector integration time, that the speckle averages to a homogeneously lighted screen. Observation of this pattern therefore requires either limiting considerably the spectrum of the source, or working with a very fast detector.

1.1.2.2 Theory

In order to measure the typical size of the speckle fluctuations, we only have to look at the spatial correlation between the intensities of two points $P_1(t)$ and $P_2(t)$ evolving at the screen. the intensities are given by:

$$I_1(t) = A_1^*(t)A_1(t), I_2(t) = A_2^*(t)A_2(t) \quad (1.1.17)$$

The intensity correlation function is obtained by:

$$\langle I_1(t)I_2(t+\tau) \rangle_t = \langle A_1^*(t)A_1(t)A_2^*(t+\tau)A_2(t+\tau) \rangle_t \quad (1.1.18)$$

If the amplitudes are random gaussian variables, that is the case for a classical light source, this expression can be developed to:

$$\langle I_1(t)I_2(t+\tau) \rangle_t = \langle A_1^*(t)A_1(t) \rangle_t \langle A_2^*(t+\tau)A_2(t+\tau) \rangle_t + \langle A_1^*(t)A_2(t+\tau) \rangle_t \langle A_2^*(t+\tau)A_1(t) \rangle_t \quad (1.1.19)$$

This can be simplified to:

$$\langle I_1(t)I_2(t+\tau) \rangle_t = I_1I_2 + \Gamma_{12}^2(\tau) = I_1I_2[1 + \gamma^2(\alpha, \tau)] \quad (1.1.20)$$

We note that the root-mean-square intensity correlation lengths and times are $\sqrt{2}$ times smaller then those obtained for the amplitude correlation.

1.1.2.3 Advantages

The single advantage of intensity correlation over amplitude correlation lies in the fact that the method is not sensitive to small relative phase fluctuations, as long as the difference in path length remains below the correlation time. If we introduce a random phase fluctuation in the amplitude, it gets eliminated as we are doing an intensity measurement.

This difference has yet huge practical consequences. As the fluctuations have no longer any effect, the measurement can be integrated over much longer times, eventually several separated nights. This makes it possible to strongly reduce the spectral width of the source or the bandwidth of the detector, having for consequence the significant increase of the correlation time.

This has for mechanical consequence that the collecting optics can be of very poor quality as well as that their relative position to the source does not need nanometric precision. Furthermore, if the bandwidth is within the acquisition possibilities of the electronics, the data acquired at both points P_1 and P_2 can be saved away and treated *a posteriori*.

Finally, the only limitation to the bandwidth narrowing is the spectral density and human patience. One still needs a significant signal to noise ratio which is obtained through averaging. If one halves the bandwidth of the detector, the measured intensity correlation is divided by a factor 4. If shot noise is limiting the signal to noise ratio, this bandwidth reduction has to be compensated by a fourfold acquisition time. This number squares with the bandwidth reduction factor.

1.1.2.4 Real World Experiment

A schematic design of the first telescope used by Hanbury Brown to measure the angular sizes of Cygnus A and Cassiopeia A is given in Figure 1.4.

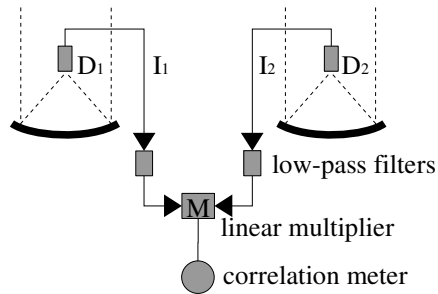


Figure 1.4: A schematic design of the first intensity interferometer at Jodrell Bank. Two radio telescopes focalise the signal on two radio detectors. A 2 kHz wide filter isolates the 150 MHz frequency. The low frequency components could be send over a telephone line for an electronic correlation.

Together with Jennison and Das Gupta, they changed a traditional radio interferometer into an intensity interferometer. They worked at 150 MHz central frequency, and, as the telescopes were eventually separated for very long distances, with a bandwidth of 2 kHz as to send the intensity fluctuations over the telephone line.

Although the interferometer was compatible with thousands of kilometers wide separations, the maximum required separation proved to be of only a few kilometers, as the sources proved much larger (several minutes of arc) than expected.

Yet the concept of intensity interferometry was proven and the results have stood the test of time so far. The next step was to build an intensity interferometer that would work in the optical spectrum. This proved yet rather difficult as some physicians were to be convinced of the impossible thing.

1.1.3 The Hanbury Brown and Twiss Effect

As long as Hanbury Brown and Twiss were working in the radio spectrum, a classical wave description of the phenomena was of common acceptance as those waves could both be visualised and generated with oscillators. The results of this work were accepted. Yet within the field of the optical spectrum, a particle description of light was prevalent among the physicists. In the particle world, the translation of this intensity correlation was that the photons would arrive grouped together at the detector. Indeed, if the intensity detectors were photon detectors, then the probability of detecting a second photon close to a first one would be double that of detecting it far away.

Physicists argued that if the source were completely random, how could those statistically independent photons be grouped, or bunched? As the theoretical work of Hanbury Brown and Twiss on that subject did not seem to convince everyone, a proof of concept experiment was necessary [1].

1.1.3.1 The Keystone Experiment

The schematic design of this Hanbury Brown and Twiss experiment is given in Figure 1.5. With the help of a mercury lamp, providing a high spectral density for certain wavelengths, a spectral filter, to keep only one wavelength, and a pinhole, they produced a very bright narrow bandwidth nearly punctual source. Two independent photon amplifiers, a quantum detector brand new at the time, were optically overlapped with the help of a beam splitter. A mechanical system allowed one of the detectors to be spatially moved, so that the angular separation as seen from the source could be tuned. They could consequently study the spatial correlation.

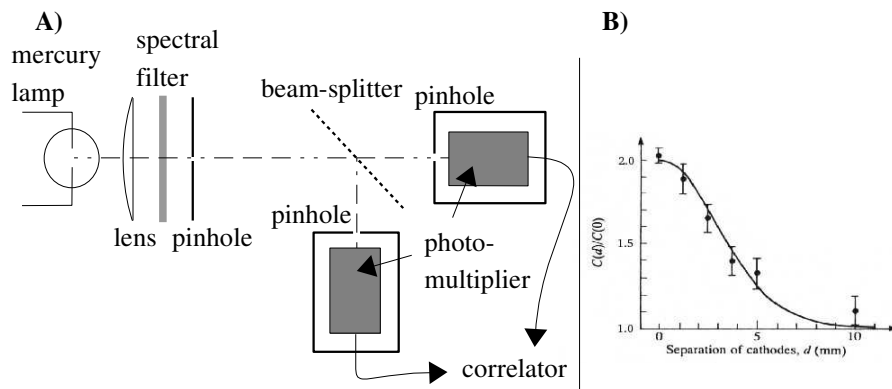


Figure 1.5: In A, the experimental setup for the Hanbury Brown and Twiss experiment for photons. A mercury source light combined with a filter produces a narrow bandwidth intense source. The lens with the pinhole produces the small size. One photo-multiplier can move transversely in respect to the optical path, changing the spatial separation between the detectors. In B, the results of the correlation measurement. For a small spatial separation, the probability of detecting two photons at the two detectors is double that probability when the detectors are separated. The thermal photons are preferably grouped. (Figures A adapted from [1], B extracted from [1])

The results were convincing and proved that indeed those independently emitted photons were actually grouped. As Hanbury Brown and Twiss stated in their conclusion:

This experiment shows beyond question that the photons in two coherent beams of light are correlated, and that this correlation is preserved in the process of photoelectric emission.

1.1.3.2 The Principle

The explanation of this phenomena resides in a proper description of the light source, that has to take into account the bosonic nature of the photons, as well as a geometrical description of the system.

Let us consider the system as displayed in Figure 1.6. We consider a photon arriving from the source to the detector D_1 . The initial position of this photon, at the point of emission, is defined within the Δx and Δy transverse sizes of the source. Yet considering the arrival of this photon at detector D_1 , we also have a

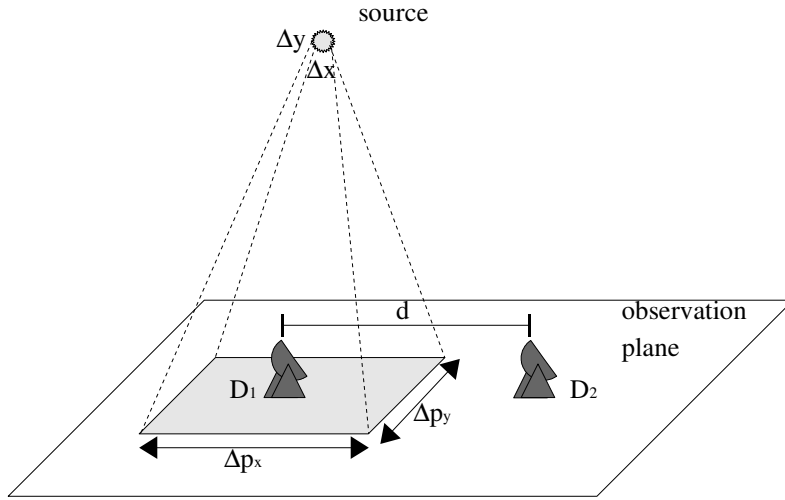


Figure 1.6: If a photon arrives from an extended source to a specific point, both its initial position and speed are defined. The product of the two have yet to remain above a quantum limit. This defines an area in the plane in which the photons belong to the same quantum state. The detectors can either be within or outside their respective geometrically defined quantum state area.

precise measurement of the equivalent momentum of the photon. We do yet know that for a particle in a specific quantum state, the product of the transverse position and momentum can only be measured within the limit $\Delta x \Delta p_x = \hbar/2$, where \hbar is the reduced Planck constant.

If we consider as previously θ the angular size of the source as seen from the detector, and L the distance from the source to the observation plane, we have $\Delta x = L\theta$. We are looking for the angular fluctuation α of the momentum h/λ possible for a same quantum state. We obtain $\alpha = \frac{\lambda}{2\theta L}$. When we consider the spatial distance d between two photons having Δp_x difference in momentum in the observation plane, we find:

$$d = \frac{\lambda}{2\theta} = l_c/2 \quad (1.1.21)$$

Consequently, if two similar photons are detected by the two detectors at a distance within $l_c/2$, those photons are in the same quantum state. If they are measured at a distance much larger than $l_c/2$, those photons behave in different quantum states.

Thermal source All we need now is a correct understanding of the quantum states occupation factors. We work with a white source at thermal equilibrium. In such a source, the average occupation factor of the quantum states is very small compared to 1. Yet for a particular quantum state, and in the case of bosonic particles, this occupation factor is either 0, 1, 2 or more with decreasing probabilities. If a new photon is produced inside the source, its probability to join an empty quantum state $|n_k = 0\rangle$ can be written $|a_k^\dagger |n_k = 0\rangle|^2 = a^2$. Its probability to join a quantum state with a 1 occupation factor is yet $|a_k^\dagger |n_k = 1\rangle|^2 = |\sqrt{2}a_k^\dagger |n_k = 0\rangle|^2 = 2a^2$.

In other words, the probability of having a second photon in a quantum state considering that there is already one, is double that of having this second photon in any quantum states.

Those two considerations together lead to the already announced result; the probability to measure two photons in a specific configuration at distance within the coherence length is double the probability to find two photons in a specific configuration at distance much larger than the coherence length.

Note that a similar explanation can be build up around the temporal coherence and the relation ship between time and energy of a quantum state.

Coherent Source If we consider the case of a coherent source, such as a transverse monomode Laser, then all the photons are in the same quantum state. Consequently, there is no consideration to as whether or not the photons are in the same quantum state. Also there will not be any spatial dependence of the normalised intensity correlation function. Note that finding a photon outside the coherence area calculated previously is of extremely low probability.

Fermionic Source As it happens, photons are bosons. Yet the explanation stated previously is absolutely not specific to photons. It depends in no way on the electromagnetic nature of those particles. Consequently, one can wonder how other, for instance massive particles, would behave. For sure one would have to define a different coherence time and length; we will address that problem in the next section.

Let us consider the case of fermionic particles. An important law ruling those particles is the Pauli exclusion principle. Two indistinguishable fermions cannot be in the same quantum state. This means that if a Hanbury Brown and Twiss type experiment were performed with fermions, at distances small compared to the correlation length, the simultaneous detection of two particles is impossible. The particles will show an antibunching behaviour!

It is interesting to realise that for the photons, we have both a classical wave theory and a quantum description to understand the bunching behaviour of photons. For the fermions, there is no such classical theory available. Only a quantum description can provide an understanding of the fermionic antibunching. The three behaviours have been summarised in Figure 1.7.

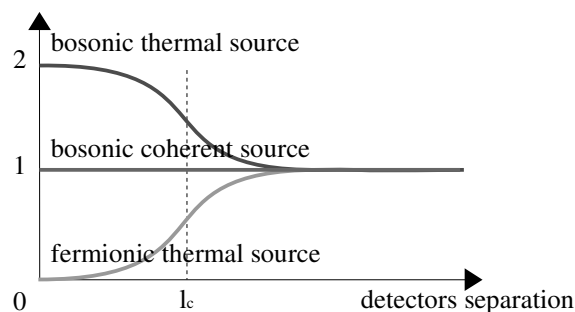


Figure 1.7: The three normalised correlation functions for respectively a bosonic thermal source, a bosonic coherent source and a fermionic thermal source.

1.1.3.3 The Theory

A complete theoretical description of the photonic quantum phenomena has been made by R. Glauber [4, 5] in 1962. The quality of the employed formalism with which he described the correlation phenomena triggered many further studies, both theoretical and experimental. It opened the way to modern quantum optics. This is why Glauber has been awarded the Nobel prize of Physics for precisely this work in 2005.

We will consider here a brief overview of this theory, and introduce some definitions. More specifically, we will have a brief overview of the properties of the quantum correlation functions for bosonic and fermionic sources

Quantum Detection The first important consideration to make is the fundamental difference in the description of the detection of light between the classical and quantum theory. Where the classical wave description measures the instantaneous squared wave amplitude, the quantum theory destroys photons. This has some important, non classical consequences. The light field is affected by the detection as it loses a photon at every single detection, and consequently one cannot perform more measurements then the light field contains photons. We will more generally call $\Psi(\mathbf{r}, t)$ the particle annihilation operator responsible for the detection at a position \mathbf{r} and at a time t . Likewise we call $\Psi^\dagger(\mathbf{r}, t)$ its Hermitian adjoint particle creation operator. Those operators can be expressed:

$$\Psi(\mathbf{r}, t) = \sum_n \phi_n(\mathbf{r}, t) \hat{a}_n \quad \Psi^\dagger(\mathbf{r}, t) = \sum_n \phi_n^*(\mathbf{r}, t) \hat{a}_n^\dagger \quad (1.1.22)$$

where $\{\phi_n(\mathbf{r}, t)\}_n$ is a basis of the system, \hat{a}_n and \hat{a}_n^\dagger respectively the traditional annihilation and creation operators in this basis.

Although those operators have sometimes been considered as mathematical constructs as the positive and the negative frequency part of the field operator, it must be realised that their individual properties are fundamental.

As we said, the detection process brings the quantum field from an initial state $|i\rangle$ to a final state $|f\rangle$, the associated probability amplitude is:

$$\langle f | \Psi(\mathbf{r}, t) | i \rangle \quad (1.1.23)$$

The probability of detecting a particle in the field $|i\rangle$ is then the sum of the probabilities over all final fields:

$$\sum_f |\langle f | \Psi(\mathbf{r}, t) | i \rangle|^2 = \sum_f \langle i | \Psi^\dagger(\mathbf{r}, t) | f \rangle \langle f | \Psi(\mathbf{r}, t) | i \rangle = \langle i | \Psi^\dagger(\mathbf{r}, t) \Psi(\mathbf{r}, t) | i \rangle \quad (1.1.24)$$

We note immediately that the two operator do not commute. If we consider the vacuum state $|vac\rangle$, we have in the general case:

$$\langle vac | \Psi^\dagger(\mathbf{r}, t) \Psi(\mathbf{r}, t) | vac \rangle = 0 \neq \langle vac | \Psi(\mathbf{r}, t) \Psi^\dagger(\mathbf{r}, t) | vac \rangle \quad (1.1.25)$$

simply because no particles can be detected, but can be created.

The two particle detection process, as considered by Hanbury Brown and Twiss' experiment, detects two individual photons at two places and times:

$$\langle f | \Psi(\mathbf{r}', t') \Psi(\mathbf{r}, t) | i \rangle \quad (1.1.26)$$

The associated probability to the double particle detection is proportional to:

$$\langle i | \Psi^\dagger(\mathbf{r}, t) \Psi^\dagger(\mathbf{r}', t') \Psi(\mathbf{r}', t') \Psi(\mathbf{r}, t) | i \rangle \quad (1.1.27)$$

In order to have a statistical description of those detection processes, one still has to average over all possible initial states.

Correlation Functions Experimentally one can rarely fully control the preparation of the initial state. It often merely obeys some statistics. We therefore define a density matrix ρ . The probability of finding the system in a state $|i\rangle$ is equal to $\rho_{ii} = \langle i | \hat{\rho} | i \rangle$. The statistical average of an observable \hat{O} of the system can then be written:

$$\langle \hat{O} \rangle = \text{tr}(\hat{\rho} \hat{O}) \quad (1.1.28)$$

where $\text{tr}()$ is the trace function of the matrix. Naturally $\text{tr}(\rho) = 1$.

The detection probability is proportional to 1.1.24 in case of a completely specified quantum state. In case of a non-fully defined initial state, this probability is more generally proportional to:

$$\text{tr}(\hat{\rho} \Psi^\dagger(\mathbf{r}, t) \Psi(\mathbf{r}, t)) = \rho(\mathbf{r}, t) \quad (1.1.29)$$

where $\rho(\mathbf{r}, t)$ is the average photonic density.

Considering that the fields can be evaluated at separated positions and times, we can define the first order correlation function as :

$$G^{(1)}(\mathbf{r}, t, \mathbf{r}', t') = \text{tr}(\hat{\rho} \Psi^\dagger(\mathbf{r}, t) \Psi(\mathbf{r}', t')) \quad (1.1.30)$$

Similarly we can also define the second-order correlation function:

$$G^{(2)}(\mathbf{r}_1, t_1, \mathbf{r}_2, t_2, \mathbf{r}_3, t_3, \mathbf{r}_4, t_4, \dots) = \text{tr}(\hat{\rho} \Psi^\dagger(\mathbf{r}_1, t_1) \Psi^\dagger(\mathbf{r}_2, t_2) \Psi(\mathbf{r}_3, t_3) \Psi(\mathbf{r}_4, t_4) \dots) \quad (1.1.31)$$

We note that Hanbury Brown and Twiss' experiment gave access to the more simple:

$$G^{(2)}(\mathbf{r}_1, t_1, \mathbf{r}_2, t_2) = \text{tr}(\hat{\rho} \Psi^\dagger(\mathbf{r}_1, t_1) \Psi^\dagger(\mathbf{r}_2, t_2) \Psi(\mathbf{r}_2, t_2) \Psi(\mathbf{r}_1, t_1)) \quad (1.1.32)$$

We can define for both correlation functions 1.1.30 and 1.1.32 the normalised correlation functions:

$$g^{(1)}(\mathbf{r}, t, \mathbf{r}', t') = \frac{G^{(1)}(\mathbf{r}, t, \mathbf{r}', t')}{\sqrt{\rho(\mathbf{r}, t) \rho(\mathbf{r}', t')}} \quad (1.1.33)$$

$$g^{(2)}(\mathbf{r}, t, \mathbf{r}', t') = \frac{G^{(2)}(\mathbf{r}, t, \mathbf{r}', t')}{\rho(\mathbf{r}, t) \rho(\mathbf{r}', t')} \quad (1.1.34)$$

We can note that both $G^{(1)}(\mathbf{r}, t, \mathbf{r}, t) = \rho(\mathbf{r}, t)$ and $G^{(2)}(\mathbf{r}, t, \mathbf{r}', t')$ are real and positively defined. Furthermore, it can be easily shown [5] that:

$$G^{(1)}(\mathbf{r}, t, \mathbf{r}, t) G^{(1)}(\mathbf{r}', t', \mathbf{r}', t') \geq \left| G^{(1)}(\mathbf{r}, t, \mathbf{r}', t') \right|^2 \quad (1.1.35)$$

that is to say:

$$\left| g^{(1)}(\mathbf{r}, t, \mathbf{r}', t') \right| \leq 1 \quad (1.1.36)$$

with in particular $g^{(1)}(\mathbf{r}, t, \mathbf{r}, t) = 1$.

Chaotic Bosonic Quantum Field We consider a chaotic bosonic ensemble of particles at high temperature thermal equilibrium. By injecting 1.1.22 into 1.1.32 and by considering only the spatial dependence, we can write:

$$G^{(2)}(\mathbf{r}_1, \mathbf{r}_2) = \sum_{klmn} \phi_k^*(\mathbf{r}_1) \phi_l^*(\mathbf{r}_2) \phi_m(\mathbf{r}_2) \phi_n(\mathbf{r}_1) \langle \hat{a}_k^\dagger \hat{a}_l^\dagger \hat{a}_m \hat{a}_n \rangle \quad (1.1.37)$$

considering the commutation relations for the bosonic annihilation and creation operators:

$$[\hat{a}_n, \hat{a}_m] = [\hat{a}_n^\dagger, \hat{a}_m^\dagger] = 0 \quad (1.1.38)$$

$$[\hat{a}_n, \hat{a}_m^\dagger] = \delta_{nm} \quad (1.1.39)$$

the correlation function can be simplified to [5]:

$$G^{(2)}(\mathbf{r}_1, \mathbf{r}_2) = \rho(\mathbf{r}_1) \rho(\mathbf{r}_2) + \left| G^{(1)}(\mathbf{r}_1, \mathbf{r}_2) \right|^2 + \sum_n |\phi_n(\mathbf{r}_1)|^2 |\phi_n(\mathbf{r}_2)|^2 \left(\langle \hat{a}_n^\dagger \hat{a}_n^\dagger \hat{a}_n \hat{a}_n \rangle - 2 \langle \hat{a}_n^\dagger \hat{a}_n \rangle^2 \right) \quad (1.1.40)$$

At high temperatures, the last term is linear with the total number of particles, whereas the first two are quadratic: it can be simplified for a large number of atoms to:

$$g^{(2)}(\mathbf{r}_1, \mathbf{r}_2) = 1 + \left| g^{(1)}(\mathbf{r}_1, \mathbf{r}_2) \right|^2 \quad (1.1.41)$$

We thereby find back, although through a quantum description, the earlier obtained results.

Chaotic Fermionic Quantum Field For a fermionic ensemble of particles, there is no classical theory available. In quantum theory, the main difference lies in the commutation relations of the annihilation and creation operators:

$$\{\hat{a}_n, \hat{a}_m\} = \{\hat{a}_n^\dagger, \hat{a}_m^\dagger\} = 0 \quad (1.1.42)$$

$$\{\hat{a}_n, \hat{a}_m^\dagger\} = \delta_{nm} \quad (1.1.43)$$

where $\{a, b\} = ab + ba$ is the anticommutator. Similar considerations as for the bosons will then lead to the simple expression:

$$g^{(2)}(\mathbf{r}_1, \mathbf{r}_2) = 1 - \left| g^{(1)}(\mathbf{r}_1, \mathbf{r}_2) \right|^2 \quad (1.1.44)$$

We note here that the fermionic nature of the particles does indeed exclude them from being in the same position.

Bosonic Coherent Quantum Field With the realisation of the maser in 1954 [23], and the first laser in 1960 [24], it became possible to produce an ensemble of particles in the same coherent state. Although various people thought that the statistical properties of those quantum fields were that of the narrow spectrum limit of a thermal source, Glauber was the first to show that this was a wrong assumption [4].

In a more general way, if all the particles are in the same quantum state $\phi_n(\mathbf{r}_1)$, the correlation function simplifies to:

$$G^{(2)}(\mathbf{r}_1, \mathbf{r}_2) = |\phi_n(\mathbf{r}_1)|^2 |\phi_n(\mathbf{r}_2)|^2 \langle \hat{a}_n^\dagger \hat{a}_n^\dagger \hat{a}_n \hat{a}_n \rangle \quad (1.1.45)$$

This normalises easily to:

$$g^{(2)}(\mathbf{r}_1, \mathbf{r}_2) = 1 \quad (1.1.46)$$

1.2 Hanbury Brown and Twiss with Cold Atoms

As we have shown in the previous section, the Hanbury Brown and Twiss effect of the photons has more to do with the symmetry of their wave-function rather than with their electro-magnetic nature. As all nature's entities have either a symmetric or an anti-symmetric wavefunction, this means that the Hanbury Brown and Twiss effect applies to all entities. Most of those entities have a massive nature.

The fact that the Hanbury Brown and Twiss effect does apply to massive particles has been demonstrated both for fermionic electrons [6, 7, 8], and very recently fermionic neutrons [25]. Also atoms are good candidates for such experiments as we will see. This is in particular thanks to the fact that they can both be easily manipulated and easily cooled. We will have a short overview of various recent experimental realisations of such measurements. We will study in particular the conceptual differences between those experiments.

1.2.1 Cold Atom Optics

When Einstein demonstrated the photoelectric effect in 1905 [26], he showed that light could need a particle-like description at times when wave based descriptions had been satisfactory. In 1924, de Broglie generalised this concept to all massive particles [27], by showing that one could associate an equivalent de Broglie wavelength λ_{dB} to all particles considering their momentum p and the Planck's constant h :

$$\lambda_{dB} = h/p \quad (1.2.1)$$

Matter waves have since been demonstrated for electrons, neutrons and atoms. The de Broglie wavelength of a sample of thermal particles can be defined as the thermal de Broglie wavelength:

$$\lambda_{dB} = h/\Delta p \quad (1.2.2)$$

where the momentum spread Δp is induced by the thermal distribution. At room temperatures, this wavelength is around the atomic electronic shell size, and therefore the potential matter wave behaviours stay confined within the atom. If one wants to observe collective matter wave behaviours, one has to significantly reduce the momentum spread, and therefore the temperature. For Helium atoms for instance, a one $1 \mu\text{m}$ wavelength is obtained only at temperatures of around $1 \mu\text{K}$.

The developements of the last two decades in terms of atom physics have made it possible to reach those temperatures with extremely high spectral densities. The use of Laser-cooling techniques on trapped dilute gases allows reaching temperatures of tens of micro-kelvins with very few losses [28, 29, 30]. The further use of evaporative cooling techniques allowed eventually to reach Bose Einstein condensation [11, 13, 12].

In atom physics, the spectral densities are of the same order as those in photonic optics. Atomic optics have therefore become an excellent candidate to repeat the Hanbury Brown and Twiss effect measurements performed formerly on photons. The reasons why those experiments are worth considering lie in the fact that atoms

are, unlike photons, massive particles. Furthermore atoms can be found, unlike photons, both in bosonic and fermionic states. This opens up to a large variety of experiments.

1.2.2 Hanbury Brown and Twiss Experiments with Cold Atoms

During the ongoing of this thesis several other groups have exploited the possibilities of cold gases for the study of the Hanbury Brown and Twiss effect. It is interesting to notice that all have taken different experimental choices, generally depending on the possibilities of their respective setups. This is why we will briefly overview those experimental realisations.

The experiments can be subdivided into two categories. On one hand we can identify the experiments that use single atom counting techniques. The present study is part of those. On the other hand we can identify the experiments that use absorption schemes. We will see how the integrating nature of this type of detection obliges the scientists to reduce the dimensionality of their source in order to study the Hanbury Brown and Twiss effect.

1.2.2.1 Counting Techniques

Neutral atom counting has until recently been reserved to the high energy metastable noble atoms. For those atoms, the high electronic internal energy makes single atom counting nearly straightforward. The present study deals with this type of detection. Yet it is worth mentioning the pioneering experiment of M. Yasuda and F. Shimizu [10], that already in 1996 obtained extremely interesting results. During the ongoing of this present study, a Fabry-Perrot cavity was used by A. Öttl & al [31]. for the counting of alkaline ^{87}Rb atoms. We will also take a glance at their results.

Yasuda and Shimizu in 1996 M. Yasuda and F. Shimizu [10] realised already in 1996 an experiment that is very close in nature to the original Hanbury Brown and Twiss experiment. The experimental setup is shown in Figure 1.8A.

It is essentially build around a metastable ^{20}Ne magneto-optical trap. In this magneto-optical trap, the temperature of the cloud is as low as 2.5 mK. The $^{20}\text{Ne}^*$ atoms are released from the source trap by the means of a 598 nm pumping laser that transfers the atoms from the trapping $3S\ ^3P_2$ state to the untrapped $3S\ ^3P_0$. The atoms fall under gravity to a gold coated mirror. As they hit the mirror, the 12 eV metastability extracts electrons from the mirror surface¹, that are attracted through an electric potential to a micro-channel plate based electron amplifier. The electric pulses produced by the micro-channel plates are detected electronically. Only temporal correlations can be studied.

This experimental realisation is a master piece. Although the temperature can seem extremely low compared to usual temperatures, it is still very high in the world of cold atom physics. This means that the associated temporal correlation time is still quite short. The equivalent spectral width of the source can be easily evaluated to $\Delta\nu = k_B T / h = 50$ MHz. This gives temporal time correlations around

¹A closer description on the detection of metastable atoms is presented in the next section, as a similar technique is used in the Orsay ^4He experiment.

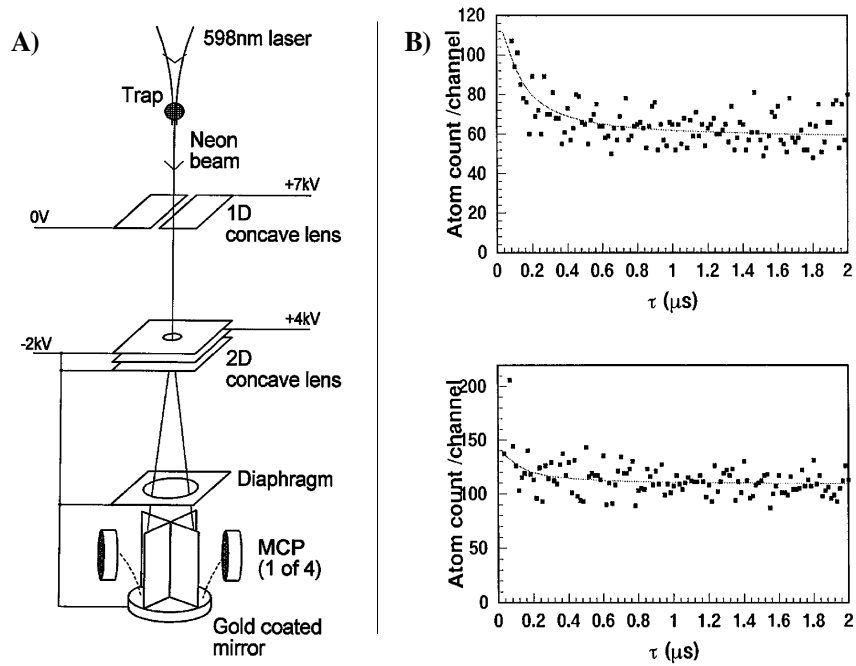


Figure 1.8: In A, the experimental setup used by Yasuda and Shimizu. A pumping laser extracts $^{20}\text{Ne}^*$ atoms from a magneto-optical trap. The falling atoms are defocused through electrostatic lenses onto a golden mirror. The electrons extracted by the atoms from the gold layer are attracted to electron amplifying devices. The outgoing signal is sent to a correlator. In B, the time correlation results. The bunching in the upper graph shows the Hanbury Brown and Twiss bunching effect of the thermal bosons. For the lower graph the electrostatic lenses have been deactivated, in such way that several coherence areas now cover the detector. This lowers the bunching height accordingly. This much lower obtained bunching demonstrates that the first obtained bunching is not related to the detection system. (Figures A and B extracted from [10])

20 ns. Effectively, this number is slightly increased as the 598 nm pumping laser outcouples only a certain spectral range. The effective vertical velocity distribution at the trap level was 28 cm/s. This results in a typical $0.5 \mu\text{s}$ correlation time.

In order to compensate for the very low spatial coherence expected from this setup, electrostatic lenses were used to defocus the coherence area over the size of the gold mirror. This gold mirror consequently had to compensate the curvature of the defocused coherence. The speed of the atoms as they reached the gold mirror was as low as 4 m/s. The vertical spatial coherence length at the level of the mirrors was consequently $2 \mu\text{m}$. The curvature of the mirror therefore had to be calculated within this limit. The radius of the curvature was 600 mm.

Also because the spectral density was still fairly low, the integration times were long. Average pulse counts ranged from 100 s^{-1} to 200 s^{-1} . That is one useful double count within the $0.5 \mu\text{s}$ correlation time every 10 kcounts. That is 0.02 useful double counts per second. Consequently, total integration times ranged in the 45 hours of acquisition for the data published.

Figure 1.8B shows the results of the experiment. The upper graph shows the result of the correlation experiment. It demonstrates the expected bunching with a height of $100 \pm 30\%$. In the lower graph, the electrostatic lenses have been deactivated such that the coherence area at the mirror level is very small compared to the mirror size. Consequently, the bunching disappears in the averaging and only a bunching of $19 \pm 15\%$ is found. The differences between those two measurements lie outside the error bars. They also showed that the bunching disappeared with the tilting of the gold mirror.

This setup had one mayor inconvenience; the still high temperature. Further cooling techniques were quite new at the time, and Yasuda and Shimizu privileged the study of the Hanbury Brown and Twiss effect over further cooling techniques of their atomic sample. They had already earlier reproduced a young slit experiment [9] with the Neon cloud. Cooler temperatures would have made the experiment (at least for the measurement part) significantly easier. In particular, they could not measure the coherent state that is the Bose-Einstein condensate.

On the other hand, they also had some advantages. All further drastic cooling techniques require a sequential type experiment. There are currently several attempts to do continuous radio-frequency cooling in an experiment [52, 53], but none of those experiments has currently managed to get down continuously to the Bose-Einstein condensate limit. In a continuous mode, integration is much more advantageous as no time is lost in the production of the cloud. Furthermore, until now nobody has managed to cool $^{20}\text{Ne}^*$ down to the Bose-Einstein condensate limit as inelastic collisions (as we will discuss a little later) induce significant losses at high densities [54]. Therefore going further with this type of experiment required a different metastable noble gas: metastable helium. We will of course discuss this extensively a little further.

Öttl & al. in 2005 The experimental setup of Öttl & al [31] is briefly described in Figure 1.9A. It performs a time-resolved counting of single atoms outcoupled from a ^{87}Rb Bose-Einstein condensate with a microwave field. It is in that sense very similar to the experiment of Yasuda & al. First we have to note though that this experiment is not performed in a fully continuous mode. The condensate is produced sequentially, and the outcoupling can only last until the complete deple-

tion of the atomic sample. Yet if the time of this outcoupling is much longer than the expected correlation length, the experiment can still be assimilated to a continuous one. The big difference lies then in the detection that is performed through a high finesse optical cavity.

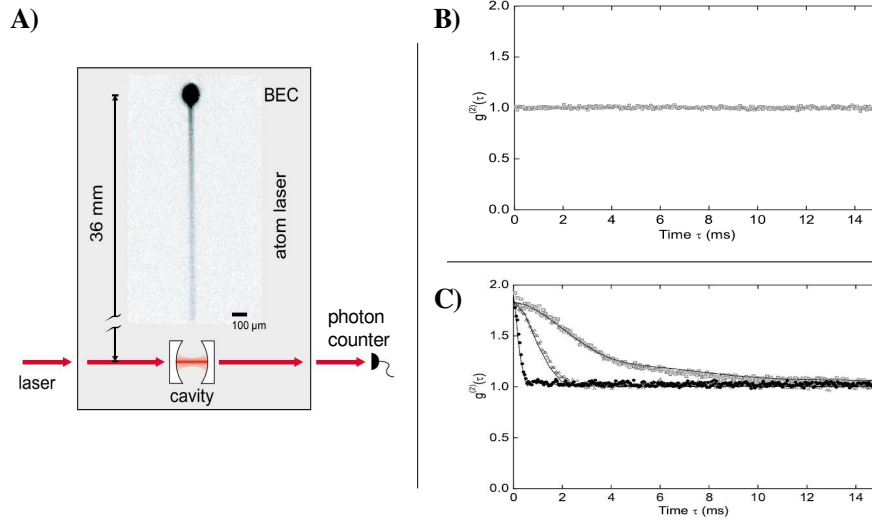


Figure 1.9: In A, a radio-frequency field outcouples Rubidium atoms from a Bose condensed cloud. After a time-of-flight the atoms are detected individually through the use of a resonant optical cavity and a probe laser. In B, the counting statistics of the outcoupled condensed atoms shows no bunching behaviour. It must be said though that the same technique applied to thermal atoms does not show a bunching behaviour. In C, the introduction of a random phase component in the outcoupling radio-frequency field destroys the coherence of the Bose condensed atoms, demonstrating consequently their initial coherence. (Figures A, B and C extracted from [31])

The idea behind such a high finesse cavity is that the transmission of a mode resonant with the ^{87}Rb optical transition drops even if just a single atom enters the cavity. In order for such a cavity to be efficient, it has to be highly stabilised through a first laser locking system. A second probe laser, resonant with the atomic transition, is given maximum transmission onto a photodiode. When an atom enters the cavity, this affects the refractive index of the vacuum between the cavity mirrors. This results in a higher absorption than emission rate, and most absorbed photons are reemitted spontaneously. If the intensity of the probe laser is low enough, those absorptions by this single atom can be retrieved in the output signal.

The waist of the detection cavity is $26 \mu\text{m}$, the mirrors are separated by $178 \mu\text{m}$. The mean velocity of the atoms through the cavity is 84 cm/s , they spend consequently $31 \mu\text{s}$ inside the cavity. With this cavity, Öttl & al. managed to study the temporal correlation of the Bose-Einstein condensate, that proved as expected flat as shown in Figure 1.9B. Practically, the unpublished correlation function of a thermal gas also proved flat. This latter result can be easily understood if we look at the characteristics of the detector.

The trapping frequencies of the cloud are $\omega_{\perp} = 2\pi \times 29 \text{ Hz}$ and $\omega_{\parallel} = 2\pi \times 7 \text{ Hz}$. The critical condensation temperature lies around 180 nK . If we consider a thermal cloud at this temperature, spatially evenly outcoupled by the microwave antenna, we can estimate a temporal coherence of $270 \mu\text{s}$, yet a spatial coherence

of respectively $2.7 \mu\text{m}$ and 650 nm for the axial and longitudinal axis. Those have to be compared respectively, considering the orientations of the setup, to $178 \mu\text{m}$ and $26 \mu\text{m}$. This leads to an expected approximate bunching height, as we will see in paragraph 1.3.3.1, of $10^{-2}\%$. In order to observe the bunching, higher trapping frequencies and eventually a lighter mass would have been necessary.

They did yet manage to show the coherence of the Bose-Einstein condensate, by outcoupling the atoms with a broadband thermal microwave field. The results are published in Figure 1.9C. It shows that a random microwave field destroys the coherence, something that would not have been possible with an already incoherent field.

1.2.2.2 Absorption Imaging

The enormous advantage of metastable atoms is the ease at which single particle detection can be performed, and therefore intensity fluctuations can be studied. Other atomic species, and in particular alkaline atoms, are generally studied through absorption imaging (besides the just mentioned resonant cavity method). In such a process, a resonant laser is sent through the atomic cloud. Induced absorption with spontaneous emission cycles extract photons from this beam, leaving a shadow on a charge-coupled-device (CCD) camera at which the laser has been pointed. The averaging of those photons, and the resolution generally available, lead to the consideration that there is no single particle detection. One can in a general case only study global, first order properties of the cloud.

Proposed by E. Altman & al [32], the idea was that in very specific cases, the intensity fluctuations on the final image generally considered as noise, did still contain useful information. They proposed that one could still study intensity correlations by studying the atom shot noise in time-of-flight images. This would work if the atom shot noise prevails over photons and technical shot noise.

They proposed various schemes, one of which is the periodic optical lattice. This experiment has consequently been performed by Fölling & al [33] and Rom & al [34].

Fölling & al. in 2005 The group of I. Bloch in Mainz has studied [33] the proposed experimental situation of a Bose gas in a 3-dimensional optical lattice. A cold gas of Rubidium is loaded into an optical lattice, and then released. An image of the expanding cloud is made through absorption imaging.

The principle behind this lattice experiment is illustrated in Figure 1.10A. We considered the example of a 1-dimensional lattice. In such a lattice, the wavefunctions of the particles are delocalised Bloch waves. The Bloch state energies are organised in band structures. Each Bloch state is characterised by its energy, and a crystal momentum $\hbar q$ defined in the first Brillouin zone of the reciprocal lattice. Effectively, a Bloch state is a superposition of states with equally spaced momenta by $2\hbar k$. If an atom is in a specific Bloch state, then the probability of the atom to be detected with any of the $\hbar q + n2\hbar k$ momenta are equal. Inversely, if an atom is detected with a specific $\hbar q + n2\hbar k$ momentum, the probability that it belongs to that specific Bloch state is high. If only the first energy band is occupied, and the lattice size is infinite, there is an exact correspondence between the $\hbar q + n2\hbar k$ momenta and a Bloch state.

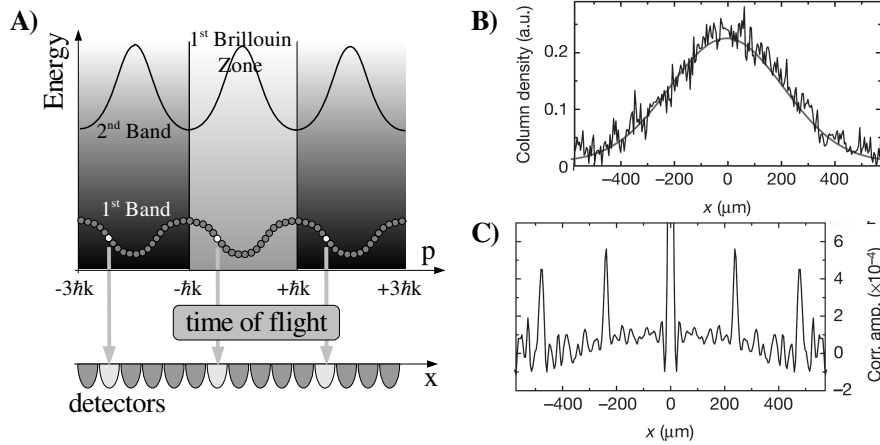


Figure 1.10: In A, the band structure in a periodic lattice. In a lattice, the wavefunctions of the particles are delocalised Bloch waves. Those are characterised by an energy and a momentum in the first Brillouin zone. The particle released from such a trap have a high probability of being detected with a $2\hbar k$ multiple momentum of the Bloch state characterising momentum. In B, the density distribution for a cloud of bosonic Rubidium atoms released from a lattice. No particular order is observed as the cloud is not superfluid. In C, the correlation function of the density distribution shows that the probability of detecting atoms within the same Bloch state is enhanced. (Figure A adapted from [34], B and C extracted from [33])

Now we consider the bosonic Hanbury Brown and Twiss effect in such a lattice. If an atom is in a specific Bloch state, the probability of finding another atom within the same Bloch state is double the probability of finding an atom in any other Bloch state. Consequently, the probability of detecting an atom with any of the same $\hbar q + n2\hbar k$ momenta, is double that of finding the second atom with any other $\hbar q' + n2\hbar k$ momentum. The trick that made this experiment feasible through absorption imaging is the fact that the second atom, although belonging to the same state, could be detected with a completely different momentum from the first. Absorption imaging is not a counting technique, and therefore the auto-correlation of the signal of the first atom outweighs any other pair correlation. But because this pair is delocalised, the correlation signal builds up outside the central autocorrelation.

Practically, the Mainz group has not been able to demonstrate the Hanbury Brown and Twiss effect of thermal bosons in such a delocalised lattice. They managed though to show a similar bosonic correlation in a Mott insulator regime. In that regime, the depth of the periodic potential is such that the quantum states are no longer delocalised. The atoms are confined to identified potential pits. Furthermore, atomic interactions and adiabatic loading of the lattice from a Bose-Einstein condensate assure that each lattice site contains an integer number of atoms in the ground state. The momentum distributions of those atoms are gaussian, and as the lattice sites are numerous and respectively incoherent, the cloud after expansion is gaussian with no noticeable first order interference pattern as shown in Figure 1.10B.

Now comes the interesting part. Inside their lattice sites, the atoms are certainly not in a delocalised Bloch state. They are in a state with a very well defined

position, and a non-defined momentum. When an atom is detected after a long time-of-flight, we measure a very well defined momentum, yet the initial lattice site is unknown. The state in which the atom has been detected can therefore only be expressed as a superposition of all the lattice site wavefunctions. As the lattice sites are countable and periodic, the resulting superposition has necessarily a periodic structure. In fact, the superposition of those states that results in a particular momentum detection is a Bloch state like structure. Therefore, the atom is, through its detection, projected into a specific Bloch state, and as usual, the probability of finding a second atom in that same Bloch state is double the probability of finding an atom in any other Bloch state and thus momentum. As the Bloch state momentum distribution is periodic, the auto-correlation of the final density distribution shows a periodic structure, as shown in Figure 1.10C. It must be clear though, that this periodic structure only arises because of the Hanbury Brown and Twiss effect, because the bosons tend to be in the same quantum state.

Experimentally, the initial trap lattice is 3-dimensional, and therefore the final periodicity is also 3-dimensional. Because of the absorption imaging, one dimension is projected, and only 2 remain. We have chosen here to display only a 1-dimensional cut of the obtained density distribution and the density auto-correlation.

Rom & al. in 2006 The same group in Mainz also managed to trap sympathetically cooled fermionic potassium ^{40}K inside the lattice [34]. As discussed previously, the Fermi exclusion principle makes it impossible for two atoms to be found in the same quantum state. In terms of the lattice experiment, this means that if an atom is detected with a certain momentum $\hbar q$, no second atom can be detected with any of the momenta $\hbar q + n2\hbar k$. They have been able to show this for a thermal cloud in a delocalised lattice.

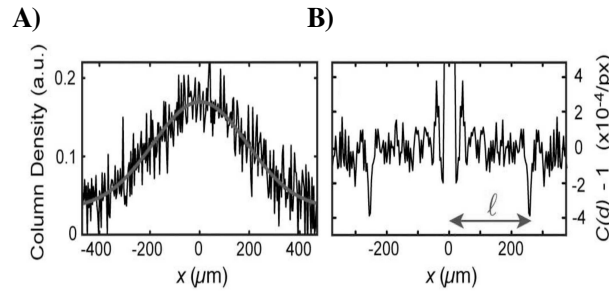


Figure 1.11: In A, the density distribution for a cloud of bosonic Potassium atoms released from a lattice. No particular order is observed. In B, the correlation function of the density distribution shows that the exclusion principle prevents two atoms from being detected within the same Bloch state. (Figure A and B extracted from [34])

Figure 1.11A shows the cut of an expanding cloud of potassium ^{40}K originating from a 3-dimensional lattice. The density profile is roughly a thermal gaussian, and no interference patterns are detected. In Figure 1.11B the auto-correlation of the density profile shows an anti-bunching in the Bloch states. The fact that the antibunching is not a hundred percent is essentially related to the resolution of the optical system.

Estève & al. in 2005 Another team of the group of Atom Optics in Orsay has performed a second Hanbury Brown and Twiss effect measurement with Rubidium on an atom-chip [35]. On such a chip, the current going through a micro-metre scaled wire, with an external homogeneous magnetic field, produces an elongated highly confining trapping potential. Trapping frequencies on this setup are 7 to 20 Hz on the longitudinal axis, and 2.85 kHz on the transverse direction. If the gas is cooled sufficiently, the trap is nearly one-dimensional. They are able to work at temperatures of $2.1 \hbar\omega_{\perp}/k_B$.

Thanks to the low dimensionality, absorption imaging can be used to study density fluctuations in situ. If two atoms are in the same quantum state, they are likely to be measured within the coherence volume defined by λ_{dB}^3 . This means that the variance of the atom number N in such a phase-space cell is provided by:

$$\delta N^2 = \langle N^2 \rangle - \langle N \rangle^2 = \langle N \rangle + \langle N \rangle^2 \quad (1.2.3)$$

Whereas the first term is completely classical, the second term results from the Hanbury Brown and Twiss effect. If a larger volume is considered, then the variance is provided by:

$$\delta N^2 = \langle N \rangle + \langle N \rangle^2 / g \quad (1.2.4)$$

where g is the number of elementary phase-space cells λ_{dB}^3 in the volume. This result had already been discussed by A. Einstein in 1925 [86]. Thanks to the low dimensionality of their trap, and to an optical resolution of $10 \mu\text{m}$, the Orsay team has been able to get g factors around 100. This made this density fluctuation measurement possible.

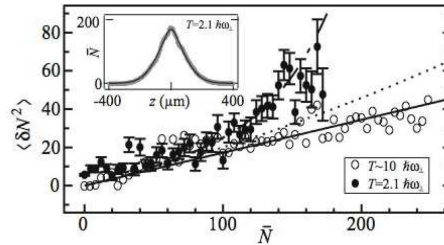


Figure 1.12: The variance of the local cloud density as a function of the mean density. At high temperatures (white circles), the phase-space cell is small compared to the resolution and the variance has a classical shot noise evolution. At low temperatures (black circles), the variance shows a quadratic evolution characteristic of the bosonic bunching effect. (Figure extracted from [35])

In Figure 1.12 has been displayed the variance as a function of the mean density on the chip experiment. The white circles correspond to a hot thermal cloud. At high temperatures, the phase-space cell is small and the g factor is large. The quantum contribution to the variance is negligible. The black circles correspond to clouds at much lower temperatures. They have a g factor around 140. The quadratic behaviour of the variance is clearly visible.

1.3 The Orsay Helium Experiment

We have just seen that cold atoms are a particularly interesting system for the study of the Hanbury Brown and Twiss effect. This in particular because the spectral density can be considerably increased with the use of cooling techniques, but also because they can be easily manipulated or eventually detected. In 2001 was first cooled down to Bose-Einstein condensate temperatures a sample of metastable atoms [14, 15]. This opened the possibility to an improved version of Yasuda and Shimizu's experiment.

We will study some of the particularities of this atom species: the triplet metastable Helium. We will see in particular how it can be cooled and detected. Then we will establish a simple experimental scheme by which we can study some correlation properties of a cold metastable cloud, and we will establish a simple theory in order to get some insight on the expected results. Finally we will study the most important experimental characteristics that influence the signal to noise ratio.

1.3.1 Triplet Metastable Helium

We will have a short look at the particularity of ^4He , and we will discover rapidly: why the use of a metastable state, the problems that raises and how those are solved. Then we will have a short overview of the recently cooled fermionic $^3\text{He}^*$ [16]. Finally we will discuss the advantages of those metastable over casual alkaline species.

1.3.1.1 $^4\text{He}^*$

The He atoms can be found in two stable isotopes: ^3He and ^4He . The first one is a fermion and has a natural abundance of 10^{-6} on earth, the second one is a boson much more abundant. The ^4He atom in its ground state is not a good candidate for dilute atom cooling. First of all because it has no global spin, so it cannot be trapped magnetically. Secondly because the first optical transition is 20 eV off, which makes it extremely difficult to find a coherent optical source for optical trapping and cooling.

The ^4He atom in its first 19.8 eV excited state, the triplet 2^3S_1 state, shows none of those inconveniences. It has a spin induced magnetic moment that allows for magnetic trapping. It has optical transitions to the 2^3P and 3^3P triplet excited states at easily accessible wave-lengths, i.e. $1.08 \mu\text{m}$ and 389 nm , as shown in Figure 1.13. More precisely, the optical transition to the 2^3P_2 state is closed (which means that the 2^3P_2 state can practically only decay to the 2^3S_1 state [36]), which permits a very efficient optical cooling. The width of this optical transition is 1.6 MHz.

Furthermore, the optical transition of this 2^3S_1 state to the ground state being forbidden both for non spin and angular momentum conservation reasons, the 2^3S_1 state has a 7900s lifetime [37, 38, 39]. This results in its qualification as the triplet metastable state²: $^4\text{He}^*$. At the timescale of atom cooling experiments, this lifetime is far from being the limiting lifetime so that it can be considered infinite³.

²The singlet 2^1S_0 state is also metastable but with a much shorter lifetime of 19 ms. The transition with the ground state conserves the spin. This state can also not be magnetically trapped.

³With current ultra-high vacuums of 10^{-11} mbar, lifetime due to collisions with background gas

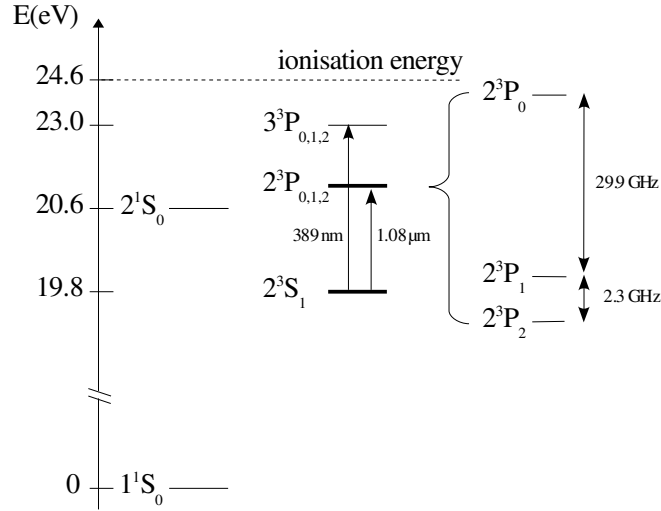
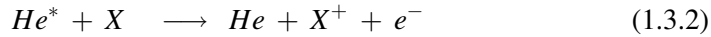
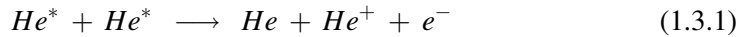


Figure 1.13: The ^4He energy levels, showing the main two optical transitions. The transition used experimentally has been highlighted. (Figure adapted from [57])

Last but not the least, the s-wave scattering length of He^* is large and positive: 7.5 nm [55, 40, 41]. This makes not only evaporative cooling efficient, but also establishes the stability of the resulting Bose-Einstein condensate.

1.3.1.2 Inelastic Collisions

Though the triplet ^4He seems to be a very good candidate for atom cooling experiments, it shows an important inelastic collision rate [42, 43]. Indeed the ionisation energy is 25eV from the ground state, such that the $2 \times 19.8\text{eV}$ energy released in a inelastic collision is enough to ionise one of the atoms, phenomena called Penning ionisation. This energy is also sufficient to ionise any other atomic species X in the vacuum chamber, leading to "one-body" Penning ionisation:



Although the one-body Penning ionisation can be controlled by the quality of the vacuum, the two-body losses are important inside the trap, and renders evaporative cooling impossible. Fortunately calculations have shown [44, 45] that in a spin polarised sample of triplet He^* atoms (i.e. atoms in the same magnetic substate), the 2 and 3-body inelastic collision rates are inhibited with a factor of 10^5 for non-spin conservation reasons. This theoretical result made the effective condensation of this species plausible, and opened the experimental race to its realisation [14, 15, 46, 47].

Though sufficiently low in order not to obstruct Bose-Einstein condensation, the low ion rate produced throughout the process, translating both the density and the atom number, provides a monitor to the dynamics inside the trap. Various studies have taken use of this monitor to analyse the properties of the cold clouds, one of which is the decay of the Bose-Einstein condensate [48, 49].

is already in order of 120 s.

1.3.1.3 $^3\text{He}^*$

Unlike ^4He , ^3He has a nuclear spin of $\frac{1}{2}$. Consequently its triplet metastable 2^3S_1 state shows a hyperfine structure of $F = 3/2$ and $F = 1/2$ (splitting 6740 MHz). Its triplet excited states 2^3P_1 and 2^3P_2 also show hyperfine structures. The optical transition between the 2^3S_1 and the $2^3\text{P}_{0,1,2}$ states is similar to the $^4\text{He}^*$ optical transitions at 1083 nm. The energy levels of the ^3He structure are shown in Figure 1.14.

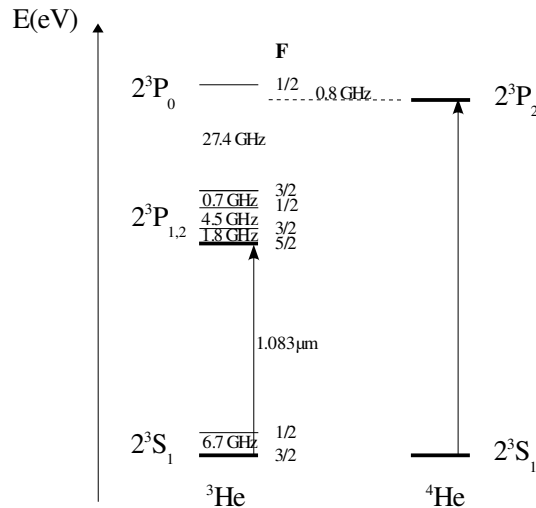


Figure 1.14: The useful ^3He energy levels, in comparison with the ^4He energy levels. The optical transitions used experimentally have been highlighted. (Figure adapted from [66])

If magnetically trapped, the 2^3S_1 $^3\text{He}^*$ atoms are necessarily in one of the magnetic sub-states $|F, m_F\rangle = |1/2, +1/2\rangle$, $|3/2, +1/2\rangle$ or $|3/2, +3/2\rangle$. As the collisions at cold temperatures between identical 2^3S_1 states are prohibited by the Pauli exclusion principle, evaporative cooling of a ^3He sample can only be performed through a mixture. Although the mixture of any of those sub-states would seem a good idea, Penning ionisation strongly inhibits the lifetime of such a mixture. It is therefore necessary to introduce another atomic species. The Amsterdam ^3He experiment naturally opted for the $^4\text{He}^*$.

The single mixture that inhibits inelastic collision is between the fermionic $|3/2, +3/2\rangle$ and the bosonic $|J, m_J\rangle = |1, +1\rangle$ states. Furthermore, the interspecies scattering length is evaluated to $a_{34} = +28.8 \pm 4$ nm [55, 16]. This ensures very effective sympathetic cooling, and the Amsterdam ^3He experiment has succeeded in this [16].

1.3.1.4 Detection

The reasons that renders the cooling of He^* specifically interesting reside in its detection possibilities. One can proceed to an optical detection through absorption of diffusion imaging, and most of the He^* condensing groups do so. Yet this detection is not very efficient due to border-line wave-lengths⁴, nor would that make some

⁴1.083 μm is at the very edge of silicone based cameras detection spectra.

studies on He^* particularly more interesting than on Alkaline atoms, that are easier to handle.

The strength of He^* atoms lies precisely in its 19.8 eV internal energy. This is enough to ionise anything but ground state helium. One of the nice aspects is the Penning ionisation we just mentioned, that gives an indirect and continuous indicator through the ion rate. But when a He^* atom hits a metallic surface, it will also extract secondary electrons. Those electrons can then be amplified through an electric potential and collisions in an electron multiplier. Thus for any single initial He^* atom, a macroscopic signal of electrons is produced, allowing single atom detection.

A particular such detector is the micro-channel plate. A micro-channel plate is a thin glass plate showing a lattice of small channels. An electric potential is applied between the two faces of the plates such that each channel works as a tiny (around $10\ \mu\text{m}$ diameter) electron multiplier. In contrast, the typical diameter of the plate is several centimeters. Each plate consequently has millions of channels, and the detection is localised on the plate. This can be used for position sensitive detection schemes. A closer description of micro-channel plates can be found in the next chapter.

A nice aspect of micro-channel plates is their virtual insensitivity to background noise. Though various types of particles can trigger off a detection (high energy photons, accelerated ions, metastable atoms...), the minimal required energy is sufficient to render those events unlikely. Hence the detection statistics are shot-noise limited, and make this detector very suitable for the study of rare events.

For those reasons, the Orsay Helium team has chosen to use a micro-channel plate from its very beginning, and made the experiment particular suitable for studying quantum atom optics.

1.3.2 The Hanbury Brown and Twiss Experiment With He^*

As we have seen, He^* is potentially an interesting species for the study of the Hanbury Brown and Twiss effect. It can be cooled down to the lowest temperature, producing high spectral dense sources, and single atom detection is straightforward. In Orsay we dispose of a source of ultra-cold $^4\text{He}^*$. The Atomic Physics group at the Vrije Universiteit of Amsterdam managed to sympathetically cool $^3\text{He}^*$ to similar temperatures. This opened the way to the study of both the bosonic bunching as well as the fermionic antibunching. We will have a brief description of the two sources. A detailed description of the two experiments can be found in the manuscripts of former students in respectively Orsay [56, 57, 58, 59, 60, 61, 62, 63] and Amsterdam [64, 65, 66, 67, 68, 69]. Then we will outline the proposed experiment, and we will proceed to a simple theoretical study of this experiment.

1.3.2.1 The Sources

If we want to perform a Hanbury Brown and Twiss like experiment, the correlation lengths far from the source essentially depend on the initial sizes of the source. Furthermore, the acquisition time depends on the spectral density. This involves in terms of atom optics both the temperature of the source as well as the number of atoms at those temperatures.

The dimensional properties of a cold cloud of atoms are mostly determined by the magnetic trap. Both experiments employ a clover-leaf trap for this purpose [50, 51]. These magnetic configurations generally produce anisotropic magnetic traps. These traps simplify, if employed at very low temperatures, to an anisotropic harmonic trap. We can thus distinguish a lower longitudinal trapping frequency, which corresponds in both experiments to the horizontal x axis. The two other transverse trapping frequencies along the horizontal y and the vertical z axis are identical. Generally, the longitudinal trapping frequency is much lower than the other two, resulting in cigar shaped atomic clouds as displayed in Figure 1.15. The trapping frequencies at the Orsay ^4He experiment are respectively $\omega_y = \omega_z = 2\pi \times 1150$ Hz and $\omega_x = 2\pi \times 47$ Hz for $^4\text{He}^*$. In Amsterdam, the trapping frequencies were respectively $\omega_y = \omega_z = 2\pi \times 506$ Hz and $\omega_x = 2\pi \times 54$ Hz for $^3\text{He}^{*5}$.

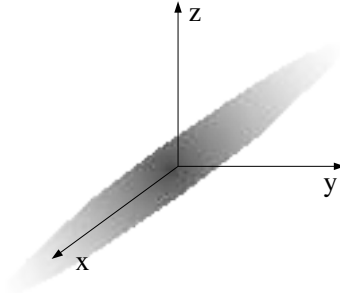


Figure 1.15: The initial atomic source is anisotropic. The transverse identical ω_y and ω_z trapping frequencies are much higher than the longitudinal ω_x trapping frequency. This results in a cigar-shaped cloud.

The effective root-mean-square sizes of a thermal cloud in a harmonic trap are given by:

$$s_\alpha = \sqrt{\frac{k_B T}{m\omega_\alpha^2}} \quad (1.3.3)$$

with α indicating one of the three dimensions. This shows that the cloud size does not only scale with the inverse of the trapping frequency, but also with the square root of the temperature. This means that cooling down the atomic sample will not simply increase the spectral density, but also increases the spatial correlation length at a far distance.

Temperatures that can be attained are typically around $1 \mu\text{K}$ for both experiments. The number of atoms ranges typically from 10^4 to 10^5 .

1.3.2.2 The Experiment

The idea behind the Hanbury Brown and Twiss experiment with the Orsay ^4He experiment seems very close to the original optical experiment. We place a He^* intensity interferometer at a far equivalent distance from the cloud, and see the correlations build up. The intensity interferometer would be some spatially sensitive

⁵Reference [16] indicates lower trapping frequencies. Those have been increased for signal to noise ratio considerations.

micro-channel plate based detector, that would assure both the counting mechanism, as well as the various detector separations.

Just as in the case of the photonic equivalent, particles still have to get to the detector. This could be done by using an outcoupling Raman Laser [10] or a radio-frequency [31], yet the resulting spatial correlation function would depend more on the characteristics of the spatial and spectral outcoupling device rather than those of the initial cloud. The simplest way of preserving the cloud properties is obtained by switching off the magnetic trap and simply have the atoms fall to the detector by gravity, as represented in Figure 1.16.

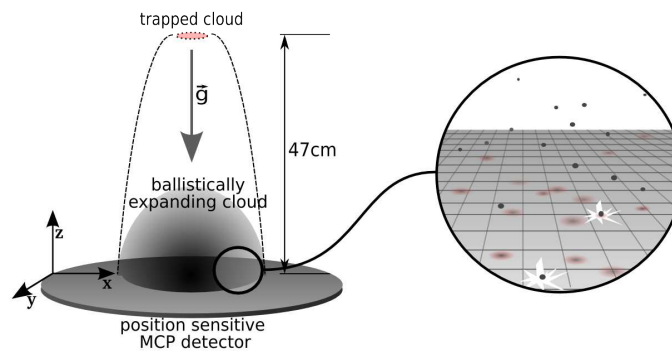


Figure 1.16: Schematic view of the experiment. A cold thermal cloud of He^* drops on a position sensitive micro-channel plate based detector. All the positions and arrival times of the individual atoms are saved and the correlation function is computed.

Though this experiment looks very alike both [10, 31] and the optical equivalent, there are some fundamental differences. Whereas the latter experiments are continuous (or semi-continuous), the Helium experiment is pulsed. When the atomic cloud is released, it expands through the momentum distribution of the atoms. If the time of flight before detection is long enough, the final spatial distribution of the cloud essentially translates the initial momentum distribution. This distribution, and its correlation, is unchanged during the diabatic switch-off of the magnetic trap.

When one takes a 3-dimensional image of the cloud after this time of flight, one can then calculate the momentum correlation function. Yet as it happens, the use of a position sensitive micro-channel plate based detector does not exactly take an instantaneous 3-dimensional image. The detector measures a flux, the flux of the cold cloud as it falls on the detector. If the thermal momentum distribution width is small compared to the speed acquired by gravity, the cloud barely expands during its detection, and the two detection processes are equivalent. The properties of the cloud correspond to those at the average arrival time. The thermal energy is given by $k_B T \simeq 8.7 \times 10^{-11} \text{ eV}$, whereas the gravitational energy is given by $mgh \simeq 5.3 \times 10^{-8} \text{ eV}$. We will therefore neglect the expansion of the cloud during the detection.

As we simply study the 3-dimensional momentum distribution, all 3-dimensions are treated equivalently. In particular, the temporal correlation that can be expected at the detector merely translates the vertical initial size of the cloud. This is unlike

[10, 31] where there is a continuous particle extraction, and the temporal correlation that can be expected at the detector is in relation with the spectral width of the source or outcoupler. This is also unlike the traditional optical experiment. It seems difficult to produce a photonic analogy. It would require a pulsed source within a dispersive extended medium in order to obtain similar results.

1.3.2.3 The Theory

For the theoretical description we will make a number of approximations. The first is, as just discussed, that we will neglect the expansion of the cloud during its detection. Furthermore, we will estimate that there are no interactions during the switch-off of the trap and during the time-of-flight. This maintains the momentum distribution during the time-of-flight. Finally, we will only consider the extreme cases of a pure gaussian thermal gas or the Bose-Einstein condensate. [70, 19, 56] treat the theory more extensively and the reader is advised to refer to them. The results of the presented simple analysis will be largely sufficient to interpret our data with the current signal to noise ratio.

We will present here a theoretical description in two extreme limits: the case of a bosonic cloud far above the condensation limit, and the one of a pure condensate. Finally we will study briefly how the bosonic thermal cloud results can be adapted to a fermionic thermal cloud.

The Bosonic Thermal Source The Hamiltonian of a 3-dimensional harmonic potential of oscillation frequencies ω_α in the α direction is:

$$\hat{H} = \frac{\hat{\mathbf{p}}^2}{2m} + \frac{1}{2}m(\omega_x^2\hat{x}^2 + \omega_y^2\hat{y}^2 + \omega_z^2\hat{z}^2) \quad (1.3.4)$$

This can be written in the momentum space representation time-independent Schrödinger equation:

$$\epsilon_j\phi_j(\mathbf{p}) = \frac{\mathbf{p}^2}{2m}\phi_j(\mathbf{p}) - \frac{1}{2}m\hbar^2 \left[\sum_{\alpha=x,y,z} \omega_\alpha^2 \frac{\partial^2}{\partial p_\alpha^2} \right] \phi_j(\mathbf{p}) \quad (1.3.5)$$

The eigenfunctions solution to this equation can be written:

$$\phi_j^0(\mathbf{p}) = \prod_{\alpha=x,y,z} A_{j_\alpha} e^{-\frac{p_\alpha^2}{2\sigma_\alpha^2}} H_{j_\alpha}(p_\alpha/\sigma_\alpha) \quad (1.3.6)$$

with $\sigma_\alpha = \sqrt{m\hbar\omega_\alpha}$ the harmonic oscillator ground-state size, H_{j_α} the Hermite polynomial of order j_α , $A_{j_\alpha} = (\sqrt{\pi}\sigma_\alpha 2^{j_\alpha}(j_\alpha!)^{-1/2})^{-1/2}$ the normalisation factor. The eigen-energies are given by $\epsilon_j = \sum_{\alpha=x,y,z} \hbar\omega_\alpha(j_\alpha + 1/2)$, that leads, at high temperature, to the Maxwell-Boltzmann occupation factor of each state $p_j = e^{-\epsilon_j/k_B T}$.

We can define both the momentum density function $\rho_{t=0}(\mathbf{p})$ and the first order momentum correlation function $G_{t=0}^{(1)}(\mathbf{p}, \mathbf{p}')$ in the trap. According to [70], one then finds:

$$\rho_{t=0}(\mathbf{p}) = \frac{N}{(\sqrt{2\pi mk_B T})^3} \prod_{\alpha} e^{-\frac{p_\alpha^2}{2mk_B T}} \quad (1.3.7)$$

$$G_{t=0}^{(1)}(\mathbf{p}, \mathbf{p}') = \frac{N}{(\sqrt{2\pi mk_B T})^3} \prod_{\alpha} e^{-\frac{1}{2} \left(\frac{p_\alpha + p'_\alpha}{2\sqrt{mk_B T}} \right)^2} e^{-\frac{(p_\alpha - p'_\alpha)^2}{2} \left(\frac{\sqrt{mk_B T}}{m\hbar\omega_\alpha} \right)^2} \quad (1.3.8)$$

For similar reasons as shown earlier, in the case of a bosonic thermal gas:

$$G^{(2)}(\mathbf{p}, \mathbf{p}') = \rho(\mathbf{p})\rho(\mathbf{p}') + \left| G^{(1)}(\mathbf{p}, \mathbf{p}') \right|^2 \quad (1.3.9)$$

As the interesting dependence of this correlation functions lies essentially in $(\mathbf{p} - \mathbf{p}')/2$, we will average this correlation function over the mean position $(\mathbf{p} + \mathbf{p}')/2$. We then obtain the following correlation function:

$$\tilde{G}_{t=0}^{(2)}(\Delta\mathbf{p}) = \frac{N^2}{(\sqrt{4\pi mk_B T})^3} \left[\prod_{\alpha} e^{-\frac{\Delta p_{\alpha}^2}{4mk_B T}} + \prod_{\alpha} e^{-\frac{\Delta p_{\alpha}^2}{2} \left(\frac{\sqrt{2mk_B T}}{m\hbar\omega_{\alpha}} \right)^2} \right] \quad (1.3.10)$$

The momenta are measured after a t_0 time of flight through a spatially sensitive detector. Neglecting the expansion of the cloud through the detection process, we can associate to every momenta the position of detection:

$$\mathbf{p} \rightarrow \mathbf{r} = \left(\frac{t_0 P_x}{m}, \frac{t_0 P_y}{m}, \frac{t_0 P_z}{m} \right) \quad (1.3.11)$$

where we consider that the surface of the detector is at $z = 0$. By introducing the transformation, we obtain the following result:

$$\rho_{t_0}(\mathbf{r}) = \frac{N\sqrt{m^3}}{(t_0\sqrt{2\pi k_B T})^3} \prod_{\alpha} e^{-\frac{r_{\alpha}^2 m}{2t_0^2 k_B T}} \quad (1.3.12)$$

$$\tilde{G}_{t_0}^{(2)}(\Delta\mathbf{r}) = \frac{N^2\sqrt{m^3}}{(t_0\sqrt{4\pi k_B T})^3} \left[\prod_{\alpha} e^{-\frac{\Delta r_{\alpha}^2}{2} \left(\frac{\sqrt{m}}{t_0\sqrt{2k_B T}} \right)^2} + \prod_{\alpha} e^{-\frac{\Delta r_{\alpha}^2}{2} \left(\frac{\sqrt{2mk_B T}}{t_0\hbar\omega_{\alpha}} \right)^2} \right] \quad (1.3.13)$$

We note that the cloud after expansion has an isotropic Gaussian distribution of root-mean-square size $\frac{t_0\sqrt{k_B T}}{\sqrt{m}}$. This leads logically to an isotropic Gaussian two-particle correlation function that is a $\sqrt{2}$ larger. We do yet notice the Gaussian bunching on top of the classical correlation function. This bunching is anisotropic. The root-mean-square size on each axis α is $\frac{t_0\hbar\omega_{\alpha}}{\sqrt{2mk_B T}}$. This is to be compared with the root-mean-square sizes of the anisotropic cloud inside the trap $\sqrt{\frac{k_B T}{m\omega_{\alpha}^2}}$. We immediately notice the inversion of the anisotropy between the initial cloud and the bunching. For consistency with [19, 17, 18], we will define the half-width half-maximum correlation length l_{α} :

$$l_{\alpha} = \frac{\hbar\omega_{\alpha}t_0}{\sqrt{mk_B T}} = \frac{\hbar t_0}{ms_{\alpha}} \quad (1.3.14)$$

Several remarks can be made. The first is that the correlation length simply scales with the time, just like the cloud itself. Therefore the further the measurement, the larger the correlation length. The second remark is that as expected, the correlation length scales inversely with the initial cloud size s_{α} , just as with the optical equivalent. Because the clouds size is temperature dependent, the final correlation length will also be so.

We can then finally write the normalised second order correlation function:

$$\tilde{g}_{t_0}^{(2)}(\Delta\mathbf{r}) = 1 + \prod_{\alpha} e^{-\frac{\Delta r_{\alpha}^2}{l_{\alpha}^2}} \quad (1.3.15)$$

The Fermionic Thermal Source In the case of fermionic thermal atoms:

$$G^{(2)}(\mathbf{p}, \mathbf{p}') = \rho(\mathbf{p})\rho(\mathbf{p}') - \left| G^{(1)}(\mathbf{p}, \mathbf{p}') \right|^2 \quad (1.3.16)$$

The rest of the calculations being identical, we end up with:

$$\tilde{g}_{t_0}^{(2)}(\Delta\mathbf{r}) = 1 - \prod_{\alpha} e^{-\frac{\Delta r_{\alpha}^2}{t_{\alpha}^2}} \quad (1.3.17)$$

The Bose-Einstein condensate As discussed previously, the fact that all the atoms are in the same quantum state simplifies greatly the calculation of the correlation functions. As all the atoms are also in the ground state, we obtain:

$$G^{(2)}(\mathbf{p}, \mathbf{p}') = \rho_0(\mathbf{p})\rho_0(\mathbf{p}') \quad (1.3.18)$$

where $\rho_0(\mathbf{p})$ is the momentum density of all the atoms in the ground state. We obtain as considered earlier:

$$\tilde{g}_{t_0}^{(2)}(\Delta\mathbf{r}) = 1 \quad (1.3.19)$$

1.3.3 Signal to Noise Ratio

The feasibility of an experiment is given by its signal to noise ratio for a certain acquisition time. Although the signal to noise ratio can generally be increased by elongating the acquisition time, the experimentalist will in the end have to deal with his own limited patience. Furthermore, for random processes the signal to noise ratio only scales with the square root of the time spend in the lab. The initial scaling factor is preferably a stimulating amount. As the densities inside the Bose-Einstein condensate time-of-flight are much higher than those for the thermal gases, and the correlation squares with the density, we did not expect major difficulties for the acquisition of the condensed clouds. We will therefore concentrate on the thermal clouds.

The cloud is detected through a detector. The properties of this detector is likely to influence the signal to noise ratio. We will see to what extent the detector can be expected to influence the signal to noise ratio, and then we will analyse the signal to noise ratio.

1.3.3.1 The Detector

The key to the Hanbury Brown and Twiss experiment is the detector, as there is no analysis without measurement. A detector has some general characteristics that require focus. It has both a finite size, a detectivity and a finite resolution.

Detector Size The effect of the finite size of the detector on the detection of the time-of-flight is essentially a geometric cut on the final shape of the detected cloud. Up to now, we considered the number of atoms in the cloud N . Experimentally though, it is easier to work with the number of effectively detected atoms N' .

In order to bring in the corrections, we will consider the use of a circular detector of radius R . N' is then defined as the integral of the atomic density with

$r_x^2 + r_y^2 = r^2 < R^2$. This leads to:

$$N' = \int_0^R \int_{-\infty}^{\infty} 2\pi r * \frac{N\sqrt{m}^3}{(t_0\sqrt{2\pi k_B T})^3} e^{-\frac{(r^2+z^2)m}{2t_0^2 k_B T}} dr dz = N \left(1 - e^{-\frac{R^2 m}{2t_0^2 k_B T}} \right) \quad (1.3.20)$$

Let us now consider the amplitude of the correlation function $\tilde{G}_{t_0}^{(2)}(\Delta \mathbf{r} = 0)$ in the absence of any quantum bunching effect:

$$\langle \rho^2 \rangle = \frac{N^2 \sqrt{m}^3}{(t_0\sqrt{4\pi k_B T})^3} \left[1 - e^{-\frac{R^2 m}{t_0^2 k_B T}} \right] = \frac{N'^2 \sqrt{m}^3}{(t_0\sqrt{4\pi k_B T})^3} \coth \left(\frac{R^2 m}{t_0^2 k_B T} \right) \quad (1.3.21)$$

with $\coth()$ the hyperbolic cotangent. The result of this calculation is fairly important, as the smaller the detector, the higher the signal. Usually one would expect the opposite, yet the wings of the gaussian time of flight participate very little to the calculation of the correlation, as the squared density is very low. A detector that would simply detect the centre of the atomic cloud would be nearly as efficient. If for some reason, the number of detected atoms were limited by the detector, limiting the size of the detector could be an interesting strategy. Of course, keeping the same number of detected atoms while reducing the detector size means that we increase the initial number of atoms in the cloud, and thus the detection rate. As in general detectors are more likely to be limited in particle rate rather than in the total number of atoms, the rate would be more interesting to study. We will come back to this point in the next chapter.

Detectivity The question of the detectivity is a fundamental question. What happens if the detector does not detect all the atoms? The question is particularly interesting because it separates the notion of correlated and entangled particles. Entangled particles can be produced for example through a two-photon emission process [71], molecular breakup [72], or as we have realised on the Orsay ⁴He experiment through a collision process [73]. Although an extremely interesting quantum system is produced in such a process [74], as the final entangled state has fundamental quantum properties, the correlation statistics are classical. In such an entangle process, the presence of a particle in a certain state establishes the existence of another particle in a related state. If several pairs are generated, the correlation can be normalised. The number of total correlations squares with the number of individual particles N , whereas the bunching related to this perfect correlation scales with N . Consequently the normalised correlation bunching evolves in $1/N$. If only $N' = \eta N$ particles are detected, due to the detectivity η , the total number of detected pairs will be $\eta N'$, whereas the background correlation scales with N'^2 . The correlation bunching height consequently evolves with η/N' . It is strongly affected by the detectivity.

For our Hanbury Brown and Twiss correlated atoms, this is not the case. There is no proper entanglement between atoms. The atoms are statistically correlated. This correlation originates from a quantum process that is the stimulated emission. In that emission, the probability for an atom to occupy a certain state depends on the occupation number of that state. The probability to end up in an occupied state is double the probability to end up in an empty state in the case of bosons. If an atom is detected through a detector of quantum efficiency η , a state is occupied

and the probability to detect an atom in the same state, whatever η , is still double the probability to detect an atom just anywhere else. Therefore the normalised correlation function is unaffected by the quantum efficiency.

The number of detected atoms changes naturally with the quantum efficiency through $N' = \eta N$. But if N can be tuned freely, as the number of atoms in the trap can be tuned, the experiment is not affected by the detector's quantum efficiency. We will see in the next chapter that some considerations can make us care about it, but for the moment we will simply state that, as long as we use the number of detected atoms N' , the correlation does not change with the detectivity.

Resolution Up to now, we have always considered that we had a perfect measurement of the 3 coordinates of each atom. In real life, the experimentalist has to deal with the resolution of the detector. If this resolution is big compared to the observed phenomena, one can imagine that the signal is just washed out over the background. This resolution hence has a direct impact on the expected bunching height. The expected bunching is convoluted with the resolution of the detector. If we call d_α the root-mean-square resolution of the detector following the α axis, and we consider d_α small both compared to the detector size and the cloud size, we expect to measure:

$$\tilde{G}^{(2)}(\Delta\mathbf{r}) = \frac{N'^2 \sqrt{m}^3}{(t_0 \sqrt{4\pi k_B T})^3} \left[\prod_{\alpha} e^{-\frac{\Delta r_{\alpha}^2}{2} \left(\frac{\sqrt{m}}{t_0 \sqrt{2k_B T}} \right)^2} \pm h \times \prod_{\alpha} e^{-\frac{\Delta r_{\alpha}^2}{l_{\alpha}^2 + 2 \times 2 \times d_{\alpha}^2}} \right] \quad (1.3.22)$$

$$\tilde{g}^{(2)}(\Delta\mathbf{r}) = 1 + h \times \prod_{\alpha} e^{-\frac{\Delta r_{\alpha}^2}{l_{\alpha}^2 + 2 \times 2 \times d_{\alpha}^2}} \quad (1.3.23)$$

with $h = \prod_{\alpha} \frac{l_{\alpha}}{\sqrt{l_{\alpha}^2 + (2d_{\alpha})^2}}$ the height of the bunching. The factor 2 with which the resolution compares to the correlation length is due for $\sqrt{2}$ to the root-mean-square definition rather than the half-width half-maximum, for $\sqrt{2}$ to the fact that the resolution is a one particle value, whereas the correlation concerns two atoms.

This means that if one wants to observe the bunching, the resolution of the detector has to be at least of comparable size, or smaller than the correlation length at the detector level. If the resolution is insufficient, the height of the bunching might well be small compared to 1, and might not distinct itself from the noise. Furthermore, for a limited resolution, we will see a temperature dependence of the bunching height h . For smaller temperatures, the correlation length l_{α} compares larger to the resolution than at higher temperatures. Depending on the temperature, we will not only observe changes in the correlation length, but consequently also in the bunching height.

1.3.3.2 The Signal to Noise Ratio

The calculation of the signal to noise ratio requires essentially a definition of signal and noise. Figure 1.17 indicate the graphically the definitions of signal and noise both for bosons 1.17A and fermions 1.17B. The signal is the area contained in the mid-gray toned area. That area corresponds to the quantum bunching effect. We will be either looking for its bosonic presence or for its fermionic absence. In the absence of any background signal, the noise will correspond essentially to the shot

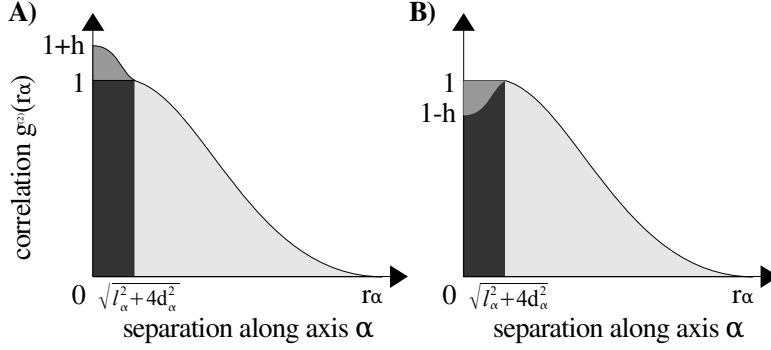


Figure 1.17: In A, the correlation expected for a thermal bosonic cloud as provided by formula 1.3.23. The mid-gray area corresponds to the Hanbury Brown and Twiss effect and is the signal. The shot noise fluctuations induced by the addition of the black and mid-gray area, will limit the contrast and is the noise. In B, the correlation expected for a thermal fermionic cloud as provided by formula 1.3.23. The signal resides in the absence of the mid-gray area. The noise is given by the shot noise fluctuations of the black area to which the mid-gray area has been subtracted. It must be noted in both cases that the resolution of the detector does not change the surface of the mid-gray area. It does affect the black area meanwhile.

noise fluctuations of the dark-gray toned area. To this area has to be respectively added or subtracted the area of the bunching in case of bosons and fermions.

As we just mentioned, the signal corresponds to the mid-gray areas in Figure 1.17. This corresponds eventually to the integral of the second term of the correlation function in Formula 1.3.22, i.e. the term corresponding to the quantum bunching, over $\prod_{\alpha}[0, \sqrt{l_{\alpha}^2 + (2d_{\alpha})^2}]$. This is nearly equivalent to an integration over the entire space. This one can be simply evaluated to:

$$Signal(T, N') = N'^2 \prod_{\alpha} \frac{\hbar \bar{\omega}_{\alpha}}{4k_B T} = N'^2 \left(\frac{\hbar \bar{\omega}}{4k_B T} \right)^3 \quad (1.3.24)$$

with $\bar{\omega}$ the geometric mean of the three ω_{α} . We immediately notice that the signal does not depend on the resolution. Although the limited resolution does smear out the detected bunching, it does not change the integral of the bunching. This is logical, in the sense that the detection does not change the physical correlation between the particles, only their measured respective distance. The resolution will yet influence the noise.

The noise is the square-root of the dark-gray area plus/minus the bunching. That is equivalent to the square-root of the integral of the total expression of 1.3.22 over $\prod_{\alpha}[0, \sqrt{l_{\alpha}^2 + (2d_{\alpha})^2}]$. In the high temperature limit, this expression can be approximated by:

$$Noise(T, N') = N' \sqrt{\left(\frac{\hbar \bar{\omega}}{2k_B T} \right)^3 \left[\prod_{\alpha} \frac{1}{\sqrt{\pi}} \sqrt{1 + 4d_{\alpha}^2/l_{\alpha}^2} \pm \frac{1}{2^3} \right]} \quad (1.3.25)$$

Finally we can write the signal to noise ratio:

$$SNR(T, N') = N' \sqrt{\left(\frac{\hbar \bar{\omega}}{4k_B T} \right)^3 \frac{1}{\sqrt{\prod_{\alpha} \frac{2}{\sqrt{\pi}} \sqrt{1 + 4d_{\alpha}^2/l_{\alpha}^2} \pm 1}}} \quad (1.3.26)$$

If we take into account the size of the detector, and considering it scales large compared to the correlation length and the resolution, we finally obtain:

$$SNR(T, N') = N' \frac{\sqrt{\left(\frac{\hbar\bar{\omega}}{4k_B T}\right)^3 \coth\left(\frac{R^2 m}{l_0^2 k_B T}\right)}}{\sqrt{\Pi_\alpha \frac{2}{\sqrt{\pi}} \sqrt{1 + 4d_\alpha^2/l_\alpha^2} \pm 1}} \quad (1.3.27)$$

We will come back to this expression as soon as we have the experimental detector characteristics.

Conclusion

We have studied throughout this chapter the Hanbury Brown and Twiss effect. In particular we studied the historical discovery of this effect by Hanbury Brown and Twiss. We have seen how the initial interest in the intensity interferometry for the study of stellar entities, raised questions in the quantum field on the nature of the particles. We have seen how theories have been experimentally approved, or disproved, and eventually led to a proper quantum description of correlations. This latest effort has only recently been awarded through the 2005 Nobel prize of Physics for R. Glauber.

That the Hanbury Brown and Twiss effect was discovered through a description of light and the observation of stars is not extraordinary. Scientists have always had their eyes pointed at the stars, and many historical advances in physics have been made through the understanding of hence observed phenomena. Nowadays, the Hanbury Brown and Twiss effect has been observed in fields ranging from optics to particle physics. The particularly high phase-space densities obtained with latest cooling techniques in cold atom physics generated hope to obtain similar signal to noise ratios as in photonic optics. A first pioneering result had been obtained by Yasuda and Shimizu in 1996, at still fairly high temperatures; the potentials of radio-frequency cooled atomic samples were looming. During the ongoing of this present study, several groups have been investigating the Hanbury Brown and Twiss effect, reflecting the fascination this quantum effect still generates among the physicists.

We investigated the particularity of the metastable helium experiments, with the possibility of a simple quantum detection scheme. The close to zero background noise rates of the micro-channel plate detectors, detectors that can convert a single particle signal into a macroscopic cloud of electrons, made them appear extremely useful for a Hanbury Brown and Twiss type experiment. A simple theory explaining the expected results has been demonstrated and enabled the calculation of the signal to noise ratio for this particular experiment.

Out of the signal to noise ratio we retain several important parameters. The main one is definitely the temperature. This affects the signal to noise ratio through several mechanisms. The first one is through its influence on the initial cloud size. The cloud is trapped in a harmonic trap. The size of the cloud in such a trap depends on the kinetic energy of the various atoms, and thus the temperature. As the correlation length after propagation scales inversely with the source size, the use of lower temperatures increases the final coherence volume, and the signal it contains accordingly. We must stress the importance of the trapping characteristics though. If the cloud were trapped in an infinitely bounding box potential, the temperature would not act upon the final correlation length.

Meanwhile, the temperature also affects the phase-space density. Atom cooling reached the Bose-Einstein condensation, because it does not simply decrease the spectral width of the atomic sample, but also increases the spectral density meanwhile. When working with colder samples, the size of the cloud after time of flight is smaller, but also denser. This higher spectral density concentrates statistically more particles in the same coherence area, and increases the signal to noise ratio accordingly. Working at the coldest possible temperatures therefore seems the key to success. In both Orsay and Amsterdam, working temperatures of the thermal gas

laid in the micro-Kelvin range. The thermal clouds in both experiments suffered a phase change around $0.5 \mu\text{K}$. Therefore we expected the experiments to be carried out around $1 \mu\text{K}$ in order to be in a correct thermal regime.

The second extremely important parameter that stands out of the signal to noise ratio study is the resolution, and a lot of energy has been invested during last years to get a hold on it. Our study shows in particular the importance of the ratio of the resolution and the correlation length. A non-favourable ratio would smear out the bunching, lowering meanwhile the bunching height. Although the total correlation volume associated to the bunching does not change, the underlying noise does increase with the increase of the apparent correlation length, consequently reducing contrast. Naturally this ratio can be reduced favourably by increasing the correlation length through a longer time-of-flight. Unfortunately, the fall height necessary for such an increase squares with the time-of-flight. For practical reasons, and also in order to maintain the versatility of the setup, we have been limiting the fall height in the 50 cm region. Note that the detector size is not an argument.

Before starting any experimental realisation, it is worth considering the correlation length we expect after a 50 cm time-of-flight at $1 \mu\text{K}$. The correlation length depends on the trapping frequency that varies with the axis. The trapping frequencies at the Orsay ^4He experiment are respectively $\omega_y = \omega_z = 2\pi \times 1150 \text{ Hz}$ and $\omega_x = 2\pi \times 47 \text{ Hz}$ for $^4\text{He}^*$. In Amsterdam, the trapping frequencies were respectively $\omega_y = \omega_z = 2\pi \times 506 \text{ Hz}$ and $\omega_x = 2\pi \times 54 \text{ Hz}$ for $^3\text{He}^*$. Consequently the correlation lengths expected are around $l_y = l_z = 800 \mu\text{m}$ and $l_x = 32 \mu\text{m}$ for the $^4\text{He}^*$ in Orsay, and $l_y = l_z = 400 \mu\text{m}$ and $l_x = 43 \mu\text{m}$ for the $^3\text{He}^*$ in Amsterdam. The z axis also has its equivalent correlation times that range $l_t = 250 \mu\text{s}$ and $l_t = 130 \mu\text{s}$ in Orsay and Amsterdam respectively. In order to have a significant bunching height and signal to noise ratio we require therefore a detector with a spatial resolution in the $30 \mu\text{m}$ range, and a temporal resolution in the $100 \mu\text{s}$ range.

The third parameter that we have not directly studied is the maximum detection rate. We will study the influence of the detection rate at the end of the next chapter, when we will be able to distinguish global and local rate. For the moment we simply note that the signal to noise ratio scales linearly with the number of detected atoms. If a single time-of-flight has an insufficient signal to noise ratio to properly observe the Hanbury Brown and Twiss effect, we will for sure be able to average over several time-of-flights. The problem is that the signal to noise ratio will only scale with the square-root of the number of realisations. It is therefore much more interesting to double the number of atoms in a single time-of-flight, rather than to double the number of realisations. Typical atom rates with which we work are 10katoms in a typical 10ms width time-of-flight. We therefore expect the detector to deal with typical mean particle rates of 1Matoms/s. Finally the detector is required to maintain similar rates over at least 10ms.

This is the book of specifications of the micro-channel plate based detector that is to fulfil the role of the intensity interferometer. In the next chapter we propose to analyse the detector that complied best with those specifications: the micro-channel plate based delay-line detector.

The Detector

The measurement of the Hanbury Brown and Twiss effect with He* requires a micro-channel plate based position sensitive detector. Several types of position sensitive devices exist, the most common in use being the phosphor screen coupled to a CCD camera. We have just determined though, that such a detector would require single atom counting capacities with incoming atomic rates in the order of 1 Matoms/s. We would also appreciate a resolution in the order of 30 μm . Finally, this detection rate has to be maintained over at least 10 ms.

We will overview in the first section of this chapter the various position sensitive detection systems types that exist. We will be able to easily eliminate most detectors for non compliance to our requirements. It must be noticed though that this overview merely deals with the current state-of-art. As the electronic technologies involved are evolving in a very rapid pace, a similar experiment in the future might take a different choice.

We then focus on the single detector we found to comply most to our needs: the delay-line detector. We study the entire detection chain, from the micro-channel plate detection down to the computer acquisition and analysis tools.

Finally specific focus is given to the detection efficiency, the detection rate and the resolution. Those are the essential physical characteristics that influence directly the outcome of the experiment. This study also provides a deeper understanding of the mechanisms involved in the detection.

2.1 Detectors Overview

Behind the micro-channel plate stack used for the detection of energetic particles, various detection schemes can be used to image the out-coming electron clouds. We will discuss in this section the various schemes that are currently employed to do so. Most of those techniques have been developed in the field of nuclear physics. They have often been designed to deal with pulsed or continuous experiments, that have an average event rate in the kHz order, and that have to deal with a few particles with low separations in time. They therefore can deal generally with very high particle rates, but only for a few particles, and for very short timings.

We will first discuss a traditional use of phosphor screens, combined with CCD cameras, that is interesting for imaging purposes, and that is specifically employed for night-vision devices. We will then study briefly the use of resistive anodes for position sensitivity. Then we will see how the delay-line detector complies to our needs. Finally we will discuss briefly some improved delay-line detector detection schemes that might prove interesting in the future.

2.1.1 Phosphor Screens

The idea behind the use of a phosphor screen with a CCD camera is illustrated in Figure 2.1. The electrons coming from the micro-channel plate stack are attracted

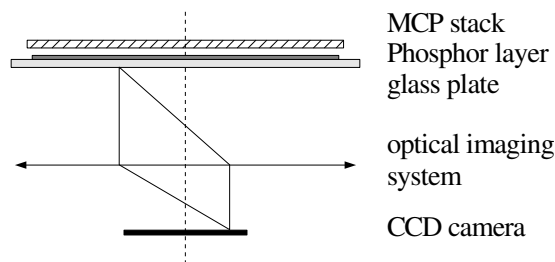


Figure 2.1: The electrons provided by the micro-channel plate stack are attracted to a phosphor coated glass plate. The photons produced by the electronic excitation of the phosphor are collected through an imaging system on a CCD camera.

towards a phosphor coated glass screen. The electrons excite the phosphor, that re-emits the energy through photonic emission. The photons are collected through an optical system and imaged on a CCD camera.

The global system is quite performing in terms of resolution. Sub-pixel analysis can lead to resolutions below $100 \mu\text{m}$. The problem of this system is the acquisition rate.

The timings we require for the proposed Hanbury Brown and Twiss experiment are around the $50 \mu\text{s}$. We therefore require a camera that can handle a 20 kHz acquisition rate. With the expected particle flux, this still produces up to 50 detected atoms on a single image. If the atoms are homogeneously spread over the image, this is still reasonable. Yet with cold atomic clouds or more specifically Bose-Einstein condensates, the spatial densities are much higher and it will be impossible to distinguish the atoms. We would therefore require a CCD camera that can take up to 200 k images per second.

Considering a 256×256 8 bits CCD matrix, this produces a data flux of 13 Gbytes/s. Currently, no electronic serial connection can handle such data transfers. This therefore requires cameras with integrated memories. Currently no such cameras exist with sufficient performances. The best CMOS based cameras currently available can deal with 5 kframes/s (Photron) in full resolution. With reduced resolution they can eventually work up to 150 kframes/s, but a reduced resolution.

If progress in terms of fast CMOS sensors continues at current pace, the phosphor screen might become an option though one day. Computer power will then also have to be available to deal with the 200 Mbytes of data of every acquisition in a reasonable time. More sophisticated CMOS technologies might also appear that could allow for selective reading of the pixels. That could lower considerably the data rate.

2.1.2 Charge Division Devices

An interesting way of getting position sensitive information from the electronic pulses provided by the micro-channel plate is to subdivide the signal and study its physical properties. An example would be a resistive anode [75], as illustrated in Figure 2.2A. The electronic pulse provided by the micro-channel plate stack drops on a resistive plate. On the four sides of the plate, a collection wire evacuates the captured electric charges. Because of a high resistivity, the electric charges will seek an optimal exit to the output channels. Consequently, the charge distribution on the four exists depends on the arrival position, and the measurement of those charges will provide after calculation the position of the particle. An alternative would be to measure the rising front slope of the impulses, that also depends on the initial position of the particle.

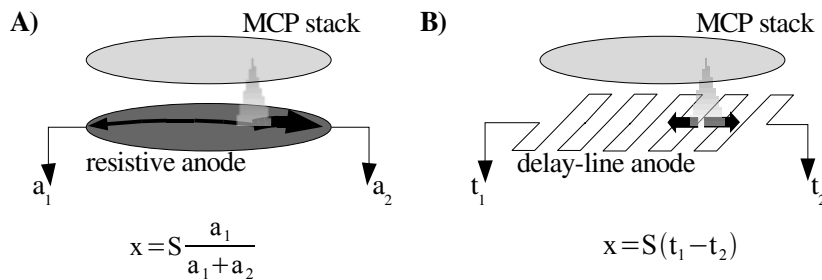


Figure 2.2: In A, an illustration of a resistive anode position sensitive device. Depending on where the electron shower occurs, the relative amplitudes at the two exits vary. This relation can be used to determine the position. In B, an illustration of a delay-line anode position sensitive device. According to the position of the electronic shower, the relative delay of the two electric signals in the two directions of the wire change. Measuring those arrival times makes it possible to retrieve the position.

Another example is a delay-line [76], as illustrated in 2.2B. In this case the impulse is collected on a wound wire. This results into a propagation of two electronic signals in each direction along the wire. If one measures the arrival time of the two impulses at the end of the wires, one can by taking the difference of the arrival times retrieve the position of the particle.

The physical measurements of the divided charges can be performed by trivial components. The charge can be measured by amplitude-to-digital converters. Arrival times can be measured by time-to-digital converters. Each particle consequently generates up to four informations. The total data rate is thus proportional to the particle rate, that for our required atom rate will generate data rates of 16 Mbytes/s. This is far more reasonable than the previous 13 Gbytes/s. Also the associated analysis times are reasonable.

The performances of the charge division devices all depend on two factors. The quality of the measurement electronics and the physical properties of the anode. They also all have in common a tradeoff between the particle rate and the resolution. For example, for a given time-to-digital converter coding step, a delay-line anode will give a better relative timing if the delay-line is longer. Yet if the delay-line is longer, it takes longer for the pulse to quit the line, and during that time no other particle can be detected. Samelike, the higher the resistivity of the resistive anode, the better the charge division, yet it also takes longer for the charges to quit the anode.

The performances of those detectors are therefore strongly related to those of the state-of-art of the electronics. At the time that we were seeking for a detector, the delay-line anodes were the commercially available detectors most tuned to our requirements. The available resistive anode detectors had made a tradeoff in favour of the resolution rather than the acquisition rate. This is understandable as most detector users work at much lower acquisition rates. At the date of our acquisition, the Roentdek Handel GmbH's DLD80, with a 80 ns delay-line, was the only heard of detector compatible with our resolution requirements and our acquisition rates. It was sold with a potential acquisition rates of several Mcounts/s, and with a 200 μm spatial resolution. The time resolution was 1 ns.

2.1.3 Advanced Charge Division Devices

The enormous benefit of charge division devices, is the simplicity of the measurement components, and the little information they generate. This key advantage is also a drawback. Those components can not deal with double counting situations, and they ultimately limit the acquisition rate.

Modern signal sampling and acquisition devices have meanwhile grown so performing that they can compete with the amplitude and time-to-digital converters. Instead of converting the analogue signal in a series of simple measurements, brute force can today be used to simply acquire the total analogue signal over extended periods. A complex post software analysis can then extract more, and eventually better information from the divided charges.

Such an advanced delay-line detection scheme has been implemented by the Groupe de Physique des Matériaux at INSA Rouen [77]. By coupling a multi-channel 4 GHz sampling rate digitiser to a delay-line, and by using deconvolution techniques, they have been able to produce a delay-line detector with a 100 μm resolution and a 1.5 ns deadtime. The draw back of the advanced detection scheme, is that they generate huge amounts of data, and that they require a time-consuming data analysis. This is currently confining the Rouen group to kHz acquisition rates. We will discuss in Appendix 3 an advanced detection scheme, though far less ambitious, we have implemented in Orsay, and we will understand why we are currently

happy with a simple delay-line detector.

2.2 The Delay-Line Detector

In this section we will have a much closer look at the implementation of a delay-line detector as overviewed in Figure 2.3.

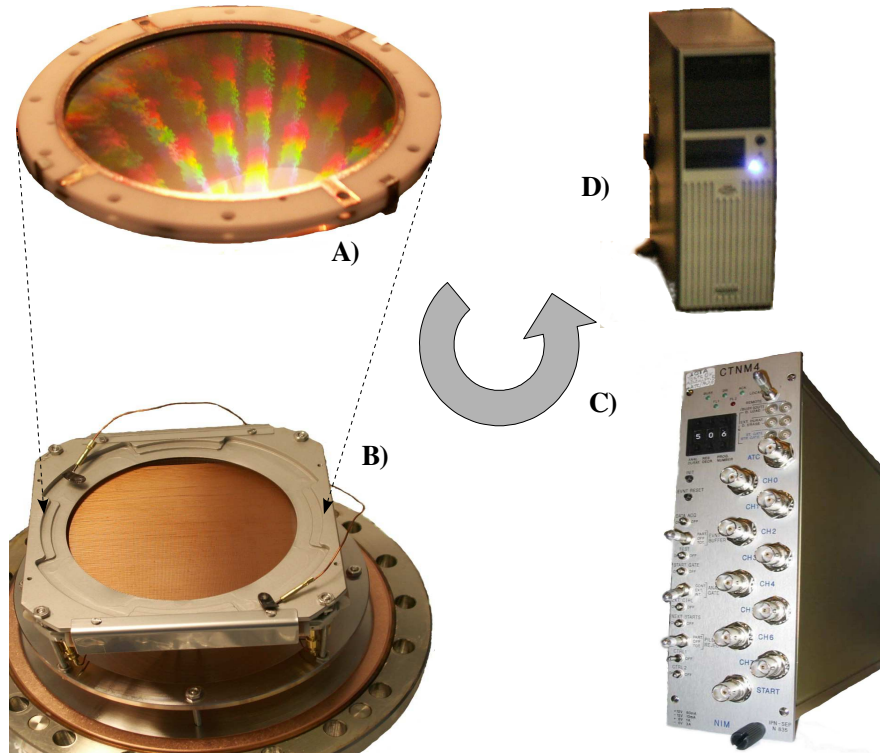


Figure 2.3: Pictures of the entire detector system. In A, the atoms trigger an electric pulse in a micro-channel plate stack. The electrons are captured in B by a Roentdek DLD80 delay-line detector mounted on a CF160 ultrahigh vacuum flange. In C, pulse amplification and discrimination is performed by Roentdek's DLATR-6 box, the discriminated pulses have their arrival time measured by a CTNM4 time-to-digital converter. Finally the digital data is send to a computer in D for acquisition and further analysis.

We will first consider a little more closely the way micro-channel plates work and behave, and conclude on the micro-channel plates we have chosen. Thereafter we will explorer in more detail the way the delay-lines work. Then we will focus on a crucial part: the electronics behind the delay-lines. Finally we will deal with an often neglected part: the computer acquisition software.

2.2.1 The micro-channel plates

Micro-channel plates can be seen as thin glass plates pierced with many tiny channels. In reality those plates are made by forming an array of millions of glass tubes, tens of microns large, that are then cut into slices around a millimetre thick. The inner coating of those glass tubes is highly resistive, the outer coating of the plates is metalised in order to provide parallel electric connection to all channels . By applying a electric potential to the plate, all channels are transformed in continuous dynode electron multipliers.

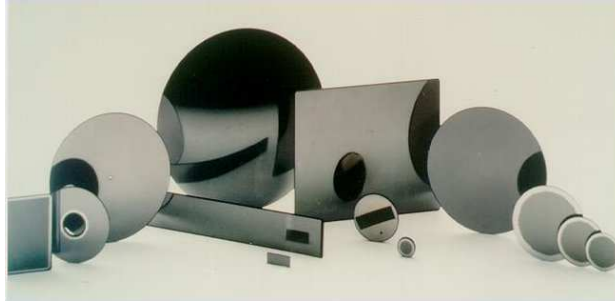


Figure 2.4: A sample of commercially produced microchannel plates (BURLE Electro-Optics, Inc).

2.2.1.1 Mechanism

Each channel is a dynode electron multiplier. In such a multiplier, electrons are accelerated in an electric potential. Those electrons are forced into collision with the channel that has a small angle with the electric field, hence ejecting secondary electrons from the substrate in number proportional to the acquired energy of the electron. Those secondary electrons are in turn also accelerated into another collision, and so on. Thus is set off an exponential amplification mechanism. Thanks to the very light mass of the electrons, such an amplification process takes around 100 ps. With proper electronics, such an event can be timed to some tens of picoseconds.

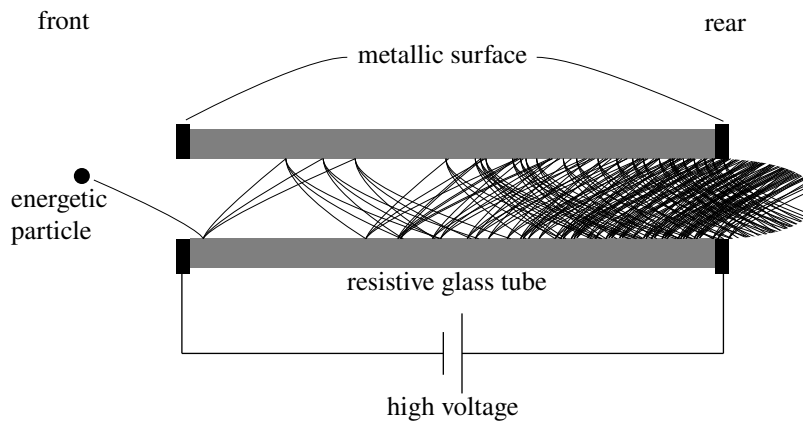


Figure 2.5: An energetic particle hitting the channel liberates its energy by extracting electrons. Those electrons are accelerated by an electric potential applied between the front and rear side metalised surfaces of the micro-channel plate. Hitting in their turn the glass tube, the number of those secondary electrons increases exponentially.

The first electrons are produced by the energy released at the impact of the to-be-detected particle. This energy therefore needs to be sufficient to extract those electrons. This energy can be introduced by energetic photons, accelerated ions or alpha-particles, or metastable atoms. The necessity for a relatively high electron extraction energy translates into a very low dark count rate, lower than $1\text{count}/\text{cm}^2/\text{s}$. Consequently micro-channel plates are very suitable for observations requiring long (typically a second) observation times.

2.2.1.2 Multiple micro-channel plates

A standard micro-channel plate has an amplification factor of $10^3 - 10^4$. The voltage, on which this gain is strongly depending, is limited by the thickness of the plate. Using too high voltages sets off destructive electric arcs. Increasing the thickness of the plates is however not the solution. Ionisation of the background gas, and corrosion of the glass coating by the increasingly dense electron cloud produce positive ions that are accelerated to the entrance of the channel. There they can trigger echo counts. This problem can be overcome by adding up 2 or 3 micro-channel plates. By opposing the angles between the successive micro-channel plates channels, as shown in Figure 2.6, the faulty ions are forced into an early collision midway. Consequently, the total thickness, and therefore the total voltage, and thus the gain, can be increased up to the requirements without affecting the quality of the detection. Most common, the double and triple stack configurations are called chevron and Z-stack configurations. A chevron configuration can produce up to 10^8 electrons for a single count.

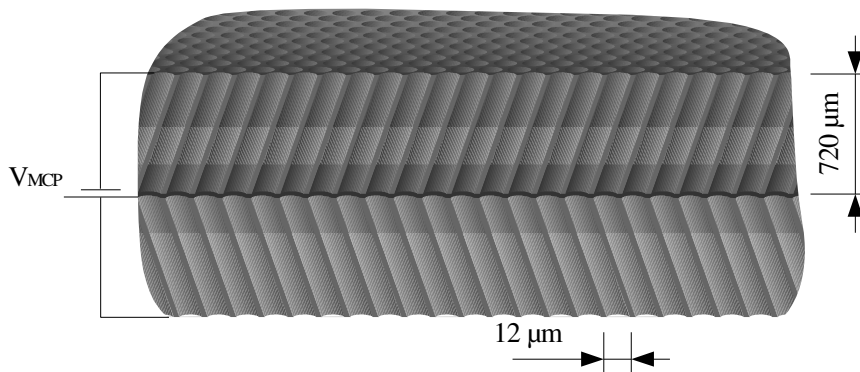


Figure 2.6: Two micro-channel plates in chevron configuration. The angles of the channels are inverted in order to prevent produced ions to reach the entrance and triggering echo counts. A single voltage can be applied to the double stack if the micro-channel plates have similar electric resistances. Inter-surface contact is then enough to assure the circuit is closed.

2.2.1.3 Gain and pulse-height distribution

The electron amplification procedure is a pure birth process, also known as a Yule process [78]. The resulting electron number distribution, after a constant amplification time, is exponential. This means that the expected amplitudes from the electronic pulses provided by the micro-channel plates have an exponential distribution. Exponential pulse height distributions are generally unhandy for particle counting. They do not allow for double counting detection schemes, as those schemes need precise information on the pulse height.

Fortunately the amplification process saturates at high gain. If the electronic density is too high, the static electric potential is screened by the electron cloud itself, strongly reducing the amplification efficiency. The exponential distribution

is then transformed into a more gaussian distribution. This effect is particularly useful for counting imaging because it assures an homogeneous image. When saturating, and as illustrated in Figure 2.7, a trigger can clearly distinguish noise from signal, and all pulses are detected. If the detector shows a inhomogenous amplitude distribution, this can be overcome through the discrimination process. In order to reach saturation, two or more micro-channel plates are generally required.

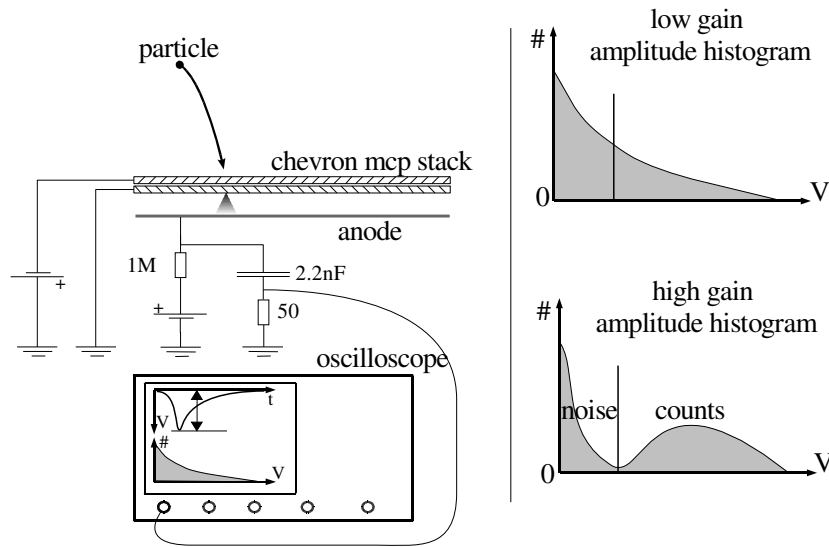


Figure 2.7: The amplitude distribution can be easily measured with a modern oscilloscope. A metallic plate is put behind the micro-channel plates, with a slightly positive potential. The electrons go into the plate, producing a current. This current is measured at both sides of a resistance. At low gain, the amplitude distribution is exponential and cannot be distinguished from the background noise. If one increases the gain, it saturates and a distinguishable counts peak appears. Noise is then easily discriminated.

Various parameters influence on the gain. One of them is the voltage. Voltage dependence is exponential until saturation of the process. Another static parameter is the channel aspect ratio. The gain of micro-channel plate is given by the ratio of the length of the channel, divided by the diameter of the channel. This ratio is generally of 60. Consequently the choice of the channel diameter does not affect the gain, but it does change the maximum particle rate.

2.2.1.4 Flux saturation

The amplification of a single count can saturate. But the detection of a particle also influences the detection of following particles. The channel that has been used for the first detection shows an electronic depletion. In the case a chevron or a Z-stack configuration has been used, the electrons coming from the first micro-channel plate spread eventually over several channels in the second micro-channel plate. Hence a small region shows an electronic depletion that strongly influences the local amplification process. Consequently micro-channel plates show a maximum local flux.

This electronic depletion is compensated by a strip current. Because of the high resistances of the channels, this current is low. If the electronic depletion is over 10% of the strip current, a micro-channel plate is often saturated [79]. For a 7.5 cm diameter chevron stack with a total resistance of 26 M Ω operated at 2300 V, if the average number of electrons per count is of 10^7 , the maximum local flux is of 125 kparticles/cm²/s.

Note that having channels with smaller diameters increases this maximum flux. Although smaller diameter does not decrease the electrical resistance of a single channel as long as the aspect ratio is conserved, it does increase the number of channels per surface unit. Hence the surface resistance is reduced and thereby the maximum flux increased.

Note that the resistance of those micro-channel plates can be reduced by applying a special coating to the channels, hence increasing the strip current and same-like the maximum flux by a factor 10. The limit of such coating is the eventual heating of the micro-channel plate and the necessity for high power high voltage supplies. Furthermore, experience shows [80] that the lifetime of such coating is still a limiting factor. Less than a year is to be expected before those micro-channel plates return to a standard behaviour.

2.2.1.5 Our Choice

Our first choice has gone to BURLE's Long-LifeTM micro-channel plates. We have bought a chevron stack of 8 cm diameter micro-channel plates, with an aspect ratio of 60, channel diameter of 12 μ m, centre-to-centre spacing of 15 μ m, detector quality. The bias angle of the channels is of 8°. We had, to say the least, some surprises.

Noise The first surprise came from the background noise. Indeed at 2300 kV of operation, our detection system showed a darkcount of 1300 counts/s. This darkcount is much higher when the micro-channel plates have just been put under vacuum, and lowers progressively with the operation time. In earlier experiments, different micro-channel plates produced by Hamamatsu Corporation did not show such darkcounts. This number was also in contradiction with the specifications of 0.3 counts/cm²/s.

Imaging of those darkcounts showed that they were spatially very localised, as shown in figure 2.8. The spikes correspond probably to some border effects with eventually trapped gas. This is how they disappear with the time as the gas is being pumped away. As they are very localised, they can, once imaging has been implemented, be cut out of the data easily. After this cut out, the noise rate is 0.3counts/s/cm², as in the specifications. It can be neglected when compared to the expected particle rate.

Gain Also the gain distribution showed some surprises. Figure 2.9A is a plot of the average amplitude of the pulses versus their position at the 2300 V operation voltage (The method through which this map has been acquired is presented in Appendix 3). It shows that the detector has regions of high gain, and regions of lower gain. Figure 2.9B shows the amplitude distributions in respectively the low and high gain region. One distinguishes that the lower gain regions have an

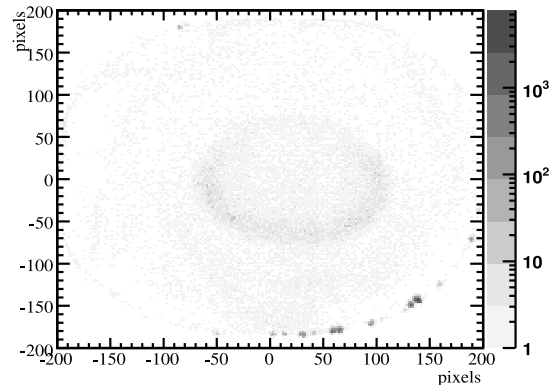


Figure 2.8: Image of the darkcounts on the detector. The signal has been integrated over 50 s. At the border of the image, one can distinguish some intense hot-spots (the intensity scale is logarithmic). The counts in the middle occur at a very low count rate, and are likely due to ambient light. The hotspots can change when the detector is put under vacuum again. They are likely due to residual gas.

exponential type distribution, whereas the higher gain regions show clearly a gain saturation.

Because the gain does not saturate at various places, this inhomogeneous gain distribution inevitably results in a inhomogeneous detection efficiency as we will see in the next section. No discriminator level can cope with the entire detector.

The reason for this spatially depending gain is not yet understood. Hypotheses do exist. The most likely is a bad mounting of the micro-channel plates. Indeed, for flux considerations we bought micro-channel plates thinner than those the mounting rings for the detector where made for. Consequently forces are not evenly applied to the outer diameter of the chevron stack and the distance between the two micro-channel plates is not evenly distributed. One can imagine this has an impact on the gain. Unmounting and remounting of the micro-channel plate stack induced a change in the gain distribution, that confirms the mechanical sensitivity of the setup. Hence the configuration at which we employed the detector in Amsterdam was different from what it was in Orsay. The only change made to the detector in between was a short unmounting of the micro-channel plate stack. The recent acquisition of a second stack of micro-channel plates and also of a spacer that can be put between the micro-channel plates will make experimentation possible, and could show the validity of this theory.

2.2.2 The Delay-Line Detector

The delay-line detector we have used is commercially distributed and designed by Roentdek Handels GmbH [81]. We opted for the DLD80, as illustrated in Figure 2.10.

This detector essentially consists of a micro-channel plate stack mounted in front of a delay-line. We will briefly study how this delay-line works. We will then have a look at the operation voltages in order to use the detector in its optimal conditions. A detailed study on the relation of the delay-line and the resolution is

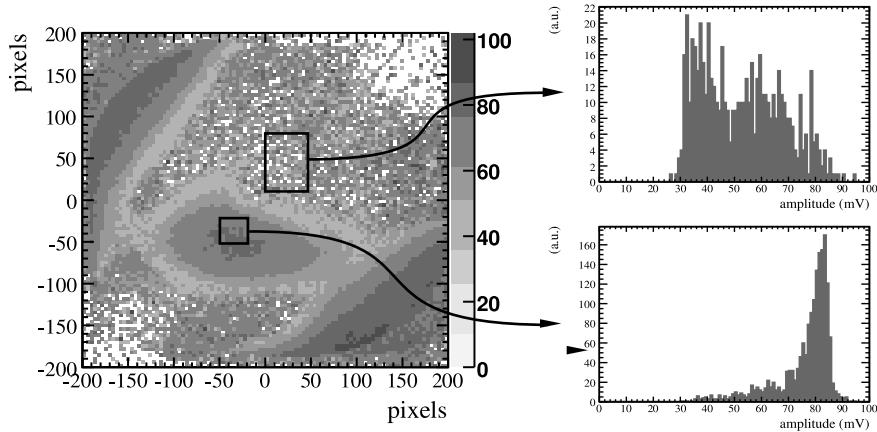


Figure 2.9: In A, the average amplitude plotted versus position. This graph has been obtained using a 4 channel oscilloscope. One can distinguish regions of low and high gains. The amplitude distributions of the squares inside the figure have been plotted in B. The lower gain regions show an exponential distribution. The lower part of this distribution is cut off because of the trigger levels used in the reconstruction method (see Appendix 3). The high gain regions show a saturated gain.

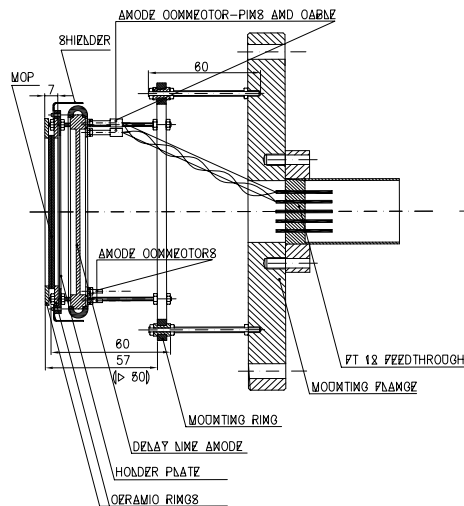


Figure 2.10: Technical drawing of the DLD80 delay-line detector. A micro-channel plate stack is mounted mechanically in front of a delay-line. The ensemble is mounted on a CF160 vacuum flange. An electric feedthrough assures the transport of the signals and the high voltages into the vacuum chamber. (Figure from [81])

provided in Appendix 1.

2.2.2.1 Mechanism

Principle A delay-line is a line for which the length cannot be neglected when compared to the speed of the electronic pulse and the typical time constants involved. If one considers now an electronic pulse released somewhere in that wire, it is possible, by measuring the arrival times at each side of the wire, to retrieve the position from where this pulse has been released (see Figure 2.11).

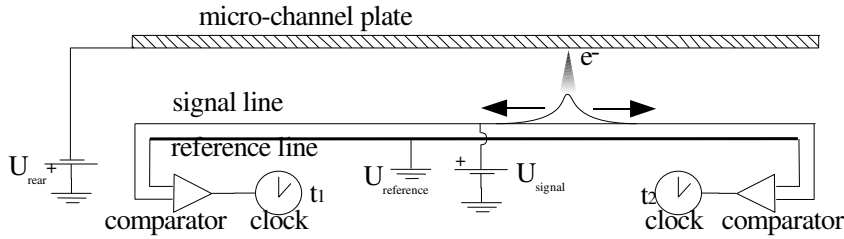


Figure 2.11: The principle of a delay-line. The electrons produced by a micro-channel plate stack is guided through a differential electric potential to a copper signal line. The resulting potential difference with a close reference line triggers the propagation of an electric signal along the two directions of the wire. At the end of the wire, the signal is amplified, discriminated and the arrival time is measured through a time-to-digital converter. the difference between the two arrival times indicate the position of the initial electronic pulse.

In the case of our detector, the electrons forming the electric pulse leave the micro-channel plates at a certain position. By a positive differential potential between the rear-side of the micro-channel plate stack and the signal line, those electrons go into the latter. This electric charge is evacuated through the transmission line. The differential DC voltage between the signal and reference line induced by those electrons can then be discriminated and their arrival time measured.

If we call t_1 and t_2 respectively the arrival times at both sides of the wire. Those can be written $t + x/v_c + C_1$ and $t - x/v_c + C_2$, where t is the arrival time of the particle on the micro-channel plate, x the position on the micro-channel plate, v_c the velocity of the charge inside the wire, C_1 and C_2 two constants depending on the global configuration and the definition of $x = 0$. The position can then indeed be obtained simply:

$$x = (t_1 - t_2) \times v_c \quad (2.2.1)$$

The velocity of the charges is in this delay-line of the order of $c/3$. Considering a time resolution of 400 ps and a micro-channel plate diameter of 8 cm, the number of pixels is then as low as 2.

Furthermore, this simple system works in case the detector is one dimensional. Yet in reality the detector has two dimensions, that have to be covered.

A Helical Delay-Line A simple way to solve those two problems is to wind the delay-line as illustrated in Figure 2.12.

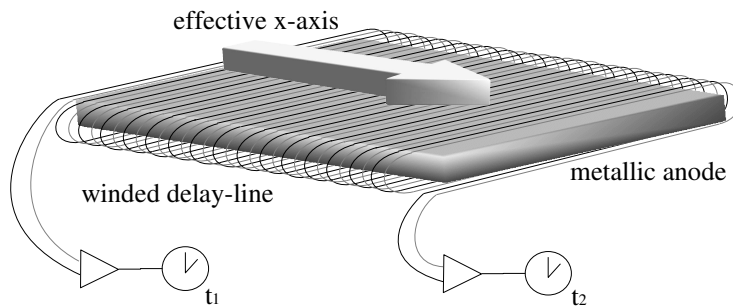


Figure 2.12: In order to increase the resolution, and to cover the entire detector surface, the delay-line is wound 100 times. The resulting apparent transverse charge velocity is then divided by 100, and with the same factor the resolution is increased. The electrons that come out of the micro-channel plates cover several wires, such that the final pulse as detected by the discriminator is the average of several. The centre-of-gravity of that pulse consequently has sub-wire resolution.

The wires are wound 100 times around a metallic anode. The winding axis is then the measurement axis. As the equivalent speed has been reduced by 100 as well, the number of pixels has increased with the same factor.

The resolution is not limited to the number of spirals as one could easily imagine. Indeed, as the dense electron cloud leaves the channels from the micro-channel plate, they spread spatially over a number of wires. Dispersion in the delay-line ensures that the different pulses in the various spirals overlap each other by the time they reach the discriminator. By evaluating the *centre-of-gravity* of the resulting pulse, one obtains sub-wire resolution in the same manner as sub-pixel resolution can be obtained with a CCD camera.

In order to obtain sensitivity in the other spatial dimension, a second wire is put between the first wire and the anode, and is wound along the other axis.

2.2.2.2 Operating voltages

The only tuneable parameters are the voltages of the signal and reference wires, as well as that of the metallic anode. The potentials applied to the X and Y wires are identical, given the electronics we bought. These potentials influence both the detectivity of the detector, as well as its resolution.

Potentials and Detectivity A particle is detected by the discriminator if the amplitude of the electronic pulse it produces goes above the threshold level. This depends not only on the ability of the micro-channel plates to amplify sufficiently, but also on the delay-lines to collect the electrons. The latter depends on the electric potentials that are applied to the wires. In Figure 2.13 we have plotted various graphs that indicate the position reconstructed counting rate as a function of the various electric potentials. Throughout all the graphs, we have used successive detected time-of-flights at 1 mK released from a magneto-optical trap with nearly identical number of atoms. In Figure 2.13A, we have plotted the number of counts

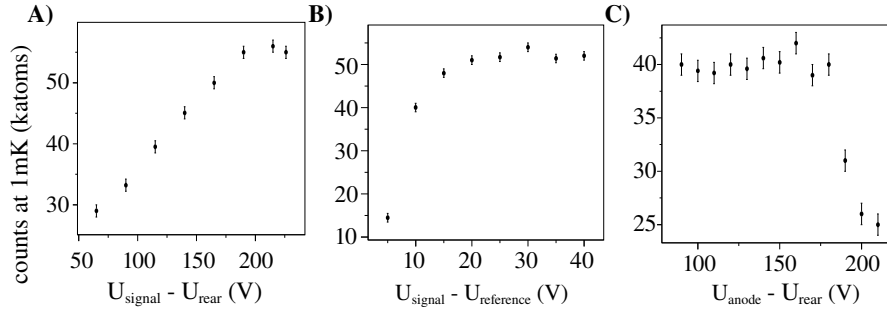


Figure 2.13: In A, the measured number counts as a function of the potential $U_{\text{signal}} - U_{\text{rear}}$ for 1 mK time-of-flights. For this measurement $U_{\text{rear}} = 0$ V, $U_{\text{signal}} - U_{\text{reference}} = 40$ V, and $U_{\text{anode}} = 15$ V. In B, the number of counts versus $U_{\text{signal}} - U_{\text{reference}}$. For this measurement $U_{\text{rear}} = 0$ V, $U_{\text{anode}} = 15$ V and $U_{\text{signal}} = 180$ V. In C, the measured number of counts versus $U_{\text{anode}} - U_{\text{rear}}$, with $U_{\text{rear}} = 0$ V, $U_{\text{signal}} = 200$ V and $U_{\text{reference}} = 160$ V.

as a function of the potential difference between the rear-side of the micro-channel plate stack (at $U_{\text{rear}} = 0$ V), and the collecting signal wire. During this measurement we kept $U_{\text{anode}} = 15$ V and $U_{\text{signal}} - U_{\text{reference}} = 40$ V. We simply note that the counting maximises around 200 V, and consequently we have fixed the voltage to that level.

In Figure 2.13B, we considered the collecting efficiency as a function of $U_{\text{signal}} - U_{\text{reference}}$. During this measurement, we kept $U_{\text{rear}} = 0$ V, $U_{\text{anode}} = 15$ V and $U_{\text{signal}} = 180$ V. If both wires detect the same number of electrons, the differential discriminator will not detect any pulse. Maximum detection is performed when the signal line collects all the electrons, and the reference line none. We simply note from the graph that as long as $U_{\text{signal}} - U_{\text{reference}} > 20$ V, the maximum counts are detected. Effectively, we tend to work with $U_{\text{signal}} - U_{\text{reference}} = 40$ V.

In Figure 2.13C, we plotted the effect of the collecting anode potential on the detection efficiency. Using $U_{\text{rear}} = 0$ V, $U_{\text{signal}} = 200$ V and $U_{\text{reference}} = 160$ V, we note that somewhere for U_{anode} between U_{signal} and $U_{\text{reference}}$, the detection starts to drop. We have therefore fixed $U_{\text{anode}} = 90$ V for usual data acquisition.

Potentials and Resolution We can also suspect the electric potentials to affect the resolution of the detector. Although the resolution, and the way it is measured, is extensively studied in the next section, we will simply consider the same data studied in Figures 2.13. Hence we plotted in Figures 2.14, the resolution for the same data as a function of the same potential differences. We note immediately that the resolution and the detectivity behave in the same way: the better the detectivity, the better the resolution. This is not surprising as we will learn a little further. Indeed, we will see that the resolution and the pulse height are intimately related, as is the pulse height and the detectivity. Those two series of graphs are consequently at first order equivalent.

A special remark had yet to be made for Figure 2.14C. In this graph, the resolution seems specifically worse between 160 V and 190 V. Above those voltages, resolution becomes better again, and stable. Actually, if one observes the resolution method closely, one would discover that the resolution goes progressively from one regime below 160 V, to another regime above 190 V. The two regimes provide

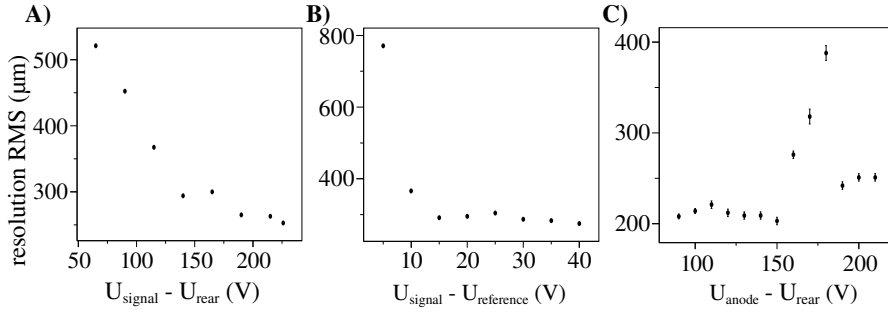


Figure 2.14: In A, the resolution as a function of the potential $U_{\text{signal}} - U_{\text{rear}}$ for 1 mK time-of-flights. For this measurement $U_{\text{rear}} = 0$ V, $U_{\text{signal}} - U_{\text{reference}} = 40$ V, and $U_{\text{anode}} = 15$ V. In B, the resolution versus $U_{\text{signal}} - U_{\text{reference}}$. For this measurement $U_{\text{rear}} = 0$ V, $U_{\text{anode}} = 15$ V and $U_{\text{signal}} = 180$ V. In C, the resolution versus $U_{\text{anode}} - U_{\text{rear}}$, with $U_{\text{rear}} = 0$ V, $U_{\text{signal}} = 200$ V and $U_{\text{reference}} = 160$ V.

two distinct distributions, and in the intermediate regime the counts are transferred progressively from one to the other distribution. This specific point might deserve more attention for better understanding of the delay-line detector.

2.2.3 The Electronics

The pulses that come out of the delay-line still have to be analysed. This can be done in several manners. One of this manner is by using an oscilloscope. This method is discussed in Appendix 3. The use of an oscilloscope proves to be particularly expensive in terms of price, but also expensive in terms of network bandwidth, storage space and computing power.

While the use of digital scopes or digital analysers has been made possible only in the past years with the very cheap prices of fast memory components, there has since long been a much cheaper, and equally effective solution. This solution is the combination of a constant fraction discriminator and a time-to-digital converter. The former associates a logical pulse to the analog pulse from the delay-line, the latter measures the arrival time of that logical pulse and writes it to a memory.

2.2.3.1 Analog to Logical

The vendor of the detector also sold us the electronics with it. The description here below is mostly their choice. The electronic box, the DLATR6 from Roentdek, takes as input the high voltages coming from the detector, it outputs the logical NIM signals for the time-to-digital converter. We will briefly see how the analogue pulses are extracted from the high voltages and then amplified. We will then study the purpose of the constant fraction discriminator.

Pulse Extraction The DLATR6 box has 6 channels. Four channels are provided for the outputs of the two delay-lines. Furthermore two channels are provided for the front and rear side of the micro-channel plates. In order to extract the high frequency signal pulse from the high voltage necessary for operation, each channel has been cabled as drawn in Figure 2.15A.

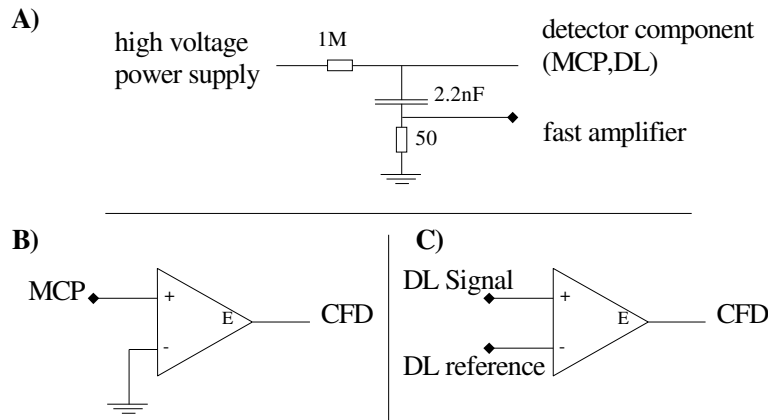


Figure 2.15: The electronic circuitry inside the Roentdek DLATR box. In A, the electronic high frequency signal is extracted from the high voltage through a simple RC circuit. The high frequency output goes to the fast amplifier. In B, the signal from the MCP channel are amplified in respect to the ground. In C, the signals from the delay-lines are amplified differentially between the signal and the reference delay-line.

The RC high pass filter sends the frequencies above 9 MHz to the amplifier. Note that the $1\text{ M}\Omega$ resistance between the power supply and the detector components is not negligible compared to the $26\text{ M}\Omega$ resistance of the micro-channel plate stack. Consequently, the high voltage supply's indication does not correspond to the effective micro-channel plate voltage. This resistance has to be taken into account.

Pulse Amplification The difference in treatment between the delay-lines and the micro-channel plate signals lies in the amplification. Whereas the signals from the micro-channel plates are amplified with respect to the ground, the outputs of the reference line and the signal line are amplified differentially in respect to each other. The latter has the great advantage of being less sensitive to electronic noise.

Indeed, apart from the detector, many electronic devices are necessary to the success of the experiment. Many of them generate radio-frequencies. In particular, the metastable helium cells used in the setup to lock the lasers employ a 27 MHz radio-frequency to maintain the discharge. The antenna of those cells happened to not have been isolated, as before this detector no other high frequencies were used. Consequently, the entire experimental room is drawn into a 27 MHz sinusoidal signal and its harmonics, who are in the middle of our signal spectrum.

If the reference line catches this noise signal, the signal line also catches it and the signal disappears at the differential amplification. For the cable that goes to the micro-channel plate, this noise elimination does not occur, and the amplified micro-channel plate signal shows a high level of background noise.

We managed to lower that noise by changing the wire configuration. Though much better, the result was not yet satisfactory. It is not clear at this point where the problem lies exactly. Overall poor grounding of the experiment might also be

an issue. As this fifth micro-channel plate signal was globally unnecessary, and considering the flux limitations of the time-to-digital converter we decided not to use the micro-channel plate timing signals in the presented experiments.

Pulse Discrimination Once the signal has been amplified, it still needs discrimination. Discrimination has a double purpose. On one hand it has to discriminate signal from noise. This is generally done by fixing a threshold under which fluctuations are considered noise. The second purpose is to associate a time to the pulse. This point deserves special care.

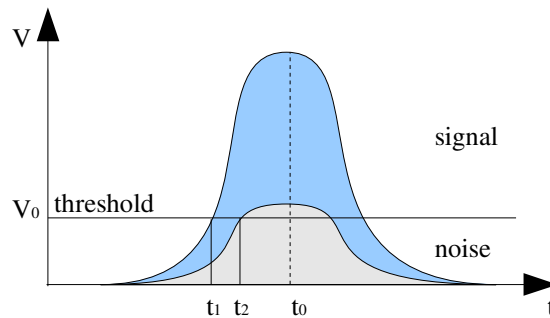


Figure 2.16: A leading edge discriminator's behaviour. A threshold is fixed. Below this threshold fluctuations are considered noise, above they are considered signal. This same level can then be used as the timing reference. Yet if two identical pulses with different amplitudes pass, they induce different timings t_1 and t_2 with respect to their maximum t_0 .

Let us consider using a leading edge discriminator as shown in Figure 2.16. In a leading edge discriminator, the timing pulse is triggered when the signal reaches a constant level. A problem arises when the amplitude of the signal is not constant, which is the case with our pulses coming from the micro-channel plates. In that case, the timing of the triggering is not constant in respect to the time of the maximum. This phenomena is called logically the walk.

The solution to the problem of the walk for identically shaped pulses with different amplitudes is the constant fraction discriminator. This discriminator behaves as indicated in Figure 2.17. The initial signal is divided in two parts. One part is amplified with a factor k generally in the order of 0.5. The other part is delayed by τ generally in the order of the half-width half-height of the pulse. A comparator then triggers the logical impulse.

This discriminator can easily be put into mathematical form. The comparator triggers at the solution of the following equation.

$$A \times f(t - \tau) - k \times A \times f(t) = 0 \quad (2.2.2)$$

The solutions of this equation are naturally independent from the amplitude factor A , which is what we were looking for. We note though that the solutions do depend on the pulse shape provided by f .

The resulting logical NIM signal is then send to the time-to-digital converter for measurement. Eventually, the delay in the constant fraction discriminator can be changed manually between 2, 4, 6, 8 and 10 ns. This affects the quality of

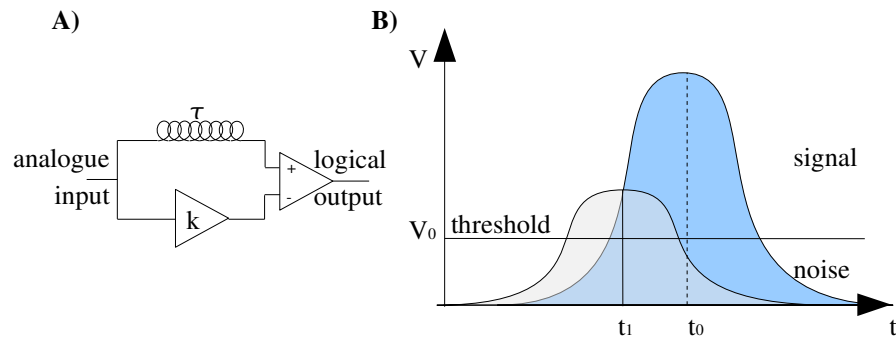


Figure 2.17: In A, the circuit of a typical constant fraction discriminator. The analog signal is, on one hand delayed by a time τ , on the other side amplified with a factor k . The resulting signals trigger the logical output in a comparator. In B, the two resulting shapes after change as they enter the comparator. The time is always triggered from the same height compared to the maximum. If the shapes of successive pulses are identical but not their amplitude, the correct timing is still respected. The constant fraction discriminator still needs a leading edge discriminator to establish the validity of the pulse height.

the constant fraction discriminator, and changes consequently the resolution of the detector (the resolution measurement method is discussed in the next section). We have plotted in Figure 2.18 the result of such a study on 1 mK clouds. The resulting

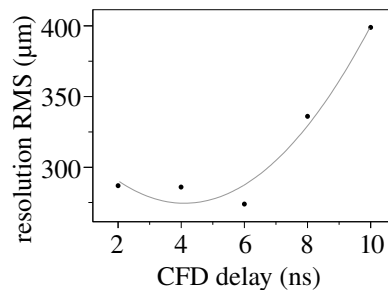


Figure 2.18: The resolution of the detector for 1 mK time-of-flights versus the delays of the delay-line discriminators.

graph shows a minimum at a delay of 6 ns. We have used the constant fraction discriminator for the data with a delay of 4 ns...

2.2.3.2 Logical to Digital

The time-to-digital converter is mainly a counter that compares the logical input pulse with a reference clock signal. Practically the quartz clock used is rarely up to the resolution of the time-to-digital converter, that requires a special design that introduces some difficulties. Furthermore, the digitising of the time-to-digital converter happens on a certain number of bits. This introduces a maximum measurable time after which the time-to-digital converter starts counting at zero again.

Differential Linearity The design of a time-to-digital converter is very close to the scheme indicated in Figure 2.19. A single time reference is split into several channels. Each channel is compared with the input pulse, but they have different time delays before reaching that signal. Those time delays are equally distributed between n and $n+1$ clock periods. The first channel in phase with the input channel triggers the detection, and writes its counting to a First-In First-Out buffer memory. The deadtime of this memory fixes the deadtime of the time-to-digital converter. Finally the output of this First-In First-Out buffer is send to a larger one through a switch, where it is mixed with the data of other time-to-digital converters.

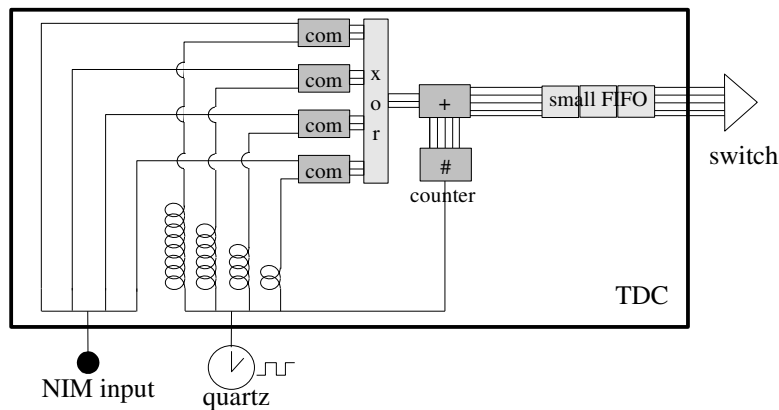


Figure 2.19: A typical design of a time-to-digital converter chip. The time period of a quartz is subdivided in coding steps by creating various channels with different delays. The clock signal in those channels is compared with the input channel. The channel most in phase with an incoming pulse adds its number to the clock pulse counter. The result is stocked into a local First-In First-Out memory.

If designed properly, each channel has equiprobability of detecting the signal. Yet if the delays in the various channels are not equally distributed, this probability can be non-uniform. The average of the differences between those probabilities and the expected value is called the non-differential linearity.

This is for physics experiments yet not the best criteria, as time is never measured in an absolute way. Events are generally measured with respect to a trigger. This is also the case for our delay-lines for which X_2 is measured with respect to X_1 . The statistics that have to be looked after is the differential linearity. This is done by checking the variations in the probabilities of all the differences for a random set of data. The quality of our image as well the resolution will depend on this differential linearity. We will though see, that for the time-to-digital converters used, the differential linearity is not a limiting factor.

Time Extension The width of the memory in use fixes generally the maximum measureable time of a time-to-digital converter. Depending on the period in which the time-to-digital converter has been designed, the FIFO memory will be either 16 bits, 32 bits and tomorrow 64 bits or more. The number of bits n effectively used is generally slightly lower. The total period T after which the counter starts counting at zero again can then simply be calculated with the coding step τ as $T = 2^n \times \tau$.

In the case of a 15bits coding time-to-digital converter at 400ps, this period is of 13 μ s. Although this may seem ages in the world of high energy physics, a branch of physics that makes most common use of time-to-digital converters, in our very low energy physics, this is far too short. The shortest time of flights we expect are already tens of milliseconds long. That means 10^3 periods! We need a time extension mechanism.

The only proper way of doing so is integrating the time extension mechanisms into the design of the time-to-digital converter. This can be done by adding an additional counter to the design, that brings in a marker to the switch between the various time-to-digital converters every period, as shown in Figure 2.20. The marker would separate the data between before and after the marker. As one marker is provided every period, one simply has to count them in order to rebuild the time.

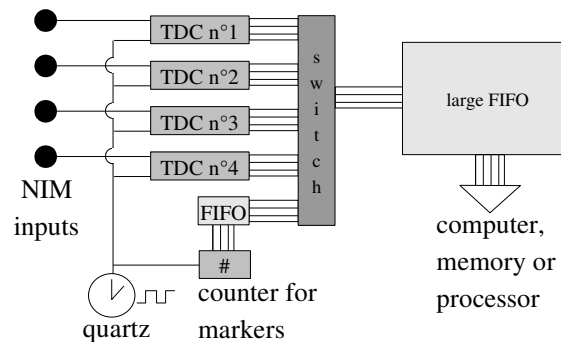


Figure 2.20: Various time-to-digital converter channels are sent to a same first-in first-out buffer through a switch. At that point, two markers per period are also added in order to allow proper time reconstruction beyond the time-to-digital converter period. The output of the FIFO buffer can be send to various supports depending on the further design of the global device.

The problem lies yet in the switch, that does not respect the chronological order of the various times and markers that it receives. It simply reads one by one each incoming channel, streaming through the data if available. If a pulse arrives close to the marker, in the sense that the switch can invert them, then we cannot determine the period in which that pulse arrived, and we have potentially period error on its arrival time.

If we call δt the maximum time difference at which the switch can potentially invert two channels, then the frequency at which the time-to-digital converter generates a marker should at least be $\frac{1}{T-\delta t}$. As in general $\delta t \ll T/2$, the easiest frequency to handle is $2/T$. In other words, the time-to-digital converter generates two markers per period; one called up, the other called down. With those two markers introduced into the flux of events (more commonly called stops), one can with a fairly simple algorithm rebuild the time scale up to infinity.

First Generation We had great difficulty in finding a time-to-digital converter that was up to our needs. With the two delay-lines the detector had, we needed at least four channel at nearly 1 Mhits/s each. That gives a total flux of several Mhits/s on the exit bus over several milliseconds. Although in high energy physics the peak

particle rates can be much higher, they only concern a very little number of hits a small and fast FIFO memory can easily deal with. The global particle rates are generally tuned down to several thousands of events per second as to be compatible with detector, electronics and computer acquisition rates. Consequently, most time-to-digital converters have been designed for those needs, and cannot cope with high mean fluxes.

Furthermore, we needed the time extension mechanism. As this is only of use in a very few cases, most of the commercial time-to-digital converters do not implement that mechanism.

Finally, we needed of course sufficiently short codings times and quality in order not to be limited by the time-to-digital converter.

The only time-to-digital converter we found that was compliant with our needs was the CTNM4 build by the electronics department at the Institute of Nuclear Physics in Orsay. As we will deal with the particle rates in the next section. We will simply state that the coding step of the CTNM4 is of 400 ps. Thanks to a clean design, the useful differential linearity is 10%. And the global maximum particle rate is of 2.8 MHz. This is the time-to-digital converter we used for the acquisition of the ^4He data.

Second Generation As we were still limited, as we will see in the next section, by the flux of the time-to-digital converter, we were looking for a new time-to-digital converter. Meanwhile, a commercial spin-off had been created at the Institut of Nuclear Physics, that implemented new technologies for the design of time-to-digital converters.

This company, IsiTech, had no time-to-digital converter compatible with our needs, yet it was fairly simple for them to design one specifically, which is what they did. The resulting IsiTime 02 has a coding step of 275 ps, a differential linearity of 1%, but more specifically a maximum global particle rate of 80 MHz. This is, as we will see, way beyond our needs. This time-to-digital converter has been used for the acquisition of the ^3He data.

2.2.4 The Computer Acquisition

The computer acquisition was a crucial part to the proposed Hanbury Brown and Twiss experiment. Not just in the sense that the data had to go from the time-to-digital converter to the computer, but also once it is in the computer, one still has to be able to analyse it in optimal conditions. It was therefore necessary to make the right choice in the platform, that is an ensemble of tools sticking together and offering a large set of possibilities. Thereafter we still had to develop a user friendly interface, that would help us scientists in acquiring the data and analysing it, but also would foresee future developments in the acquisition devices. Finally, we decided for a central server implementation as to maximise ease of maintenance and use.

2.2.4.1 The Platform Root

The choice of a platform is not straightforward. Several parameters have to be taken into account, some of which might be easily overseen. We will discuss most

of those parameters and will conclude on the platform we have chosen.

User Requests The choice of a platform is a technical choice as much as a political one. The political choice of a working platform is a fair one, and has to be taken into consideration. As the experiments are largely evolving by the work of PhD students, the programmer of one program will be gone 3 years later and other must be able to follow their work achieved. A platform with a low adoption barrier is therefore of high importance. Furthermore, the experimental work achieved in the laboratories by those students, is also considered as a preparation to further life in, for instance, industry. Developing skills during this period that are actually useful is preferable. Finally for most scientists the platform is just a tool. At some point they learnt to master one of those tools, they like to stick with it. Also students that come in have generally been formed in a limited set of languages, remaining compatible with those is a nice thing to do. Several objections have yet to be expressed in regard to those considerations.

Considering the fact that all programming languages are fairly similar, if a student has indeed developed a complex interface with a specific language, the entry barrier to the understanding of that code will, if under-documented, be very high whatever the platform is. Another student, without proper skills and will, will not be able to amend that program whatever it has been programmed in. Experience in the laboratory shows that this is indeed the case for a specific Matlab program. The entry barrier should yet remain low so that simple tasks can be executed by everyone.

Statistics on the former students from the Institute of Optics show that the most common computer languages used after school are C/C++, Matlab, Visual Basic and Java. If the first two languages are common for people with a scientific background, the other two languages are rarely taught to technical engineers. Those languages are indeed more dedicated to financial spreadsheets or Internet based applications. It is therefore impossible to please all needs, and some choice has to be taken.

Concerning the abilities of both scientists in place, and students coming in, they are of a large variety. The older generation is generally proficient in Fortran. The newer generations know languages as wide as Fortran (Paris Sud), Java (Polytechnique), C/C++ (Institute of Optics), Scilab (Polytechnique), Matlab (Institut of Optics). Furthermore, those languages taught are still changing as the IT industry is far from being stable. We currently see new upcoming languages such as Python or C#. Sticking to all of them is impossible.

In the end a choice has to be made. Considering the fact that most scientists have little or no knowledge in information technology, it is best to establish a certain number of objective technical criteria and make ones choice according to them. Finally, one has to take into account the request of a graphical user interface.

Performance The main concern we had about the analysis of the data was the performance of the platform. Indeed, we were about to do statistical physics and we wanted to see physical details that would need a lot of averaging.

Time would prove that for a single data point we needed to average over 1500 time of flights of around 10,000 particles, to each of which we had to apply a

$O(N^2)$ correlation algorithm. If the user really wanted to eventually multiply his calculations on this data, all this had to be done in a reasonable amount of time.

When one is looking for performance, one is thinking of basic hard compiled languages: that means that the end program can run directly on the processor. Most modern languages (such as Java, Visual Basic, C#) are run inside some "sandbox", that take care of memory management, buffer overflow and other security issues. This has a strong performance cost. Other languages are not even compiled, yet simply interpreted (such as Matlab, Igor Pro, Python). Although very handy for prototyping, this has a severe speed cost.

The only performing structured languages are Fortran and C/C++. The former compilers have undergone with the time heavy optimising for scientific use, whereas the second language is mostly used for hardware driving (nearly all modern operating systems are written in C/C++). Benchmarks show a general performance gain of those languages from 10 to a 100 times faster than the sandboxed languages.

In particular, Matlab has been programmed for a large part with Java, a language that is only starting to worry about performance. Even preprogrammed optimised algorithms can show a factor 100 performance lost in comparison to a plain handwritten algorithm under C.

Available Tools The choice is not just a language, but also the tools provided with this language. Although one can of course use external scriptable plotting tools such as GnuPlot, for user convenience and experience consistency having an integrated platform is better. Matlab is such an integrated platform, offering a large set of toolkits for nearly any needs. Scilab, an open source imitation of the first, is faster yet is less rich in its possibilities. Languages such as Java, C# or Visual Basic offer no real integrated platform for scientific purposes.

Fortran and C/C++ have several scientific libraries available, yet only a few complete integrated platforms. The most known Fortran library is the open source Paw, that has turned into a mess after 30 years of existence. The upcoming C/C++ library, heavily used in particle physics, is Root [82]. A very extended platform that offers possibilities ranging from data storage, network computing, plotting and fitting. Furthermore, this platform even offers a C/C++ interpreter that allows mixing of compiled and interpreted code written in the same language. It consequently offers performance of the compiled code with the ease of use of interpreted code.

Data Structures The memory of the computer, just as its storage space, behaves like a single long array. Consequently, many calculating platforms, and in particular Matlab, exploit this layout by adopting arrays or matrices. Although this is very convenient, and highly optimisable, in the case the data also has an matrix type layout, if the data has nothing to do with matrices, one still has to fit with it.

The use of different structures can help the understanding of what one is programming. If this may not be a critical parameter, it certainly influences the ease-of-use of the platform.

The Paw and Root platforms both showed data structures, and tools, for the statistical analysis of particles. Those two platform have indeed been developed at the CERN for use at their experiments. It happens that we are doing the same

physics in that sense.

Compatibility Last but not the least, a language has to show a certain level of compatibility. If the platform scores insufficient in a certain domain, it must be possible to use and fit in an external library. Specifically for the hardware acquisition, drivers provided by the hardware vendors are necessary.

Generally, the fallback language is C. All drivers are written in C. Many additional libraries are written in C. Many platforms offer the possibility to integrate C. Matlab even offers its own compiler, and C modules can be written to compensate its overall bad performance. It must also be said that all major hardware vendors offer a driver interface specifically for Matlab.

Yet in nearly all cases, that means mixing up languages, increasing significantly the complexity of that chosen platform. Only the choice of the already C/C++ Root offers a coherent user experience.

The Choice The choice has logically gone to Root. This platform offers a large set of possibilities, specifically oriented to the way we study physics. It is the only integrated platform that offers easily the performance we need. Note that it has been developed with in mind the Terabytes of data it has to handle with the opening of the Large Hadron Collider (CERN).

Documentation is fine. A beginners manual gives a very nice introduction to its possibilities. Advanced documentation could have been better, yet is compensated by the open source code. We have through our use encountered a certain number of bugs. Those can yet easily be spotted through the source code, and the Root development team proved very responsive in fixing those bugs. The main worry has gone to the still unstable interpreter, that does not allow for much programming mistakes.

Furthermore, Root is multiplatform in the sense that it runs under various operating systems. This allowed for interesting network setups. The license of Root is very liberal, enabling free use of nearly any kind. Global user experience is positive, yet the need of a graphical user interface was an evidence. This ended up in the programming of Heevman.

2.2.4.2 The Interface Heevman

Root is mainly a console type program, requiring large amounts of code to be lined up. As to render Root useable to everyone, an advanced acquisition platform was to be developed that would make it possible to acquire and access the data easily, but that can also be updated easily in order to integrate new devices. We have invested a large effort into this interface we call Heevman.

Heevman stands for the HELium EVent MANager. As its name indicates, its main purpose is to give the user access to the various events that are the experimental cycles of the He* clouds. This is done in two stages: acquisition of the data and analysis of the data.

Acquisition The key words for the a good acquisition are persistence and consistency. One of the flaws in data acquisition can indeed be the scattering of the data in various formats, in various places with various conventions. This makes

analysis of the data for users different from the one that acquired the data close to impossible. By imposing the way data is saved, the program assures that anybody will be able to retrieve the data at any point.

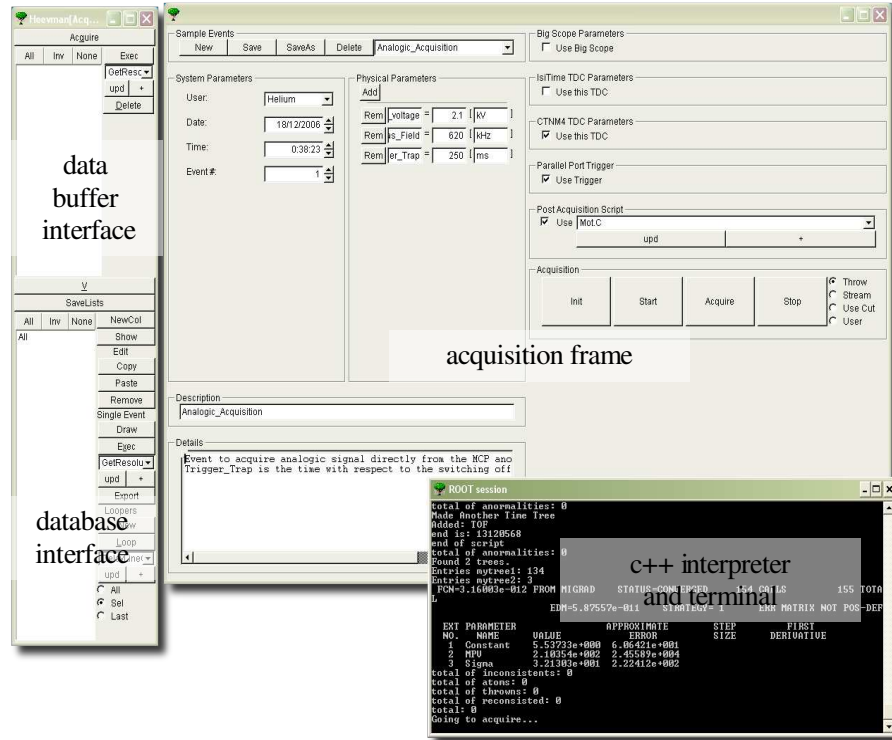


Figure 2.21: A screenshot of the acquisition program during the acquisition of some 1 mK clouds. At the right bottom we distinguish the terminal from which Root is launched. We then open the left window corresponding to the Heevman interface. From that point is launched the upper right windows that is in charge of the acquisition. Several parameters and properties can be tuned for later understanding of the acquired data. A plugin mechanism ensures forward compatibility with eventually new devices. We can distinguish 3 plugins corresponding to the acquisition of 1 oscilloscope and 2 time-to-digital converter. Only one is activated though. Additional properties allow for automatic acquisition as well as the running of analysis scripts on the freshly acquired data. If saved, the acquired data is streamed to the data buffer whereafter it can be written definitely to the database.

The acquisition frame, showed in Figure 2.21, attributes a certain number of properties to each event. Those include the date of the acquisition as well as a unique identifier number for that date. Together, those assure a unique identity to all events, and thereby also its name. Furthermore they are attributed the name of the user that acquired the data, the type of data the user has saved in the event and a more detailed description of what the user had in mind when he acquired the data. This replaces favourably the experiment logbook, that is often insufficiently maintained and where information is difficult to retrieve. Eventually, some physical parameters can be saved with the event, if those are crucial for the analysis of the data. It makes it also possible to automate studies depending on specific parameters.

A versatile plugin system assures that the acquisition frame is and remains compatible with changes in the acquisition devices. This plugin system assures

with little difficulty, the integration of all devices in the acquisition philosophy. The data structure of the event is sufficiently open, yet limiting, that further improvements are possible without breaking the consistency. Currently plugins exist for the acquisition from two time-to-digital converters as well as two oscilloscopes. A second type of plugin triggers the acquisition. We currently use the LPT1 port (commonly known as the parallel port) for this, as it is TTL compatible.

Scripts can be used inside the acquisition frame in order to visualise the data as they are acquired. The realtime changes the user can bring to those scripts make them a very powerful tool, as the user can analyse immediately the details he is looking for. Altering or changing of script is a button click away. Those scripts can eventually be compiled if the task is heavy.

The user has the option for saving away automatically the data. This data is written away to a single database type structure, that is lightly compressed. This slight compression does not simply assure that the data takes less space, it also assures a maximum throughput from disk to memory. Indeed, in that transaction, the bottleneck lies in reading from disk. Reducing the size of the data and sending it through the processor for decompression can increase the transaction time. This is even more crucial if you plan to use the data from the network. Although this was initially planned, a better solution is presented a little further.

Analysis Once all the events are saved in the single data structure, the main difficulty is to access them easily. This is done through the analysis interface shown in Figure 2.22. In this frame data is originally organised by date. Possibility is however given to organise the data in ones own convenience through the creation of specific selections. Those selections only contain references such that only a single copy of each event exists.

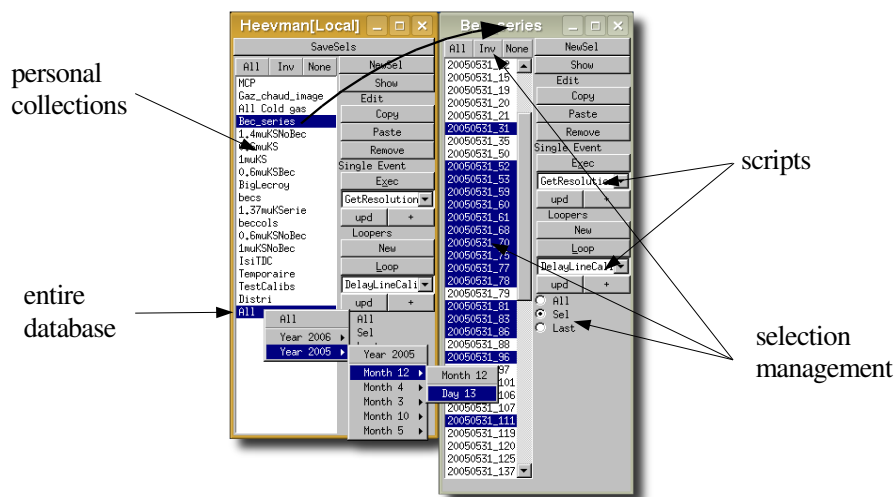


Figure 2.22: A screenshot of the analysis program. The left windows gives access to the root of all the data in the database, through a dropdown menu. Personal collections can also be made. Various selections can be managed and two type of scripts applied to them.

Besides organising the data, one has to analyse them. Two type of scripts can be applied to them: individual scripts that analyse the events independently, and

grouped scripts that are capable of extracting statistical informations. Together, those scripts offer nearly unlimited possibilities.

Conclusions Heevman has proven fairly useable. It is able to handle the 70 gigabytes of data we acquired already, and all the results presented in this thesis have been analysed through this interface.

Documentation has been written that enables installation and use of the program. Development documentation is still lacking. A website has been set up in order for other institutes to use it, and the website has been referenced at Root's website.

Heevman is still in an early development stage. Some important functionalities are still missing, and various irritating flaws and bugs still lie around. Overall user experience is yet very positive.

2.2.4.3 The Computer Setup

The acquisition and the analysis of the data require a physical support. This is realised through an acquisition desktop computer and an analysis server. The acquisition desktop runs a Microsoft operating system as currently most device manufactures only ship drivers for those operating systems. The server runs a GNU/Linux operating system. Although initially we planned to run it as a simple data server, distant graphical access possibilities made a computing intensive server a much more powerful solution.

Data Access The initial idea behind the central server was to have a single place for the data. The idea was to share the data on a single computer on the network, and that other clients would access it for analysis.

The problem with network access for data is the throughput of the network. Even if the data is compressed, this still remains low. If a correlation is calculated, this may not be the limiting factor. But when one scans for simple information, the lost time is significant. This kind of setup also makes the use of the scheme beyond high speed connections a pain.

The highest data access is thus provided if the data is computed at the same place as where it remains. This can be done by copying the data to all working desktops, or having a powerful server to which everybody can access. Maintenance and cost favour the second solution.

Maintenance The great advantage behind central servers are the low maintenance costs. Indeed, with both Root and Heevman as heavily evolving programs, updates were, specifically in the beginning, of common tasks. Furthermore, also the database increased daily.

Updating those entities at a single server takes much less time than updating a whole park of computers.

Cost A correlation calculation is potentially a processor power and memory consuming activity. Achievement in a minimum time requires a powerful computer. Acquiring such a computer for each user would yet be a loss of power. Indeed,

although a must when doing calculations, most of the time the possibilities of the computer are highly unexploited.

Putting into place a single server that serves several users drastically increases the user time over total time ratio. In order to circumvent overload, an overpowered dual processor solution is preferable. Consequently, two users can launch calculations at the same time without speed loss.

The Setup The server is a dual Intel Xeon solution with 2 Gigabytes of memory. Furthermore, two 160 Gigabytes harddisks in RAID 1 (mirroring) configuration assure both minimal access time as well as backup in case one disk brakes.

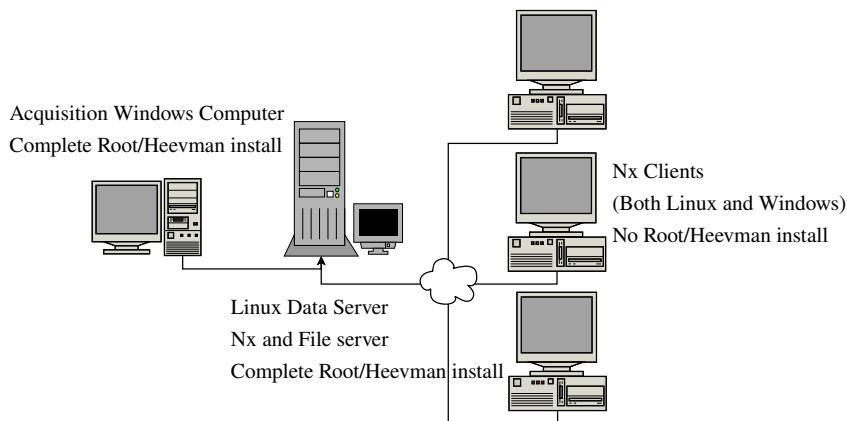


Figure 2.23: Computer network solution. The acquisition is performed with a Windows desktop computer. The acquired data is immediately transferred to a workhorse server. Access to this server is provided through a graphical protocol and various networked thin clients. Only the acquisition computer and the server have a Root/Heevman installation.

The network access is provided through the open source FreeNX server. This server enhances the traditional X protocol with compression and lower latencies, making it even feasible over a modem connection. This graphical server gives a graphical desktop access to the computer from practically anywhere in the world.

On the client side, users only have to install the free NX client, multi-platform, solution distributed by Nomachine. When providing a SSH access through the local firewall, the server can be accessed from the local network as well as from the internet.

This solution proved extremely handy and powerful.

2.3 Detector Characteristics

In the previous section we had a detailed overview of the various components of the detection system. We have seen in the previous chapter that several characteristics of this detection system are crucial to the signal to noise ratio of the proposed Hanbury Brown and Twiss experiment. We therefore propose an extended overview of those properties. We will in particular analyse the detection efficiency, the detection rate and the resolution of the detector.

2.3.1 Detection Efficiency

The exact knowledge of the detection efficiency is not of primal importance to the proposed Hanbury Brown and Twiss experiment. As we discussed in paragraph 1.3.3.1, the phenomena we are looking at is a statistical property. If only a part of the atoms is detected, this statistical property remains.

Yet even in the proposed experiment, the detection efficiency can have its importance. The signal to noise ratio shows a severe dependence on the temperature of the atomic sample. This leads us to work at as low temperatures as possible. For the study of the properties of an atomic cloud, we will be limited by both the condensation threshold temperature T_C or the Fermi temperature T_F , where the statistical properties are likely to change. Neglecting mean field effects, those temperatures in a harmonic trap are given respectively by:

$$k_B T_C = \hbar \bar{\omega} (N/1.202)^{1/3} = \hbar \bar{\omega} (N'/(\eta 1.202))^{1/3} \quad (2.3.1)$$

$$k_B T_F = \hbar \bar{\omega} (6N)^{1/3} = \hbar \bar{\omega} (6N'/\eta)^{1/3} \quad (2.3.2)$$

where $\bar{\omega}$ is the geometrical trapping frequency, N the total number of atoms in the trap, N' the number of detected atoms with the detection efficiency η . If we want to work at low temperatures, while keeping the number of detected atoms as high as possible in order to preserve the signal to noise ratio we will ultimately be limited by the condensation threshold. This limit can be increased if we have an as high detection efficiency as possible.

We will discuss the two essential parts on which depends the total detection efficiency: on one hand the efficiency of the analog part of the detector, on the other hand the atomic reconstruction.

2.3.1.1 Analog Part

The analog part of the detection can be subdivided into two processes. The first one is the effective detection by the micro-channel plate of the incoming particles. This process is accounted for by the triggering by the particle of the electron amplification process. The second part lies in the detection of the produced pulse. This happens if the amplitude of the electronic pulse is above the discriminator threshold. Practically, one can detect more signals then effectively produced.

Quantum Efficiency The probability for a particle to extract secondary electrons as it hits the micro-channel plate, we will call the quantum efficiency of the detector, mostly depends on the nature of the particles. This probability is very high in

the case of 2 keV accelerated ions, and can be brought to nearly 100%. In the case of metastable atoms, the electronic extraction mechanism is quite different [87]. The associated energy is much lower, yet still fairly high compared to the metallic electron extraction energy (typically 3 eV).

Once some initial secondary electrons have been extracted, those still have to go into the channels for amplification. This is not a problem if the extraction process took place inside the channel, but particles have also a chance to hit the outer surface of the micro-channel plate. Although the secondary electrons can be forced into the channel by the use of external electric field [83], the quantum efficiency in the case of energetic ions is generally associated to the probability of falling into a channel. This can be simply calculated as the holes over total surface ratio. In the case of our micro-channel plates, this reaches 60%.

The total quantum efficiency has previously been estimated on a different micro-channel plate for He* to $25\% \pm 15\%$ [59]. [43] states a detection efficiency of 9%.

Electronic Detectivity Each time a particle has extracted secondary electrons, those are amplified inside the micro-channel plate. The resulting electronic pulse, collected by the delay-lines, still need sufficient amplitude for detection by the discriminator. The inhomogeneous gain distribution of our micro-channel plates, as shown in paragraph 2.2.1.5, consequently has a direct impact on the detectivity distribution. As we have seen before, the micro-channel plate shows regions of high saturating gains and regions of low non-saturating gains. Whereas in the regions of high gain we can employ a threshold that discriminates all the electronic pulses, in the low gain regions we necessarily lose some counts through the discrimination.

The electronic detectivity maps of the micro-channel plates at 2300 V as employed in Orsay and in Amsterdam are shown in respectively Figure 2.24A and 2.24B. Assuming that the quantum efficiency is homogenous, those maps account for the spatial probability of electronic detection of a particle that has triggered an electronic shower. They have been produced by integrating a homogeneous particle flow on the detector surface. This homogeneous flux is obtained when producing 1 mK time-of-flights. The normalisation procedure is discussed a little later.

We notice the evolution of the detectivity map between Orsay and Amsterdam. This evolution has simply been induced by the mechanical unmounting and mounting of the micro-channel plate stack. This indicates that the current problem is essentially mechanical. In particular we notice that even the detectivity hole in the middle of the Orsay map disappeared.

On the lower Figures 2.24C and 2.24D we displayed the electronic detectivity distribution. We note first of all, just as the maps already showed, that the detectivity in Amsterdam was more evenly distributed over the detector surface. In both cases though, we notice a local maximum around 1 for the detectivity. As a matter of fact, we have defined this maximum to be of electronic detectivity 1. The reason for this is fairly simple. If we consider the lower amplitude distribution as presented in Figure 2.9, that has been taken in a high gain region, the discriminator levels can be and is placed below the amplitude distribution. This means that all electronic pulses are effectively detected by the discriminator. This region has therefore a 100% detectivity from the electronic point of view. A region that has a slightly lower gain will still have the essential part of the pulse heights above the

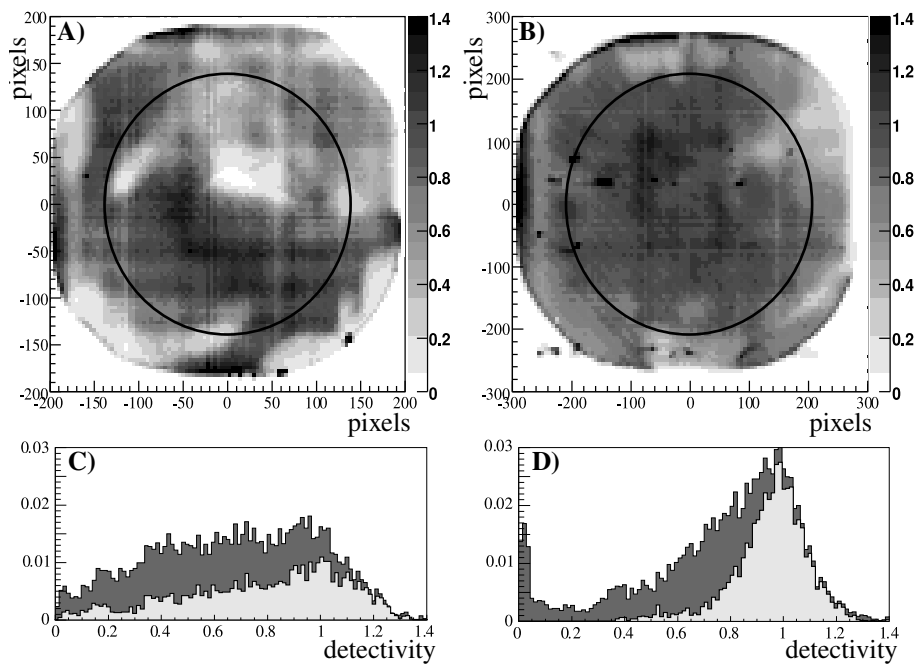


Figure 2.24: In A, the spatial detection efficiency of the detector as employed in Orsay at 2300 V. The map has been obtained by integrating a homogeneous flux. In C has been plotted the detectivity distribution for this map. We identify the maximum in the distribution as a 100% detection efficiency. In dark gray has been plotted the distribution for the entire detector map, in light gray only the area within the black circle. In B and D have been plotted the map and the distribution as obtained in Amsterdam in similar experimental conditions.

discriminator level. It will therefore also show an electronic detectivity of 1. Consequently, the electronic detectivity map has a more favourable distribution than the amplitude map. It must be said though that we work precisely at the maximum micro-channel plate voltage for the electronic detectivity to be as homogeneous as possible. This has consequences on both the resolution and the particle flux, as we will see a little further.

The choice of this maximum as 100% detectivity is not straightforward though. The number of particles used for those images is significant and the shot noise associated is negligible compared to the maximum's distribution width. In particular, it seems difficult to understand how certain regions could have a detectivity above 100%, as currently displayed in Figure 2.24. Image deformations mostly account for this. If one considers that the image is supposed to be a perfect disc, one realises that the imaging procedure is not fully linear. For a homogeneous flux, this non-linearity produces regions of increased and decreased intensities, and broadens the detectivity distribution. In particular, the non-linearity of the detector occurs essentially at the border of the detector where electric fields are less homogeneous. If we do not consider the border of the detection region, we effectively observe a narrowing of the detectivity distribution, as shown in Figure 2.24. We will therefore simply consider that the choice is reasonable, without saying it is the single possible choice.

If we consider the maximum of the detectivity distribution to correspond to a 100% electronic detectivity, the average electronic detectivity of a homogeneous flux in Orsay and Amsterdam were respectively 67% and 77%. We must note that those images also depend on our capacity to rebuild the positions of the atoms, as we will see a little further.

Detection Overshot The discriminator is supposed to discriminate the signal from background noise. Effectively, if no physical signal arrives at the micro-channel plate, few, or very localised, signals are detected. A problem remains though with noise that is generated by the detection of the electronic pulses. The analog pulses generate sinusoids and echos due to impedance mismatch in the analog detection chain. The amplitudes of these echos can be enough to trigger the discriminator.

An easy way of spotting those echos is through observation of the delay function. We simply plot in a graph the time difference between two successive counts, and if in the final histogram bins go beyond a usual statistical behaviour, the overshoot can be attributed to the echos. In Figure 2.25 we have plotted the delay functions for the four outputs of the delay-lines we use. The black curve indicates the usual statistical behaviour expected.

The afterpulsing count depends strongly on both the amplification level, the constant fraction discriminator level and the spatial distribution of the clouds. For the 1 mK time-of-flight data shown in Figure 2.25, the overshoot represents respectively 11.9%, 9.8%, 10.7% and 13.6% for the channels x_1 , x_2 , y_1 and y_2 . If a specific channel is to be used for a detection efficiency measurement, those percentages have to be subtracted.

In order for the afterpulsing to be problematic, it still requires reconstruction. After reconstruction, the afterpulsing overshoot only represents 2% of the total flux. Still for delays below 300 ns they are 60% of the signal, and in terms of correla-

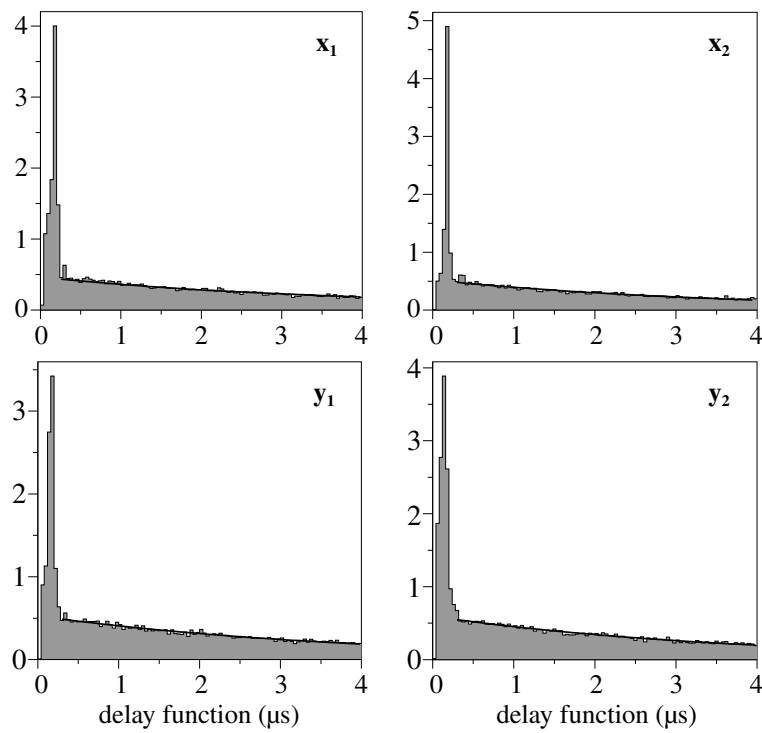


Figure 2.25: The delay functions for respectively channels x_1 , x_2 , y_1 and y_2 . The black curves indicate a normal statistical behaviour, that would have been exponential in a continuous Poissonian flow. The bins outreaching the normal behaviour account for the echo counting. Most of the aftershots occur within 300 ns.

tions they will strongly affect the correlation function of the atomic flux at lower times. This is the reason why we will consider a 300 ns dead-time at the moment we will be calculating the correlations.

2.3.1.2 Atomic Reconstruction

Once the different pulses from the delay-line detector have been discriminated, their arrival time is measured by the time-to-digital converter and this arrival time is sent to the computer. The computer then contains a long list of arrival times with their corresponding channel number. Those arrival times then have to be correlated in order to define the position of the incoming particles. As we will only be able to use the atoms if we are able to define their position, this reconstruction process is entirely part of the total detection efficiency. In Appendix 2 has been detailed the reconstruction algorithm employed, labeled the Time Bulb algorithm.

We will briefly highlight some considerations related to this correlation necessary to the reconstruction and discuss how this reconstruction mechanism exacerbates the detectivity inhomogeneity. Finally we express the reconstruction efficiency in respect to a single channel detection.

Some Considerations When working with time-of-flights, it is more convenient to consider the time-of-flight as detected on a single channel, i.e. before atomic reconstruction. As is demonstrated a little further, the one channel detection is fairly insensitive to the particle rate in the limits we work. It does not change the shape of the time-of-flight distribution. We will therefore always take a single channel count as reference.

In order for an atomic detection to be useable, we require to rebuild its position and arrival time. Although theoretically we need only 3 different arrival times among x_1 , x_2 , y_1 , y_2 and t , where t is the arrival time as measurable from the micro-channel plate, Appendix 2 explains why we practically need x_1 , x_2 , y_1 and y_2 . The atom is thus effectively taken into consideration only if we measure the 4 delay-line arrival times. This means that the number of reconstructed atoms is at maximum the least of the individual number of counts on the various channels. We will therefore always take x_1 as a reference as it happens to have the minimum number of counts of the 4 channels.

The probabilities of detection of the pulses on the various delay-lines are not independent. The amplitudes of the 4 electric delay-line pulses coming from one single atom are indeed related. As the discriminators have been set in such manner that the counts on each line are roughly identical, if a pulse height is higher than the threshold for one discriminator, it is likely to be so for all the others as well.

Reconstruction Inhomogeneity The probability of detection of a pulse is strongly related to the pulse height, that depends on the position. In Figure 2.26 we have displayed approximately the probability of electronic detection on one of the channels as a function of X . In order to build this graph, we have divided the number of counts at a position X that had the 4 signals necessary to its reconstruction, by all that had at least the two signals necessary for the definition of the X axis position. If we call $p(X)$ the probability of detecting a signal on one of the delay-lines, and assuming that this probability is equal on the 4 delay-lines, the numerator is given

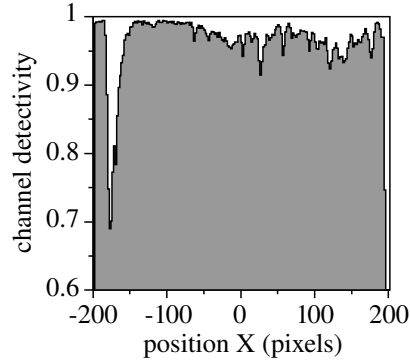


Figure 2.26: The approximate electronic channel detectivity as a function of X . It is the square root of the average probability of detecting 4 signals on the 4 delay-lines divided by the average probability of detecting the 2 x_1 and x_2 signals.

by $\langle p(X)^4 \rangle_Y$. The denominator is given by $\langle p(X)^2 \rangle_Y$. We therefore take the square root:

$$\sqrt{\langle p(X)^4 \rangle_Y / \langle p(X)^2 \rangle_Y} \sim \langle p(X) \rangle_Y \quad (2.3.3)$$

The graph shows clearly that in certain regions, the electronic detectivity is close to 1, underlining previous statements. But in other regions, detectivity falls below 70%. When not averaged over Y , this is expected to be even lower. As the plotted values must be taken to the power 4 before three dimensional reconstruction can be performed, the reconstruction stresses even more the spatial detectivity inhomogeneity.

This has further consequences. If we consider that a pulse is detected when it is detected by at least one of the delay-lines, then the total number of detected atoms is likely to be larger than the number of counts on a single channel. This has to be taken into account when one is willing to determine the quantum efficiency of the micro-channel plates using a single channel count.

Reconstruction Efficiency In particular, as the reconstruction efficiency is position sensitive, the global reconstruction efficiency depends on the density distribution of the cloud on the detector. If compared to a single channel count, at low particle rates, a homogeneous particle flow shows a reconstruction efficiency of 81%. Cold clouds around 1 μK show a reconstruction efficiency of 93%.

Those numbers have to be compared with the previously stated electronic detectivity of 67% for a homogenous flow. If we consider a small 1 $m\text{K}$ time-of-flight, and we consider the number of detected atoms of channel X_1 , 81% of those counts will effectively be rebuilt into spatially defined atoms. The resulting map will yet only represent 67% of the expected counts. This means that the used channel missed $1 - 67/81 = 17\%$ of the atoms that triggered the micro-channel plate. Considering that 12% of the counts were due to an overshoot, the discriminator has missed $1 - 67/81 \times (100 - 12)/100 = 27\%$ of the physical counts.

2.3.1.3 Measurements

In order to measure the total detectivity, several possibilities are available. Either one can compare the detector measurement with a differently calibrated method, or one can study the statistical properties of the cold clouds. We present here two methods. The first one uses an optical calibration as performed in Amsterdam on the experiment. The second one uses the condensation threshold as point of comparison.

Amsterdam A cold cloud of helium atoms can also be observed through absorption imaging. One shines a resonant laser on the cold cloud. The atoms absorb some photons that are remitted spontaneously in random directions. Spatially, the laser lacks photons as a function of the cloud density. One can therefore easily measure the density distribution of the cloud over the waist of the laser. Eventually, through knowledge of both the atomic properties and the characteristics of the camera, one can give a fairly precise measurement of the physical atomic density.

Through the use of such a camera, the research team in Amsterdam has been able to characterise their own micro-channel plate based detector. The comparison between the measurements performed by their micro-channel plate detector and ours therefore allowed for an indirect calibration of our detection efficiency. Through the measurement of both a $1 \mu\text{K}$ cloud of ^3He and ^4He this resulted in a single channel detection efficiency of respectively 11.3% and 13.7%. This is the comparison between the number of atoms we expected to measure, considering the temperatures of the clouds and the total time-of-flight, and those that we effectively measure on channel x_1 . Considering our previous statements as to the electronic efficiency and the reconstruction efficiency, this brings us to approximate values of the micro-channel plate quantum efficiency of respectively 13.6% and 16.4% for the ^4He and ^3He measurements.

The quality of this measurement is difficult to estimate. We have not been personally involved into the calibration measurement. Furthermore we have understood that the calibration is already several years old. The performances of their micro-channel plate may have changed significantly in between.

Condensed Fraction During the acquisition of the many cold clouds required for the Hanbury Brown and Twiss measurement, we had in particular for the $0.6 \mu\text{K}$ population, a large number of clouds that had a condensed fraction of atoms. As we will explain in the next chapter, this condensed fraction can be easily spotted, and we can discriminate the two populations. In particular, neglecting atomic interactions, the cold clouds that have no condensed fraction obey the relation:

$$k_B T_C \geq \hbar\bar{\omega} (N/1.202)^{1/3} = \hbar\bar{\omega} (N'/(\eta 1.202))^{1/3} \quad (2.3.4)$$

If we plot in a graph for all cold clouds the number of detected atoms N' versus the measured temperature of the cloud, all the obtained points have to be situated under the condensation threshold curve that is consequently defined by:

$$N'_C(T) = \eta 1.202 \left(\frac{k_B T}{\hbar\bar{\omega}} \right)^3 \quad (2.3.5)$$

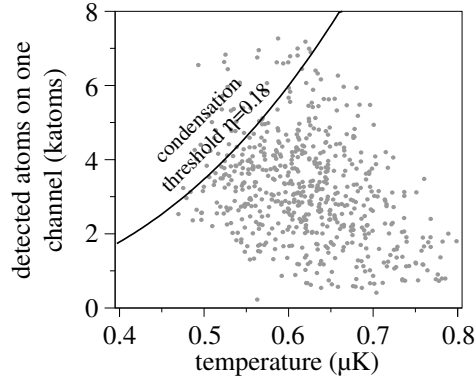


Figure 2.27: The number of thermal atoms detected as on channel x_1 versus the measured temperatures of the clouds. The clouds were part of a statistical ensemble that also contained thermal clouds with condensed fractions. Those have been eliminated from the group as saturation processes falsify the statistics. Consequently the condensation threshold black curve is to adjust right above the thermal clouds. This happens for a single channel detection efficiency around $18 \pm 2\%$. The clouds plotted above the condensation threshold do not have a detected Bose-Einstein condensate. The condensation threshold has been placed considering effective errors in temperature measurements.

This function is parametrised by the detectivity η . In Figure 2.27 we have plotted the number of one channel detected atoms versus the temperature for a large set of cold clouds. Statistically we have found in this sample of clouds, a large number of clouds that actually contained a Bose-Einstein condensate. Although the plotting of those clouds is irrelevant, as the saturation of the micro-channel plate severely deteriorates the statistical properties of those clouds (as will be shown in paragraph 3.2.2.1), this knowledge assures us that the condensation threshold is supposed to adjust neatly to the data points. This can be done by fitting by hand the detectivity parameter of the black curve. We then find the detectivity of $\eta = 0.18 \pm 0.02$ to be a reasonable value.

This measurement leads to quantum efficiencies in the order of 20%. Although this number seems reasonable, we have not yet accounted for the coupled fraction of the cold atoms in the measured magnetic substate. The atoms are trapped in the 2^3S_1 $m = 1$ magnetic substate. Once the trap currents are switched off, Foucault currents appear that make the magnetic field change sign. Consequently the triplet state redistributes itself over the three magnetic substate. As only the $m = 0$ magnetic substate is field insensitive, it has been decided to only perform the detection on this substate. The two other substate are eliminated through the use of a magnetic gradient. This is unlike the experiment in Amsterdam where no such redistribution occurs, and where we do not have to account for this coupling factor. The coupled fraction is in the order of 10%. Latest estimates seem to indicate that at those low temperatures, the coupled fraction would be around 14.3% [56]. But that would still mean that nearly all those coupled atoms are effectively detected. This is not just unlikely, but also in total contradiction with the previous Amsterdam measurement. Therefore, this result is inconsistent in its present state. We have neglected in this description the atomic interactions. Taking into account those interactions and the use of a better thermometry might provide more consistent results.

2.3.2 Detection Rate

As we have seen in the previous chapter, the signal to noise ratio is directly proportional to the total number of detected atoms. For the time-of-flight at a given temperature, the maximum number of detected atoms will be directly related to the maximum particle flow that can be acquired. An extensive study of the maximum detection rate is therefore a requirement.

The total detection rate is limited through the various sub-systems that compose the detector. Some induce a local limitation on the particle flow, others behave globally. Some have as an effect to lower the detection efficiency, others will simply impose an absolute barrier. We will study first the parts of the detector that impose local flux limitations. Then we will study in detail some dead-time mechanisms that drastically reduce the detection efficiency at high particle flows. Finally we will have a short look on some flow limitations of the electronics.

2.3.2.1 Local Saturation

Most of the sub-devices are essentially sensitive to a global particle rate. One large exception is the micro-channel plate stack. The highly resistive channels of the micro-channel plate are parallelised through the use of a metallic coating on the outer sides of the plate. When one channel has been emptied of its electrons because it has been used for a detection, its efficiency for a second detection is lowered. Each detection leaves a large number of positive charges inside the channel. The emission of secondary electrons is expected to lower with nearby positive charges.

We have stated in paragraph 2.2.1.4 that this saturation mechanism would limit the local particle flow to 125 kparticles/cm²/s, as the micro-channel plate stack we use complies to the physical characteristics we mentioned. This was only an estimation. We have performed a measurement of this saturation. Through the use of an oscilloscope, using the method described in Appendix 3, we are able to retrieve both the position, arrival time and pulse height for each detected atom. In Figure 2.28 we have plotted the result of a saturation measurement.

A large 1.6 μ K cold cloud falls on the detector. The reason why we work at low temperatures is in order to have a maximum local/global particle rate ratio. With the constant fraction discriminator and the time-to-digital converter, we record the arrival times simultaneously from one of the delay-lines. With the oscilloscope we also save the analog signals from the delay-lines that enables reconstruction of the atomic position through the procedure described in Appendix 3. The time-of-flight histogram plotted has been obtained with the time-to-digital converter. The small inset in the graph shows the evolution of the mean analog pulse height as a function of time.

We can distinguish clearly that the pulse height drops at 1.7 ± 0.2 Matoms/s global particle rate. At this temperature, and also considering the detectivity map, this corresponds to a maximum local particle rate of 82 ± 10 katoms/cm²/s. This is fairly close to the expected maximum rate for this detector. Furthermore we see that the cold cloud is not symmetric compared to the 308.3 ms theoretical average arrival time. This means that there is a time constant involved in the saturation process. Considering the reestablishment of the pulse height, this constant is in the

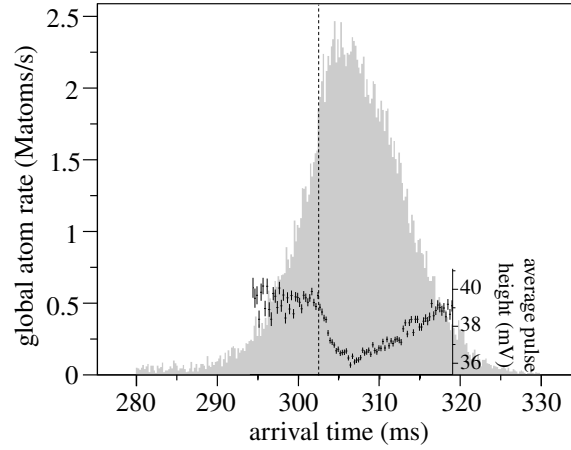


Figure 2.28: The gray histogram plots the time-of-flight distribution of a $1.6 \mu\text{K}$ cloud. We note that the cloud is not symmetric compared to the 308.3 ms arrival time because of the detector saturation. By studying the average pulse height distribution as a function of time, we note a clear drop in the pulse height that corresponds to a $1.7 \pm 0.2 \text{ Matoms/s}$ global particle rate. This produces equivalently a $82 \pm 10 \text{ katoms/cm}^2/\text{s}$ local detected particle rate.

milliseconds timescale.

2.3.2.2 Deadtimes

The delay-line detector has several dead-times. A dead-time is a period after a single detection during which no further signal can be detected. We will see how we can distinguish the simple electronic dead-time, and an additional dead-time related to the atomic reconstruction procedure. Finally we will state on the total dead-time behaviour.

The Electronic Dead-Time The electronic detection of the various atomic pulses, and more specifically the constant fraction discriminator and the time-to-digital converter shows an electronic dead-time. The constant fraction discriminator produces a NIM pulse, and during the build-up of this pulse, no further pulse can be detected. The time-to-digital converter on the other hand requires a certain time to write the data of the pulse measurement to the first FIFO buffer. During this time, no other pulse can be encoded, and this results in a dead-time.

As those two operations, discrimination and encoding, occur simultaneously, the total electronic dead-time is the maximum of the two dead-times. This happens to be $\tau_{elec} = 30 \text{ ns}$. Note that the various channels of detection behave independently. This means that the detection of a pulse on one channels does not influence the detectivity on an other channel. Furthermore, the dead-time is non-cumulative. This means that during the detection of an initial pulse, no second pulse can trigger the electric components that would elongate the effective dead-time. The detectivity for each channel $d_{channel}$ as a function of the incident pulse rate ϕ_i with Poissonian statistics is then traditionally provided by:

$$d_{channel} = 1/(1 + \phi_i \tau_{elec}) \quad (2.3.6)$$

For $\phi_i = 1/\tau_{elec} = 33$ Matoms/s this results in a 50% detection efficiency. Note that the effectively detected channel pulse rate can be written $\phi_{ec} = d_{channel} * \phi_i$. This expression shows a high incident atom rate asymptote at $1/\tau_{elec} = 33$ Matoms/s. This is therefore the maximum detected atom rate. In the lower limit, the detectivity is constant and equal to 1.

The Reconstruction Dead-Time A detected atom has both a position and an arrival time, that need to be rebuilt from the data provided by the various channels. This is done through the reconstruction procedure detailed in Appendix 2. The problem with the currently employed Time Bulb algorithm lies in its unimplemented ability of rebuilding atoms with overlapping time signals.

If two signals provided by two distinct channels of the four delay-line outputs arrive within a 85 ns period corresponding to the delay-line length τ_{dl} , they belong potentially to a same atom. If two atom arrive within a 85 ns period, their various impulses provided by the various channels necessarily verify this mentioned relation, and the reconstruction algorithm currently does not rebuild any of the two atoms. It would require further testing as to what signal goes with what atom.

The effect of this reconstruction procedure is equivalent to that of a dead-time. The difference with the electronic dead-time lies yet in the fact that this dead-time is cumulative. The detection of a second atom within the dead-time of a first atom results in the annihilation of both the detections, and elongates the total dead-time.

In order for an atom to be effectively detected, no other detection should occur one τ_{dl} period after its detection, and should not have occurred one period τ_{dl} before its detection. In the case of our Poissonian incident atom rate ϕ_i , the probability of such an occurrence is provided by $d_{reconstr} = \exp(-2\phi_i\tau_{dl})$. Note that the use of additional $\tau_{error} = 5$ ns error bars in the reconstruction procedure lowers this detectivity to $d_{reconstr} = \exp(-2\phi_i(\tau_{dl} + \tau_{error}))$. This results in a maximum effective detection rate of $1/(2(\tau_{dl} + \tau_{error})) = 2.04$ Matoms/s at an incident rate of 5.56 Matoms/s.

The just mentioned result does not take into account though that the various signals from a single atom are also separated up to as much as 85 ns, depending on the position of the atoms. If an atom falls in the middle of the detector, the time difference between the various channels is zero. Yet if an atom falls at the border of the detector, this time difference is maximum and has to be taken into account for the flux calculation. The detectivity results consequently in $d_{reconstr} = \exp(-2\phi_i(2\tau_{dl} + \tau_{error}))$ in the worse case scenario. Effectively, the detectivity depends on the position distribution of the atoms. This can be easily simulated and we find respectively the efficiencies $d_{1mK} = \exp(-2\phi_i(1.56\tau_{dl} + \tau_{error}))$ and $d_{0.5\mu K} = \exp(-2\phi_i(1.26\tau_{dl} + \tau_{error}))$ in the case of a homogeneously distributed cloud, and that of a centred gaussian distribution of 1 cm root-mean-square width (considering a homogeneous detection efficiency).

The Effective Dead-Time The effective dead-time characteristics of the detector combines both the electronic dead-time and the reconstruction dead-time. This has some none trivial consequences. Naively, one would expect that the addition of the two effects would lower the detection efficiency. This is not the case. If an atom has a missing signal, it cannot be rebuilt. Consequently, each signal that

is not correlated to at least one signal per other channel, is eliminated, as it can not participate to the reconstruction of an atom anyway. If two successive atoms have their various channels overlapping, then the electronic dead-time is likely to eliminate some of the signals. This results in the fact that one of the atoms, and its signals, is likely to get eliminated, resulting eventually in the reconstruction of the other atom.

Developing a simple model in this case is slightly more difficult, so we will simply consider some simulations. In Figure 2.29A we plotted the simulated reconstruction efficiency as a function of the incident atom rate (note that we consider that all atoms are detected by the micro-channel plate and the discriminators). The dashed line considers a $0.5 \mu\text{K}$ time-of-flight and does not take into account the electronic dead-time. It lies effectively in the gray area between the best case and worse case scenarios discussed previously. The continuous line, also at $0.5 \mu\text{K}$ corresponds to the simulation that takes into account the electronic dead-time. We note that this electronic dead-time does indeed improve the efficiency of the reconstruction. Furthermore, the curve seems exponential. It is easily approximated through the formula $\exp(-\phi_i \tau_{final})$, with $\tau_{final} = 138 \text{ ns}$.

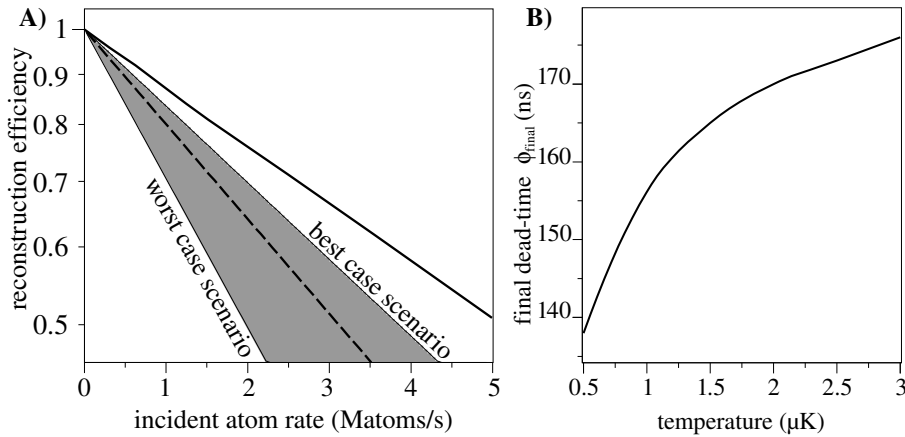


Figure 2.29: In A, the simulated reconstruction efficiency as a function of the total particle rate. The vertical axis is logarithmic. The dashed line indicates the efficiency for ^4He $0.5 \mu\text{K}$ clouds with a 308.3 ms time-of-flight without taking into account the electronic dead-time. The continuous line corresponds to the same clouds considering the electronic dead-time. The worst and best case scenarios correspond respectively to homogenous and centered particle flows without considering the electronic dead-time. In B has been calculated the effective dead-time for ^4He clouds falling for 308.3 ms versus their temperature. The increase of the dead-time with the temperature simply results from the larger spreading of the atomic clouds.

Considering that within our working limits, the reconstruction remains exponential as a function of the incident atom rate, we have plotted in Figure 2.29B the simulated τ_{final} for bosonic clouds after a 308 ms time-of-flight as a function of the temperature. We note in particular that for homogeneously spread clouds, such as for 1 mK time-of-flights, $\tau_{final} = 183 \text{ ns}$.

Experimental Values The just mentioned simulations suppose that all signals are physical and none are missing. This is not the case for our experimental data.

We therefore have to measure the reconstruction dead-time experimentally. We have seen in paragraph 2.3.1.2, that the low-rate reconstruction efficiencies are 81% for 1 mK clouds, whereas respectively 95%, 93% and 92% at 0.6 μK , 1 μK and 1.5 μK . This is unlike the simulations that assume a 100% reconstruction efficiency for low particles rates.

The associated experimental dead-times are measured, for ^4He clouds falling for 308.3 ms, 120 ns for the 1 mK clouds, and respectively 158 ns, 140 ns and 132 ns for the 0.6 μK , 1 μK and 1.5 μK clouds. This is unlike the simulations. Those measurements have though been performed for total particle rates below 700 katoms/s as this was a limiting acquisition rate as shown in the next paragraph. In this range, the measured reconstruction efficiencies are smaller than the those of the simulations. Although the measurements do not show the expected behaviour, they are not yet in contradiction with the simulations. It is difficult to extrapolate what happens experimentally at higher particle flows, although the simulations can be expected as a higher bound.

2.3.2.3 Global Detection Rates

Finally, the detector has some additional flux limitations that are given by the speed of the electronics. In particular the time-to-digital converters show a maximum particle rate, related to the speed of its components. We will first have a small overlook of our first time-to-digital converter, the CTNM4. Then we will easily understand what brought us to the design of a second time-to-digital converter, the IsiTime02.

The CTNM4 The CTNM4 (standing for Convertisseur Temps NuMérique) is an already fairly old time-to-digital converter build at the Institute of Nuclear Physics in Orsay. The originality of this time-to-digital converter lies in the fact that it had been designed with in mind the many possible applications, and several features had been implemented that had been unnecessary until our use. The two essential features were the ability to define with an external control the acquisition frame length, and the second was the use of the extended time feature in order to measure periods larger than the internal 5.6 μs cycle.

In addition though, we also wanted to drive the time-to-digital converter into the high acquisition rate regime. The global architecture of the time-to-digital converter, as presented in Figure 2.30, had in mind the various uses that could be made of it. The time coding is performed by an Application Specific Integrated Circuit (ASIC). This is mainly a micro-processor specifically designed for the time-to-digital conversion. The measured data streams through a first FIFO memory buffer to a Digital Signal Processor. The latter is a programmable micro-processor. This means that one can implement various hard-coded algorithms, that can apply various tasks to the data. This DSP streams the data in its turn to a second FIFO buffer, whereafter the data is sent through a handshaking protocol to a National Instruments NI6534 acquisition card. The last sends the data through the PCI bus to the memory of a desktop computer.

As in all acquisitions, this system has a bottleneck. That means that there is one specific place in the acquisition frame that limits the total data flux. We have indicated in Figure 2.30 the various maximum flows. The unit W indicates a Word,

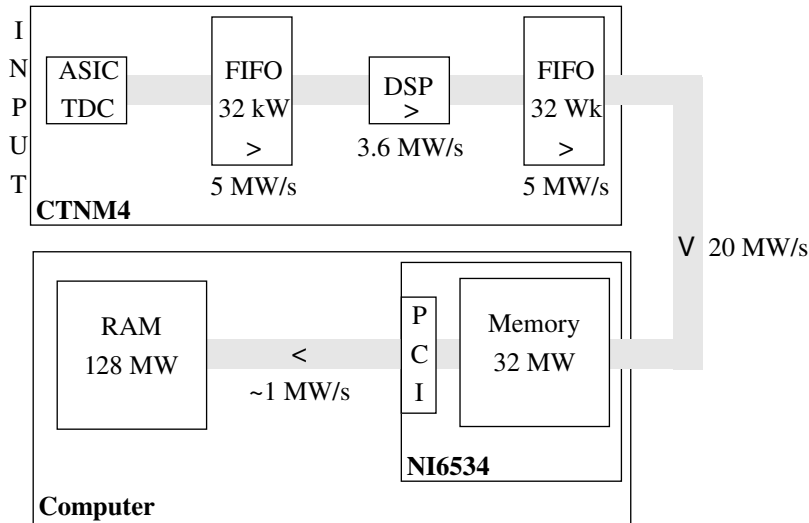


Figure 2.30: The schematic design of the CTNM4 time-to-digital converter. The unit W indicates a 32 bit integer called word. A specifically designed ASIC performs the time-to-digital conversion. The results streams to a FIFO memory where it waits for analysis in a DSP. The latter is programmed to simply stream the data to the output where a second FIFO regulates the transfer to a National Instruments NI6534 digital acquisition board. The large onboard memory of the NI6534 ensures a smooth streaming of the data to the computer memory. The bottleneck of this system is the DSP at 3.6 MW/s.

that is a 32 bit integer. Each time coding requires a 32 bit integer, and each particle therefore requires either 4 or 5 words. The bottleneck is not provided by the 1 MW/s PCI transfer rate. Let us note first of all that the theoretical transfer rate of the PCI bus is 33 MW/s, yet the many other components that use this parallel bus, limit its performance. Yet as the total number of detected atoms is in our experiment far lower than the 32/4 Matoms, the NI6534 memory completely screens the PCI bus.

Consequently the acquisition rate is limited to the 3.6 MW/s transfer rate of the DSP, this despite the fact that the program implemented in this processor has been limited to simply copying the input to the output. This time-to-digital converter consequently limits the acquisition rate to either 700 katoms/s in the case of a 5 channels use, or 900 katoms/s in the case of a 4 channels use. In a single channel use, the time-to-digital converter would be limited to 3.6 MW/s. As we were limited by this 4 channel acquisition rate, we have sought for a faster time-to-digital converter.

The IsiTime02 The IsiTime02 has been specifically designed for our use by a company, IsiTech, based in Orsay. The number of possibilities have been kept sober, and limited to our requirements. Thanks to the sober design, the time-to-digital converter can yet deal far better with our high atom rates. The layout of the time-to-digital converter has been provided in Figure 2.31.

The time-to-digital conversion has been implemented in a modern high-frequency FPGA. The total acquisition rate of this device is 80 MW/s. That brings us to 12 MW/s per channel, the total acquisition rate. Note that even if one uses a single

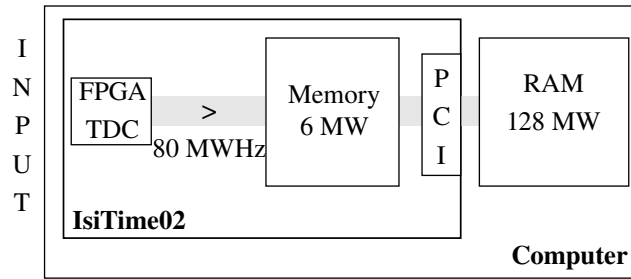


Figure 2.31: The schematic design of the IsiTime02 time-to-digital converter. The time-to-digital converter is programmed in a Field-Programmable Gate Array, the data streams directly to a large fast onboard memory. After the time-of-flight, data can be acquired easily to the computer.

channel, 12 MW/s will still be the maximum acquisition rate. This is due to the serialisation procedure described in paragraph 2.2.3.2. The data is directly streamed to an onboard 6 MW total memory, that can handle all the data we need. Finally, the data is transferred towards the computer memory over the PCI bus. Considering all the other flux saturations, this time-to-digital converter can handle more than effectively required.

2.3.3 Resolution

The signal to noise ratio of the Hanbury Brown and Twiss experiment depends strongly on the detector's spatial resolution. The ultimate resolution one can expect from a delay-line detector depends on the time-to-digital converter coding step and are for this specific detector respectively $79 \mu\text{m}$ and $55 \mu\text{m}$ when using the CTNM4 or the IsiTime02 time-to-digital converter. Demonstration of this is provided in Appendix 1. Those resolutions are both in the order of the expected l_x correlation length, and the resulting bunching heights are expected in the order of 40%. Practically, the resolution is expected worse because noise has to be considered, and special focus is required. In particular, we will show that the resolution strongly depends on the experimental conditions.

We will first outline the methods we have used to actually measure the resolution. Then we will study some of the resolution dynamics that will eventually influence the proposed experiment.

2.3.3.1 Measurement Methods

Usually, in order to measure the resolution, one would put a mask in front of the detector, and study the edge properties of the obtained image. We have undergone this process only recently, and further studies are still required before we can conclude on this. We have not undertaken this method earlier because it requires to break the ultra-high vacuum, which is always a time consuming procedure. Also we have found different methods to measure the resolution, that we will briefly outline here.

Time Sum Method The Time Sum method has been studied exhaustively in Appendix 1. We will therefore simply summarise its main characteristics.

The essential point is to realise that the two signals coming from the opposite sides of the same delay-line initiated by a single particle have a logical relation between them. Their total time of propagation through the delay line is indeed equal to delay-line length. If we add those two times, and subtract twice the arrival time, one should get a single constant as a result. Likewise, if we sum the two signals provided by one delay-line and subtract the sum of the signals of the other delay-line, the result should also be a constant. If this is not the case, and if the resulting distribution of what we will call the Time Sum, has a certain width, then this width necessarily affects the resolution. Consequently, this measurement can be linked in some extent to the resolution.

The enormous advantage of this method is the ease at which we can measure a resolution. When one changes a parameter on the experiment, one single time-of-flight spectrum provides enough information for the measurement of the resolution during that time-of-flight. Figure 2.32 shows such a distribution as acquired through a single 1 mK time-of-flight of 40 katoms. The measured width, through the gaussian fit, attributes a $180 \mu\text{m}$ average root-mean-square resolution to this time-of-flight.

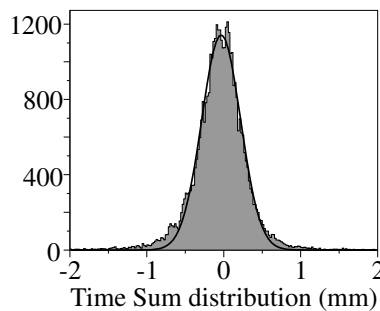


Figure 2.32: A Time Sum distribution obtained for a 1mK time-of-flight. The distribution has been fitted with a gaussian. The resolution is measured to $180\mu\text{m}$.

The first conclusion we have to draw from this method is that we do not measure the total resolution. We simply measure the effect of the electronic detection of the pulses. We can not measure the resolution induced by the micro-channel plate stack detection, nor any other physical principle that would disturb the detection. Practically, the electronic detection proves to be the main limit to the resolution though. Second conclusion, this measurement is equivalent to the measurement of the resolution only under a certain number of hypotheses explained in Appendix 1. Although those hypothesis seem very reasonable, we have no way to check them, and we will have to live with them. The last point is, as explained in Appendix 1, that we depend on an average Time Sum map in order to subtract a spatial dependence of the supposed Time Sum constant. Although in Orsay this map proved relatively stable over time, for the data taken in Amsterdam we do not have the same behaviour. Furthermore, if a parameter is changed, it is difficult to estimate the impact on this map, and rebuilding this map for every parameter change can prove extremely time and disk-space consuming.

Another important aspect to notice is that the graph in Figure 2.32 has been

fitted with a gaussian function. Although this seems reasonable as to the usual definition of the resolution, it must be said that the difference between this gaussian fit and the effective resolution will have to be taken into account for a better calculation of the expected bunching height and signal to noise ratio. We will discuss this point in paragraph 3.1.4.1. The simple gaussian fit is enough for studying the resolution dynamics.

The Oscilloscope Method Instead of detecting the pulses through a constant fraction discriminator, one can also choose to acquire the signal through a four-channel oscilloscope, and rebuild the arrival times through post-analysis of the acquired analog signals. This method has been detailed in Appendix 3. The final resolution can then as previously be measured through the Time Sum method, although one circumvents some key electronic components, and in particular one preserves the pulse heights. Eventhough this method does not provide an in-the-end useful measurement, it does allow for some specific studies and deeper understanding of the resolution limiting processes. We will therefore mention some of the results obtained with this analysis.

The Correlation Method The above measurements give a nice indication of how the resolution can behave. They are yet build upon a certain number of hypothesis that might well be completely false. Those hypothesis are the equivalence between the various detection channels, and their respective independence of the fluctuations. It is therefore important to see whether those methods provide a right order of magnitude as to the real resolution.

The only way of effectively measuring a resolution is by using a physically defined signal. This can be done by adding a mask between the source and the detector, but the correlations we would like to observe also constitute a physical signal. In particular, we have previously made estimates of the correlation length along the x axis of around $32 \mu\text{m}$. This compares small to the $\sqrt{2} \times \sqrt{2} \times 180 = 360 \mu\text{m}$ two particle half-width half-maximum resolution measured just above. This means that the spatial extend along the x axis of the (anti)bunching will be limited essentially by the detector resolution function. The success of the proposed experiment would therefore provide us with an independent resolution measurement.

To cut a long story short, we did succeed in the correlation measurement, and we have been able to measure the resolution independently. We will come back to this point in the next section, so we will simply state the two main conclusion to this. The first is to notice that in order to get this measurement, we need typically 1000 time-of-flights, and still the signal to noise ratio is much lower then the one we have seen in the Time Sum method. This method is consequently interesting, and important as to our statements, yet not very useful for a practical resolution measurement. Changing parameters freely with this method is an extremely time consuming practise. The second point is that, at first order, the bunching widths measured do correspond very well to the results obtained through the Time Sum method. Consequently, although the Time Sum method does not provide an absolute measurement tool, we do feel quite confident in its use. We will come back to this point as we will analyse the measured bunching widths.

2.3.3.2 Dynamics

In paragraph 2.2.2.2 we have shown some detector operating voltages that influence the resolution, and that have been optimised. It would yet be wrong to assume that the resolution of the detector is some absolute constant. Through our use of the detector, we have experienced various fluctuations of this resolution, that depends strongly on various dynamic properties. We will discuss the way the bunching height affects the resolution. We will then deduce logically the spatial dependence of the resolution. We will then address the particle flux dependence of the resolution. Finally we will discuss the sensitivity of the resolution to the electro-magnetic environment.

Pulse Height Through the oscilloscope method described earlier, we can access both the position and the pulse height of all atoms falling on the detector. We can therefore, by using in addition the Time Sum method, measure the resolution of the detector as a function of the pulse height. The result of this measurement on several 1mK clouds has been displayed in Figure 2.33. The graphs shows that the

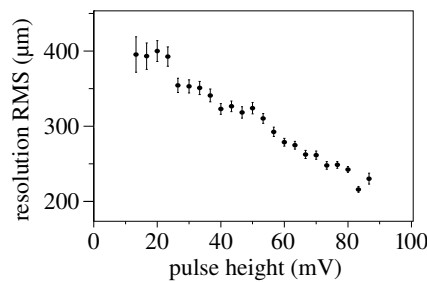


Figure 2.33: The resolution of the detection versus the pulse height of the atoms. Both the position and the pulse height have been measured through an oscilloscope acquisition. Therefore this curve does not correspond to the effective resolution dependence in usual experimental conditions.

higher the pulse height, the better the resolution. The graph can not be used in the present state though. Normally data is acquired through the discriminator time-to-digital converter system, and we are concerned by the corresponding resolution. This curve is specific to the oscilloscope acquisition. It allows though for a better understanding of the eventual pulse height dependence, as finally the two detection procedures are conceptually similar. This subject is addressed more deeply in Appendix 3.

If the pulse height is low, the fluctuations of the signal are less negligible compared to the signal, and the resolution is strongly affected by background noise, or component jitters. For large pulse heights, jitters and background noise can eventually be neglected, and the resolution is optimal.

Position In the previous section, we have studied briefly the position sensitivity of the electronic pulse height distribution. Although this dependence is simply related to mechanical constraints, and has no relation with some fundamental parameter of the micro-channel plates, it does affect the resolution. We have just studied the dependency of the resolution on the pulse height, we can expect this

to directly produce a spatial resolution distribution. That specific distribution is shown in Figure 2.34. In this Figure we have plotted the resolution as a function

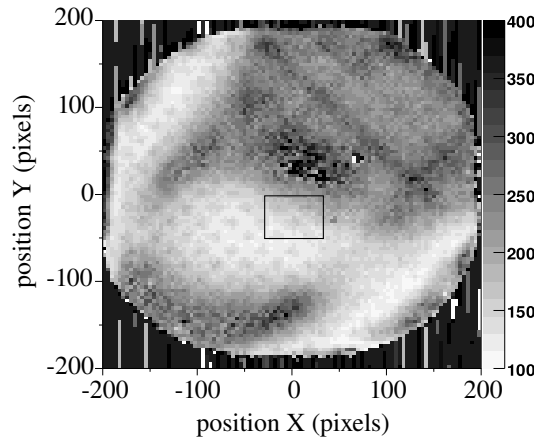


Figure 2.34: The spatial dependence of the resolution. The resolution has been averaged and measured over a series of 1mK clouds using the Time Sum method.

of the spatial variables X and Y as acquired for some 1mK time-of-flights. The resolution has been obtained through the Time Sum method. We note that we have regions where resolutions are as good as $120 \mu\text{m}$. The detector is consequently close to the specifications. The equivalence of this resolution map with the previously shown amplitude map (Figure 2.7) is striking. This seems to stress the previous hypothesis that the resolution depends strongly on the pulse height.

This makes it also feasible to use the resolution as a tool to characterise the micro-channel plate. An inhomogeneous resolution seems to indicate directly an inhomogeneous pulse height distribution. The advantage of this method over the analysis of the detection efficiency map is that the influence of the discriminator level is much smaller.

The consequence of this position sensitivity for the proposed Hanbury Brown and Twiss study is straightforward. The various temperatures we would like to study average differently over the detector surface, and consequently we are to expect different resolutions for the various clouds. This means that we will have to study the average resolution for each temperature if we want to be able to interpret correctly the results. The effective impact of this spatial dependency is though not very important in our specific situation. The centre of all the clouds will indeed cover the same area, and it is precisely the centre of the cloud that participates most to the correlation buildup. It is yet to be considered.

Particle Rate A more important aspect is the particle rate effect on the resolution. We have seen previously how the average pulse height lowers at local saturating particle rates. Consequently, we can expect an effect of the particle rate on the resolution. The study of this effect is not simple though.

Two different particle rates can affect the resolution: the global and the local particle rate. The reasons are different. The global detection rate is easily expected to deteriorate the analog amplification and discrimination process. The electronic pulses provided by the delay-lines are separated from the high potential through a

capacitor and a resistance as shown previously in Figure 2.15A. The typical time scale associated to this operation is $RC = 110$ ns. This means that if two consecutive signals are expected to undergo an identical analog process, they should be separated by an similar time scale. Else, in particular, the discrimination of the second pulse will be affected by the first pulse. Typical global particle rates at which we are looking are around 500 katoms/s. This is in the same order of magnitude.

For the local particle rate, we have shown a distinct drop in the pulse height at 82 ± 10 katoms/cm²/s. It is not clear why the resolution would change before this pulse height drops, yet this idea cannot be set aside that easily.

We therefore need an experimental study of those parameters. The problems is the spatial dependence of the resolution, and our current inability to completely control the shapes of the falling clouds. It is consequently fairly difficult to dissociate a local particle rate, from a global particle rate study. Currently, we do not have that possibility on the Orsay ⁴He experiment. In Figure 2.35 we have plotted the fluctuations of the resolution as a function of a local detected, and rebuild, particle rate.

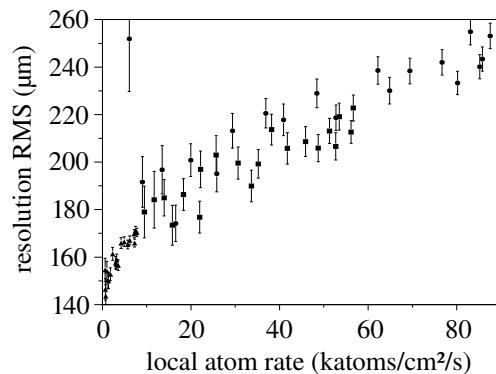


Figure 2.35: The resolution in the centre of the detector as a function of the locally detected and rebuild atom rate. Three different samples of clouds have been used. The triangles correspond to 1 mK clouds, the squares and the circles to respectively 1 μ K and 0.61 μ K clouds.

The graph is effectively build out of 3 different data sets. The triangles are data provided by 1 mK time-of-flights. The squares and the circles were respectively 1 μ K and 0.61 μ K data sets. Each data set has been averaged over various time-of-flights. The resolution has been measured through the Time Sum method. The detection area has been considered in the middle of the detector, as indicated with the black rectangle in Figure 2.34, that can be associated the maximum detection rates.

First observation is of course that the higher the particle rate, the worse the resolution. One can easily loose 60% in the resolution between a large and a small time-of-flight. We further observe that the three data sets are relatively consistent among each-other. This leads to think that the rate dependence is locally defined. A closer look at the graph shows a slight offset between the various data sets though. It is difficult to say whether this is due to the fact that the data has been taken on various days, or to the fact that the global particle rates affect the resolution. The ratio between the maximum local particle rate, and the average particle rate,

depends on the temperature after all.

We have tried further attempts to map the resolution spatially, and study its local fluctuations as a function of the particle rate. This study has not given clear evidence though, that the local saturation is the reason to the resolution loss. We will therefore simply state that the fluctuation of the resolution as a function of the particle rate has to be taken into consideration when using the delay-line detector. More specifically to our proposed experiment, as we will always work at the maximum global particle rates, we can expect a severe difference in the average resolutions between the various temperatures we will study. This will be all the more important as the correlation procedure will privilege high local particle rates.

Background Noise A last parameter, that has little to do with the data acquired, is the effect of the background noise on the resolution. Three plasma Helium cells are used for the locking systems of our lasers. The plasma is established and maintained through a ~ 27 MHz oscillating fields. Those fields have not been isolated, and consequently the entire room is modulated at those frequency fields. Although the physics of the experiment are barely affected by those fields, they and their harmonics lie precisely in the bandwidth of our delay-line detector.

The intensity of the radio-frequency fields can be modulated with the level of the amplification of the electronic resonators. Although this modulation is not linear, as various resonances may appear, we can study easily the resolution of the detector in various electronic situations. Keeping all other parameters identical, we have measured resolutions of respectively $200 \mu\text{m}$, $174 \mu\text{m}$ and $197 \mu\text{m}$ with respectively a low, medium and high amplification level of the electronic oscillators. This test shows clearly the sensitivity of the detector setup to the electronic background.

We have tried to shield the electronic detector equipment from the global environment through the use of various Faraday isolation techniques. Although this has substantially lowered some part of the noise, success has not been up to the expectations, likely due to the 10 m wavelength of the noise for which we always are in the near field. The problem is currently being solved by shielding better the radio emitters.

Conclusion

In Chapter 1, we have seen how the use of a micro-channel plate based detector would enable us to measure the Hanbury Brown and Twiss effect with a cold gas of He* atoms. We have in particular established the signal to noise ratio for such an experiment, and we have seen what characteristics of the detector are essential to the experiment.

Throughout this Chapter, we have focused on the implementation of such a detector. We have considered first of all the various implementations that exist of micro-channel plate based detectors. We have discussed in particular the use of phosphor screens and resistive anodes that enable position sensitivity. We have seen that unfortunately, despite the excellent resolutions those systems offer, they can not handle the high particle flows we need to detect. We have dealt briefly with the delay-line based detector, that seemed more adequate to our needs. Eventually, we have discussed some more advanced delay-lines based solutions, that offer better position sensitivity, but that are currently not yet ready for our use.

We then have focused much closer on our implementation of a delay-line detector as bought from Roentdek Handels GmbH. We have analysed closely the characteristics to be expected from a chevron micro-channel plate stack, and we have noticed in particular the severe spatial pulse height inhomogeneity we experienced with our Burle Industries Inc micro-channel plate stack. We then discussed some aspects of the delay-lines, and in particular we have dealt with the operating voltages. Then we have focussed on the electronic part of the acquisition chain, with in particular the amplification, discrimination and time measurement of the electronic pulses coming from the delay-lines. Finally we have discussed quite extensively the computer and software implementation of the detector. This implementation did not only require a lot of time, but also proved to be a key to the success of the proposed experiment.

In the last section of this Chapter, we have focussed deliberately on three fundamental characteristics of the detector: the detection efficiency, the detection rate and the resolution.

Although the proposed study of the Hanbury Brown and Twiss effect does not depend on the detection efficiency, optimisation of signal to noise ratio and general interest for further experiments have drawn our attention to this point. We have seen how to characterise the detectivity in respect to some of the measurements we can perform. We have also noticed how the total detection efficiency depends on both the mechanical situation of the micro-channel plate stack and the shape of the detected cloud. We have eventually performed two measurements of the detection efficiency, but the results are inconsistent.

The study of the detection rate has provided us with some fundamental limitations. We consequently have noticed the local saturation of the micro-channel plates, that will have dramatic consequences as to the detection of Bose-Einstein condensates. Then we have studied the dead-times induced by both the electronics and the atomic reconstruction, that impose an ultimate limit to the use of a delay-line detector. We must add though that the previously detailed improved detection scheme pushes those limits slightly further. Finally we have dealt with some technical limitations of the time-to-digital converter we had planned. We also showed how the realisation of a new time-to-digital converter made it possible to overcome

those limitations.

The last point we have discussed extensively, and on which the signal to noise ratio is highly dependent, is the resolution. We have detailed the methods through which we were able to analyse this resolution. Further reference on this is provided in the Appendixes. We then have analysed various dynamics that influence the resolution such as the pulse height and consequently the position. Also the particle rate and the electronic background noise influence strongly the resolution. The effective resolution will have to be measured specifically in the experimental conditions in order to be relevant.

This detailed overview of our implementation of the delay-line detector now enables us to come back to the proposed Hanbury Brown and Twiss effect experiment, and in particular we will be able to establish the effective signal to noise ratio to expect. We recall the previously established formula:

$$SNR(T, N') = N' \frac{\sqrt{\left(\frac{\hbar\omega}{4k_B T}\right)^3 \coth\left(\frac{R^2 m}{t_0^2 k_B T}\right)}}{\sqrt{\Pi_\alpha \frac{2}{\sqrt{\pi}} \sqrt{1 + 4d_\alpha^2/l_\alpha^2} \pm 1}} \quad (2.3.7)$$

with:

$$l_\alpha = \frac{\hbar\omega_\alpha t_0}{\sqrt{mk_B T}} \quad (2.3.8)$$

Considering that we know now the characteristics of the detector, we can establish the effective signal to noise ratio for the proposed experiment. We recall the trapping frequencies for the 308.3 ms time-of-flight of the ^4He atoms to be $\omega_y = \omega_z = 2\pi \times 1150$ Hz and $\omega_x = 2\pi \times 47$ Hz in Orsay. In Amsterdam the trapping frequencies for the ^3He atoms with their 359 ms time-of-flight are $\omega_y = \omega_z = 2\pi \times 506$ Hz and $\omega_x = 2\pi \times 54$ Hz.

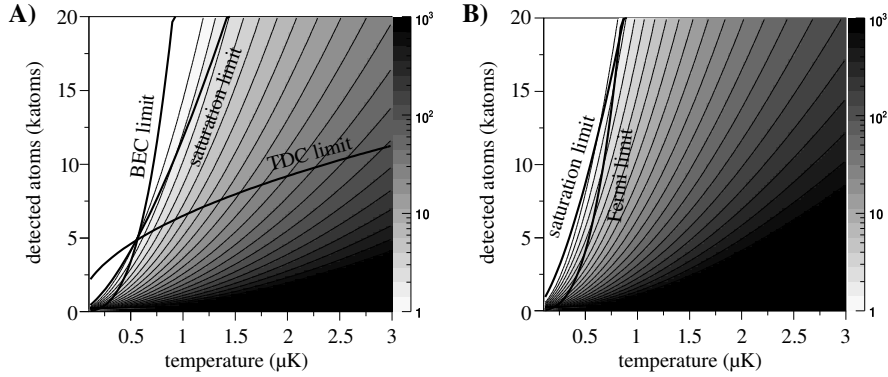


Figure 2.36: In A, the number of time-of-flights required for a given temperature and a number of detected atoms, in order to get a signal to noise ratio of 1 for the ^4He clouds in Orsay. The black curves correspond to various upper bounds the acquisition has to respect. In B, the same graph for the ^3He to be acquired in Amsterdam.

In Figure 2.36 we have plotted the number of time-of-flights, as a function of the detected number of atoms and the temperature, required to obtain a signal to noise ratio of 1. In Figure 2.36A we have plotted the corresponding graph for Orsay. The plotted graph considers an average resolution of $250 \mu\text{m}$. We have

furthermore introduced several limitations of the detector and the physics. We plotted the curve corresponding to the limitations introduced by the maximum flux of the time-to-digital converter. We cannot acquire data above this limit. We also note the micro-channel plate local saturation limit above which signals can lose their physical significance. We also introduced the previously discussed condensation threshold, that keeps us from working with lower temperatures.

In Figure 2.36B we have plotted the corresponding graph for Amsterdam. Here we have also considered a resolution of $250 \mu\text{m}$. Here we have no longer the limit of the time-to-digital converter as we introduced the IsiTime02 time-to-digital converter. The Fermi limit, linking the number of detected atoms to their Fermi temperature, is not really a limit. There is indeed no phase transition as we cross the barrier. It separates the classical from the quantum statistical behaviours though.

We note that, especially in Orsay, we are at the limit of the feasibility of the proposed experiment. We will have to acquire clouds in the μK temperature range, and we will need several hundreds of thermal clouds as to have an appreciable signal to noise ratio. Having signal to noise ratios significantly exceeding 1 is yet quite possible, and we can hope to perform measurements beyond the measurement of the bunching volume.

We now simply have to proceed to the acquisition and analysis the data.

The Results

The feasibility of the experiment has been shown through the study of the signal to noise ratio and the detailed analysis of the detector characteristics. This chapter deals with the experimental demonstration of this feasibility.

Data for the Hanbury Brown and Twiss effect measurement has been acquired in two tides. The first tide consisted of the measurement of the $^4\text{He}^*$ data in spring 2005 in Orsay. Those results have been published in [17]. The second tide consisted of the measurement of both $^4\text{He}^*$ and $^3\text{He}^*$ clouds in the summer of 2006 in Amsterdam. Those results have been published in [18].

In this chapter we first present the acquisition, analysis and measurements on the thermal $^4\text{He}^*$ clouds as acquired in Orsay. We will in particular note how the results fit to the theory.

We then study in detail the acquisition and analysis of the Bose-Einstein condensates. We will notice that the implementation of the detector reached its limits as to this experiment.

In the last part we will only focus on the $^3\text{He}^*$ clouds acquired in Amsterdam. We will discuss briefly the acquisition conditions. The analysis techniques used are identical as for the thermal bosons, and require no further focus. Emphasis is therefore put on the measurements performed on this data.

3.1 Thermal Cloud of Bosonic Atoms

The measurement of the Hanbury Brown and Twiss effect in a thermal cloud was expected to be the most difficult part to realise, as compared to the Bose-Einstein condensates for which the atomic densities seemed favourable. As we discussed before, the resolution of the detector is just within acceptable values, and also the time-to-digital converter limited the particle flow. A. Öttl & al. [31] have not succeeded in visualising the thermal correlation precisely for this reason.

We will see how additional difficulties have limited us to the acquisition of three data sets. Then we will study in detail the way those data sets have been analysed. Finally we will discuss the results.

3.1.1 The Acquisition

During the acquisition of data on a working experiment, the human patience is among the main limiting properties. A working experiment is rarely completely autonomous. Even in the case of the Orsay ^4He experiment, where both experiment piloting and data acquisition have been completely automated, there still has to be a human supervisor to deal with the experiment's particularities as well as to decide on the data that is to be acquired.

We will briefly study some of those particularities, that in the long run tickle the patience of the experimentalists, and we will see briefly the time it took to acquire the data for the present measurement. Finally we will outline the acquired data.

3.1.1.1 Experimental Conditions

The experiment has several points that need constant surveillance.

Source Temperature The first is the temperature of the liquid nitrogen cooled Helium source. This temperature influences directly the longitudinal speed of the atoms as they enter the Zeeman slower, thus the efficiency of the Zeeman slower and consequently the loading rate of the magneto-optical trap, the number of atoms in the magneto-optical trap, and anything that follows. Two reasons make those temperature fluctuations particularly unhelpful.

The first one lies in the fact that when working with cold gases, the high non-linear efficiency of the evaporation cooling mechanism as to the number of the atoms in the trap, makes one end up either with or without atoms in the end. Yet many problems can come up that prevent a final cold cloud to be produced. Therefore a certain time is necessary each time to identify this cause.

The second reason lies in the fact this problem does not occur that often, the fluctuations lie in the order of 5 to 6 hours. Therefore, this is rarely the problem one thinks of first when the cold clouds disappear.

The reasons for this problem lies either in the fact that the bottle is empty, something that can be foreseen. Or in the fact that ice (H_2O) is stuck inside the tube that brings the liquid nitrogen through the source. This can only be solved by heating up the source, and cooling it down again. An operation that takes at least 40 minutes of active operation.

A recent installation of a pressurised withdrawal tube has made the cooling procedure much more efficient, and the problem today is generally limited to the empty bottle.

Laser Locking The laser system we have is exclusively made of distributed Bragg reflector diode lasers. Although they have a linewidth of around 2MHz, that is fairly large compared to the 1.6MHz large transition, they are very easy in use. This in particular in comparison with the use of solid state LNA lasers.

They yet have to be locked to a $^4\text{He}^*$ transition and this is done with some radio-frequency excited Helium cells. The age of the electronic circuits that rule those Helium cells do not inspire absolute stability, and interruptions in the plasma excitations are frequent. Furthermore, the low power output of the laser diodes (50mW typically) forces us to use only the minimal power necessary for the locking system. Further small misalignments and fluctuating cell intensities make the locking system relatively sensitive to the electronic and mechanical environment.

Consequently, one of the three lasers unlocked on average every 30 minutes. This is including night-time data acquisition, when the outside environment is more stable. Each time the lasers have to be relocked, loosing at least two experimental runs: the first for the discovery, the second to lock in again.

The Bias Field A big problem with a clover-leaf magnetic trap configuration is the difficulty of producing a stable bias field. This bias field controls both the depth of the trap, that is important for the temperature control by the radiofrequency evaporative ramp, as well as the trapping frequencies. This small field is produced by the difference of two intense magnetic fields. The fluctuations are generally low as the same electric current is used for the two magnetic dipole and quadrupole fields. An additional independent current is yet used to control beyond the geometrical defined properties.

Formerly, the Orsay ^4He experiment used a Hall probe to measure the fluctuations of that additional current in order to stabilise it [58, 56]. This led to 20 kHz fluctuations of the bias field. During the new build up of the experiment, we decided to do without this locking system, and to rely on the current control of the power supplies solely. Although we have no precise measurement on whether we gained or lost, we ended up with two problems. One is a 10 Hz oscillation of the bias field. The second is a large thermal fluctuation of the bias field. When we use the high intensity power supplies with the magnetic coils for a long period, both the temperatures of the power supply and the coils increase, and thereby their electrical resistance. This affects the current control, and we observe fluctuations of the bias field.

This problem is easily solved by running the experiment continuously. The system requires fifteen minutes to stabilise. Once it has been stabilised, we just keep it running and it remains stable. It implies that we do not like stopping the experiment for whatever reason.

The time-to-digital converter A new problem we introduced with the Hanbury Brown and Twiss experiment was the CTNM4 time-to-digital converter. The problem of this time-to-digital converter does not simply lie in its 700 kparticles/s lim-

itation, but more worryingly in the fact that when it reaches that limit, it goes out of control. A time-to-digital converter that would simply stop the acquisition when saturating would have been nice. This time-to-digital converter decides that when saturated, it stops for that run, yet it renders all following data completely unusable. This means that when the time-to-digital converter reaches that limit, we have to reinitialise it manually (as this has not been software implemented). In order to avoid that limit, and considering the high intensity instabilities of our cold clouds (typically 100% fluctuations), we had to work far from the time-to-digital converter limits. This was certainly not profitable to the signal to noise ratio.

Outside Temperature A last problem we had is more of an anecdote order, yet pretty interesting as we had a similar problems in Amsterdam. The data has been acquired during spring 2005. As acquisition and parallel analysis went on, time passed. Eventually, by the end of the acquisition, summer was just around the corner. As the outside temperature increased, the cooling filtered tap water we use for the magnetic coils also increased in temperature. As we were working at the very edge of the possibilities of the power supplies, the slight cooling efficiency decrease affected the resistance of the coils that brought the power supplies over their limit. We then had to work with slightly reduced fields.

3.1.1.2 Acquisition Time

Several parameters influenced on the total acquisition time. The importance of this acquisition time is that the signal to noise ratio evolves with the square root of it. That means that if one wants to double the signal to noise ratio, one has to quadruple the number of time-of-flights and thus the acquisition time. Ultimately the acquisition time will be affected by, and limited by, the patience of the experimenters. Those are unlikely to enjoy doubling the signal to noise ratio after already 4 weeks of data acquisition. That would indeed mean spending an additional 3 months on that acquisition.

The problem was that the setup was not in its best shape. Cold clouds had only a few atoms (typically 8 katoms od detected atoms), and this number was strongly fluctuating. Each production of a cold cloud takes around 1 minute. In total, around 4000 useable cold clouds have been acquired, and some other 1000 unused. This is already two weeks of data acquisition. With the various laboratory issues raised above and other, the total time spend in the lab for the simple acquisition of the data has been close to three weeks. Those were spread out over 5 weeks as the parallel analysis had to provide some understanding and directions.

3.1.1.3 Data Sets

All the above considerations have ended up in the acquisition of three distinct cold cloud populations. An overview of the global data set has been produced in Figure 3.1.

In this figure, we plotted a histogram representing the integrated squared number of atoms of the time-of-flights versus their temperature. The signal to noise ratio is proportional to the square root of the selected area. The large distribution in the number of atoms of the time-of-flights renders this graph more practical then

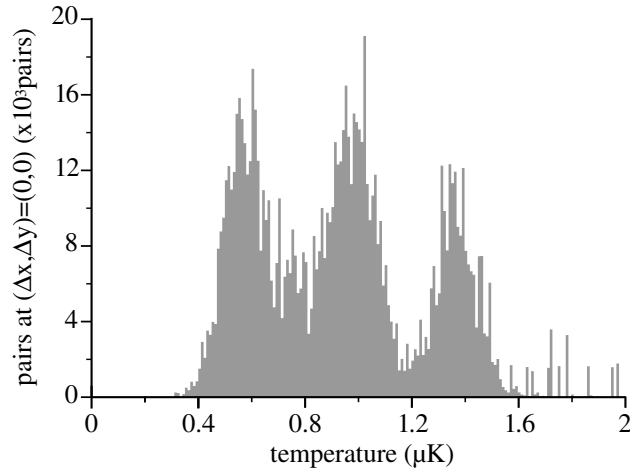


Figure 3.1: Temperature distribution of the time-of-flights weighted with their squared number of atoms. The respective areas of the three distinct data sets give an estimate of their respective signal to noise ratios.

a simple summing of the number of atoms in each time-of-flight. Identical areas hence indicate very similar signal to noise ratios.

Bose-Einstein Condensates Closer analysis of the data, and in particular the two dimensional y versus x plotting of the atoms, show that some time of flights have small Bose-Einstein condensated fractions. This is not what we want at this point as we only want to analyse pure thermal clouds. The problematic clouds then have to be removed. Thanks to the 3-dimensional detector, they can be spotted very easily.

Formerly, when the setup was equipped with a 1-dimensional micro-channel plate detector, the detection of small Bose-Einstein condensates within large thermal clouds was problematic and required some smart fitting scheme [59, 58, 56]. In Figure 3.2A it is hard to distinguish the characteristic features of a Bose-Einstein condensate. With the three dimensions, one can make a 2-dimensional image where the human eye can spot the condensate, as in Figure 3.2B. One can also project this image on the x axis of the condensate, and by cutting out the unuseful wings of the thermal cloud, increase significantly the detectability of the condensate. The obtained figure has been plotted in 3.2C. A simple computer analyses can then be used to discriminate the cloud population with a condensated fraction.

The possibility of measuring the density distribution in three dimensions is currently specific to our Orsay ^4He experiment. This ability could be used in the future to study small condensed fractions within thermal clouds.

Three Populations The temperature of the first population is around $0.61 \mu\text{K}$, the second is around $1.03 \mu\text{K}$, the last population is around $1.48 \mu\text{K}$. From now on we will refer to these three populations by their temperature. On the global data set has been applied a cut, that besides discriminating the condensated clouds, only keeps certain data ranges. We consequently distinguish a first set of 615 clouds at $0.61 \mu\text{K}$ average temperature with a $0.064 \mu\text{K}$ RMS spread. The second data set

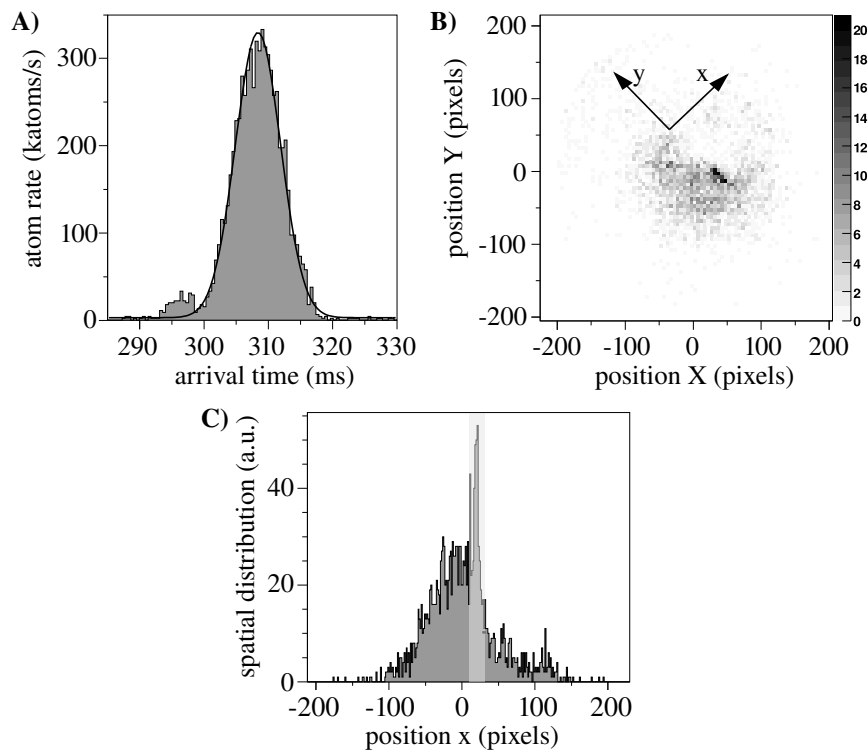


Figure 3.2: In A, The traditional time-of-flight distribution for a $0.6\mu\text{K}$ cloud. One can not distinguish a condensed fraction of ^4He . In, B the spatial distribution shows an intense cigar-shaped condensed fraction. The projection along the x axis in C shows clearly the condensed fraction in the highlighted region. In this distribution, a Bose-Einstein condensate can be spotted with a simple algorithm.

contains 1174 clouds at $1.03 \pm 0.093 \mu\text{K}$. Finally the last data set of 1976 thermal clouds ranges $1.48 \pm 0.11 \mu\text{K}$.

Reference Data We also acquired some reference data. If we would manage to show that we observe a bunching in the correlation function of the data, then we would still have to prove that this bunching is not due to the detector itself.

For this data we simply acquired some "hot" time-of-flights. The thermal clouds at temperatures around 1 mK have correlation lengths that are far too short for us to observe, at least with the current resolution. They amount to $25 \mu\text{m}$ for the largest correlation lengths. The expected bunching height at this temperature is consequently reduced to less than 0.05%. Luckily those data points are very quick to acquire as we can produce a new cloud every second. We have used 500 time-of-flights for this result.

3.1.2 The Analysis

The analysis of the thermal bosonic clouds is fairly straightforward. Background noise is very low so we can simply apply the definition of the normalised correlation function $\tilde{g}^{(2)}(\Delta\mathbf{r})$. In that case the particle correlation function is divided by the local average density correlation.

3.1.2.1 The Correlation

The correlation procedure simply consists in histogramming all the differences in time and position between the various atoms belonging to a single time-of-flight. This means that within a time-of-flight all pairs are taken into consideration, and for each $\Delta\mathbf{r}$ effectively encountered in a single time-of-flight, the corresponding bin of a 3-Dimensional histogram is incremented by 1. At the end of this procedure, one ends up with the $\Delta\mathbf{r}$ distribution of all the pairs. For a large number of atoms, this distribution tends towards $\tilde{G}^{(2)}(\Delta\mathbf{r})$.

Note that whereas the binning in the Oxy plane is imposed by an already limiting pixel size, the resolution on the z axis is four orders of magnitude preciser than the phenomena we plan to measure. In order to increase the number of pairs per bin we increase the bin size to a value in the range of the correlation length. The z bins sizes have been chosen to respectively $50 \mu\text{s}$ in the Orsay experiment and $25 \mu\text{s}$ in the Amsterdam experiment.

In order to get the statistical distribution, and thus the correlation function, one simply has to average this distribution over a large number of experimental realisations. This is done by adding up all those histograms for each time-of-flight. When added up, the histograms are not weighted. This is important to realise. The number of atoms fluctuates strongly, and the number of pairs goes as the square of the number of atoms. Consequently large clouds participate more than the smaller clouds to the final correlation function. By adding up simply the histogram, we assure the same statistical weight to all pairs. As background noise can be neglected even for the smaller time-of-flights, all pairs are equally of physical interest. We consequently obtain:

$$\tilde{G}^{(2)}(\Delta\mathbf{r}) = \sum_i \tilde{G}_i^{(2)}(\Delta\mathbf{r}) \quad (3.1.1)$$

This method assures the best signal to noise ratio. Let us assume that each correlation histogram of time-of-flight i containing N_i atoms is weighted with $\lambda_i \propto N_i^\alpha$ before addition. The total correlation signal is proportional to $\sum_i \lambda_i N_i^2 = \sum_i N_i^{2+\alpha}$, whereas the total correlation shot noise can be written proportional to $\sqrt{\sum_i (\lambda_i N_i)^2} = \sqrt{\sum_i N_i^{2+2\alpha}}$ (the shot noise for a single cloud scales linearly with the weight factor). The signal to noise ratio ratio can then simply be written as:

$$snr(\alpha) \propto \frac{\sum_i N_i^{2+\alpha}}{\sqrt{\sum_i N_i^{2+2\alpha}}} \quad (3.1.2)$$

This function maximises for $\alpha = 0$, in other words, when the histograms are simply added up. Note that this result would have been different if, for instance, background noise was limiting the signal to noise ratio.

As we have initially 3 variables, the correlation histogram is also 3-dimensional. As the display of such a histogram is awkward, we plotted in Figure 3.3B a 1-dimensional extract of the 3-dimensional correlation. The plotted curve is the total correlation of all the Orsay bosonic time-of-flights at $0.61 \mu\text{K}$ plotted versus Δt and averaged over various couples of $(\Delta x, \Delta y)$ that have been chosen within the coherence zone. In Figure 3.3A we plotted the time-of-flight integrated over xy for comparison, and integrated over all the time-of-flights as well. We note first of

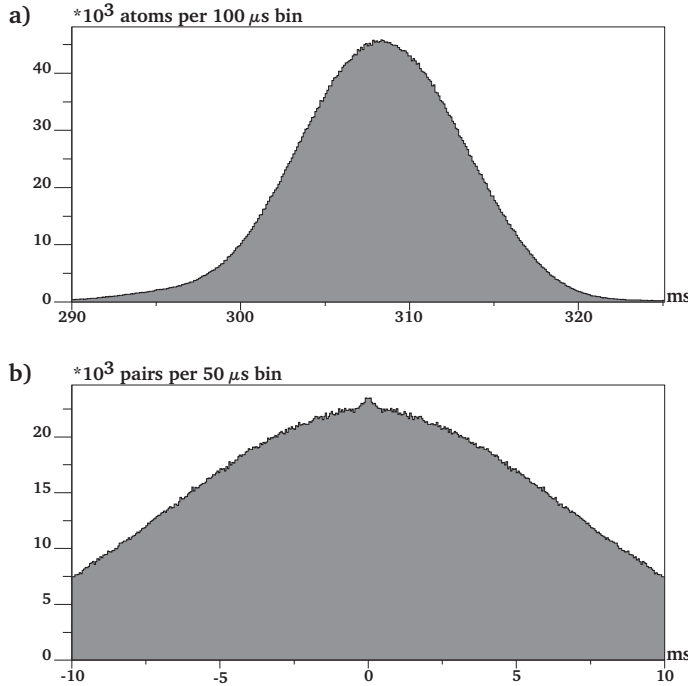


Figure 3.3: Figure A shows a temporal slice of the averaged time-of-flight distribution. One can recognise the Gaussian shape of the thermal cloud. Figure B shows a temporal slice of the raw averaged pairs-histogram as a function of Δt . The overall Gaussian shape results from the auto-convolution of the thermal cloud. The small bunching at $\Delta t = 0$ corresponds to the Hanbury Brown and Twiss effect.

all that the correlation function retrieves the gaussian temporal shape of the time-

of-flights. The root-mean-square width is a $\sqrt{2}$ larger, as established in paragraph 1.3.2.3. But more importantly, we notice the small bunching in the centre of the correlation function. As expected, the height is only a few percent, yet this is clearly the bosonic bunching statistics we were looking for.

3.1.2.2 The Normalisation Procedure

In order to normalise the correlation, it should be divided by the auto-correlation of the density distribution. We can not normalise each cloud by it self, as the auto-correlation of each density distribution shows the same fluctuations as the pair distributions. We would simply eliminate the quantum bunching like any other fluctuation. We therefore use an averaged time-of-flight obtained by summing up all the time-of-flights. The density fluctuations disappear at averaging. We hence effectively measure:

$$\tilde{g}'^{(2)}(\Delta\mathbf{r}) = \frac{\sum_i \tilde{G}_i^{(2)}(\Delta\mathbf{r})}{\int (\sum_i \rho_i(\mathbf{r})) (\sum_i \rho_i(\mathbf{r} + \Delta\mathbf{r})) d\mathbf{r}} \quad (3.1.3)$$

We must note that this normalisation is insufficient. We must consider both the atom number fluctuations as well as the temperature distribution over which we average. The correlation amplitude goes as the square of the number of atoms N_i per time of flight. The prefactor α_i depends on the shape of the time-of-flight, and therefore on the temperature. The integrated pairs correlation amplitude is therefore provided by $\sum_i \tilde{G}_i^{(2)}(\mathbf{0}) = \sum_i \alpha_i N_i^2$, whereas the amplitude of the auto-correlation of the averaged time-of-flights is provided by $\int (\sum_i \rho_i(\mathbf{r}))^2 d\mathbf{r} = \alpha' (\sum_i N_i)^2$, where we consider α' as a function of all (α_i, N_i) couples. Finally:

$$\tilde{g}'^{(2)}(\mathbf{0}) = \frac{\sum_i \alpha_i N_i^2}{\alpha' (\sum_i N_i)^2} \quad (3.1.4)$$

The values N_i are known, and consequently the normalisation can be improved by multiplying with $(\sum_i N_i)^2 / \sum_i N_i^2$. The problem with the normalisation procedure lies in α' and the α_i distribution, that can not be accounted for. Taking correctly into consideration the atom number fluctuations, we managed to normalise the amplitude of $\tilde{g}'^{(2)}(\mathbf{0})$ to 0.97 instead of 1. The three remaining percent are due to the temperature distribution.

Consequently, as shown in Figure 3.4, also the temporal shape is not correctly normalised in its full extend, specifically at the lower temperatures. A mistake of a few percent characterises the temporal shape of the normalisation procedure. Consequently, a naive normalisation does not work out correctly. As the normalisation of the Bose-Einstein condensates will show even more difficulties, a different method is necessary.

As adjustments were to be made, we decided to simplify the normalisation procedure meanwhile. The function we use for the normalisation of $\tilde{G}^{(2)}(\Delta t)$ is limited to the auto-correlation of the averaged time-of-flight only with $(\Delta x, \Delta y) = (0, 0)$. This result is obtained by averaging the auto-correlation calculated for each temporal column of the averaged 3-dimensional time-of-flight. We consequently obtain a 1-dimensional function that will have to normalise a 3-dimensional pairs correlation histogram. Each temporal column of this pairs correlation histogram is then divided by this function. We thus perform only a temporal normalisation.

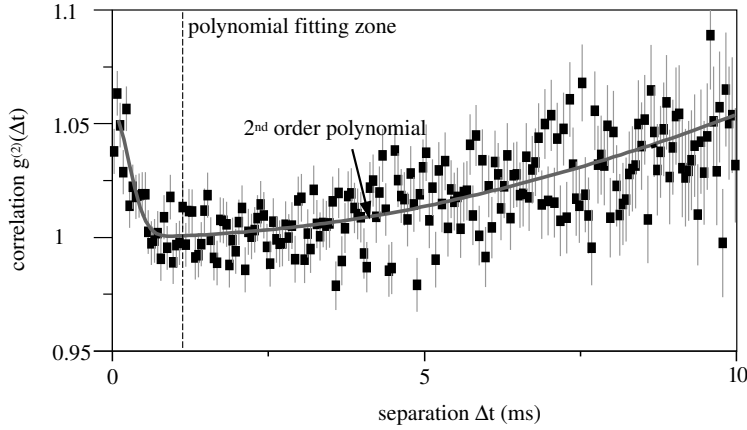


Figure 3.4: The normalised correlation function for the $0.61 \mu\text{K}$ clouds plotted versus Δt . The fact that the correlation function is not fully flat results from an imperfect normalisation procedure. This can not deal with the temperature distribution of the time-of-flights. For the fitting procedure, this fluctuation is taken into account through a second order polynomial fit.

We then use a second degree polynomial to fit the naively normalised correlation column. The first order of the polynomial is fixed to zero in order to preserve the symmetry of the correlation. We consequently fit the amplitude of $\tilde{g}^{(2)}(\Delta t = 0)$ with the zero order, and its curvature through the second order. In this fit the coherence zone is excluded, as we do not want to normalise the bunching amplitude. The constant coefficient obtained from the fit for each temporal column is used to divide that specific column. Consequently, in the absence of a quantum bunching behaviour, the correlation at $\Delta t = 0$ is fit to 1. The dark gray curve in Figure 3.4, for Δt larger then 1 ms, is an example of a fitted polynomial. Its value at $\Delta t = 0$ is necessarily 1 due to the division of the correlation by its zero order.

Several objections can be raised by this method. The fact that the density auto-correlation at $(\Delta x, \Delta y) = (0, 0)$ has been used to normalise the pairs correlation with $(\Delta x, \Delta y) \neq (0, 0)$ seems problematic. However even at the lowest temperatures, the root-mean-square size of the atomic cloud is several centimetres large, whereas the interesting coherence zone amounts to a maximum of millimetres. Consequently the correlation function does not evolve a lot within the study area. Furthermore, the temporal dependence of the gaussian time-of-flight is independent of x and y . Therefore the temporal dependence for all the auto-correlation functions with $(\Delta x, \Delta y) \neq (0, 0)$, within the study area, are identical. Using the same function for the normalisation procedure makes no theoretical difference.

A more important objection is the induced systematic error. If the same correlation function is used to normalise all the temporal correlation columns, then a noise fluctuation in this normalising auto-correlation function induces a systematic error in each column measurement. Although this is true, we can notice that the error bars on this auto-correlation function are orders of magnitude smaller then those of the pairs correlation histogram. If we consider n time-of-flights with on average N atoms in each time-of-flight, the signal to noise ratio comparison can be written as $\frac{SNR_{auto-correlation}}{SNR_{pairs\ histogram}} = \frac{1/\sqrt{(\sum N_i)^2}}{1/\sqrt{\sum N_i^2}} = \frac{\sqrt{n}N}{nN} = \frac{1}{\sqrt{n}}$. In the typical case of 1000

time-of-flights, this amounts $1/30$. In order for this procedure to introduce a significant systematic error in the results, we would need an anomaly of 30 standard deviations off. Such an occurrence is very unlikely.

3.1.3 The Results

The normalised pairs correlation function shows, as we have just seen in Figure 3.4, an increased signal for small time separations that could be attributed to the quantum Hanbury Brown and Twiss effect. In order to prove that this is indeed the case, we will prove first that the signal is not produced by some characteristics of the detector. Then we will study this temporal correlation for various temperatures, and show that it behaves as expected. We will study the spatial dependence of the observed bunching and see how this agrees with the theory.

3.1.3.1 Reference Data

The bunching we observe in Figure 3.4 has a typical temporal dependence of $200 \mu\text{s}$. Most typical time constants involved in the detection process are far shorter. The electronics related to the delay-lines have typical time constants of less than 300 ns (see paragraph 2.3.1.1 and 2.3.2.2). It seems unlikely that those electronics induce such long signal correlation. The only device that is expected to have comparable time scale behaviours is the micro-channel plate stack (see paragraph 2.2.1.4). We have dealt with the saturation of those devices. Yet the correlation expected from a saturating appliance would rather be an anti-correlation. Consequently it seems very unlikely that the observed phenomena can be attributed to any technical issue.

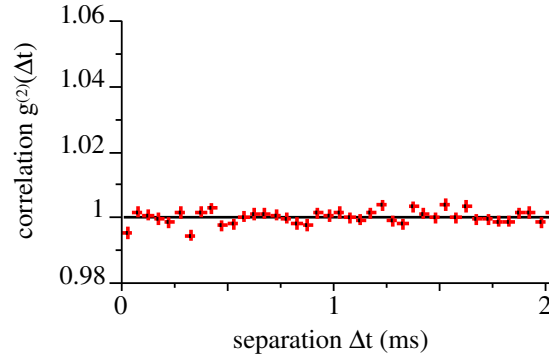


Figure 3.5: The temporal correlation function of the 1 mK clouds. The expected bunching height is, considering the detector resolution, far below noise. Therefore this correlation function is expected flat. The fact that it is indeed, show that the previously shown bunching is not related to any technical noise.

In order to be sure about this, we analyse the series of thermal clouds at milli-Kelvin temperatures. At the temperature, the cloud after expansion is much larger than the detector. Also the time-of-flight distribution is several hundreds of milliseconds large rather than the typical 10 ms for the micro-Kelvin temperatures. Figure 3.5 shows the temporal correlation of those hot clouds integrated over the same coherence area as earlier. This correlation has been fitted and normalised

with a simple constant. The time constants at which the time-of-flights at those temperatures evolve are indeed much longer than the observation time scale, and consequently the correlation seems flat.

More important, we do not observe any correlation or anti-correlation signal at the same time scale as before. This is an important prove that the previously observed bunching is the result of a physical process rather than a technical.

3.1.3.2 Temporal Correlation

The temporal normalised correlation functions for the three cold thermal sets have been plotted in Figure 3.6. In those graphs, the time dependence has been replaced by the previously discussed spatial dependence. The short time during which the cloud is effectively detected compares small to the average time-of-flight of $t_0 = 308.3\text{ms}$. This makes this flux detection nearly equivalent to a local 3-Dimensional picture. We therefore simply replace the arrival times of the particles through the simple operation $z \rightarrow (t - t_0)v_0$, where $v_0 = gt_0 \simeq 3\text{ m/s}$ is the mean arrival speed. Furthermore, the error-bars displayed are simply the square root of the number of pairs in each $50\text{ }\mu\text{s}$ bin.

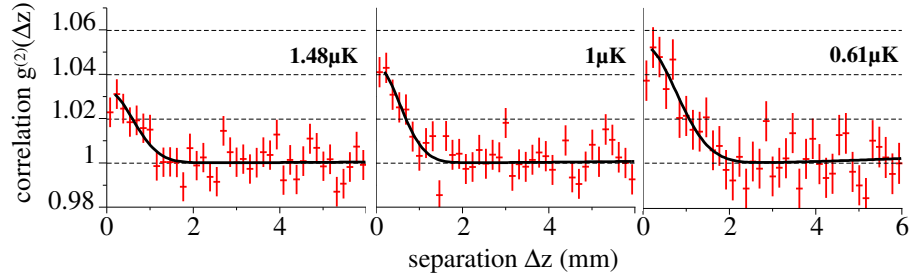


Figure 3.6: The correlation functions of the various cold samples along the z axis. The correlations have been averaged over a coherence area detailed in Figure 3.8. The observed bunchings for small separations correspond to the Hanbury Brown and Twiss effect. The black curves are the result of a Gaussian fit of the bunchings. We note that, as expected, both the bunching heights and sizes increase inversely with the temperature.

We observe a positive bunching of the ^4He for the three temperatures. Furthermore we observe that the width of this bunching increases as the temperature decreases. This behaviour is expected as at lower temperatures the initial source cloud is smaller (see paragraph 1.3.2.3). As with the cooling all correlation lengths increase in comparison to the resolution of the detector, this has as a direct result the increase of the bunching height (see paragraph 1.3.3.1). This bunching height increase is easily spotted in the graphs as well. The signal hence behaves as expected for the Hanbury Brown and Twiss effect.

3.1.3.3 Spatial Correlation

The three dimensions of the correlations are identical from the physical point of view. Yet the use of a detector with different effective spatial resolutions along the 3 axis, combined with the anisotropy of the initial cloud, results in various qualities of the rendering of the bunching along the 3 axis. The extremely well

defined temporal (z) resolution makes that dimension privileged for a quantitative analysis of the bunching properties. In particular, the fits of Figure 3.6 give a fairly well defined value of l_z . But this figure has been obtained by averaging over several couples of $(\Delta X, \Delta Y)$ already. For a single couple of $(\Delta X, \Delta Y)$, the signal to noise ratio is 3 times lower. Once we have determined the experimental value of l_z , we can then use this value to fit just the height of the bunching along the z axis for each single $(\Delta X, \Delta Y)$. The results of those fits have been plotted versus $(\Delta X, \Delta Y)$ in Figure 3.7.

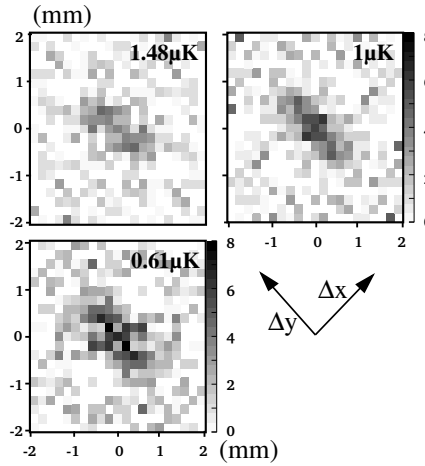


Figure 3.7: The spatial correlation functions of the various cold samples. Those histograms result from a temporal fit of the 3-dimensional normalised correlation histogram at variable spatial separations, with only the bunching height as a free parameter. The observed spatial buncings are inversely anisotropic in respect to the trapped cloud sizes. The bunching width is limited by the resolution of the detector, that also lowers the bunching height. The 50° angle in respect to the axis of the detector is because the detector is rotated with precisely that angle.

In order to understand the shape of the observed bunching, we first note that the magnetic trapping properties induce a cigar-shaped trapped cold cloud. As the correlation lengths after expansion of the clouds are inversely proportional to the cloud size (see paragraph 1.3.2.3), we expect the correlation volume to be pancake-shaped. Once projected on the detector, that leaves another cigar shape. The axis of the magnetic trap have an angle of 50° with those of the delay-lines, and consequently the cigar-shaped bunching should appear rotated in respect to the axis of the detector.

If we observe the figure, this is indeed what we see. Furthermore, the bunching seems to be both higher and larger at lower temperatures, just like we stated in paragraph 1.3.3.1. The cigar shape of the coherence area does not respect the aspect ratio of 20 of the trapped cloud. This problem is related to the limiting resolution of the detector, and is precisely the reason why we do not observe a bunching height of 1. This also means that the observed bunching width along the x axis should barely change with the temperature.

The view of this Figure 3.7 makes it possible now to understand over which coherence area the previously shown time correlations have been averaged. We stated previously that the temporal pair correlation displayed had been averaged

over a certain number of couples $(\Delta X, \Delta Y)$ in order to increase the signal to noise ratio. The couples effectively used are displayed in Figure 3.8. In comparison to

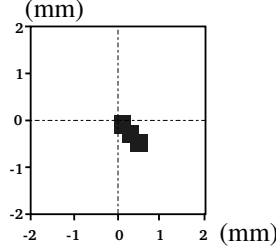


Figure 3.8: The black area correspond to the coherence area over which all the temporal correlation signals have been averaged. The anisotropy of this area is to adapt it to the effective anisotropic coherence area. In total, 10 spatial separations are used, increasing by $\sqrt{10}$ the signal to noise ratio in the various curves. They correspond to the couples $(\Delta X, \Delta Y) \in \{(0,0), (1,0), (0,-1), (1,-1), (2,-1), (1,-2), (2,-2), (3,-2), (2,-3), (3,-3)\}$.

Figure 3.7, we note that all those pixels have been chosen within the anisotropy of the bunching. The total noise evolves with the square root of the number of pixels, whereas the signal increases as a linear addition of the bunching signal for each couple $(\Delta X, \Delta Y)$. As long as the correlation pixels averaged are chosen near the centre of the bunching, the averaging increases the signal to noise ratio. When the additional contribution to the quantum bunching is smaller than the additional contribution to the noise, the averaging over the additional pixels decreases the signal to noise ratio. Consequently, as soon as the correlation pixels are chosen too far from the centre, where the bunching signal is smaller, the signal to noise ratio decreases. We note that in all cases the observed bunching height is decreased through this averaging procedure. Consequently, the real bunching heights measured are not those displayed in Figure 3.6. The heights can only be extracted from an appropriate fit of the XY -correlation.

3.1.4 Measurements

The expected bunching height we have mentioned in Chapter 1 has been calculated considering a resolution that is both homogeneous and gaussian. In Chapter 2 we have seen that although the resolution function can be well approximated with a gaussian, it is not. The error on the area made by the gaussian fit approximation is 13%, and this error affects the bunching height in at least an equivalent amount.

In order to make some meaningful measurements on the data, we will measure correctly the normalised resolution function of the detector. We will then see how this resolution function affects the bunching. Then we will perform some measurements and discuss the results.

Note that the following analysis has not been performed identically in [17]. In that article we had a simpler approach, that provides similar results though. Also the quantity of data used here is 30% larger than presented in [17].

3.1.4.1 The Resolution Functions

In the previous Chapter we have seen that the resolution depends on the position as much as on flux characteristics. The real resolution that influences our Hanbury Brown and Twiss measurement is therefore not the average resolution of the detector surface, as we have studied previously, yet rather the average resolution over our cold time-of-flights. Officially, even this is insufficient though. The correlation procedure is not sensitive to the average resolution weighted with the density, yet rather to the average resolution weighted with the density squared. We can obtain this distribution relatively easily. We correlate the atoms, and if two atoms are situated in a small correlation volume, their respective time sum are added to the squared density time sum distribution.

Futhermore, the use of a gaussian function to fit the resolution is inappropriate. The use of such a fit leaves out up to 13% of the Time Sum distribution area. Those 13% are concentrated in the wings of the Time Sum distribution, that due to their large extend, lower the measured bunching height. If we simply use the fitted gaussian as the resolution function, we will overestimate the expected bunching by 13%. We therefore require a more accurate analytical description of the experimental resolution distribution. As gaussians are convenient to our theoretical description, we decided to use the sum of three gaussians:

$$f_{resol}(\Delta x) = \frac{1}{\sum_{i=1,2,3} \sqrt{2\pi} A_i \sigma_i} \sum_{i=1,2,3} A_i e^{-\frac{\Delta x^2}{2\sigma_i^2}} \quad (3.1.5)$$

Note that this is the two-particle resolution function. Futhermore, the use of Δx as a variable should not hide the identical role of both the y and x dimension in this measurement. We proceeded to the fit by fitting the wings with the first gaussian of amplitude A_3 and root-mean-square width σ_3 . We fix those parameters in a second fit in which we add the second gaussian of free parameters A_2 and σ_2 , and we also fit a more central part of the distribution. Finally we add the third gaussian with parameters A_1 and σ_1 , fix the parameters of the other two gaussians, and fit the entire distribution. Figure 3.9 shows the normalised Time Sum distribution for the time-of-flights at $0.61 \mu\text{K}$ fitted with the three gaussian sum.

The fitted values we obtain at $0.61 \mu\text{K}$ are respectively $A_1 = 0.79$, $A_2 = 0.198$ and $A_3 = 0.014$ for the amplitudes, and $\sigma_1 = 278 \mu\text{m}$, $\sigma_2 = 576 \mu\text{m}$ and $\sigma_3 = 1178 \mu\text{m}$ for the standard deviations. At $1 \mu\text{K}$, the resolution is measured to $A_1 = 0.82$, $A_2 = 0.164$ and $A_3 = 0.017$ for the amplitudes, and $\sigma_1 = 265 \mu\text{m}$, $\sigma_2 = 578 \mu\text{m}$ and $\sigma_3 = 1121 \mu\text{m}$ for the standard deviations. Finally, at $1.48 \mu\text{K}$ the resolution is described by $A_1 = 0.95$, $A_2 = 0.05$ with $\sigma_1 = 255 \mu\text{m}$ and $\sigma_2 = 706 \mu\text{m}$ (A_3 is negligible). It seems from this measurement that the hotter clouds show better resolutions, as the local particle flux was lower.

The correctness of the Time Sum procedure is not yet demonstrated. We have established in Appendix 1, that this measurement is at best equivalent to the resolution measurement. But we do not really measure the resolution. We will therefore introduce an adjustment parameter γ , that scales all the standard deviations $\sigma'_i = \gamma \sigma_i$. As long as $\gamma \simeq 1$, the final measured time sum function should not be too far from the real double atom resolution function. The measurement of this parameter will give us also a final indication as to the validity of the Time Sum method.

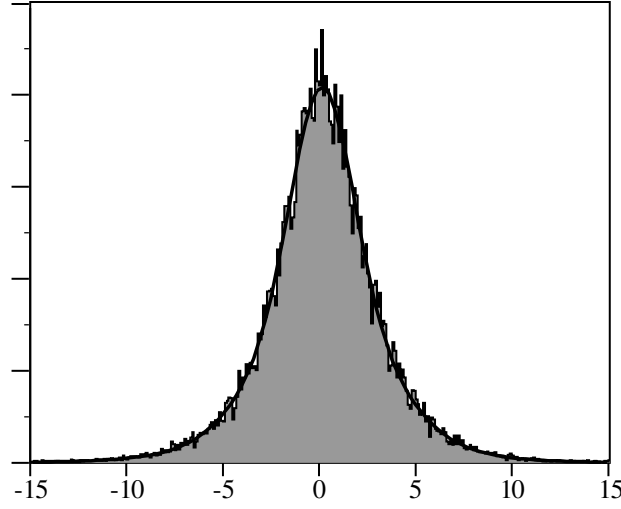


Figure 3.9: The correlated Time Sum distribution for the clouds at $0.61\mu\text{K}$. The measurement of this distribution through a three gaussian sum is relevant for the use in the spatial fitting procedure. Equivalent distributions are produced and fitted for the other two temperature samples.

The measured correlation is the convolution between $\tilde{g}^{(2)}$ and the two atom resolution function:

$$\begin{aligned} \tilde{g}_{\text{expected}}^{(2)}(\Delta x, \Delta y, \Delta z) &= f_{\text{resol}} \otimes \tilde{g}^{(2)}(\Delta x, \Delta y, \Delta z) \\ &= 1 \pm \frac{1}{(\sum_{i=1,2,3} A_i \sigma_i')^2} e^{-\frac{\Delta z^2}{l_z^2}} \prod_{\alpha=x,y} \sum_{i=1,2,3} \frac{A_i \sigma_i l_\alpha}{\sqrt{2\sigma_i'^2 + l_\alpha^2}} e^{-\frac{\Delta \alpha^2}{2\sigma_i'^2 + l_\alpha^2}} \end{aligned} \quad (3.1.6)$$

We can now use this function to fit the various results. In particular we use the function:

$$b'_{\text{measured}}(\Delta z) = h' e^{-\frac{\Delta z^2}{l_z^2}} \quad (3.1.7)$$

as explained previously to fit the temporal axis. The value of h' obtained through this fit is not physically significant. As the histogram has been averaged over the coherence area for higher signal to noise ratio, the value of h' does not reflect directly the bunching height.

We fit the 2-dimensional histograms previously detailed through the function:

$$b_{\text{measured}}(\Delta x, \Delta y) = \frac{h}{(\sum_{i=1,2,3} A_i \sigma_i)^2} \sum_{i=1,2,3} A_i \sigma_i e^{-\frac{\Delta x^2}{2\gamma^2 \sigma_i^2}} \sum_{i=1,2,3} A_i \sigma_i e^{-\frac{\Delta y^2}{2\gamma^2 \sigma_i^2 + l_y^2}} \quad (3.1.8)$$

This function has as free parameters γ the resolution factor, l_y the correlation length along the y axis, and h the bunching height. The correlation length along the x axis is expected to be small compared to $\gamma \sigma_i$ and is therefore fixed to zero.

3.1.4.2 The Correlation Lengths

In Figure 3.10 we have plotted the results of the fit measurements. The first graph we will consider is in Figure 3.10C. In this graph we have plotted the results

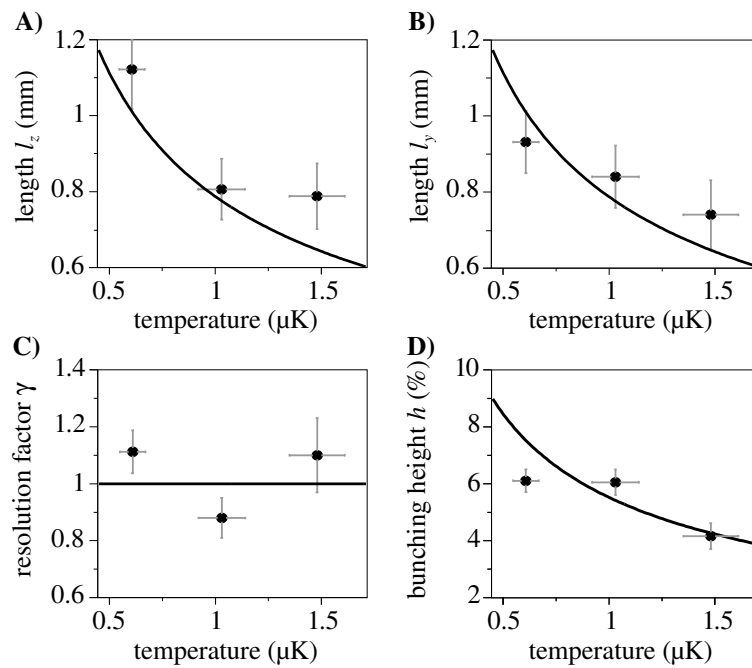


Figure 3.10: The results provided by the free parameters from the 1-dimensional, and 2-dimensional fitting procedures. The indicated error bars are the root-mean-square errors provided by the fitting procedure. In A is plotted the fitted correlation lengths along the z axis. In B is plotted the fitted correlation lengths along the y axis. In C is plotted the resolution factor that accounts for the eventual inadequacy between the resolution measurement by the Time Sum method, and the effective resolution influencing the bunching width. In D has been plotted the measured bunching heights. The theoretical curve has been chosen to correspond to the bunching height as resulting from the resolution functions measured for the 1 μ K sample.

of γ . This resolution factor emerges essentially from the x axis fitting of the 2-dimensional bunchings presented in Figure 3.6. They translate the ratio between the two particle resolution as measured on the bunching width, that is mainly determined by the resolution on the x axis, and the two particle resolution as measured through the Time Sum method. The black line represents the statistical average of those three measurements, and is equivalent to 1. This means that the Time Sum seems to present coherent results as to the resolution measurement, and confirms this method as an excellent tool for monitoring the resolution.

The next two graphs that deserve attention are in Figure 3.10A and 3.10B. In those graphs we have plotted respectively the fitted correlation length along the z and y axis. The former have been obtained on the data presented in Figure 3.6, whereas the latter have been obtained through the 2-dimensional fit. Note that the measurement of the latter also depends on the integration of the resolution function. The fact that the resolution factor provides us with satisfactory results gives us high confidence in those correlation length measurements. We can consequently conclude that the experimental measurements coincide within error bars with the theoretical black curves defined by $l_\alpha = \frac{\hbar\omega_\alpha t_0}{\sqrt{mk_B T}}$.

Finally we draw the attention to the graph presented in Figure 3.10D, that plots the 2-dimensional fitted bunching heights for the three temperatures. The black curve plotted is the theoretically expected bunching height considering the three gaussian resolution function as found for the 1.03 μK sample. Although the two higher temperature's bunching heights are in good agreement with the expectations, the 0.61 μK data point is several error bars off the theory. Although no proper study has been carried out yet in the full understanding of this phenomena, this could have to do with the interactions during the expansion of the cloud.

The results of nearly all these measurements have a strong relation with the resolution of the detector. We can avoid this dependence if we measure the bunching volume.

3.1.4.3 The Bunching Volume

The measured correlation bunching results from the convolution of the Hanbury Brown and Twiss effect and the resolution functions. This convolution strongly changes both the measured correlation lengths as well as the bunching height. Yet as the resolution function is normalised, the volume of the initial bunching is conserved. A more physical way of saying so would be to consider that the finite resolution smears out the bunching over a larger area, but does not change the number of correlated atoms. Consequently the bunching volume is independent of the resolution. Only the signal to noise ratio of its measurement is affected by it.

The resolution on the experiment is not constant, as we have seen in the previous chapter. It depends for instance on the particle rate, local saturation processes and the spatial distribution of the atoms. Also the measurement method of the resolution is imperfect, and can induce errors in the interpretation of the results. The measurement of the bunching volume on the other side is independent of any experimental conditions, and does not depend on any resolution model.

The easiest way of measuring the correlation volume is by integrating the normalised correlation function over the coherence volume. The results of this procedure has been plotted in Figure 3.11. The black circles correspond to the integrated

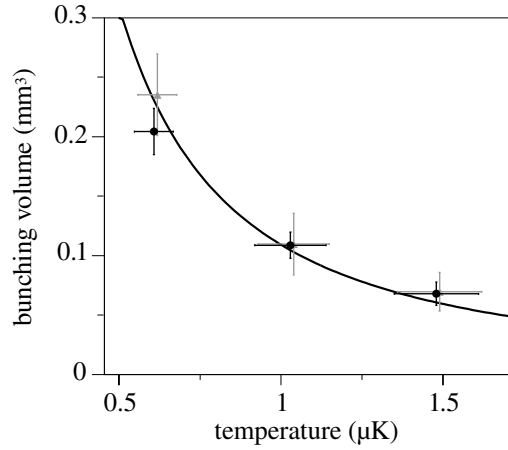


Figure 3.11: The measured correlation volumes. The black circles correspond to a basic integration of the bunching in the 3-dimensional normalised pairs histogram. The error bar correspond to the integrated error on those pairs. The gray triangles correspond to the integrated fitting functions, using the fitted parameters. The error bars result from a statistical sum of the error bars of those fitted parameters. The black curve corresponds to the resolution independent theory.

bunching signals. The measured signal to noise ratios are in increasing order of temperature respectively 10.3, 9.8 and 6.94.

The gray triangles correspond to the integration of the earlier defined fit function, introducing the fitted parameters displayed in Figures 3.10, as well as the earlier defined resolution parameters. We note that the results of this operation fit very well to the simply integrated results, except for the 0.61 μK sample. The error bars are higher as the error bars of the various used parameters were supposed independent. Through the use of a fit procedure, this is not true, and the gray error bars are consequently overestimated.

Finally the black curve corresponds to the theoretical formula:

$$V(T) = \sqrt{\pi}^3 l_x l_y l_z \quad (3.1.9)$$

We note that this volume does not depend on the resolution We note that the experimental results fit within the error bars to the theoretical values.

3.2 Bose-Einstein Condensate

We have just shown that the statistical disorder in a thermal gas induces quantum correlations, and that we are able to show them. In the case of a Bose-Einstein condensate, the situation is completely different. All the atoms have the same wave-function, and consequently have the same density and momentum distribution (if we do not consider interactions, else see [70]). A Bose-Einstein condensate is a coherent object, as all the atoms are in the same quantum state. This results not only in a completely different second-order correlation function, but also has an important impact on the way the experiment can be performed, and the interpretation that can be given to the results.

We will study briefly how the concept of the condensate influences the correlation measurement and we will have a look at the data we acquired. Then we will study the way we circumvented some technical difficulties raised by the acquisition of the Bose-Einstein condensate and we will finally discuss the results.

3.2.1 The Condensates

The properties during the expansion of a Bose-Einstein condensate are completely different from those of a thermal gas. We will discuss what those properties are, how they influenced the way we acquired the data, and finally how they lead to a saturation of the detector.

3.2.1.1 Finite Size

In a thermal gas, the kinetic energy is isotropically distributed through thermalisation. Even though the initial shape of the cloud can show a strong anisotropy due to an anisotropic trapping potential, the final density distribution of a thermal cloud after a long time-of-flight reflects the initial momentum distribution that is isotropic. For a Bose-Einstein condensate it is a different story.

As we have seen before, all atoms are in the fundamental eigen-state of the trapping potential. The associated eigen-state wave function inherits from the geometric properties of the trap, and the trapped Bose-Einstein condensate is cigar shaped. All the atoms have the same momentum distribution. When the atoms are released from the trap, they all leave with the same momentum distribution. The reason why they will not all hit the detector at the same time and position, is because this momentum distribution has a certain width defined by the initial confinement parameters. The higher the confinement, or trapping frequencies, the larger the momentum distribution. If the trapping potential is anisotropic, then so is the initial momentum distribution, and the cigar shaped cloud evolves into a pancake shape.

All the atoms remain in the phase-space cell defined by the initial cigar and the final pancake. This cell is elementary and therefore very small. What we are looking for are the correlations of the atoms within this single elementary phase-space cell. What we would like to demonstrate is the coherence of the atoms over the total limited size of the final condensate. This is intrinsically problematic as error-bars at the edge of the condensate diverge. We must state consequently that even in the best case scenario, the result of the second order correlation measurement of

the Bose-Einstein condensate in this time-of-flight scheme is intrinsically subject to debate.

We have not considered here the interactions between the atoms. These add an additional difficulty to the analysis.

3.2.1.2 Density and Interactions

The thermal clouds with which we have worked are nearly perfect gases. This means that the atom-atom interactions lead to thermalisation, but induce no macroscopic properties. This consideration is only true as long as the interaction energy $\frac{4\pi\hbar^2 a}{M}\rho^2$ (with a the scattering length, ρ the atomic density and M the atomic mass) is small compared to the thermal energy $k_B T$. The Bose-Einstein condensate corresponds to a macroscopic population of atoms in the most dense of all eigen-states, of ground state energy $3\hbar\bar{\omega}/2$, with $\bar{\omega}$ the mean trapping frequency. Depending on the number of atoms in this ground state, and thus on the density, the mean field effect of the atomic interactions can no longer be neglected.

This mean-field produces an equivalent pressure that compensates the trapping potential and goes as the square of the number of atoms in the Bose-Einstein condensate. This has as a direct consequence that the size of the Bose-Einstein condensate in the trap depends on its number of atoms. At switch off, during the first phase of the expansion of the Bose-Einstein condensate, the interactions can no longer be neglected and the mean-field energy is converted into kinetic energy. This energy conversion increases further the size of the Bose-Einstein condensate after expansion. Finally, the size of the Bose-Einstein condensate after expansion depends on the number of atoms, over which we have currently little experimental control.

This point is particularly problematic for the analysis. We discussed before that small fluctuations, not in the amplitude but the shape of the clouds, induce imperfections in the normalisation procedure. With the experimental atom fluctuations we have, it is extremely difficult to acquire a large number of time-of-flights that have the same characteristics. Consequently, besides the finite size restrictions, we have to deal with an imperfect normalisation procedure due to the cloud size distribution.

3.2.1.3 Saturation

As we just mentioned, the density of the Bose-Einstein condensate is an order of magnitude larger than the density in a thermal cloud. This is still true after expansion. This raises the problem of the local saturation of the micro-channel plate. We have seen in the previous chapter that the maximum local flow is 82 kcounts/cm²/s before saturation of the micro-channel plate. A condensate of typically 10 katoms produces atomic flows of typically 800 katoms/cm²/s. This amounts far above the detection possibilities. We will therefore expect a saturation of the detection, that affects the temporal signal severely. This will limit even more the analysis of the Bose-Einstein condensate as we will see a little further.

3.2.1.4 The Data

Bose-Einstein condensates do have some advantages however. The main advantage that we already have mentioned in the previous section is the influence of its characteristic shape on its detectability. If we produce a Bose-Einstein condensate with a small uncondensed thermal cloud, it is extremely easy to separate the condensed fraction from the thermal cloud. As the density of the Bose-Einstein condensate is much higher, we can in particular neglect the part of the thermal cloud that overlaps with the Bose-Einstein condensate. We therefore do not need to acquire pure Bose-Einstein condensates, and that was an experimental simplification.

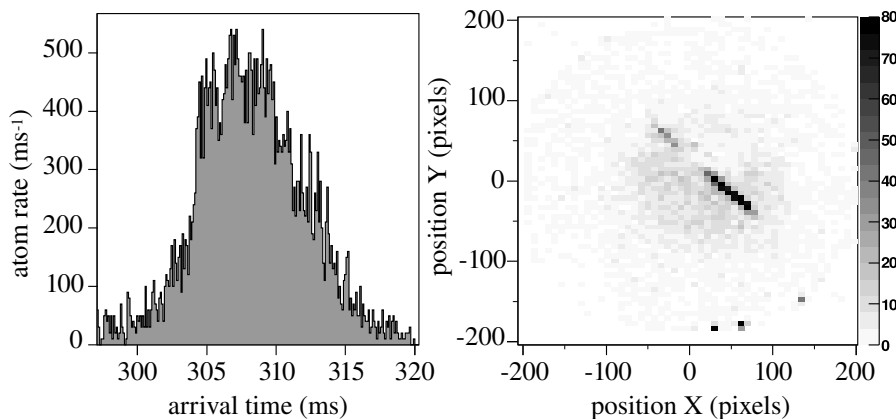


Figure 3.12: A typical cloud as acquired and used for the analysis of the Bose-Einstein condensate second order correlation. The left graph shows the arrival time distribution. The right image displays the image. We can distinguish clearly the dense regions corresponding to the Bose-Einstein condensate. We cut the data of the Bose-Einstein condensate out of the 3-dimensional picture. The much lower densities of the background thermal gas remaining inside the Bose-Einstein condensate region are negligible.

We acquired 1500 time-of-flights, some of which still had some noticeable thermal fraction. Figure 3.12 shows a typical time-of-flight as acquired in this process. Practically, we will use the 3-dimensional properties of the detector to extract only the Bose-Einstein condensate out of the time-of-flight for analysis.

3.2.2 The Analysis

Initially, the analysis performed on the Bose-Einstein condensates was identical to the analysis applied to the thermal bosons. The problem was the normalisation. A different strategy was to be followed. We will outline first the difficulties we encountered. Then we will discuss the solution we adopted.

3.2.2.1 Saturation

The analysis of the Bose-Einstein condensates suffers two major difficulties. On one hand we have the inhomogeneous detection efficiency, that shows a detectivity hole in the middle of the Bose-Einstein condensate. On the other hand we have the saturation of the micro-channel plate, that strongly deforms the temporal signal.

Figure 3.13 shows how strongly the time-of-flight of a Bose-Einstein condensate is affected by the two phenomena. In the left figure, we can see the image of a Bose-

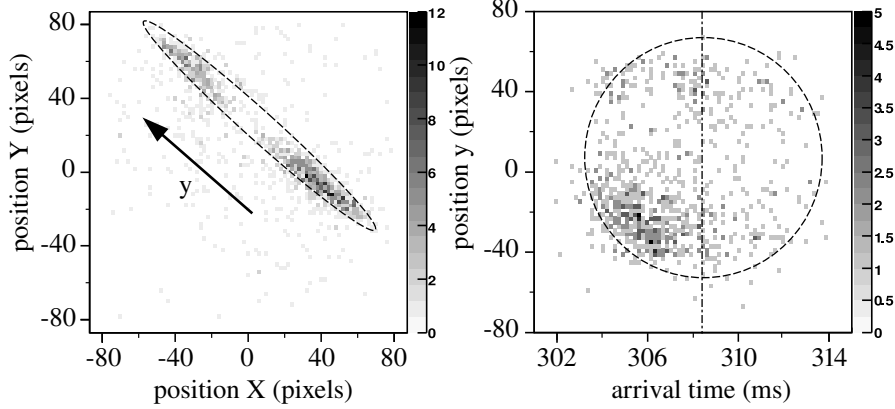


Figure 3.13: Another time-of-flight as acquired for the Bose-Einstein condensate correlation measurement. In the left graph, the image of the acquired Bose-Einstein condensate shows distinctly a hole in the middle of the cloud. The oval drawn corresponds to the shape the cloud is supposed to have. The right image displays the cloud density projected on the Oty plane. Along the y axis, we retrieve the detectivity hole of the detector. But along the t axis, the cloud also does not fill up the oval region that corresponds to the theoretical shape. This is due to the saturation of the detector. We can distinguish clearly that at the early arrival times, the atoms are detected. Then the electronic depletion of the micro-channel plate drastically reduces the detectivity, and the cloud is no longer symmetric with respect to the 308.3 ms arrival time.

Einstein condensate on the detector. Whereas the theoretical shape should have been oval like, the quantum gas seems to be separated in two parts. Eventually, one half seems far less intense than the other one. This results directly from the detectivity map shown in the previous chapter. Note that this effect is not specific to the Bose-Einstein condensates.

In the right figure has been plotted the long axis of the Bose-Einstein condensate versus the arrival times of the atoms. We distinguish clearly the arrival front of the cloud, yet after this arrival front the detector saturates. The root-mean-square time-width of the cloud is consequently in the order of some milliseconds. The average arrival time, in respect to the theoretical 308.3 ms, also evolves in the millisecond scale depending, on the position. The detected density distribution depends strongly on the number of atoms in the Bose-Einstein condensate. Consequently none of the detected Bose-Einstein condensates are alike and the normalisation procedure will fail as we will see.

3.2.2.2 Problematic Normalisation

In order to understand a little better why the normalisation procedure is to fail, we will study some of the correlation function properties. We will neglect any quantum statistical behaviour, and we will simply consider the normalisation procedure of the correlation of various density distributions. Those density distributions ρ have a spatial dependence essentially in y , a time dependence in t , and will also change with the realisation i . We can therefore write $\rho(y, t, i)$. If we write the averaging

procedure over the variable x of quantity $Q(x)$ as $\langle Q(x) \rangle_x$, we can note that for two independent variables x and y we have $\langle \langle Q(x, y) \rangle_x \rangle_y = \langle \langle Q(x, y) \rangle_y \rangle_x = \langle Q(x, y) \rangle_{x, y}$. The previously used normalisation procedure can then be considered proportional to:

$$\tilde{g}^{(2)}(\tau) \propto \frac{\langle \rho(y, t, i) \rho(y, t + \tau, i) \rangle_{y, t, i}}{\langle \rho(y, t, i) \rangle_i \langle \rho(y, t + \tau, i) \rangle_{i, y, t}} = \frac{n(\tau)}{d(\tau)} \quad (3.2.1)$$

If there is an inconsistency of the density distributions between the various realisations, this normalisation fails. As the correlation will be performed on the temporal variable, we can expect different influences of the temporal and spatial fluctuations of the densities on the normalisation. Let us consider a simple model of our Bose-Einstein condensates samples, that will bring understanding of the various cloud characteristics that influence this normalisation.

We will consider each Bose-Einstein condensate density distribution as some simple statistical sample, in such way that $n(\tau)$ and $d(\tau)$ are two gaussian distributions. If they have respectively as width σ_n and σ_d , then we can approximately express the half-width half-maximum of the correlation function σ_g as:

$$\sigma_g = \frac{\sigma_n}{\sqrt{1 - \sigma_n^2 / \sigma_d^2}} \quad (3.2.2)$$

In the ideal situation, the normalised correlation function should be flat, and therefore the half-width half-maximum be infinite. This corresponds of course to $\sigma_n = \sigma_d$. We will now extract from the individual cloud properties the expressions of σ_n and σ_d , and see that they are not equal for our Bose-Einstein condensates.

For each cloud realisation we will define the average arrival time $T(y, i) = \frac{\langle t \rho(y, t, i) \rangle_t}{\langle \rho(y, t, i) \rangle_t}$ that has as standard deviations $\sigma_T^i(y)$ and $\sigma_T^y(i)$. The latter is to be distinguished from the cloud's temporal width $s_t(y, i)$, that has as a standard deviations $\sigma_{s_t}^i(y)$ and $\sigma_{s_t}^y(i)$.

The width of the correlation $\langle \rho(y, t, i) \rho(y, t + \tau, i) \rangle_t$ is $\sqrt{2} s_t(y, i)$. Once averaged over position and realisations, this amounts up to $\sigma_n = \sqrt{2} \sqrt{s_t^2 + (\sigma_{s_t}^i)^2 + (\sigma_{s_t}^y)^2}$. On the other hand $\langle \rho(y, t, i) \rangle_i$ has a width of $\sqrt{s_t^2 + (\sigma_T^i)^2}$. This multiplies with $\sqrt{2}$ once correlated and finally $\sigma_d = \sqrt{2} \sqrt{s_t^2 + (\sigma_T^i)^2 + (\sigma_{s_t}^i)^2 + (\sigma_{s_t}^y)^2}$. Note that we do not retrieve σ_T^y in the latter width, that shows that only the differences between the realisations have an impact. The difference lies solely in the term $(\sigma_T^i)^2$, that should compare small to the others if we want the normalisation to be successful. This means that the average arrival time, as a function of y , should not vary between the various realisations.

If we analyse the data in order to extract some typical values, we obtain a typical cloud width of $s_t(y, i) = 1.32$ ms with $\sqrt{(\sigma_{s_t}^i)^2 + (\sigma_{s_t}^y)^2} = 0.54$ ms. Yet on the other hand we have an arrival time distribution width of $\sigma_T^i = 1.66$ ms. Consequently the expected half-width half-maximum for the normalised correlation function is as low as 2.7 ms. Previously we have studied a thermal bunching of 5% over 200 μ s. For the Bose-Einstein condensate we will see a 50% evolution over 2.7 ms of the correlation function even without any quantum behaviours. This means that the fluctuations of the normalised correlation function for the Bose-Einstein condensates due to the imperfect normalisation procedure are as large as

the quantum bunching we have been observing. Under those circumstances, it is impossible to show that the Bose-Einstein condensate does not show a bunching effect, as we will not be able to distinguish the normalisation error from the eventual bunching signal.

3.2.2.3 Solution

The solution lies for sure in the annihilation of σ_T^i . This can be done fairly easily as illustrated in Figure 3.14. For each Bose-Einstein condensate, projected as earlier on the y axis, we only consider the part of the Bose-Einstein condensate with $y > -5$ pixels. This is to get rid of the problems induced by the detectivity hole. We simply keep the larger part of the signal. We then cut the cloud between $y = -5$ pixels and $y = 80$ pixels into 8 slices. For each slice we determine the average arrival time $T(y, i)$, as well as the root-mean-square cloud width $s_t(y, i)$. We can then fit $T(y, i)$ in function of y with a second order polynomial as shown in the left graphs of Figure 3.14. In those graphs have been displayed the density distributions $\rho(y, t)$ for three different realisations. The centres of the dark-gray crosses indicate the average arrival times measured in function of y , the vertical length of the cross indicates the error-bars. This error-bar is taken into account during the fitting of the black lined polynomial.

The polynomial value with corresponding y is subtracted for each atom from its temporal coordinate, and 307 ms is added. The time-of-flights hence obtained have been displayed in the right graphs. Consequently $T(y, i)$ is the same for any y and i , and $\sigma_T^i = 0$ ms. The normalisation should perform much better.

We still have to debate the relevance of this method though. Although we merely focus on the temporal correlation behaviour of the Bose-Einstein condensate time-of-flights, and that a temporal translation does not affect the correlation, we will average over the same coherence area as previously. This induces an average temporal shift over the coherence area of $T_s = 140 \mu s$. This value has been obtained by averaging over all the time-of-flights, and by averaging over the entire condensate. If some quantum phenomena produces a temporal correlation that has a typical time scale small compared to this time shift, then the shift will smear out the correlation. If the correlation is much longer then the time shift will have little effect.

If we consider that the eventual correlation is gaussian along the time axis t , with a correlation length l_t , and is constant over the coherence area, then the dimming effect of the time shift $d(l_t)$ can be simply expressed by:

$$d(l_t) = \frac{l_t \sqrt{\pi}}{T_s} \operatorname{erf} \left(\frac{T_s}{2l_t} \right) \quad (3.2.3)$$

In Figure 3.15 we have plotted the attenuation factor due to the time shifts as expected for a gaussian temporal bunching. We have plotted the graph in the spatial coordinate z in order to be consistent with previous calculations. We note that as long as the eventual correlation length is larger then $200 \mu m$, the bunching should remain visible. Considering that at $0.5 \mu K$, the z axial correlation length for a thermal gas is 1 mm, this shifting operation seems reasonable.

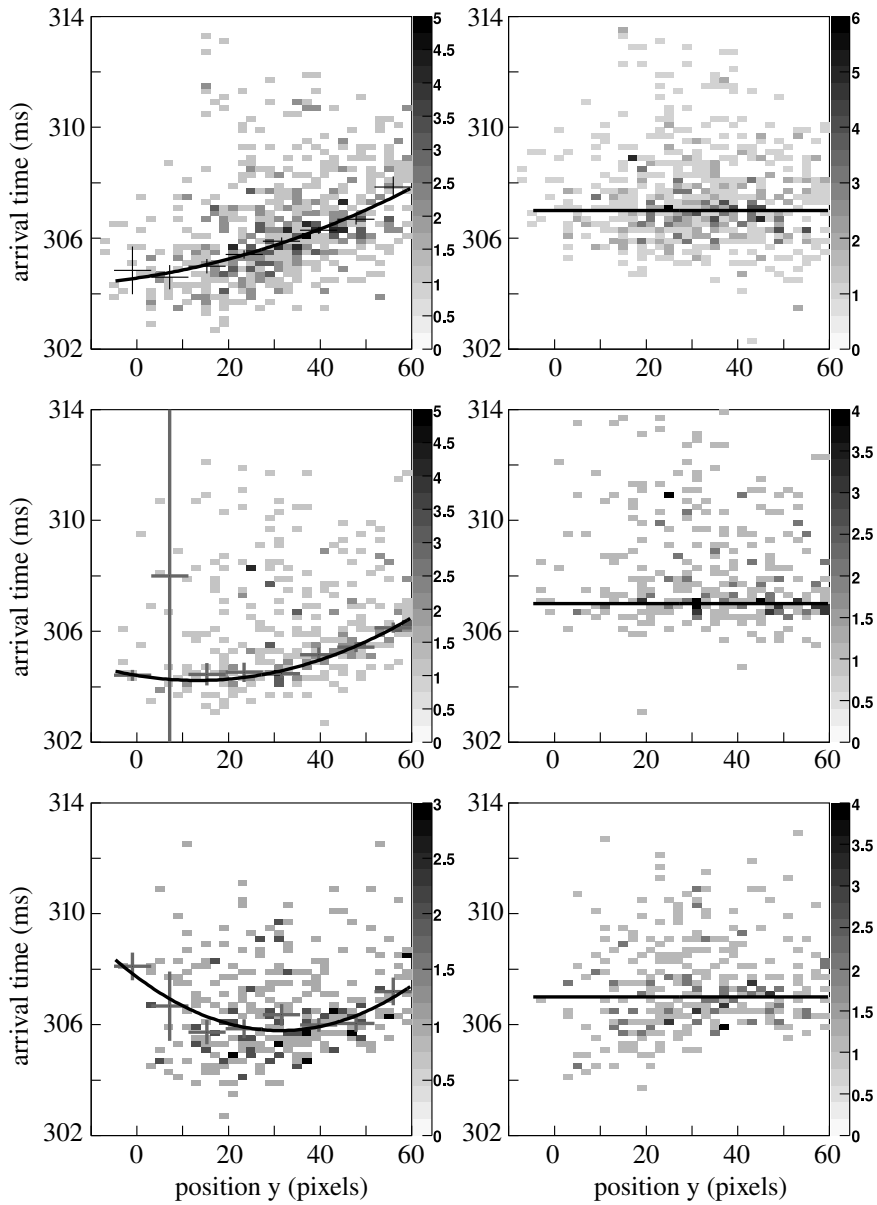


Figure 3.14: The left graphs show the density distributions projected onto the Oyt plane of three different Bose-Einstein condensates. For each time-of-flight, the average arrival time as a function of y is fitted through a second order polynomial. The arrival times of the atoms are then shifted as a function of y , in such manner that it straightens the fitted polynomial. The density distributions resulting from this procedure have been displayed in the right graphs.

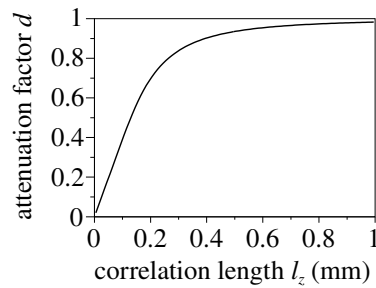


Figure 3.15: This curve indicates the eventual additional bunching reduction that has to be considered due to the time shift procedure. It shows that despite the procedure, we could still easily detect correlation lengths along the z axis above $200 \mu\text{m}$.

3.2.3 The Result

In Figure 3.16 we have plotted the result of the temporal correlation function. We

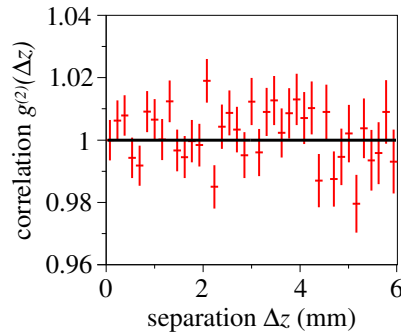


Figure 3.16: The result of the second order correlation measurement along the z axis for a sample of 1500 Bose-Einstein condensates. The function remains effectively flat up to 10 mm before the limitations of the analysis procedure induce uncontrolled fluctuations.

see that the correlation function is flat up to 6 mm. Actually, the correlation remains flat up to 10 mm after which we reach the limits of this analysis. That means that we cannot study the coherence of the condensate above those correlation lengths. In this sense the work performed by [31] is very complementary, even though they consider quite different temporal correlations. Their methods allow for a study of the coherence properties over much longer time scales. The use of a radio-frequency outcoupler makes it possible to get beyond the finite size limit we have necessarily in this time-of-flight method. On the other hand, we have been able to show that the condensate shows no correlations within the typical thermal bounds.

3.3 Thermal Cloud of Fermionic Atoms

Early 2006, the group of Atomic Physics of the Vrije Universiteit obtained, through the leading of W. Vassen, the first degenerate Bose-Fermi mixture of metastable atoms. With our recent success of the measurement of the Hanbury Brown and Twiss effect on ^4He , this was an excellent opportunity to measure the Hanbury Brown and Twiss for the fermionic ^3He . Although the Amsterdam setup has never been specifically designed to receive a detector as large as our delay-line detector, it happens that there was just the space to add the detector. This led to a our fruitfull collaboration.

We will discuss first of all how this collaboration has worked out effectively, and brought to the acquisition of the data. Then we will briefly discuss the results of the acquisition. Finally we will study the measurements we have been able to perform.

3.3.1 The Acquisition

The acquisition of the fermionic data has taken place in Amsterdam. Consequently the experimental setup required some preparation in order for the detector to fit. We will oversee briefly how we have prepared this collaboration. Then we will detail some characteristics of the experimental setup in Amsterdam, and in the way they differ from the Orsay setup. Then we will study briefly the data we acquired.

3.3.1.1 Preparation

In order to implement the detector to the setup, it required a new vacuum chamber. The chamber that is currently used in Orsay did not fit in the mechanical support of the Amsterdam ^3He experiment. We therefore designed a new chamber that would receive a turbo-pump as well as an ion pressure gauge.

The Amsterdam team installed a vacuum valve at the lower part of their setup, to which the detector chamber would be attached. The use of the valve would simplify greatly the installation as no baking of the upper chamber would be necessary. Only the detector chamber would require some minimal baking. The pressure in this lower chamber could have some defects as the pumped chamber was also separated from the trapping chamber by two additional turbo-pumps. We could consequently open up the detector chamber after only 3 days of baking at some 100°C .

We had moved the detector by truck from Orsay, as well as some electronic equipment. The latter included all the necessary electronics for the detection scheme: constant fraction discriminator, voltage supplies, time-to-digital converters, acquisition computer. The time-to-digital converter and the computer were synchronised to the driving system of the Amsterdam ^3He experiment. The acquired data was send to the server in Orsay for analysis. At that point, besides some severe background noise on the micro-channel plate, the detector was ready for acquisition.

3.3.1.2 The Experimental Setup

The Amsterdam ^3He experiment experiment has many similarities to the Orsay ^4He experiment. Only the technical implementations differ. We will see in a first

time the fundamental consequences of working with the isotope mixture. Then we will discuss some particularities of the Dutch time-of-flight in terms of magnetic fields, and we will address some additional technical instabilities.

The Isotope Separation The ${}^3\text{He}$ is cooled sympathetically by the ${}^4\text{He}$, yet we only want to observe the ${}^3\text{He}$. The micro-channel plate based detector does not distinguish the two species, and therefore we need to clean the mixture from the ${}^4\text{He}$ before we let it drop. Let us consider some of the trapping properties of the two species.

The Landé factor for the employed $2^3S_1 |1, +1\rangle$ ${}^4\text{He}$ state is $g_J = g_S \simeq 2.002$. The Landé factor for the trapped $2^3S_1 |3/2, +3/2\rangle$ ${}^3\text{He}$ state is $g_F = \frac{2}{3}g_S + \frac{1}{3}g_I \simeq 1.335$. This has as a consequence that the magnetic potentials seen by the two atoms, provided respectively by $\mu_B g_J m_J B$ and $\mu_B g_F m_F B$, are identical. They do not have the same mass though, and consequently the trapping frequencies of the ${}^3\text{He}$ atoms are $\sqrt{4/3}$ times larger than those of ${}^4\text{He}$, and the fermions are more confined. On the other hand, the two isotopes have the same temperature in the mixture, and consequently the velocity of the ${}^3\text{He}$ atoms also scales $\sqrt{4/3}$ times larger. Finally, at high temperature, both end up with the same density distribution.

Although at first sight the magnetic and kinetic properties of the two isotopes seem alike, we can still use a simple radio-frequency knife in order to extract the ${}^4\text{He}$ from the mixture only. The radio-frequency ramp couples the magnetic sub-states of the atoms. Hence the ${}^4\text{He}$ is transferred from the trapped state $|1, +1\rangle$ to the non-trapped $|1, 0\rangle$ state. The ${}^3\text{He}$ is transferred from the trapped $|3/2, +3/2\rangle$ state, to the also trapped $|3/2, +1/2\rangle$ state. This state switches to the non-trapped $|3/2, -1/2\rangle$ state. The energy quanta associated to those two transitions are respectively $h\nu_4 = \mu_B g_J (1 - 0)B$ and $h\nu_3 = \mu_B g_F (3/2 - 1/2)B$. The ratio consequently amounts to $\nu_3/\nu_4 = g_F/g_J \simeq 0.667$. This induces that during the radio-frequency evaporation ramp, essentially the ${}^4\text{He}$ atoms get coupled, as the ${}^3\text{He}$ atoms get cooled down sympathetically by the bosons before the radio-frequency knife can reach the fermionic population. The loading of the magnetic trap therefore requires significantly more bosons than fermions.

In particular, at the centre of the trap, the magnetic field is non-zero as that would induce spin flip losses. The magnetic bias field we worked with in Amsterdam was 0.75 G, inducing centre trap coupling frequencies of respectively $\nu_4 = 2.1$ MHz and $\nu_3 = 1.4$ MHz for ${}^4\text{He}$ and ${}^3\text{He}$. Using a radio-frequency ramp that goes down to ν_4 ensures consequently the complete depletion of bosonic helium atoms in the trap. The fact that the frequency difference $\nu_4 - \nu_3 = 0.6$ MHz is much larger than $k_B T/h \sim 21$ kHz at the temperatures we work ensures us that the fermionic thermal distribution is not affected by the radio-frequency ramp. Figure 3.17 illustrates this.

Practically the last radio-frequency ramp goes down from 3 MHz to 2 MHz, cooling down the mixture to micro-Kelvin temperatures as well as depleting the ${}^4\text{He}$ atoms. The fact that those two operations are performed by a single ramp implies that the mixture is not at thermal equilibrium at the end of the ramp. In particular, once the ${}^4\text{He}$ has left the trap, there is no reason for the cold ${}^3\text{He}$ gas to thermalise, as elastic collisions are forbidden. This means that we are not quite in the theoretical situation we have described previously. We do not expect though to measure any difference with the current signal to noise ratio.

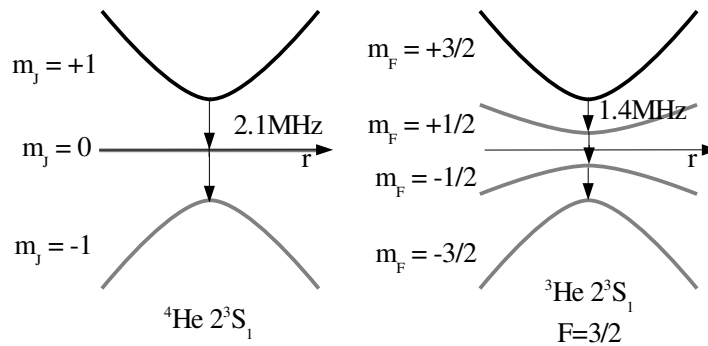


Figure 3.17: The splitting of the various magnetic substates of ${}^4\text{He}^*$ and ${}^3\text{He}^*$ in a harmonic magnetic field with an additional bias field. In the experimental conditions, a 0.75 G bias field produces a 2.1 MHz energy shift between the bosonic substates, whereas only a 1.4 MHz shift between the fermionic substates. This makes it possible to empty the magnetic trap of the bosons through the use of a radio-frequency ramp, without affecting the fermionic population.

Switch Off Unlike the Orsay ${}^4\text{He}$ experiment we do not detect a magnetic field insensitive cloud. This is not only related to the fact that there is no magnetic insensitive sub-state for ${}^3\text{He}$. The switch off of the magnetic field is not as sudden as on the Orsay ${}^4\text{He}$ experiment, and we do not observe the same population spreading over the various magnetic substates neither for ${}^4\text{He}$ nor ${}^3\text{He}$. The ${}^3\text{He}$ atoms observed at the level of the detector remained in the same $2^3S_1 |3/2, +3/2\rangle$ state.

The logical consequence is that the cloud is affected by the magnetic fields during the free fall. There are non-zero eddy currents that remain after the switch off, producing magnetic fields. Magnetic field gradients produce a force on the atoms, yet only localised second order field fluctuations change the statistical properties of the cloud. Whereas the latter are unlikely, the time-of-flight is definitely affected by the magnetic field gradients. This means that there is possibly a systematic error on the temperature measurement.

More importantly, the various currents of the quadrupole and dipole coils are switched off with a controlled 10 μs delay in order for the cloud to fall to the detector. This does not simply mean that the magnetic fields have their importance during the time-of-flight, but also that the switch off is not as adiabatic as we could have hoped.

Additional Instabilities In addition, various unforeseen technical difficulties have complicated the procedure of this enterprise. The first element to bring up difficulties has been the micro-channel plate stack. We expected the 3 days of baking to deal with the gases trapped in the stack. Practically, 3 weeks have been necessary for the micro-channel plates to reach stability.

Also the freshly employed IsiTime02 time-to-digital converter is suspected to having influenced the stability. Previously mentioned Time Sum maps, globally stable over the Orsay acquisition period, have shown instabilities in Amsterdam. It is not clear how those Time Sums have changed exactly, but the new time-to-

digital converter has been the only new element in the acquisition chain. Eventual electronic background noise had been measured to much lower levels than in Orsay and can reasonably be eliminated as a cause. Though this undoubtedly influenced our resolution measurements, it is not clear whether the resolution itself changed as well.

Also the bias field of the magnetic trap has shown significant fluctuations. This influences directly the transverse trapping frequencies, that fluctuated up to 4%. A post selection on the data therefore also had to be performed in order to guarantee consistency in this issue.

An anecdote: even the outside temperature had some interesting effects on the data acquisition. As we were taking data in July, we were in mid heat wave, and unlike the Dutch norm, the weather was extraordinary. Sufficiently indeed for the temperature regulator not to be able to cope with the temperature fluctuations. With an additional high level of humidity, water condensed to the cooled water supplies in the ceiling, and we have been literally taking data in the rain. This has eventually contributed to a much larger stability of the experiment during the early morning, and has shifted the acquisition hours accordingly.

3.3.1.3 The Data

Initially, we had foreseen 4 weeks of data acquisition in Amsterdam. Although we ended up with doubling this period, the order of magnitude was correct, even though at the cost of intensive acquisition periods. Two weeks have been necessary to get both the detector installed and running, and for the setup to produce cold ^3He clouds. As soon as we had the first cold ^3He clouds, and after a long night of data acquisition, we had the first proof of the fermionic antibunching, right in time for the ICAP conference. This produced the sufficient motivation to work on to the improvement of the results, as well as the acquisition of ^4He data. Finally data has also been acquired with a defocusing laser beam, not presented in this manuscript.

We will first deal with the ^4He data acquired. Then we will study the various ^3He populations acquired.

The Dutch Bosons One of the desires had been to check again the bosonic bunching behaviour in Amsterdam. Therefore we simply had to produce a cold ^4He cloud, a step easier to produce than the mixture. Confident in our new time-to-digital converter and its high acquisition rates, we acquired a large set of time-of-flights. After analysis of the data, we surprisingly did not discover any noticeable bunching. Later, data has been acquired at more reasonable acquisition rates, and eventually a bunching showed up. The bunching height was yet not up to the expectations.

The data is not presented in this study as it definitely deserves closer attention. The ^4He and ^3He suffer, despite their mass difference, essentially the same magnetic fields during the expansion. As the ^3He as we will see, behaves correctly, the effect cannot be explained by this alone. There is though a major difference between ^4He and ^3He : the first can have elastic collisions between undistinguishable atoms, the second can not. The ^4He cloud therefore suffers hydrodynamic expansion at the beginning of the switch off. The thermalisation occurring during such an expansion tends to cool down the cloud, but also to increase the apparent size

of the initial cloud. Consequently the expectations, depending on the temperature measurement, increase, whereas the effective bunching size decreases.

Although such a theory could explain the obtained results, it is still unclear why this would have occurred in Amsterdam rather than in Orsay. Trapped atomic densities were of the same order of magnitude, and even higher in Orsay in the experimental conditions. The difference lies only in the switch off. In Amsterdam we had this unusual delay between the various coils that could have produced non-trivial expansions, and the atoms remain mainly in the same magnetic $|1, +1\rangle$ field sensitive substate. In Orsay we worked with the atoms transferred to the $|1, 0\rangle$ magnetic substate, at an early stage of the expansion. A thorough study would therefore have to be carried out for comparison of those two situations in order to fully explain the results obtained in Amsterdam. At least the density dependence of this effect leads us to strongly suspect the non-linear interactions.

The Fermions Just like in the Orsay experiment, we have tried to address several temperature groups. After a post selection, based on flux, detectivity topography and bias field considerations, we were left with three distinct populations. The first data sample is composed of 1139 time-of-flights and has an average temperature of $0.53 \pm 0.05 \mu\text{K}$. The second population is composed of 1361 time-of-flights of average temperature $0.99 \pm 0.06 \mu\text{K}$. The last population is 2482 time-of-flights of average temperature $1.4 \pm 0.1 \mu\text{K}$. In Figure 3.18 we have plotted the number of

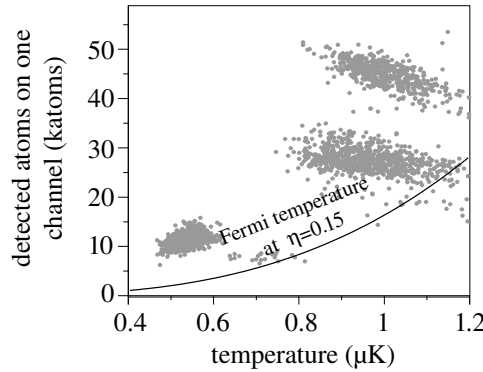


Figure 3.18: The dots represent the number of atoms versus the temperature for various clouds belonging to the $0.53 \mu\text{K}$ and $0.99 \mu\text{K}$ populations. The black curve corresponds to the Fermi limit considering a $\eta = 0.15$ detectivity. If this detectivity is of the right order, this means we work with clouds having degeneracy parameters down to $T/T_F = 0.5$.

detected atoms versus the temperature for the two sets of $0.53 \mu\text{K}$ and $0.99 \mu\text{K}$ clouds. We have also plotted the Fermi temperature limit defined by:

$$k_B T_F = \hbar \bar{\omega} (6N)^{1/3} = \hbar \bar{\omega} (6N'/\eta)^{1/3} \quad (3.3.1)$$

considering a detection efficiency of $\eta = 0.15$. Although we are still not clear about the detection efficiency, if η is indeed of this order, we have clouds with degeneracy parameters down to $T/T_F = 0.5$. This brings us to the consideration that those clouds are not obeying to Boltzmann statistics any longer as we have been assuming. Effectively, the difference between the measured temperature through a

gaussian fit, and the real temperature would be 10%. The Fermi pressure enlarges the cloud, and therefore the temperature is overestimated through the simple fitting procedure. On the other hand, the initial cloud size is no longer as simply related to the temperature as previously. Here the Fermi pressure also enlarges the cloud size. If we consider the temperature fit as a simple cloud size measurement though, the definition of T as the temperature might be wrong, but both errors compensate and the theory defined previously remains correct as long as we also measure the correlation length with gaussians. We will therefore stick to this simple theory for those clouds. It must be added also, that attempts to measure the real temperature of the clouds through more advanced fitting schemes have failed. As we do not know the detection efficiency with certainty, and that independent degeneracy measurements do not give consistent results, this seems currently the better option.

3.3.2 Results

For the analysis, we proceeded in an identical way as for the ^4He atoms in Orsay. We can therefore advance directly to the observation of the results.

3.3.2.1 Temporal Correlation

The temporal normalised correlation functions for the three fermionic sets have been plotted in Figure 3.19. We observe first of all the antibunching related to the

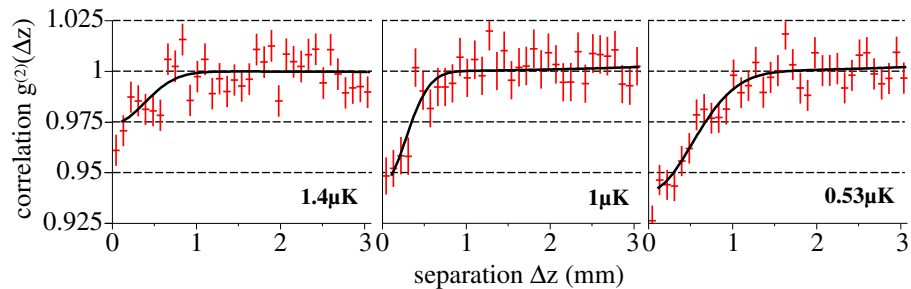


Figure 3.19: The correlation functions of the various cold samples along the z axis. The observed dips for small separations correspond to the antibunching Hanbury Brown and Twiss effect. The black curves are the result of a Gaussian fit of the antibunchings. We note that, as expected, both the antibunching depths and sizes increase inversely with the temperature.

Hanbury Brown and Twiss effect applied to fermions. The correlation at $\Delta z = 0$ should have been zero, yet just like for the bosons, the depth is limited by the resolution of the detector. The correlation length is clearly longer for the lower temperatures, which induces indirectly also larger depths of the observed anti-bunching. Those observations agree with our expectations (see paragraph 1.3.2.3).

3.3.2.2 Spatial Correlation

Again we use the position sensitivity of the detector to observe the spatial correlations. The results have been displayed in Figure 3.20. First at all, at $0.53 \mu\text{K}$, we distinguish clearly the anisotropy inversion of the initial cigar-shaped cloud. We

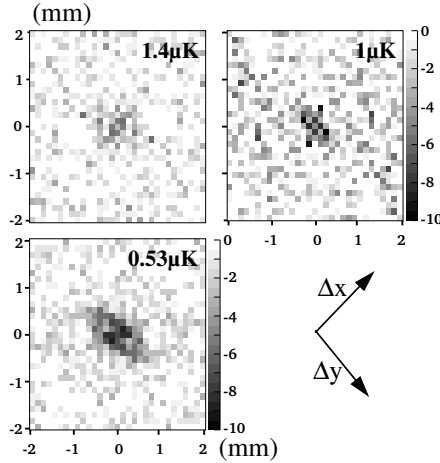


Figure 3.20: The spatial correlation functions of the various cold fermionic samples. The observed spatial antibunchings are inversely anisotropic in respect to the trap densities. The antibunching width is limited by the resolution of the detector, that also lowers the antibunching height.

also observe the x axis bunching width, that is enlarged by the resolution function of the detector. The other two correlations are not as clear. In particular the spatial correlations for the $1 \mu\text{K}$ sample seems to be much thinner than the correlations for the $0.53 \mu\text{K}$ clouds. The correlations for the $1.4 \mu\text{K}$ clouds do not even show clearly the anisotropy inversion. We will perform some measurements in order to quantify those deviations.

3.3.3 Measurements

In order to measure correctly, we need the resolution functions of the detector in the various situations. We will expose the results of those resolution measurements. Then we will analyse the correlation measurements we performed, and conclude on the correlation volumes.

3.3.3.1 The Resolution Functions

Concerning the resolution function, we hoped for a better resolution in Amsterdam as the time-to-digital converter we used had a smaller coding step, and also the electronic environment was measured much cleaner than in Orsay. Experimentally, this was not the case.

We use the same Gaussians sum function as previously. We then obtain $A_1 = 0.49$, $A_2 = 0.48$, $A_3 = 0.03$ and $\sigma_1 = 244 \mu\text{m}$, $\sigma_2 = 460 \mu\text{m}$, $\sigma_3 = 1280 \mu\text{m}$ for the $0.53 \mu\text{K}$ clouds. At $1 \mu\text{K}$ we measure $A_1 = 0.51$, $A_2 = 0.43$, $A_3 = 0.06$ and $\sigma_1 = 244 \mu\text{m}$, $\sigma_2 = 460 \mu\text{m}$, $\sigma_3 = 1290 \mu\text{m}$. At $1.4 \mu\text{K}$ the parameters are $A_1 = 0.47$, $A_2 = 0.45$, $A_3 = 0.08$ and $\sigma_1 = 251 \mu\text{m}$, $\sigma_2 = 481 \mu\text{m}$, $\sigma_3 = 1280 \mu\text{m}$.

The first observation is that those three resolution functions are roughly identical. This does not necessarily mean that the resolutions are identical. We have noticed throughout the Amsterdam acquisition process that the Time Sum map was not as stable as in Orsay. The limiting element may well be the Time Sum map,

that has been taken identical for those three measurements.

Furthermore we note that the resolution is of the same order as in Orsay. Considering the fact that the effective particle rates used are much higher, we may eventually attribute this to the rate dependence on the resolution. It is not clear though whether this has to do with the more homogeneous detection efficiency rather than the use of better electronics in a cleaner environment.

3.3.3.2 The Correlation Lengths

Through the use of the upper parameters for the spatial resolution functions, we fit the various antibunchings. The results have been displayed in Figure 3.21. The

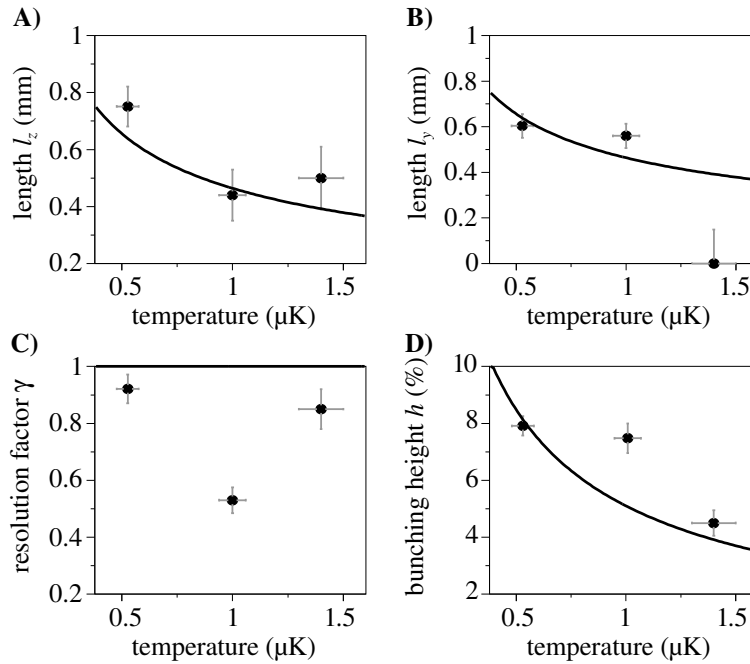


Figure 3.21: The results provided by the free parameters from the 1-dimensional, and 2-dimensional fitting procedures. The indicated error bars are the root-mean-square errors provided by the fitting procedure. In A is plotted the fitted correlation lengths along the z axis. In B is plotted the fitted correlation lengths along the y axis. In C is plotted the resolution factor that accounts for the possible inadequacy between the resolution measurement by the Time Sum method, and the effective resolution influencing the bunching width. In D has been plotted the measured antibunching heights. the theoretical curve has been chosen to correspond to the antibunching height as resulting from the resolution functions measured for the $1 \mu\text{K}$ sample.

results of the fit confirm the observations made previously. The graph in Figure 3.21C shows the resolution factors γ . We note that at both $0.53 \mu\text{K}$ and $1.4 \mu\text{K}$, the resolution factor is smaller but still close to 1. For the $1 \mu\text{K}$ sample, the antibunching width is half the resolution. Meanwhile the antibunching height, in Figure 3.21D, is also higher than expected from the resolution, indicating that the observed deviation could be explained effectively by a better resolution. For the $1.4 \mu\text{K}$ clouds, we measure a y axis correlation length shorter than the resolution, confirming our previous observations. There is no proper explanation to this. Fi-

nally only the temporal correlation lengths, shown in Figure 3.21A, are consistent with the theory.

As the fitting method can be error prone, we will see how the correlation integration behaves.

3.3.3.3 The Bunching Volume

In Figure 3.22 we have displayed the measurements of the correlation volumes. As previously, the black dots correspond to the correlation histogram integration whereas the gray triangles correspond to the integrated fit functions, using the fitted parameters. We observe that, unlike for the correlation lengths, the measured

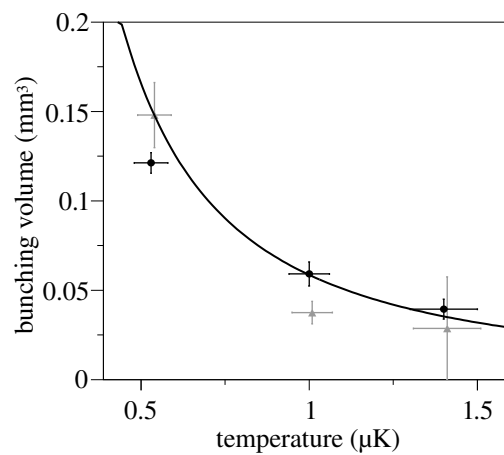


Figure 3.22: The measured anticorrelation volumes. The black circles correspond to the absolute value of a basic integration of the bunching in the 3-dimensional normalised pairs histogram. The error bars correspond to the integrated error on those pairs. The gray triangles correspond to the absolute value of the integrated fitting functions, using the fitted parameters. The error bars result from a statistical sum of the error bars of those fitted parameters. The black curve corresponds to the resolution independent theory.

integrated antibunching volumes for the two higher temperatures behave according to theory. Even the fitted correlation volume is still within acceptable error from theory. We note though, that for the lowest temperature, the integrated volume is several error bars off theory, whereas the fit seems to provide a consistent result. The signal to noise ratios are respectively 20, 8.7 and 7 for the 0.53 μK, 1 μK and 1.4 μK samples.

Conclusion

Throughout this thesis, we have studied the experimental measurement of the Hanbury Brown and Twiss effect with metastable helium atoms. We have started this study by describing the Hanbury Brown and Twiss effect from a general and historical point of view. We have then been quick to realise how cold atoms could be an excellent candidate to its measurement, and we have dealt with some other interesting experimental realisations. We then came to the description of the present study, and after analysis of the particularities of the metastable helium condensing setups, we have seen how those systems are particular good candidates to the Hanbury Brown and Twiss effect measurement. We have finally provided the reader with a simple, but complete theoretical model of the presented experiment, and we have in particular established the signal to noise ratio.

The understanding of the signal to noise ratio has provided us with some key characteristics necessary for the detection system in order for the measurement to be viable. This has strongly oriented the choice of the detector. The use of a micro-channel plate based delay-line detector imposed itself as the best solution. We have studied thoroughly the implementation of such a detector, through the entire acquisition chain. Finally we have focused on three mayor characteristics as to the present and further studies. We discussed the detection efficiency, the detection rate as well as the resolution of the detector.

The characteristics of detector showed clearly that the experiment was feasible in terms of signal to noise ratio. Consequently, all we had to do was to acquire the data. The last part of this thesis showed how we effectively succeeded in the measurement of Hanbury Brown and Twiss effect. We have shown how the bosonic ^4He atoms bunch together in an expanding thermal gas. We have even been able to measure precisely the bunching volume and some correlation lengths. We have shown to some extend, that the coherent Bose-Einstein condensate has no such atomic bunching effect. Finally we have demonstrated that the fermionic nature of the ^3He atoms induces an atomic anti-bunching effect as two fermions cannot occupy a same quantum state.

The interest of this present study lies not that much in the demonstration of the Hanbury Brown and Twiss effect. Sure, the results presented have a particularly high signal to noise ratio compared to previous studies, and the conceptual simplicity of the experiment makes it a particularly illustrating realisation. Yet previous studies should not be undermined, and fundamentally this present work brings little news as to the Hanbury Brown and Twiss effect in physics.

The main interest of this work lies in the fact that it provides the scientific community with an extremely powerful tool as to the analysis of quantum atomic optics. We have seen throughout this thesis, that the detection system employed has many lacks. In particular we have been regretting the inhomogeneous gain, that induced many non trivial detection effects, and that has not favoured the micro-

channel plate local saturation as it forced us to work at high gain. This brought ill problems as to the detection of Bose-Einstein condensates. The very recent implementation of a new micro-channel plate stack build by a different industrial, Hamamatsu Photonics, seems to provide much more encouraging results. We have also seen that the resolution is not up to the expectations. Other users of similar detections systems pretend to have $100\ \mu\text{m}$ resolutions. It is therefore not excluded that progress can still be made on this side. Yet even with all its deficiencies, the combination of He^* and a micro-channel plate based delay-line detector system outperformed all the other cold atom experimental setups by the quality of its signal to noise ratio, and the versatility of the clouds configurations it can work with.

The high signal to noise ratio, the high resolution of the system, the large detection area covering two optical recoils of the He^* atoms, makes it possible to perform individual particles correlations on a wide variety of physical systems. Since the first publication of the results, new theoretical systems are proposed for experimental study with this unique setup. In particular, during the ongoing of this work, we have been able to study such a different system.

The experiment, that will be thoroughly described in the thesis of Aurélien Perin who has been leading this work, consist of a mechanical collision between two Bose-Einstein condensates. A condensate is divided into two parts that are each accelerated optically to one photon recoil. The resulting differential velocity induces collisions between individual atoms of both condensates. Those ponctual collisions redistribute the momentum angularly between the two colliding atoms, and as the condensates separate further on one axis, a collisional sphere is formed containing all the collided atoms. The idea of the two particle collision mechanism necessarily leads to the fact that if a particle is found at a certain angular position in the collision sphere, its entangled counter part is heading in the opposite direction. Thanks to the use of the delay-line detector, we have been able to experimentally prove this particle correlation.

Even more interestingly, this experiment has brought us back to the Hanbury Brown and Twiss effect. The Hanbury Brown and Twiss effect is often seen as a quantum effect resulting from some thermal distribution. This can be in terms of an optical classical light source, or in the presented study of a thermal gas. But the Hanbury Brown and Twiss effect applies to any incoherent quantum phenomena. In particular, the random angular distribution of the atomic pairs after collision is such an incoherent quantum phenomena. This means that the angular distribution of the atoms after the collision will obey Hanbury Brown and Twiss like statistics. Just as previously in the thermal gas, the atoms are preferably grouped on the collision sphere. We have demonstrated this effect experimentally.

What we currently have not yet been able to show, is that the Hanbury Brown and Twiss effect applies to the atomic pairs rather than to the individual atoms of the collision. Doing so would be an experimental prove of the quantum entanglement of the two colliding atoms, and would project the metastable helium setup right into the modern world of quantum optics. All tools are now ready for this to happen.

Appendixes

In the Appendixes we propose to come back to several aspects of the position sensitive delay-line detector. We analyse those specific points as they raised many questions during the ongoing of this research.

The first Appendix deals with the resolution measurement we have been using extensively for the characterisation of the detector: the Time Sum method. It proved some insight on the combination of the analogue delay-line with the digital time-to-digital converter. It then makes understanding of the Time Sum method straightforward, and a brief case study is proposed.

The second Appendix deals with the atomic reconstruction method. The four signals provided by the delay-lines must be correlated in order to define the position and arrival times of the atoms. The algorithm to do so is not universal, and we study here our implementation. The understanding of this algorithm provides with some insight as to the ultimate limitations of the delay-line technique.

The third Appendix deals with the characterisation we have performed of the detector through the use of an Oscilloscope. The combination of a high performance oscilloscope with the delay-line detector has provided us with some insight as to the poor performances of the micro-channel plate stack. It also learned us to appreciate the usual electronic acquisition chain.

A.1 The Resolution Measurement

One of the major properties of the time-to-digital converter is that it discretises the initially continuous time. This discretisation has little effect on the arrival times of the atoms, as the physical times constants range much larger than the discretisation time. Yet we also use those discretised times to establish the position on the detector through the delay-line mechanism. The resulting pixels size is in the $200\mu\text{m}$ order, that can in no way be neglected compared to the expected $30\mu\text{m}$ correlation lengths. We will therefore study in detail in this annex the effect of the discretisation on the position definition.

We will proceed by first defining correctly the resolution of the detector. Then we will see how, what we will call the Time Sum, enables the measurement of the resolution. Finally, we will end with some real case studies.

A.1.1 Some Considerations

Let us consider a particle arriving at a time t at position (x, y) . The time is in seconds and the positions x and y are measured in meters from the centre of the detector. Both x and y belong to the interval $[-R, R]$ with R the radius of the micro-channel plate. The electron shower of the micro-channel plate produces the various pulses on the two delay-lines, and analogically the pulses arrive with a time $t_{x1} = t - x/v_x + C_{x1}$, $t_{x2} = t + x/v_x + C_{x2}$, $t_{y1} = t - y/v_y + C_{y1}$ and $t_{y2} = t + y/v_y + C_{y2}$ at the end of the delay-lines. v_x and v_y are the apparent speeds of the signals respectively along the x and y axis through the winded delay-line. We recall that the delay-lines have different lengths and thus $v_y \neq v_x$, yet they are relatively close and we will consider them equal $v_y = v_x = v_c$. C_{x1} , C_{x2} , C_{y1} and C_{y2} are different time constants that can be determined experimentally (we will see a little further that they depend on the position though).

The effective signal produced by the time-to-digital converter and send to the computer are the number of clock cycles of time period d_t that separate the signal from the start trigger of the time-to-digital converter. This value is digital and we can write:

$$X_1 = E(t_{x1}/d_t) = E\left(\frac{t - x/v_c + C_{x1}}{d_t}\right) \quad (\text{A.1.1})$$

$$X_2 = E(t_{x2}/d_t) = E\left(\frac{t + x/v_c + C_{x2}}{d_t}\right) \quad (\text{A.1.2})$$

$$Y_1 = E(t_{y1}/d_t) = E\left(\frac{t - y/v_c + C_{y1}}{d_t}\right) \quad (\text{A.1.3})$$

$$Y_2 = E(t_{y2}/d_t) = E\left(\frac{t + y/v_c + C_{y2}}{d_t}\right) \quad (\text{A.1.4})$$

where $E(x)$ is the function that takes the highest lower integer value to the real x . We note that X_i and Y_i are dimensionless. They have to be multiplied with d_t in order to retrieve a temporal dimension. From now on we will work dimensionless as it proves convenient.

A.1.1.1 Number of Pixels

Let us consider a particle arriving at specific time t_0 such that $E(\frac{t_0+C_{x1}}{d_t}) = \frac{t_0+C_{x1}}{d_t}$. If we consider that $N = E(\frac{2R/v_c}{d_t})$, then $X_1 = E(\frac{-x/v_c}{d_t})$ can have N possible values depending on the position. The question is, what are the number of values for the pair (X_1, X_2) ?

Suppose we have a detector for which $E(\frac{C_{x2}-C_{x1}}{d_t}) = \frac{C_{x2}-C_{x1}}{d_t}$, in that case X_2 can be simply evaluated to:

$$X_2 = \frac{t^0 + C_1}{d_t} + \frac{C_{x2} - C_{x1}}{d_t} - X_1 - 1 \quad (\text{A.1.5})$$

In other words, X_2 changes in the same fashion as X_1 , and there are only N possible values for the pair as a function of x .

Yet if the particle arrives at $t_1 = t_0 + \tau$ with $\tau \in [0, d_t[$, X_1 still has N possible values evaluated to $\frac{t_0+C_{x1}}{d_t} + E(\frac{-x/v_c+\tau}{d_t})$. But in that case we have:

$$X_2 = \frac{t_0 + C_{x1}}{d_t} + \frac{C_{x2} - C_{x1}}{d_t} + E(\frac{x/v_c + \tau}{d_t}) \quad (\text{A.1.6})$$

Depending on the value of x this can lead to either one, two or three different values of the couple (X_1, X_2) for the same position but various τ . This has as a consequence that the difference $X_2(x, t) - X_1(x, t)$ can take effectively $2N$ different values, and the pixels size s_p is $d_t v_c / 2$ rather than $d_t v_c$. This does not mean that the resolution is the root-mean-square width of a single $d_t v_c / 2$ pixel!

A.1.1.2 The Resolution

We define the resolution along the x axis as the root-mean-square width of the distribution $v_c \frac{X_2 - X_1}{2} - x$. Experimentally we will rather measure the dimensionless $X_2 - X_1 - \frac{2x}{v_c d_t}$ distribution width. The relation between the two is simply a s_p multiplication. The latter distribution has been drawn in Figure A.23. The distribution is

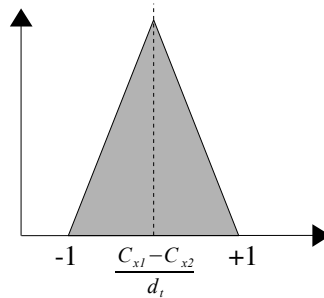


Figure A.23: The theoretical distribution of $X_2 - X_1 - \frac{2x}{v_c d_t}$ of particles randomly detected by the delay-line detector. The results is the convolution between the squared error functions induced by the discrimination process.

simply a triangle centred in $\frac{C_{x2}-C_{x1}}{d_t}$, with a base of 2. The root-mean-square width of such a distribution is 0.41. The best theoretical resolution to be expected from a delay-line detector therefore is $0.41s_p$. That is to be compared with the $0.29s_p$ root-mean-square width of a s_p width squared pixel. We note that $\sqrt{2} \times 0.29 = 0.41$

and that the observed triangle is also the autoconvolution of the the s_p square. The result is finally self explanatory as this width simply translates the convolution between the typical one unit error induced by the digitising process on each channel. Note also that the result is smaller then 2×0.29 , that would have been the width of the pixel if we simply had the time-to-digital converter resolution. The partial redundancy of the information between X_1 and X_2 does provide us with sub-time-to-digital converter resolution.

We have seen in Chapter 2 that the constants C_{x1} , C_{x2} , C_{y1} and C_{y2} are constant in time, but can show a position dependence. At least, we have observed that both $C_{x1} + C_{x2}$ and $C_{y1} + C_{y2}$ show a position dependency. If we introduce the position dependency of those constants, then we will have to look after the local resolution. That means that we have to consider the distribution width of $X_2 - X_1 - \frac{2x}{v_c d_t} - \frac{C_{x2} - C_{x1}}{d_t}(x)$. By definition, the width of this distribution is identical.

A.1.1.3 The Jitter

Let us now consider that the micro-channel plate makes a δx root-mean-square error on the detection of the position. A simple simulation shows immediately that the measured root-mean-square width of the $X_2 - X_1 - \frac{2x}{v_c d_t}$ distribution is $\sqrt{2 \times 0.29^2 + (\delta x / s_p)^2}$. For a large error, the width of this distribution measures directly the resolution of the detection.

We have to note that measuring in an exact way the wrong position is identical to having a jitter on the discriminator and measuring the exact position. It is hence easy to demonstrate that two independent $\delta t_x = \sqrt{2} \delta x / v_c$ jitters on the two channels produce the same result. If this distribution were to be studied, and a width larger then 0.41 were to be measured, it would be impossible to say what caused the resulting resolution. It does not really matter though. The width of this distribution tells us the resolution we have to work with.

A.1.2 The Time Sum

Experimentally, we do not have access to the exact position of the atoms as they fall on the detector. We have only access to the 4 mentioned signals and eventually the 5th micro-channel plate signal. The latter is equal to $T_{MCP} = E(t/d_t)$. Out of those 5 signals, we can distinct 3 interesting relations:

$$SUM_1 = X_1 + X_2 - 2T_{MCP} \simeq \frac{C_{x2} + C_{x1}}{d_t} \quad (\text{A.1.7})$$

$$SUM_2 = Y_1 + Y_2 - 2T_{MCP} \simeq \frac{C_{y2} + C_{y1}}{d_t} \quad (\text{A.1.8})$$

$$SUM_3 = (Y_1 + Y_2) - (X_1 + X_2) \simeq \frac{(C_{y2} + C_{y1}) - (C_{x2} + C_{x1})}{d_t} \quad (\text{A.1.9})$$

Naturally, those three sums are distributions that have widths. We will study how we can relate those widths to the resolution of the detector.

A.1.2.1 The Plain Distributions

Let us simply consider the simulations of SUM_1 and SUM_3 . They have been shown respectively in Figure A.24A and Figure A.24B. Several observations can be made.

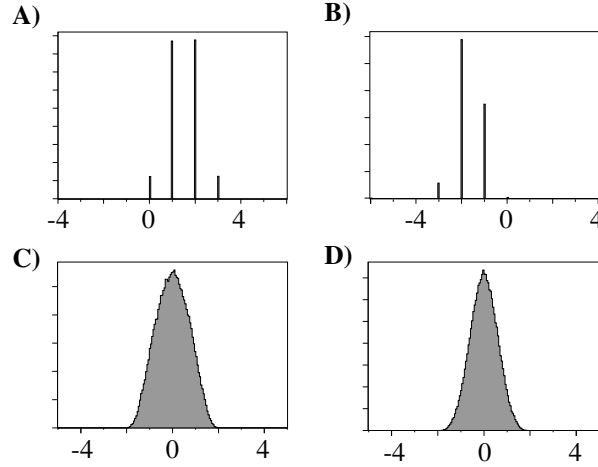


Figure A.24: Respectively in A and B, the simulated distributions of SUM_1 and SUM_3 . In C and D, we have introduced a spatial dependency of both $\frac{C_{x2}+C_{x1}}{d_t}$ and $\frac{C_{y2}+C_{y1}}{d_t}$ that has been subtracted before histogramming.

The first is that those distributions are discrete combs. This is simple to explain as, unlike previously, we do not subtract a continuous variable. The individual time sums are all made out of digital values. The result can only be an integer. The second observation is that the two distributions are centred at respectively $\frac{C_{x2}+C_{x1}}{d_t} = 1.5$ and $\frac{(C_{y2}+C_{y1})-(C_{x2}+C_{x1})}{d_t} = -1.7$. This is also what we expected. The last observation is not much more surprising as the root-mean-square width of SUM_1 is 0.71 and the width of SUM_3 is 0.59. The second value corresponds to $\sqrt{(4)} \times 0.29$, and the distribution is simply the convolution of the 4 channels' one pixel errors. The first distribution corresponds to the convolution of the 2 channels with one pixel error, and the third channel whose error suffered the multiplication by 2. The resulting distribution has therefore a $\sqrt{1^2 + 1^2 + 2^2} \times 0.29 = \sqrt{6} \times 0.29$ width.

We have mentioned earlier that we discovered experimentally a spatial dependence of both $\frac{C_{x2}+C_{x1}}{d_t}$ and $\frac{C_{y2}+C_{y1}}{d_t}$. This has to be accounted for and we will have to either study only the local distribution or subtract the average constant sums. The second possibility is realised fairly easily and provides us with the continuous variable we were hoping for. The resulting distributions for both SUM_1 and SUM_3 have been plotted in Figure A.24C and A.24D. This operation preserves all the properties of the distribution, besides the mean values that has been subtracted to 0. We observe much better though the results of the various convolutions.

A.1.2.2 The Link to the Resolution

We propose to reuse our two radical scenarios used previously for the establishment of the resolution. In the case the electron shower does not quit the micro-channel plate at the right position but is mistaken again with a root-mean-square error of δx and δy , we notice directly that the introduced random variable gets eliminated through the summing process. The discretisation process does not change anything to this fact, and the final distribution is changed in no way. This is rather reassuring. The opposite would have meant that the delay-line could detect the supposed to be

position of particles: a fair selling argument though... The delay-line can utmost account for its own mistakes thanks to the information redundancy.

When we introduce the same $\delta t_x = \sqrt{2}\delta x/v_c$ and $\delta t_y = \sqrt{2}\delta y/v_c$ gaussian jitters in the timing of all the 4 delay-line channels, and also a δt_{MCP} jitter on the micro-channel plate channel, we can then easily discover (and foresee) the distributions to take a gaussian shape. The widths of the distribution adopt respectively:

$$\sigma_{SUM_1} = \sqrt{6 \times 0.29^2 + \delta x^2/s_p^2 + 4\delta t^2/d_t^2} \quad (\text{A.1.10})$$

$$\sigma_{SUM_3} = \sqrt{4 \times 0.29^2 + \delta x^2/s_p^2 + \delta y^2/s_p^2}. \quad (\text{A.1.11})$$

The second result simplifies to $\sqrt{4 \times 0.29^2 + 2\delta x^2/s_p^2}$ if the two spatial dimensions are equivalent and finally we can establish the following relations:

$$d_x = d_y = d = \frac{1}{\sqrt{2}}\sigma_{SUM_3} \times s_p \quad (\text{A.1.12})$$

Using the SUM_3 is therefore totally equivalent to using the definition of the resolution for its determination. This is true though as long as the resolution is lost because of the propagation through the wire, the amplification, the discrimination or the time-to-digital converting. Any physical process that would affect the hit point of the atom, the propagation of the electrons through the micro-channels or the behaviour of the electronic cloud in the space between the micro-channel plates and the delay-lines, cannot be detected. Therefore the result of this measurement is only a lower limit to the effective resolution.

A.1.2.3 Discussion

Two questions remain. How far is this measurement equivalent to the measurement of the resolution? We note that as long as the behaviour of the detector is identical along the x and the y axis, the measurement of SUM_3 is to produce the same result as $(X_1 + Y_1) - (X_2 + Y_2)$. Experimental study of those two axis indicates that those behaviours are indeed alike.

Considering this equivalence, can we improve artificially the resolution of the detector by imposing a boundary on SUM_3 ? Unfortunately, the answer is no. Imposing constraints on the distribution of SUM_3 does not affect the distribution of $(X_1 + Y_1) - (X_2 + Y_2)$, nor $X_1 - X_2$ or $Y_1 - Y_2$. Consequently, the equivalence of those measurements is only guaranteed as long as the four components keep their statistical independence.

A.1.3 Real Case Study

We propose to analyse some real data. This will enable us to discuss a mayor subjects. We did suppose indeed there was an equivalence between, d_x and d_y . We will study how far this is true

A.1.3.1 The Time Sum Maps

In order to study the time sum distributions, we will first have to map $\frac{C_{x2}+C_{x1}}{d_t}(x, y)$ and $\frac{C_{y2}+C_{y1}}{d_t}(x, y)$. We proceed by first rebuilding all the atoms, with their arrival

time produced by the micro-channel plate channel. During the reconstruction process, we associate to each atom its value of SUM_1 and SUM_2 . Once build, we simple draw into two maps the values that get averaged locally. In other words, we obtain the maps of $\langle SUM_1 \rangle_N(x,y)$ $\langle SUM_2 \rangle_N(x,y)$. Yet as we have noticed earlier, those are identical to the maps $\frac{C_{x2}+C_{x1}}{d_t}(x,y)$ and $\frac{C_{y2}+C_{y1}}{d_t}(x,y)$.

Later on, for technical reasons mentioned earlier, we did no longer use the micro-channel plate channel. The arrival times of those atoms have therefore been calculated through $d_t(X_1 + X_2)/2$. Although those arrival time are slightly less precise as $\frac{C_{x2}+C_{x1}}{d_t}(x,y)$ gets involved, the fact that the time resolution is overkill anyway implies that this does not matter at all. The consequence of this is though that we can no longer calculate SUM_1 and SUM_2 . For the data in Amsterdam we therefore only dispose of the SUM_3 map, that is obtained through a similar procedure as SUM_1 and SUM_2 . For each atom we simply stock the value of $(Y_1 + Y_2) - (X_1 + X_2) = SUM_3$. This is mapped and averaged to $\langle SUM_3 \rangle_N(x,y)$. This map is equal to $\frac{(C_{y2}+C_{y1})-(C_{x2}+C_{x1})}{d_t}(x,y)$. In Figure A.25A, B and C we respectively plotted $\langle SUM_1 \rangle_N(x,y)$, $\langle SUM_2 \rangle_N(x,y)$ and $\langle SUM_3 \rangle_N(x,y)$ in Orsay acquired with the CNTM4 time-to-digital converter. In Figure A.25D we plotted $\langle SUM_3 \rangle_N(x,y)$ in Amsterdam acquired with the IsiTime02 time-to-digital converter.

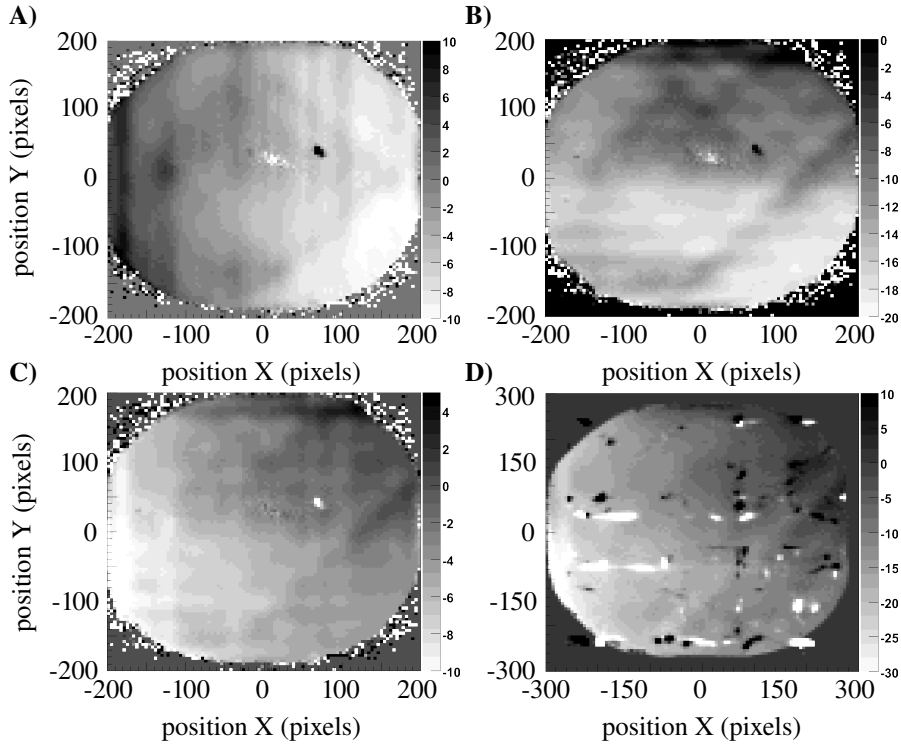


Figure A.25: In A is plotted the Time Sum map corresponding to SUM_1 as acquired in Orsay with the CNTM4 time-to-digital converter. In B and C are respectively plotted the averaged maps of SUM_2 and SUM_3 processed over the same data. In D has been plotted SUM_3 as acquired in Amsterdam with the IsiTime02 time-to-digital converter.

Out of those maps, we can make several remarks. The first is to notice the amplitude of the time sum maps. Those lay in the 10 units scale. Our earlier consideration of the $\langle SUM \rangle_N(x,y)$ as continuous variables compared to the discrete

$SUM(x, y)$ makes sense.

The second remark is that we can see that the SUM_1 map shows a horizontal gradient, whereas the SUM_2 maps shows a vertical gradient. It thereby makes sense to say that the constants C_{x2} and C_{x1} essentially depend on x , the same can be said for C_{y2} and C_{y1} and y considering the SUM_2 map. This is rather reassuring. It means that the variations are not related to some problem with the micro-channel plate, yet rather to the geometry of the delay-lines. We do not understand yet why this dependence occurs exactly. The SUM_3 map is the difference of those two maps.

The last remark concerns the numerous anomalies we can identify in the Amsterdam SUM_3 map. Those anomalies do not necessarily appear in the detectivity maps presented earlier. This illustrates what we mentioned just above. The time sums only measure the resolution if the jitters behave symmetrically. Apparently, this is not always the case, although we do not understand why this would be a localised phenomena.

A.1.3.2 The Time Sums

Now that we have obtained the constants fluctuations map, we can effectively study the sum distributions. We plot in a histogram simply $SUM(x, y) - \langle SUM \rangle_N(x, y)$. The results have been shown for SUM_1 , SUM_2 and SUM_3 in Orsay and the CTNM4 time-to-digital converter in respectively Figure A.26A, B and C. The SUM_3 of the data acquired in Amsterdam with the IsiTime02 time-to-digital converter is shown in Figure A.26D. The gaussian fit measures respectively for Orsay $\sigma_{SUM_1} = 1.38$, $\sigma_{SUM_2} = 1.46$ and $\sigma_{SUM_3} = 1.30$. For Amsterdam we obtain $\sigma_{SUM_3} = 2.93$. Let us recall furthermore that the pixels sizes are $s_p = 192 \mu\text{m}$ with the CTNM4 and $s_p = 133 \mu\text{m}$ with the IsiTime02. We consequently measure a resolution of respectively $d_{xy} = 180 \mu\text{m}$ in Orsay and $d_{xy} = 275 \mu\text{m}$ in Amsterdam. Further comments on those values can be found in Chapter 2.

The resulting values for the Jitters are $\delta t_x = 200 \text{ ps}$, $\delta t_y = 250 \text{ ps}$, $\delta t_{MCP} = 180 \text{ ps}$. Those are all of the same order of magnitude. They are equivalent to an error on the positions of the atoms of $\delta x = 160 \mu\text{m}$. In Amsterdam the average jitter $\delta t_{xy} = 395 \text{ ps}$ induced an additional error of $\delta x = 270 \mu\text{m}$.

The stability of this method is still not clear. In Orsay we globally experienced a good stability of this measurement. In Amsterdam, with the new time-to-digital converter overall feeling was a bad stability. It is likely that this is related to a lower stability of the new electronics.

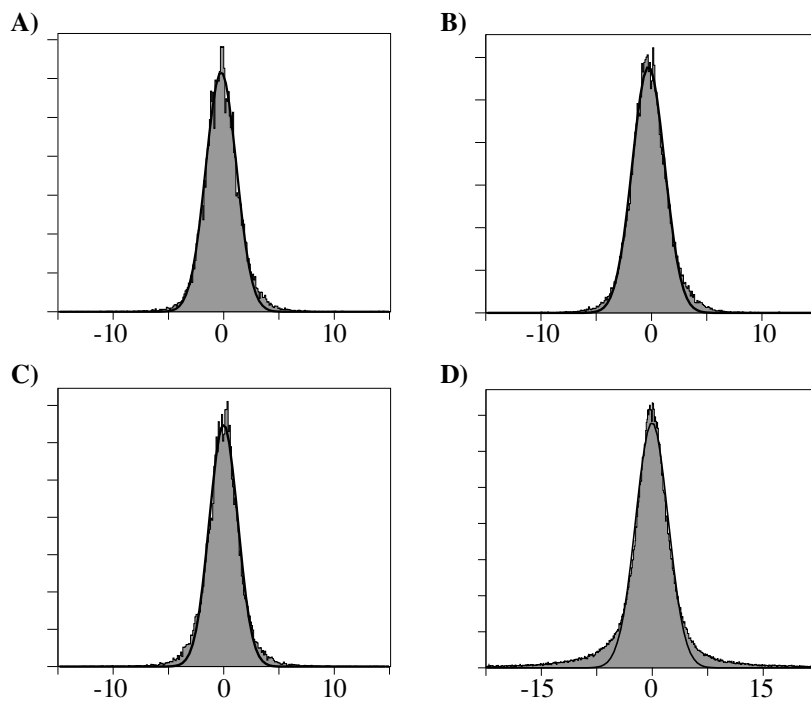


Figure A.26: In A, B and C have been plotted the experimental distributions of $SUM(x,y) - \langle SUM \rangle_N(x,y)$ for respectively SUM_1 , SUM_2 and SUM_3 as acquired in Orsay with the CNTM4 time-to-digital converter. In D has been plotted the same distribution of SUM_3 for the data acquired in Amsterdam. The Gaussian curves are fits.

A.2 The Atomic Reconstruction Algorithm

We propose here to describe the algorithm that is used for the reconstruction of the 3-dimensional time-of-flight from the data provided by the time-to-digital converter. Depending on the acquisition rate, the reconstruction can indeed be more or less complicated, and thinking about the optimal way of doing so has already produced numerous headaches.

Thinking about all the complicated intricate situations in which we have fake signals, echos, or overlapping atoms keeps us from the fact that a vast majority of the atoms are easy to reconstruct. Consequently we have adopted a reconstruction algorithm, called the "Time Bulb" algorithm, that enabled us to progressively set aside the difficulties. We will present the algorithm in its principle, and then we will study the various steps that take us progressively into the complications.

A.2.1 The Time Bulb Algorithm

In order to understand the algorithm, we will first recall the aspect of the incoming data. Then we will deal with the idea behind the Time Bulb notion. Finally we will see how the algorithm scales with the number of total atoms N .

A.2.1.1 The Data

The logical pulses produced by the constant fraction discriminator enter the time-to-digital converter for time measurement. The black box corresponding to the time-to-digital converter has various input channels that share the same data transfer mechanism as discussed in paragraph 2.2.3.2. The fact that we use a single box with various channels is a necessity as those various channels need to be synchronous. The consequence is though that the output data of the various channels is mixed up in a single serial buffer memory. Each time signal has off course been stamped with the corresponding channel number.

Initially, we used 5 channels of the time-to-digital converter. The first was for the signal discriminated from the micro-channel plate input voltage t_{MCP} , the other four correspond to the outputs of the two delay-lines t_{x1} , t_{x2} , t_{y1} and t_{y2} . When the times quit the time-to-digital converter, they correspond to an integer number that is the count of clock-cycles between the measured pulse and the start trigger of the time-of-flight measurement. Before being saved, this integer is though multiplied with the clock-cycle period.

Finally, the apparent data we get from the time-to-digital converter behaves as a long list. Each entry of this list contains two informations: the channel of the time-to-digital converter that measured the entry and the physical arrival time. This is the input to the Time Bulb algorithm.

A.2.1.2 The Time Bulbs

As we have seen previously, the data between the various channels is correlated. We know that if the 5 signals t_{MCP} , t_{x1} , t_{x2} , t_{y1} and t_{y2} come from a single physical atom, we have a number of relations between them. We could check all those relations between all the signals, yet that would be a $O(N^5)$ correlation algorithm.

Furthermore, inconsistent or impossible choices would produce a rather complicated algorithm.

In order to reduce significantly the complexity and processing time we make use first of all of the rough temporal order of the data provided by the time-to-digital converter. As we have seen in Chapter 2, the serialisation mechanism of the parallel data acquisition cannot guarantee the exact temporal order of the various signals. But at larger time scales, order is respected. We therefore correlate the data over significantly shorter time scales. We currently consider a loose $5\mu\text{s}$ time scale. Furthermore we take a vague correlation criteria. Hence we simply state that for two signals to be from a single atom, they need to be separated within a certain interval. This can be seen as each signal building up a time bulb around it. If two time bulbs from two signals touch each other, the two signals may belong to a single atom, and they will be linked explicitly. This leads to a graphical overview as in Figure A.27. The size of each time bulb is essentially related to

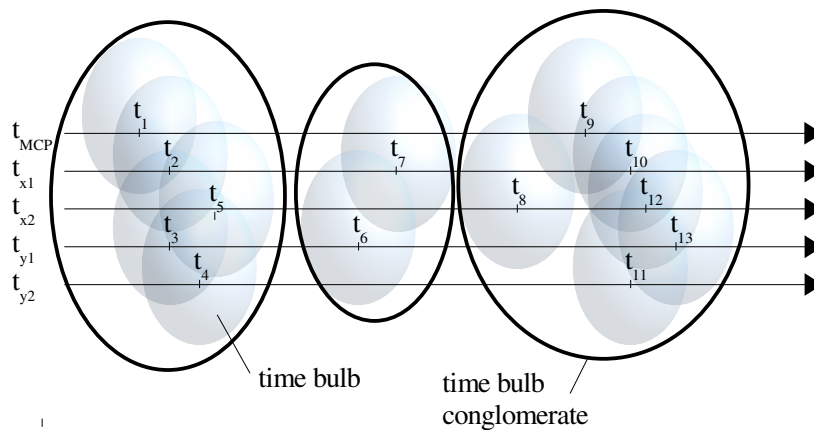


Figure A.27: An overview of the time bulb procedure. All the individual arrival times on the various time-to-digital converter channels are associated a time bulb. If the time bulb of two signals overlap, they belong to the same conglomerate. This means that they potentially belong to the same initial particle.

the delay-line length, with some additional error bars. It has been determined experimentally through the analysis of the width of the distributions of the time differences between distinct channels. All signals that potentially belong to the same atom then form a time bulb conglomerate. If the acquisition rate is not too high, those conglomerates are distinguishable heaps, that can be correlated individually to reconstruct definitely the atomic arrival times and positions.

A.2.1.3 Scaling

Thanks to the initial rough order of the data, the complexity of this algorithm is $O(N)$, still with a signification prefactor. The reconstruction rate with a modern 3 GHz Intel Xeon based server is close to 15 katoms/s. The memory consumption would also have a linear dependency. This can yet be significantly reduced if we consider that the conglomerates are statistically limited in size. A conglomerate with a temporal time extension above the $5\mu\text{s}$ are most unlikely, although not technically impossible. If such a heap were yet to exist, there would be not logical

relation between the first and the last time bulb, apart from the overlap of all the time bulbs that separate them. Its analysis could be easily split.

Consequently the analysis of the total list can be cut into many small parts. A single 4000 time bulbs stack is allocated, and the list is analysed through 2 k time bulb bits. Border effects are avoided through the use of circular buffer techniques. The advantage of this procedure is that one can potentially analyse infinitely large lists of data with a very low memory consumption.

A.2.2 The Extraction Procedure

Once the data has been organised in a heap of conglomerates, we still have to disentangle everything in order to produce the atomic positions and arrival times. This is done through several lectures of the bulb stack. Here we detail the various lectures processed. We should note first though that the t_{MCP} channel is not in use today anymore, for reasons explained previously. We will therefore no longer consider it.

A.2.2.1 Round 1: the Cleaning

The first thing to be noticed is that in order to correctly rebuild an atom, we require a precise position. The arrival time is not that important as the time resolution is already overkill. We rather lose an atom than have an atom with an incorrect position. Consequently we require the four t_{x1} , t_{x2} , t_{y1} and t_{y2} signals for an atom to be rebuildable.

We can therefore eliminate all the individual time bulbs that are not overlapping at least one bulb on each critical channel. This cleans up considerably the time bulb stack, and also lightens many conglomerates. If we consider again Figure A.27, we would eliminate in this process not only time bulbs 6 and 7, but also time bulb 8. Although this bulb is indeed attached to a conglomerate containing all the required signals, it has no direct overlap with them. This process can break up in smaller parts many large conglomerates and its execution in the first round is fundamental.

A.2.2.2 Round 2: the Simple Cases

The key to this round is to notice that a large majority of the conglomerates, especially after the cleaning round, has no specific problems and contain only the 4 required signals. We measure that 80% of the conglomerates after cleaning are ready for reconstruction. We associate to each of those conglomerates a new signal we call an atom, for which we calculate both the position and arrival time. Note that no further testing is performed on the 4 signals. The quality of the final result is only assured by the large statistical improbability of an error.

All the data presented in this thesis has been build up to this second round. We do indeed assure the reconstruction of a large majority of the data with a high quality factor. Any further mechanism will mean extricating complex conglomerates, and will need the introduction of discriminatory criteria. Not only is that process more complicated, it is also prone to systematic errors. As the quantum efficiency of the detector was not a critical criteria to the proposed study of the Hanbury Brown and Twiss effect, this effort has not been applied to this study.

A.2.2.3 Round 3: the Disentanglement

Although the third round has not been applied, its case has been studied. Let us recall that the only conglomerates left are those containing at least the 4 critical signals plus at least 1 other. In such a heap, we have to apply additional selection criteria for the reconstruction of an atom. The criteria we have adopted concerns what we have called the time sum $(t_{x1} + t_{x2}) - (t_{y1} + t_{y2})$ previously. We expect this time sum to equal 0 ± 15 ns for an atom to be valid. We study all the possible quadruplet combinations, until one quadruplet satisfies the discrimination criteria. We then use the specific quadruplet to build an atom, and continue the study of the quadruplets left. The right image in Figure A.28 shows the image of a reconstruction of a 1 mK time-of-flight taking into account the complex case as opposed to the left image in Figure A.28 that stops at round 2. The right images counts

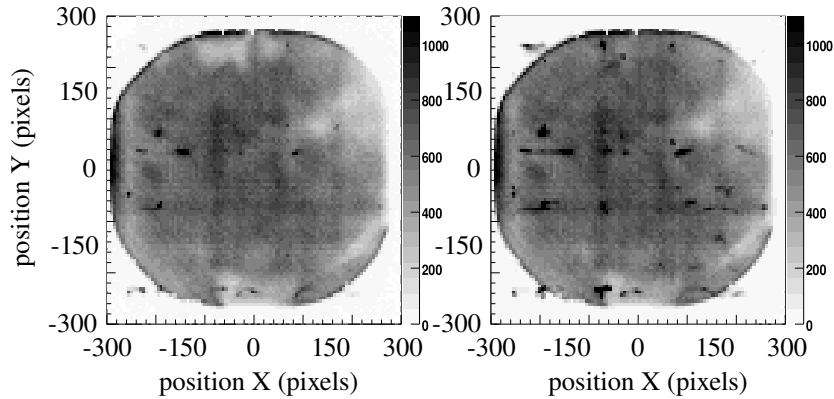


Figure A.28: In the left picture, only the atoms build through the simple reconstruction have been plotted. In the right figure the complex build atoms have been added.

8% more atoms than the left image. Yet, a significant number of black spots have appeared on the image. Also the signal outside the circle of the micro-channel plate has increased significantly. The latter means that also a background noise inside the image has appeared. This can be observed in the upper middle zone that shows clear in the left image and dark in the right image. This is easily under-

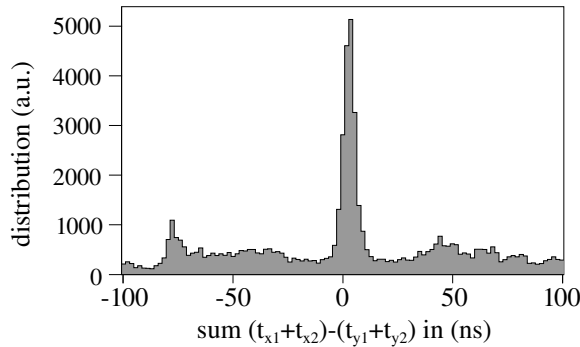


Figure A.29: The distribution of $(t_{x1} + t_{x2}) - (t_{y1} + t_{y2})$. Unlike the distributions shown earlier, the signals do not necessarily belong to the same atoms. Therefore a large wing exist beyond the central spike.

stood as we look at Figure A.29. This graph shows the distribution of the time sum $(t_{x1} + t_{x2}) - (t_{y1} + t_{y2})$ of all the possible quadruplets in the conglomerates left after the second round. The central spike deals with the atoms we were looking for. The width of this spike accounts for the ± 15 ns error bar we left to the time sum for reconstruction. We observe though outside the spike an important background signal, that accounts for all the random unrelated quadruplets that can appear. This is all the more important as the atom rate is high, and is already not negligible at this average 300 katoms/s rate. For cold time-of-flights, the introduced relative fake atoms number can be far larger.

It seems clear from this graph though that the use of a smaller error bar would also decrease the number of wrongly rebuild atoms. The only way of doing so is by introducing the time sum map presented earlier. One can then find for each quadruplet the expected average time sum, and the error bars can then be reduced to $2 \times \sqrt{2}$ the spatial resolution. This requires though that the user keeps track of the time sum map, that can show inconsistencies between time-to-digital converters, cables and eventually micro-channel plate evolutions. It will also result in an artificially imposed resolution. That raises a lot of pain the present study can do without. The recent atom-pairs experiment we have performed is a little more sensitive to quantum efficiency, and work has been oriented into this direction.

A.3 The Oscilloscope Detection

In general, the signals provided by the delay-line detector are amplified, then discriminated with a constant fraction discriminator and finally measured with a time-to-digital converter. The enormous advantage of this method is that the amount of data generated scales linearly with the amount of particles, and the quality of the measurement can be fairly high. The drawback of this method is that one loses the information on the bunching height, one is ultimately limited by the resolution of the time-to-digital converter, and overlapping signals result in erroneous information.

We have already mentioned how "advanced" delay-line techniques have enabled other groups [77] in improving the performances of the delay-line detector through the use of digitisers. By acquiring the entire analogue signal over the time-pulse period, the use of post processing techniques can extract both arrival times and amplitudes from the signals. The use of envelope detection techniques enable [77] even to separate overlapping signals and they claim a 35 ps error on the arrival times of their impulses at 4 GHz sampling rate and a 1 GHz bandwidth.

If this method is applied with real-time analysis of the data, the final quantity of the data still scales linearly with the total number of atoms, yet requires huge processing power. With their current implementation, the group is limited to a 2 kHz particle acquisition rate. The technique seems therefore of no particular interest to our setup. Yet with the recent progress of fast electronics, oscilloscopes with high memory depths have made their appearance in the market. In particular LeCroy proposes oscilloscopes with over 50 M samples memory per channel for "reasonable" pricing.

We will study briefly in this Appendix the way we have been working with a Lecroy WaveMaster oscilloscope (borrowed from Lecroy) and our delay-line detector to get a wider understanding of our detector performances. We will study in a first time the rough implementation of the technique and its fundamental limitations. Then we will focus more precisely on the method with which we have measured the arrival times of the pulses, and will comment on the resolution of this method.

A.3.1 The Setup

The four channels of the scope are connected to the outputs of the amplifiers of the delay-line signals. Because the oscilloscope used had no additional trigger channel, the signal of x_1 goes through a radio-frequency switch. This additional switch slightly lowers the amplitude of this first channel, but it allows us to trigger on the first channel. The acquisition gate is consequently externally controlled.

The characteristics of the oscilloscope are generous. A 6 GHz bandwidth, up to 10 GHz sampling rate of 8 bits, 4 channels with each 50 M acquisition points. Considering an effective sampling rate of 1 GHz, this allows an entire cold time-of-flight to be measured, and thus to study saturation effects. Practically, a bug in the scope driver only allowed us to acquire 25 Mps per channel at our sampling rate.

The scope is connected to the local network, and the data can be transferred easily to the acquisition computer. Each time of flight takes however 100 Mbytes of scope data. This has to be transferred to the acquisition computer. The acquisi-

tion computer compresses the data and sends it to the dataserer. After the basic compression, the four channels acquisition takes 40 MBytes of disk space. The whole process, not specifically optimised though, takes over 40 s.

Those number have to be compared with a typical time-to-digital converter acquisition. A 25 ms acquisition at 1 Matoms/s produce an uncompressed amount of 900 kbytes. The data ratio is 100. We have also acquired data at 2.5 Ghz sampling, where the data ratio is 250. The simple discriminator time-to-digital converter approach has some fundamental advantages.

A.3.2 The Analysis

Once the analog signal has been acquired it needs processing. We want to extract from all the pulses, on the four channels, their characteristic arrival time. Once we have found the arrival times for the four channels, the resulting data can then undergo the same reconstruction procedure as mentioned earlier. We can then also, through the Time Sum mechanism measure the resolution, and therefore the quality of the procedure. The first thing to do is to define a trigger level above which the pulse is considered detected. Once a pulse has been detected and is isolated, we have tried essentially two different techniques in order to define the arrival time.

The first technique consists of fitting the pulse with, what we considered, an appropriate fitting function. In Figure A.30A, we have plotted a pulse as provided by the Lecroy scope. The sampling rate was of 1 GHz. The amplitude provided is in mV. We see clearly that the pulse is not symmetric in respect to its maximum. We have tried to take this into account by using asymmetric fitting functions. The best result we have obtained though, was by simply using a gaussian fit. An explanation for this can probably be found in the enhancement of the gaussian fit procedure in the analysis framework Root.

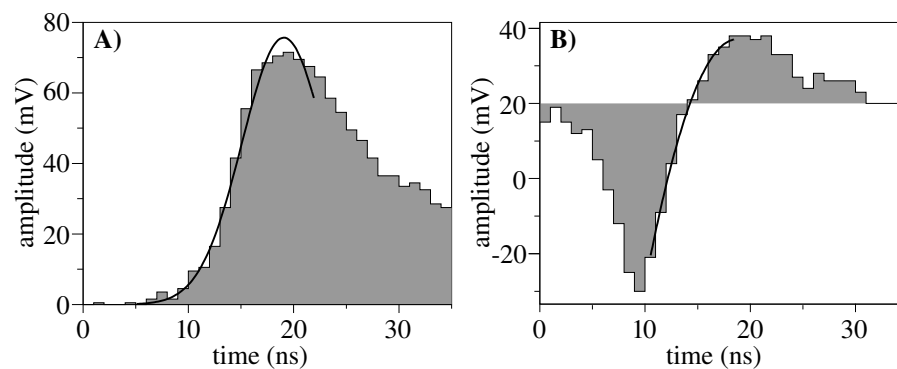


Figure A.30: In A, an electronic pulse as detected with the Lecroy oscilloscope. The arrival time of the pulse has been fitted with a gaussian function. In B, the same pulse undergoes the constant fraction discriminator process. The zero point is obtained through the fitting of a second order polynomial.

For the fitting procedure, we first determine the maximum of the pulse. Then we fit the pulse with user defined boundaries in respect to this maximum. Figure A.30A shows the result of a gaussian fit. Although this fit seems inappropriate, we must note that the systematic errors due to the fitting procedure occur on the 4 channels. When defining the position, the systematic errors are subtracted, and

have far less influence as to the quality of the result. Although the systematic errors depend strongly on the amplitude of the pulse, the fact that for a same atom, the four pulses have similar amplitudes also reduces this problem. Consequently, the quality of the fitting procedure is more related to the stability of the fit rather than the choice of the function. As the gaussian function has been most optimised, it provides the best results.

The second approach we have tried was to simulate the constant fraction discriminator. In the constant fraction discriminator, the signal is split into two. One signal is delayed by a time τ , the other is amplified with a factor k generally smaller than 1. The two signals are then compared. Figure A.30B shows the result of the comparison, with $\tau = 4$ ns and $k = 1$. The point at which the resulting pulse equals zero corresponds to the arrival time. In order to obtain sub-nanosecond resolution, the pulse is fitted through a second-order polynomial.

A.3.3 Discussion

It is interesting to consider that the constant fraction discriminator method provides better results than the fitting procedure. For the same data samples, the fitting procedure provides us with $316 \mu\text{m}$ average resolution, whereas the constant fraction discriminator method has a $272 \mu\text{m}$ resolution. The constant fraction discriminator is the tool currently employed electronically on the experiment. It is interesting to realise that its concept stands up against more complex methods.

We have also changed both the amplification factor k and the delay τ . The best results have clearly been obtained with $k = 1$. This can be explained by the relatively high noise level on the 8 bits oscilloscope. We can consider that 2 bits were lost to noise, and one bit has been lost to inappropriate scaling. Therefore, we effectively worked with a 5 bits scope. This is not overwhelming. In the constant fraction discriminator method, the effective noise is reduced as different acquisition points are compared. This noise reduction is maximised if the two pulses have equal weight.

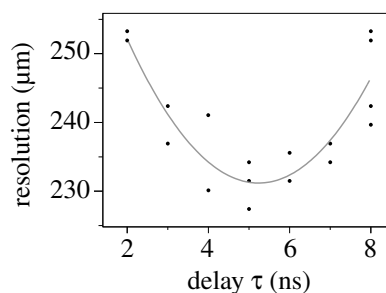


Figure A.31: The resolution of the detector for 1 mK time-of-flights versus the delays of the simulated delay-line discriminators. The data has been acquired at 2.5 GHz sampling rate.

More interestingly, the quality of the constant fraction discriminator procedure as a function of τ shows a behaviour similar to the delay of the electronic device as considered in Figure 2.18. In Figure A.31 we have plotted the average resolution as a function of τ as measured with the oscilloscope. We observe a similar optimum for $\tau = 5$ ns. For this data, a sampling rate of 2.5 GHz has been used.

Concerning the 2.5 GHz sampling rate, we observe globally a better resolution than at 1 GHz. We are not yet up to the standards we have obtained with a classical electronic constant fraction discriminator for similar clouds. This means that either an even higher sampling rate, or a better resolution of the scope is required. In both cases, this means an even higher amount of data for similar performances as obtained with simple electronics. The fact that also the oscilloscope is much more expensive than the electronic equivalent, makes us fairly happy with our current detection system.

An interesting advantage of the oscilloscope method is though that it provides us with the pulse height for all the atoms. This enabled us to produce the graphs depending on the pulse height shown in Chapter 2. Furthermore, a more complicated analysis as implemented by [77] might give us better resolution through the oscilloscope method. We have not taken the time yet to implement their algorithm.

Résumé

Introduction

L'effet Hanbury Brown et Twiss a été mis en évidence pour la première fois en 1956 [1], par Robert Hanbury Brown et Richard Q. Twiss. Leur recherche initiale portait sur le contournement des contraintes intrinsèques à l'interférométrie de Michelson dans la mesure des tailles angulaires des objets célestes. Ceci les a amenés à inventer le concept d'interférométrie d'intensité [2]. Dans leur domaine de l'astronomie radio, cette méthode ouvrait de nouvelles mesures [3]. Mais ce fut quand ils appliquèrent une technique similaire à une source de lumière thermique [1], que les corrélations qu'ils mirent en évidence étonnèrent la communauté scientifique.

Ils montrèrent que les photons provenant d'une source de lumière chaotique étaient corrélés; la probabilité pour des photons d'arriver de manière groupée était supérieure à la probabilité que ces photons arrivent de manière totalement aléatoire. Cette tendance au groupement de photons indépendants allait à l'encontre de l'idée classique que certains scientifiques se concevaient des photons. Cette expérience fut par conséquent une véritable percée dans la physique moderne, et il a fallu attendre 1962 pour que Roy J. Glauber définisse une description théorique complète de ce phénomène photonique quantique [4, 5]. Cette expérience et sa théorie ouvrirent la voie à l'optique quantique moderne. En 2005 le prix Nobel de physique a été attribué à Roy J. Glauber précisément pour son travail sur l'effet Hanbury Brown et Twiss et sa description quantique des champs de lumière.

De nos jours, l'effet Hanbury Brown et Twiss est utilisé dans des domaines variés allant de l'astronomie à la physique des particules. Des observations ont été réalisées avec les photons bosoniques, autant qu'avec des électrons fermioniques [6, 7, 8]. L'observation sur des atomes massifs était encore un défi à relever. Masami Yasuda et Fujio Shimizu l'ont relevé en 1996 en observant des corrélations entre atomes de Néon provenant d'un nuage d'atomes refroidis par Laser [10].

Le domaine des atomes froids a depuis atteint des températures autrement plus froides, en particulier à travers le refroidissement évaporatif, et le seuil de condensation de Bose-Einstein a été franchi en 1995 [11, 13, 12]. La condensation de Bose-Einstein d'atomes d'hélium métastables en 2001 [14, 15] a ouvert la voie à une étude plus approfondie, et particulièrement le changement fondamental de l'effet Hanbury Brown et Twiss au seuil de condensation. Le refroidissement évaporatif d'atomes métastables d'hélium fermioniques en 2006 [16] a en particulier permis de mesurer l'effet Hanbury Brown et Twiss sur des particules fermioniques électriquement neutres.

La réussite de la mesure dans une expérience de l'effet Hanbury Brown et Twiss avec des atomes d'hélium métastables serait sans aucun doute intéressante. Mais plus particulièrement, cette réussite démontrerait notre capacité à étudier des

systèmes quantiques à l'échelle d'une cellule de l'espace des phases. Cela signifie encore que nous pourrions mesurer des corrélations quantiques dans virtuellement toutes les systèmes quantiques que nous propose la physique des atomes froids moderne. C'est cette motivation qui soutient le travail présenté.

Cette Thèse

Cette thèse décrit la réalisation de ces expériences conduites sur la période 2003-2006. En tant que membre de l'équipe Hélium Métastable du groupe d'Optique Atomique de l'Institut d'Optique à Orsay, mon travail a été supervisé par Christoph Westbrook. Pendant ces années, nous sommes passé progressivement de la préparation du montage expérimental, ce qui a entraîné une lutte acharnée avec le système de refroidissement des atomes, à la réalisation expérimentale des expériences et l'analyse des données. Des efforts particuliers ont été investi dans la mise en oeuvre et la compréhension de la chaîne d'acquisition.

Cette thèse décrit avec application l'effet Hanbury Brown et Twiss et notre proposition expérimentale de sa mesure. Elle se concentre longuement sur la méthode de détection dans la mesure où le détecteur est la clé de l'expérience. Enfin, cette thèse décrit les mesures expérimentales effectuées sur les nuages thermiques et les condensats de Bose-Einstein de ^4He en 2005 à l'Institut d'Optique à Orsay, et sur les nuages thermiques fermioniques de ^3He en 2006 en collaboration avec le Laser Centrum à l'université Libre d'Amsterdam [18].

Bien que l'auteur de cette thèse ait participé activement à l'aboutissement de ces recherches, les résultats présentés proviennent indiscutablement d'un travail d'équipe. Avec Rodolphe Hoppeler et Denis Boiron, nous avons entrepris le démontage et remontage difficile du montage expérimental, nécessaire à l'accueil du détecteur. Nous avons été rejoint pendant l'été 2004 par Aurélien Perrin. Les connaissances et analyses d'Alain Aspect et Christoph Westbrook se sont montrées particulièrement utiles lors de notre compréhension, analyses et publications des résultats. L'équipe perdit Rodolphe Hoppeler, mais fut complétée par Hong Chang et Valentina Krachmalnicoff pendant l'été 2005. Avec cette dernière, nous nous sommes penchés plus intensivement sur les faiblesses du détecteur et son amélioration. Le travail expérimental réalisé par John McNamara, Tom Jeldes et Wim Vassen, et leur maîtrise de leur dispositif expérimental, a permis le succes de notre collaboration à Amsterdam. L'étude théorique a pour l'essentiel été réalisé par Denis Boiron, Jose Viana Gomes et Michael Belsley [19].

Le Plan

Cette thèse est subdivisée en trois chapitres. Le premier chapitre analyse l'effet Hanbury Brown et Twiss. Nous détaillerons ainsi l'histoire liée à sa mesure, et arriverons à une compréhension simple de sa théorie. Nous aborderons alors l'intérêt de l'optique atomique en rapport avec l'effet Hanbury Brown et Twiss, et nous étudierons brièvement quelques autres mesures de l'effet Hanbury Brown et Twiss qui ont été réalisées dans ce domaine avant ou pendant cette thèse. Enfin nous nous concentrons sur l'étude présente : la mesure de l'effet Hanbury Brown et Twiss dans un gaz d'atomes d'hélium métastable à travers un détecteur sensible en position à base de galettes à micro-canaux. Nous produirons une description

théorique simple mais complète de l'expérience.

Le deuxième chapitre analyse la chaîne de détection. Nous discuterons brièvement les options que nous avons quant au détecteur. Nous passerons ensuite en revue toute la chaîne de détection d'un détecteur à base de galettes à micro-canaux combinées à des lignes à retard, le seul détecteur qui était compatible avec nos besoins. Nous nous attarderons finalement sur trois caractéristiques primordiales du détecteur : l'efficacité de détection, le taux d'acquisition et la résolution.

Dans le troisième chapitre, nous aborderons l'acquisition et l'analyse de données expérimentales. Nous évoquerons d'abord les nuages thermiques de ^4He que nous avons produites à Orsay, et qui font état de l'effet Hanbury Brown et Twiss. Ensuite nous analyserons l'acquisition faite de quelques condensats de Bose-Einstein, dont les propriétés de cohérence conduisent à l'absence de l'effet Hanbury Brown et Twiss. Enfin, nous parlerons des nuages thermiques des fermions ^3He que nous avons produites à Amsterdam, et qui montrent un effet Hanbury Brown et Twiss négatif.

L'Effet Hanbury Brown et Twiss

L'effet Hanbury Brown et Twiss a été découvert en 1952 [2, 3] quand l'astrophysicien Robert Hanbury Brown (1916-2002) chercha un moyen de mesurer la taille angulaire d'objets célestes, en contournant quelques limitations d'ordre technique de l'interférométrie de Michelson dans le domaine des ondes radios. Pour l'interférométrie de Michelson, la lumière émise par une source se voit interférer avec elle-même après avoir parcourue deux chemins optiques différents. Deux télescopes spatialement séparés collectent ainsi la lumière émise par une source thermique, et les deux faisceaux ainsi reçus sont superposés. Le contraste de la figure d'interférence obtenue renseigne alors sur la cohérence des deux faisceaux. Pour une source non-punctuelle, l'étendue de la zone de cohérence au niveau des télescopes est alors donnée par la longueur de cohérence:

$$l_c = \lambda/\theta \quad (\text{A.3.1})$$

où λ correspond à la longueur d'onde de la source, θ la taille angulaire de la source vue des télescopes.

Hanbury Brown et Twiss décidèrent, plutôt que de faire interférer les deux amplitudes, de mesurer l'intensité lumineuse reçue sur chaque télescope, et de corrélérer les fluctuations d'intensité. Lorsque les deux télescopes se trouvent dans la même zone de cohérence, ces fluctuations sont corrélées, tandis que si les détecteurs sont trop éloignés, il n'y a pas de corrélation. L'avantage de cette méthode était qu'elle permettait entre autres un dispositif beaucoup moins coûteux. C'est quand ils répétèrent l'expérience sur une source de lumière visible [1] que l'expérience souleva une véritable contreverse. En utilisant des photo-multiplicateurs, et donc en faisant une détection de photons uniques, ils montrèrent que les photons issus d'une lampe de Sodium étaient corrélés. Ceci allait à l'encontre de l'image classique que de nombreux physiciens avaient de la statistique photonique.

Il a fallu attendre 1962 pour que R. Glauber [4, 5] écrive une théorie permettant de comprendre pleinement ce phénomène quantique. La raison de cette corrélation s'expliquait simplement par la nature bosonique des photons. Dans la statistique

d'apparence chaotique d'une source, l'émission d'un photon est stimulé dans les modes contenant déjà des photons. Par conséquent, la probabilité de détecter un photon dans un mode où on a déjà détecté un premier photon, est plus élevée que de détecter ce photon dans un mode quelconque. Si les particules avaient été des fermions, le principe d'exclusion de Pauli aurait précisément interdit des nombres d'occupation supérieurs à 1, et la corrélation aurait manifesté une anti-corrélation dans la zone de cohérence. Enfin, si la source de lumière avait été une source cohérente, tel un laser, tous les photons auraient été dans le même mode quantique, et leur détection individuel à l'intérieur de ce mode serait parfaitement aléatoire. Les photons provenant d'une source cohérente ne sont pas corrélés. Étant donné que l'effet Hanbury Brown et Twiss n'est dû qu'à la nature bosonique ou fermionique des atomes, cette corrélation peut se mesurer sur l'ensemble des particules. En particulier, elle s'applique aux atomes massifs.

L'avènement des méthodes de refroidissement des atomes [28, 29, 30] a permis d'étendre largement les propriétés quantiques des atomes. La création de sources d'atomes cohérentes [11, 13, 12] permettait ainsi d'étudier l'ensemble des trois cas mentionnés. Une première mesure de l'effet Hanbury Brown et Twiss a été faite par M. Yasuda et F. Shimizu en 1996 en utilisant une source thermique de bosons, du néon métastable $^{20}\text{Ne}^*$. La métastabilité de cet atome permet la détection d'atomes uniques à travers des galettes à micro-canaux. C'est cette même particularité que nous exploitons dans notre expérience. L'étude menée par Yasuda et Shimizu porte sur un nuage d'atomes à 1 mK. La condensation de l'hélium métastable ^4He réalisée en 2001 [14, 15] ainsi que le refroidissement sympathique de l'hélium métastable ^3He en 2006 [16], vont nous permettre d'étudier ces effets dans d'autres configurations.

Le principe de l'expérience est simple. Un nuage piégé d'hélium métastable est refroidi à des températures de l'ordre de $1\ \mu\text{K}$. Éventuellement, le refroidissement se poursuit jusqu'à la condensation de Bose-Einstein dans le cas des ^4He . Le piège est alors coupé afin que les atomes tombent sous l'effet de la gravité sur le détecteur un demi mètre plus bas. Les atomes sont détectés individuellement. Le temps de coupure du piège étant très bref, les positions et temps d'arrivée des atomes sont essentiellement déterminés par la distribution de vitesse initiale. L'effet Hanbury Brown et Twiss se traduit par la corrélation en temps et en position d'arrivée des atomes, qui suivent une trajectoire balistique. Les longueurs de corrélation attendus dans l'axe α au niveau du détecteur sont données par:

$$l_\alpha = \frac{\hbar t_0}{m s_\alpha} \quad (\text{A.3.2})$$

où s_α est la taille du nuage piégé selon cet axe, t_0 le temps de chute et m la masse des atomes. Considérant les températures à laquelle nous travaillons, ainsi qu'aux propriétés anisotropiques du piège, cela nous donne des longueurs de corrélation de respectivement $l_y = 800\ \mu\text{m}$ et $l_x = 32\ \mu\text{m}$ selon les deux axes communs au piège et au détecteur. Pour que nous puissions effectivement mesurer cette corrélation, il nous faut un pouvoir de résolution de l'ordre de $100\ \mu\text{m}$ au niveau du détecteur, et cela avec des taux de 10^6 atomes/s. Le détecteur que nous avons trouvé compatible avec ces besoins est le détecteur à base de galettes à micro-canaux combinées à des lignes à retard de Roentdek [81].

Le Détecteur

Les galettes à micro-canaux sont des plaques de verre, percées de trous, qui transforment l'arrivée d'une particule énergétique en un nuage d'électrons à travers une amplification en cascade. Les électrons ainsi produits par l'arrivée d'une seule particule, peuvent, vu leur nombre de 10^7 à 10^8 , être détectés à travers de l'électronique traditionnelle. La détection spatiale au niveau des galettes peut être effectuée à travers des dispositifs électroniques qui récupèrent localement les électrons. Celui à base de lignes à retard a retenu notre attention. Ainsi une simple ligne recueille, à travers des différences de potentiel, les électrons issus des galettes. De chaque côté de la ligne, on mesure les temps d'arrivée des impulsions électriques ainsi produites. En faisant la différence de ces temps, on remonte au point d'impact des électrons sur la ligne. En réalité, la ligne est bobinée sur la totalité de la surface, tant pour augmenter la précision de la mesure, que pour couvrir l'intégralité de la surface du détecteur. Sa longueur temporelle est ainsi de 80 ns. Enfin, la seconde dimension du positionnement est assurée par une deuxième ligne à retard bobinée perpendiculaire à la première.

Les performances du détecteur dépendent du système dans sa globalité. Ce système contient ainsi les galettes à micro-canaux et les lignes à retard, l'électronique de discrimination et de détection des impulsions, mais aussi notre capacité à comprendre et analyser informatiquement ces résultats. Une description complète du détecteur est donc nécessaire.

Nous constatons d'abord, une grande in-homogénéité de l'efficacité de détection. Cette in-homogénéité nous conduit à utiliser de grandes tensions d'opération pour ces galettes, que nous exploitons dans le mode comptage. Cela abaisse par contre les taux de saturation de ces galettes. Pour les lignes à retard nous nous contentons essentiellement d'une description et d'une caractérisation des tensions électriques d'opération. Nous utilisons un discriminateur à fraction constante pour avoir un temps d'arrivée qui ne dépend pas de la hauteur de l'impulsion électrique. Ce temps est mesuré avec un convertisseur temps-numérique d'une résolution de 400 ns. Ce convertisseur transfère les données vers l'ordinateur chargé de l'enregistrement et de l'analyse.

Le système de détection est caractérisé par trois propriétés essentielles. L'efficacité de détection n'influe que peu sur le résultat de la mesure de l'effet Hanbury Brown et Twiss. Elle serait primordiale pour des expériences d'intrication. Sa calibration n'a jamais été faite de manière très approfondie. Nous proposons toutefois deux mesures, avec des méthodes sans doute plus intéressantes que les résultats.

Le taux maximal de détection a été un des facteurs limitants de l'expérience. Plusieurs éléments interviennent. Les galettes saturent quand le nombre d'électrons extraits est trop important. Cela conduit essentiellement à une saturation locale estimée à 82 katomes/cm²/s. Il y a un temps mort attribué à l'électronique de conversion, mais aussi à l'utilisation des lignes à retard. Il est ainsi impossible de reconstruire les positions de deux atomes qui sont arrivés dans un interval de temps trop court. Dans la pratique, cela vaut 140 ns pour le détecteur. Le dernier facteur limitant a été le convertisseur. Un premier convertisseur nous limitait ainsi à 700 katomes/s. Cette limitation forte nous a amené à faire développer un nouveau convertisseur qui a une limite théorique de 12 Matomes/s.

La résolution s'avère aussi une propriété complexe. Le premier point à con-

stater est que la redondance partielle des mesures, 4 temps d'arrivée pour les deux lignes pour trois coordonnées, va permettre de mesurer cette résolution à la volée sur des données quelconques. Elle dépend ainsi de la hauteur des impulsions électroniques extraites des galettes, de la position sur la galette, du taux local d'atomes et même du bruit électronique ambiant. En pratique cette résolution est de l'ordre de $250 \mu\text{m}$.

Ainsi, de part ses caractéristiques, ce détecteur est juste compatible avec nos besoins. La résolution, au moins 10 fois plus grande que ce qu'il nous faudrait pour les longueurs de corrélation les plus courtes, devrait baisser le contraste de la corrélation d'autant. Par ailleurs, les taux de détection devraient limiter nos ambitions en termes de flux. En particulier, le flux maximal local risque de compromettre la détection des condensats.

Les Résultats

Nous présentons les trois groupes de résultats principaux. Le premier groupe concerne les nuages thermiques de bosons. Nous avons pris trois séries d'environ 1000 mesures autour de $0.61 \mu\text{K}$, $1.03 \mu\text{K}$ et $1.48 \mu\text{K}$. Parce que le piège est harmonique, la taille de la source initiale dépend de la température. L'utilisation de ces séries permettra ainsi de vérifier les dépendances des longueurs de corrélation. Pour observer les corrélations, on fait l'histogramme tridimensionnelle de toutes les différences de positions et de temps d'arrivée des atomes. On observe alors aisément une petite excroissance dans la fonction de corrélation gaussienne (la distribution de vitesse est gaussienne), de l'ordre de 5%, qui correspond, compte tenu de la résolution, à l'effet Hanbury Brown et Twiss recherché. Après normalisation, on peut procéder à des mesures des longueurs de corrélation selon les trois axes. Ces mesures sont en accord avec les résultats attendus. En particulier, le volume équivalent du regroupement dans la fonction de corrélation ne dépend pas de la résolution; sa valeur est en parfait accord avec les résultats attendus. Le rapport signal à bruit est de l'ordre de 10 sur cette dernière mesure.

Le deuxième groupe concerne les condensats de Bose-Einstein. Il convient d'abord de remarquer que ces condensats ne sont pas purs. Pour un grand nombre de nuages, la partie thermique de la distribution était encore significative. L'utilisation de la résolution tridimensionnelle du détecteur permet toutefois d'éliminer l'essentiel des atomes thermiques, la fraction thermique sous le condensat étant en densité négligeable par rapport à celle du condensat. Cette densité va d'ailleurs saturer le détecteur localement. De part le mécanisme de saturation, cela se traduit dans les faits par une détection quasi exclusive des fronts d'arrivée des condensats. Afin que le moyennage puisse se faire, et que la normalisation de toutes ces nuages différentes puisse s'effectuer, cette saturation va nécessiter un redressement spatio-temporelle des données. Ce redressement limite un peu l'interprétation des données. Dans la limite des séparations supérieures à $200 \mu\text{m}$, la fonction de corrélation ne montre pas de corrélations particulières, comme attendue pour une source cohérente.

Enfin, le dernier groupe concerne les fermions acquis à l'université d'Amsterdam. Là encore nous avons trois séries autour de $0.53 \mu\text{K}$, $0.99 \mu\text{K}$ et $1.4 \mu\text{K}$. En procédant de la même manière que pour les bosons, on observe un anti-groupement dans

la fonction de corrélation. Cet anti-groupement s'accorde à la théorie avec une qualité similaire que dans le cas des bosons. Le rapport signal à bruit varie de 20 à la température la plus basse, à 7 pour la température la plus élevée.

Conclusion

L'intérêt de l'étude présentée ne se situe pas particulièrement dans la démonstration de l'effet Hanbury Brown et Twiss. Naturellement, les résultats apportés ont un rapport signal à bruit particulièrement élevé comparé à des études précédentes, et la simplicité conceptuelle de l'expérience la rend particulièrement illustratrice.

L'intérêt principal de ce travail se situe dans le fait qu'elle apporte à la communauté scientifique un outil particulièrement puissant quant à l'étude de l'optique quantique atomique. Nous avons constaté à travers cette thèse que le système de détection employé manifeste beaucoup de faiblesses. En particulier, nous avons regretté le gain in-homogène, ce qui a induit de nombreux effets complexes, ce qui a amplifié le problème de la saturation dans la mesure où il nous forçait à travailler à des gains élevés. Cette saturation a rendu particulièrement hasardeuse la détection des condensats. La mise en oeuvre très récente d'un autre paire de galettes à micro-canaux produites par un autre industriel, Hamamatsu Photonics, semble produire des résultats encourageants. Nous avons aussi constaté que la résolution n'était pas au niveau attendu. D'autres utilisateurs de systèmes de détection similaires disent avoir des résolutions de $100 \mu\text{m}$. Il n'est donc pas exclu que du progrès puisse être réalisé dans ce domaine. Néanmoins, même avec tous ces défauts, la combinaison de He^* avec un détecteur à base de lignes à retard et de galettes à micro-canaux a détrôné l'ensemble des autres expériences d'atomes froids par la qualité de son rapport signal à bruit, et la multiplicité des configurations qu'elle est en mesure d'explorer.

Le rapport signal à bruit élevé, la haute résolution du système et la taille de la zone de détection couvrant plus de deux vitesses de recul rendent possible l'étude des corrélations de particules individuelles sur une grande variété de systèmes physiques. En particulier, pendant ces travaux, nous avons pu étudier un tel système différent.

L'expérience, qui sera décrite exhaustivement dans la thèse d'Aurélien Perrin, est une collision entre deux condensats de Bose-Einstein. Un condensat est divisé en deux parties qui sont accélérées optiquement à une vitesse de recul de photon. Le différentiel de vitesse provoque des collisions entre des atomes individuels des deux condensats. Ces collisions ponctuelles redistribuent l'impulsion de manière angulaire entre les deux atomes, et à mesure que les condensats se séparent de plus en plus, une sphère collisionnelle est formée contenant tous les atomes ayant subis une collision. Le principe même d'une collision à deux particules induit que si on trouve une particule à un angle donné dans la sphère de collision, on retrouve nécessairement son partenaire intriqué dans la direction opposée. Grâce à l'utilisation des lignes à retard, nous avons pu mettre en évidence expérimentalement cette corrélation.

Plus intéressant encore, cette expérience nous a ramené à l'effet Hanbury Brown et Twiss. L'effet Hanbury Brown et Twiss est souvent considéré comme un effet quantique résultant d'une certaine distribution thermique. Cela est le cas pour

une source thermique optique classique, ou comme dans cette étude pour un gaz atomique. Mais l'effet Hanbury Brown et Twiss s'applique à toute phénomène quantique incohérente. En particulier, la distribution angulaire aléatoire des paires atomiques est un phénomène quantique incohérent. Cela signifie que la distribution angulaire des atomes après la collision obéit à des statistiques du type Hanbury Brown et Twiss. De la même manière que précédemment pour le gaz thermique, les atomes se regroupent préférentiellement sur la sphère de collision. Nous l'avons démontré expérimentalement.

Ce que nous n'avons pas pu démontrer jusqu'à présent, c'est que cet effet Hanbury Brown et Twiss s'applique au pairs atomiques plutôt que sur les atomes individuels de la collision. Y parvenir reviendrait à démontrer expérimentalement l'intrication quantique des deux atomes, et lancerait le dispositif de l'hélium métastable directement dans le monde moderne de l'optique quantique. Tous les outils sont prêts pour cet évènement.

Bibliography

- [1] R. HANBURY BROWN & R. Q. TWISS, “Correlation between photons in two coherent beams of light”, *Nature* **177**, 27 (1956)
- [2] R. HANBURY BROWN & R. Q. TWISS, “A new type of interferometer for use in radio astronomy”, *Phil. Mag.* **45**, 663–82 (1954)
- [3] R. HANBURY BROWN, R. C. JENNISON, & M. D. DAS GUPTA, “Apparent Angular Sizes of Discrete Radio Sources: Observations at Jodrell Bank, Manchester”, *Nature* **170**, 1061 (1952)
- [4] R. J. GLAUBER, “Photon correlations”, *Phys. Rev. Lett.* **10**, 84 (1963)
- [5] R. J. GLAUBER, “The quantum theory of optical coherence”, *Phys. Rev.* **130**, 2529 (1963)
- [6] M. HENNY, S. OBERHOLZER, C. STRUNK, T. HEINZEL, K. ENSSLIN, M. HOLLAND & C. SCHÖNENBERGER, “The fermionic Hanbury Brown and Twiss experiment”, *Science* **284**, 296-298 (1999)
- [7] W. D. OLIVER, J. KIM, R. C. LIU & Y. YAMAMOTO, “Hanbury Brown and Twiss-type experiment with electrons”, *Science* **284**, 299-301 (1999)
- [8] H. KIESEL, A. RENZ & F. HASSELBACH, “Observation of Hanbury Brown-Twiss anticorrelations for free electrons”, *Nature* **418**, 392-394 (2002)
- [9] F. SHIMIZU, K. SHIMIZU & H. TAKUMA, “Double slit interference with ultracold metastable Neon atoms”, *Phys. Rev. A* **46**, (1992)
- [10] M. YASUDA & F. SHIMIZU, “Observation of two-atom correlation of an ultracold Neon atomic beam”, *Phys. Rev. Lett.* **77**, 3090 (1996)
- [11] M. H. ANDERSON, J. R. ENSHER, M. R. MATTHEWS, C. E. WIEMAN, & E. A. CORNELL, “Observation of Bose-Einstein condensation in a dilute atomic vapor”, *Science* **269**, 198 (1995)
- [12] C. C. BRADLEY, C. A. SACKETT, J. J. TOLLETT, & R. G. HULET, “Evidence of Bose-Einstein condensation in an atomic gas with attractive interactions”, *Phys. Rev. Lett.* **75**, 1687 (1995)
- [13] K. B. DAVIS, M.-O. MEWES, M. R. ANDREWS, N. J. VAN DRUTEN, D. S. DURFEE, D. M. KURN, & W. KETTERLE, “Bose-Einstein Condensation in a Gas of Sodium Atoms”, *Phys. Rev. Lett.* **75**, 3969 (1995)
- [14] A. ROBERT, O. SIRJEAN, A. BROWAEYS, J. POUPARD, S. NOWAK, D. BOIRON, C. I. WESTBROOK, & A. ASPECT, “A Bose-Einstein condensate of metastable atoms”, *Science* **292**, 461 (2001)

- [15] F. PEREIRA DOS SANTOS, J. LÉONARD, J. WANG, C. J. BARRELET, F. PERALES, E. RASEL, C. S. UNNIKRISHNAN, M. LEDUC, & C. COHEN-TANNOUJJI, “Bose-Einstein Condensation of metastable helium”, *Phys. Rev. Lett.* **86**, 3459 (2001)
- [16] J. M. MCNAMARA, T. JELTES, A. S. TYCHKOV, W. HOGERVORST, & W. VASSEN, “ Degenerate Bose-Fermi mixture of metastable atoms”, *Phys. Rev. Lett.* **97**, 080404 (2006)
- [17] M. SCHELLEKENS, R. HOPPELER, A. PERRIN, D. BOIRON, A. ASPECT & C. I. WESTBROOK, “Hanbury Brown Twiss effect for ultracold quantum gases”, *Science* **310**, 648-951 (2005)
- [18] T. JELTES, J. MCNAMARA, W. HOGERVORST, W. VASSEN, V. KRACHMALNICOFF, M. SCHELLEKENS, A. PERRIN, H. CHANG, D. BOIRON, A. ASPECT & C.I. WESTBROOK, “Hanbury Brown Twiss effect for bosons versus fermions”, *Nature* **445**, 402 (2007)
- [19] J. VIANA GOMES, A. PERRIN, M. SCHELLEKENS, D. BOIRON, C. I. WESTBROOK & M. BELSLEY, “ Theory for a Hanbury Brown Twiss experiment with a ballistically expanding cloud of cold atoms”, *Phys. Rev. A* **74**, 053607 (2006)
- [20] G. GALILEI, “ Dialogo sopra i due massimi sistemi del mondo”, (1632)
- [21] A. A. MICHELSON, “On the application of interference methods to astronomical measurements”, *ApJ* **51**, 257 (1920)
- [22] A. A. MICHELSON & F. G. PEASE, “Measurement of the diameter of α -Orionis with the interferometer”, *ApJ* **53**, 249 (1921)
- [23] J. P. GORDON, H. J. ZEIGER & C. H. TOWNES, “Molecular microwave oscillator and new hyperfine structure in the microwave spectrum of NH_3 ”, *Phys. Rev.* **95**, 282-284 (1954)
- [24] T. H. MAIMAN, “Stimulated optical radiation in ruby”, *Nature* **187**, 493-494 (1960)
- [25] M. IANNUZZI, A. ORECCHINI, F. SACCHETTI, P. FACCHI, & S. PASCAZIO, “ Direct Experimental Evidence of Free-Fermion Antibunching”, *Phys. Rev. Lett.* **96**, 080402 (2006)
- [26] A. EINSTEIN, “Über die Erzeugung und Verwandlung des Lichtes betreffenden heuristischen Gesichtspunkt”, *Ann. d. Phys.* **17**, 132 (1905)
- [27] L. DE BROGLIE, “Recherches sur la théorie des quanta”, *Thèse de doctorat, Faculté des Sciences de Paris*, (1924)
- [28] S. CHU, L. HOLLBERG, J. E. BJORKHOLM, A. CABLE & A. ASHKIN, “Three-dimensional viscous confinement and cooling of atoms by resonance radiation pressure”, *Phys. Rev. Lett.* **55**, 48-51 (1985)

- [29] P. D. LETT, R. N. WATTS, C. I. WESTBROOK, W. D. PHILLIPS, P. L. GOULD & H. J. METCALF, “Observation of atoms laser cooled below the Doppler limit”, *Phys. Rev. Lett.* **61**, 169-172 (1988)
- [30] J. DALIBARD & C. COHEN-TANNOUDJI, “Laser cooling below the Doppler limit by polarization gradients: simple theoretical models”, *J. Opt. Soc. Am. B* **6**, 2023-2045 (1989)
- [31] A. ÖTTL, S. RITTER, M. KÖHL & T. ESSLINGER, “Correlations and counting statistics of an atom laser”, *Phys. Rev. Lett.* **95**, 090404 (2005)
- [32] E. ALTMAN, E. DEMLER, & M. D. LUKIN, “Probing many-body states of ultracold atoms via noise correlations”, *Phys. Rev. A* **70**, 013603 (2004)
- [33] S. FÖLING, F. GERBIER, A. WIDERA, O. MANDEL, T. GERICKE & I. BLOCH, “Spatial quantum noise interferometry in expanding ultracold atom clouds”, *Nature* **434**, 481 (2005)
- [34] T. ROM, TH. BEST, D. VAN OOSTEN, U. SCHNEIDER, S. FÖLLING, B. PAREDES & I. BLOCH, “Free fermion antibunching in a degenerate atomic Fermi gas released from an optical lattice”, *Nature* **444**, 733-736 (2006)
- [35] J. ESTEVE, J.-B. TREBBIA, T. SCHUMM, A. ASPECT, C. I. WESTBROOK, & I. BOUCHOULE, “Observations of density fluctuations in an elongated Bose gas: ideal gas and quasicondensate regimes”, *Phys. Rev. Lett.* **96**, 130403 (2006)
- [36] J. POUPARD, “Mesure de deux caractéristiques de l’hélium métastable importantes pour le refroidissement radiatif”, *Thèse de doctorat, Université Paris-Sud*, 2000.
- [37] G. LACH & K. PACHUCKI, “Forbidden transitions in the helium atom”, *Phys. Rev. A* **64**, 042510 (2001)
- [38] J. R. WOODWORTH & H. W. MOOS, “Experimental determination of the single-photon transition rate between the 2^3S_1 and 1^1S_0 states of He_I ”, *Phys. Rev. A* **12**, (1975)
- [39] G. W. F. DRAKE, “Theory of relativistic magnetic dipole transitions: life time of the metastable 2^3S state of the heliumlike ions”, *Phys. Rev. A* **3**, (1971)
- [40] S. MOAL, M. PORTIER, J. KIM, J. UGUÉ, U. D. RAPOL, M. LEDUC, & C. COHEN-TANNOUDJI, “Accurate determination of the scattering length of metastable Helium atoms using dark resonances between atoms and exotic molecules”, *Phys. Rev. Lett.* **96**, 023203 (2006)
- [41] J. KIM, S. MOAL, M. PORTIER, J. DUGUÉ, M. LEDUC, & C. COHEN-TANNOUDJI, “Frequency shifts of photoassociative spectra of ultracold metastable Helium atoms : a new measurement of the s-wave scattering length”, *Europhys. Lett.* **72**, 548-554 (2005)
- [42] F. BARDOU, O. EMILE, J.-M. COURTY, C. I. WESTBROOK & A. ASPECT, “Magneto-optical trapping of metastable helium: collisions in the presence of resonant light”, *Europhys. Lett.* **20**, 681 (1992)

- [43] P. J. J. TOL, N. HERSCHBACH, E. A. HESSELS, W. HOGERVORST, and W. VASSEN, “Large numbers of cold metastable helium atoms in a magneto-optical trap”, *Phys. Rev. A* **60**, R761-R764 (1999)
- [44] G. V. SHLYAPNIKOV, J. T. M. WALRAVEN, U. M. RAHMANOV & M. W. REYNOLDS, “Decay kinetics and Bose condensation in a gas of spin-polarized triplet Helium”, *Phys. Rev. Lett.* **73**, 3247 (1994)
- [45] P. O. FEDICHEV, M. W. REYNOLDS, U. M. RAHMANOV, G. V. SHLYAPNIKOV, “Inelastic decay processes in a gas of spin-polarized triplet helium”, *Phys. Rev. A* **53**, 1447 (1996)
- [46] A.S. TYCHKOV, T. JELTES, J.M. MCNAMARA, P.J.J. TOL, N. HERSCHBACH, W. HOGERVORST & W. VASSEN, “Metastable helium Bose-Einstein condensate with a large number of atoms”, *Phys. Rev. A* **73**, 031603 (2006)
- [47] R.G. DALL & A.G. TRUSCOTT, “Bose-Einstein condensation of metastable helium in a biplanar quadrupole Ioffe configuration trap”, *Optics Communications* **270**, 255 (2007)
- [48] O. SIRJEAN, S. SEIDELIN, J. V. GOMES, D. BOIRON, C. I. WESTBROOK, A. ASPECT & G. V. SHLYAPIKOV, “Ionization rates in a Bose-Einstein condensate of Metastable Helium”, *Phys. Rev. Lett.* **89**, 220406 (2002)
- [49] S. SEIDELIN, O. SIRJEAN, J. V. GOMES, D. BOIRON, C. I. WESTBROOK, and A. ASPECT, “Using ion production to monitor the birth and death of a metastable helium Bose-Einstein condensate”, *J. Opt. B* **5**, 112 (2003).
- [50] N. HERSCHBACH, P. TOL, A. TYCHKOV, W. HOGERVORST & W. VASSEN, “Magnetic trapping and evaporative cooling of metastable triplet helium”, *J. Opt. B: Quantum Semiclass. Opt.* **5** (2003)
- [51] S. NOWAK, A. BROWAEYS, J. POUPARD, A. ROBERT, D. BOIRON, C. WESTBROOK, & A. ASPECT, “Magnetic trapping of metastable helium atoms”, *Appl. Phys. B* **70**, 455 (2000)
- [52] A. P. CHIKKATUR, Y. SHIN, A. E. LEANHARDT, D. KIELPINSKI, E. TSIKATA, T. L. GUSTAVSON, D. E. PRITCHARD, W. KETTERLE , “A continuous source of Bose-Einstein condensed atoms”, *Science* **296**, 2193-2195 (2002)
- [53] T. LAHAYE, Z. WANG, G. REINAUDI, S. P. RATH, J. DALIBARD & D. GUÉRY-ODELIN, “Evaporative cooling of a guided rubidium atomic beam”, *Phys. Rev. A* **72**, 033411 (2005)
- [54] P. SPODEN, M. ZINNER, N. HERSCHBACH, W. J. VAN DRUNEN, W. ERTMER & G. BIRKL, “ Collisional Properties of Cold Spin-Polarized Metastable Neon Atoms”, *Phys. Rev. Lett.* **94**, 223201 (2005)
- [55] M. PRZYBYTEK & B. JEZIORSKI , “ Bounds for the scattering length of spin-polarized helium from high-accuracy electronic structure calculations”, *J. Chem. Phys.* **123**, 134315 (2005)

- [56] J. VIANA GOMES “Thermométrie de propriétés de cohérence d’un gaz quantique ultra-froid d’hélium métastable” *Thèse de doctorat, Université de Paris XI*, (2007)
- [57] R. HOPPELER, “De la condensation de Bose-Einstein à l’effet Hanbury Brown et Twiss atomique de l’Hélium métastable”, *Thèse de doctorat, Université de Paris XI*, (2005)
- [58] S. SEIDELIN, “Collisions dans un gaz d’hélium métastable au voisinage de la dégénérescence quantique”, *Thèse de doctorat, Université de Paris XI*, (2004)
- [59] O. SIRJEAN, “Collisions ionisantes: un nouveau diagnostic pour les condensats d’hélium métastable”, *Thèse de doctorat, Université de Paris XI*, (2003)
- [60] A. ROBERT, “Réalisation d’un condensat de Bose-Einstein d’Hélium métastable”, *Thèse de doctorat, Université de Paris XI*, (2001)
- [61] A. BROWAEYS, “Piégeage magnétique d’un gaz d’Hélium métastable : vers la condensation de Bose-Einstein”, *Thèse de doctorat, Université de Paris VI*, (2000)
- [62] J. POUPARD, “Mesure de deux caractéristiques de l’hélium métastable importantes pour le refroidissement radiatif”, *Thèse de doctorat, Université de Paris XI*, (2000)
- [63] G. LABEYRIE, “Deux outils pour l’optique atomique : Jet intense d’hélium métastable et Miroir d’onde évanescente exaltée”, *Thèse de doctorat, Université de Paris XI*, (1998)
- [64] J. MCNAMARA, to be published, *Academisch Proefschrift, Vrije Universiteit Amsterdam*
- [65] A. TYCHKOV, to be published, *Academisch Proefschrift, Vrije Universiteit Amsterdam*
- [66] R. STAS, “Trapping fermionic and bosonic helium atoms”, *Academisch Proefschrift, Vrije Universiteit Amsterdam*, (2005)
- [67] P. TOL, “Trapping and evaporative cooling of metastable helium”, *Academisch Proefschrift, Vrije Universiteit Amsterdam*, (2005)
- [68] J. KOELEMEIJ, “Interaction of UV light with cold metastable helium atoms”, *Academisch Proefschrift, Vrije Universiteit Amsterdam*, (2004)
- [69] N. HERSCHBACH, “Trapped triplet helium atoms; Inelastic collisions and evaporative cooling”, *Academisch Proefschrift, Vrije Universiteit Amsterdam*, (2003)
- [70] M. NARASCHEWSKI & R. J. GLAUBER, “Spatial coherence and density correlations of trapped Bose gases”, *Phys. Rev. A* **59**, 4595-4607 (1999)
- [71] C. A. KOCHER & E. D. COMMINS, “Polarization correlation of photons emitted in an atomic cascade”, *Phys. Rev. Lett.* **18**, 575 (1967)

- [72] M. GREINER, C. A. REGAL, S. T. STEWARD & D. S. JIN, “Probing pair-correlated fermionic atoms through correlations in atom shot noise”, *Phys. Rev. Lett.* **94**, 110401 (2005)
- [73] A. PERRIN & AL. “Observation of correlated atom pairs through Bose-Einstein condensates collision”, to be published (2007)
- [74] A. ASPECT, P. GRANGIER & G. ROGER “Experimental realization of Einstein-Podolsky-Rosen-Bohr Gedankenexperiment: a new violation of Bell’s inequalities”, *Phys. Rev. Lett.* **49**, 91-94 (1982)
- [75] G. BATTISTONI, P. CAMPANA, V. CHIARELLA, U. DENNI, E. IAROCCI & G. NICOLETTI “Resistive cathode transparency”, *Nucl. Instr.* **202**, 459-464 (1982)
- [76] U. SPILLMANN, O. JAGUTZKI, L. SPIELBERGER, R. DÖRNER, V. MERGEL, K. ULLMANN-PFLEGER & H. SCHMIDT-BÖCKING “A novel delay-line anode design for position and time sensitive read-out of MCP-based detectors”, *Physica Scripta* **T92**, 225-226 (2001)
- [77] G. DA COSTA, F. VURPILLOT, A. BOSTEL, M. BOUET & B. DECONIHOUT “Design of a delay-line position-sensitive detector with improved performance”, *Rev. Sci. Instr.* **76**, 013304 (2005)
- [78] G. UDNY YULE “A mathematical theory of evolution, based on the conclusions of Dr. J. C. Willis, FRS”, *Philosophical Transactions of the Royal Society of London* **213**, 21-87 (1924)
- [79] J. WIZA, “Microchannel plate detectors”, *Nucl. Instr. and Meth.* **162**, 587 (1979)
- [80] Private communication at “Comité Utilisateurs de la plate-forme DTPI”, LCAM, Orsay (2006)
- [81] <http://www.roentdek.com/>
- [82] <http://root.cern.ch/>
- [83] B. DECONIHOUT, F. VURPILLOT, M. BOUET & L. RENAUD “Improved ion detection efficiency of microchannel plate detectors”, *Rev. Sci. Instr.* **73**, 1734-1740 (1996)
- [84] L. MANDEL & E. WOLF “Optical Coherence and Quantum Optics” , *Cambridge University Press*, (1995)
- [85] M. BORN & E. WOLF “Optics” , *Pergamon Oxford*, (1980)
- [86] A. EINSTEIN “Quantentheorie des einatomigen idealen Gases”, *Sitzungsber. Ber. Preuss. Akad. Wiss.* **1**, 3-14 (1925)
- [87] N. BONINI, G. P. BRIVIO & M. I. TRIONI “Theory of metastable deexcitation spectroscopy on simple metals”, *Phys. Rev. B* **68**, 035408.1-035408.9 (2003)

Publications

Here we provide the three letters that we have published in respect to the work presented in this thesis. The first letter deals with the theory associated to the experiment. It provides a theoretical description of the first and second order correlation functions in a ballistically expanding non-interacting bosonic clouds. Unlike the description found in this thesis, this letter also analyses the correlation around the condensation threshold.

The second letter deals with the bosonic data acquired in Orsay. It demonstrates our ability to detect the bosonic bunching behaviour in 3 dimensions. It shows in particular the temperature dependence of the correlation length for the thermal clouds. It also shows the correlation function for a Bose-Einstein condensate, demonstrating the second order coherence of those clouds.

The third letter deals with the data acquired in Amsterdam. It shows that we have been able to detect both the fermionic anti-bunching behaviour, as well as the bosonic bunching, on the same apparatus considering both $^3\text{He}^*$ and $^4\text{He}^*$. Furthermore, it demonstrates the increase of the coherence length through a defocalising atomic lens. This affects directly the measured anti-bunching height.

Theory for a Hanbury Brown Twiss experiment with a ballistically expanding cloud of cold atoms

J. Viana Gomes,^{1,2} A. Perrin,¹ M. Schellekens,¹ D. Boiron,^{1,*} C. I. Westbrook,¹ and M. Belsley²

¹Laboratoire Charles Fabry de l'Institut d'Optique, UMR 8501 du CNRS et Université Paris 11, 91403 Orsay Cedex, France

²Departamento de Física, Universidade do Minho, Campus de Gualtar, 4710-057 Braga, Portugal

(Received 19 June 2006; published 7 November 2006)

We have studied one-body and two-body correlation functions in a ballistically expanding, noninteracting atomic cloud in the presence of gravity. We find that the correlation functions are equivalent to those at thermal equilibrium in the trap with an appropriate rescaling of the coordinates. We derive simple expressions for the correlation lengths and give some physical interpretations. Finally a simple model to take into account finite detector resolution is discussed.

DOI: [10.1103/PhysRevA.74.053607](https://doi.org/10.1103/PhysRevA.74.053607)

PACS number(s): 03.75.Hh, 05.30.Jp

I. INTRODUCTION

Whether a source emits photons or massive particles, if it is to be used in an interferometric experiment, an essential property is its coherence. The study of coherence in optics has shown that more than one kind of coherence can be defined [1]. The most familiar type of coherence is known as first order coherence and is related to the visibility of interference fringes in an interferometer. It is proportional to the value of the correlation function of the associated field. Second order coherence is less intuitive and corresponds to the correlation function of the intensity or squared modulus of the field. From a particle point of view, second order coherence is a way of quantifying density correlations and is related to the probability of finding one particle at a certain location given that another particle is present at some other location. Particle correlations can arise simply from exchange symmetry effects and exist even when there is no interaction between the particles. This fact was clearly demonstrated in the celebrated Hanbury Brown Twiss experiment which showed a second order correlation for photons coming from widely separated points in a thermal source such as a star [2].

Analogous correlations in massive particles have also been studied, particularly in the field of nuclear physics [3–7]. Spatial correlations using low energy electrons have also been studied [8,9]. The advent of laser and evaporative cooling techniques has also made it possible to look for correlations between neutral atoms and recently a wide variety of different situations have been studied [10–16]. Correlation phenomena are generally richer when using massive particles because they can be either bosons or fermions, they often have a more complex internal structure and a large range of possible interactions with each other. In the field of ultracold atoms, the many theoretical papers to date have included treatments of bosons in a simple three-dimensional (3D) harmonic trap [17,18], a one-dimensional (1D) bosonic cloud in the Thomas-Fermi regime and Tonks-Girardeau limit [19–21], the Mott insulator or superfluid phase for atoms

trapped in optical lattices [22] and the two-dimensional (2D) gas [23].

Almost all these theoretical treatments have dealt with atomic clouds at thermal equilibrium. On the other hand, all the experiments so far except Ref. [16] have measured correlations in clouds released from a trap which expand under the influence of gravity and possibly interatomic interactions. It is generally not trivial to know how the correlation properties evolve during expansion. Moreover, matter waves have different dispersion characteristics than light. All this raises interesting questions concerning the value of the correlation lengths during the atomic cloud expansion. In particular we would like to know how to use the results of Ref. [17] to analyze the experimental results of Ref. [15], a conceptually simple experiment in which second order correlations were measured in a freely expanding cloud of metastable helium atoms. The correlation length was defined as the characteristic length of the normalized second order correlation function. We will use the same definition in this paper (see Sec. II A for details).

To illustrate a more general question that comes up in thinking about the coherence of de Broglie waves, consider a beam of particles with mean velocity v hitting a detector. Two obvious length scales come immediately to mind, the de Broglie wavelength $\hbar/(m\Delta v)$ associated with the velocity spread Δv and the length associated with the inverse of the energy spread of the source $\hbar v/m(\Delta v)^2$. These two scales are obviously very different if v is large compared to the velocity spread. In this paper, we will show that in an experiment such as Ref. [15], the correlation length corresponds to neither of the above length scales, although they can be relevant in other situations. We find that the correlation length after an expansion time t of a cloud of initial size s is $\hbar t/ms$. This result is the atom optical analog of the van Cittert-Zernike theorem [24]. It has also been stated in a different form in Ref. [25]. For the special case of an ideal gas in a harmonic trap of oscillation frequency ω , the correlation length can be recast as $\lambda\omega t$ where λ is the thermal de Broglie wavelength. Hence the correlation length after expansion is simply dilated compared to that at equilibrium with the same scaling factor as the spatial extent of the cloud itself.

We will confine ourselves here to the case of a cloud of noninteracting atoms released suddenly from a harmonic

*Electronic address: denis.boiron@institutoptique.fr; <http://www.atomoptic.fr>

trap. The paper is organized as follows. We will begin in Sec. II with some simple definitions and general results about the correlation properties of a noninteracting cloud both at thermal equilibrium in a trapping potential and after a ballistic expansion. Without making any assumptions about the form of the trapping potential, we can only find simple analytical results in the limit of a nondegenerate gas. Next we will make a more exact and careful treatment by specializing to the very important case of a harmonic potential. We introduce the flux operator [26] involved in the experimental electronic detection with metastable helium and then calculate the correlation function of the flux. We will summarize the results and give a physical interpretation in Sec. IV. This interpretation will allow us to comment on the rather different case of a continuous beam as in the experiments of Refs. [7,10,14]. In Sec. V we will use our results to analyze the experimentally important problem of finite detector resolution. Finally, the Appendix adds some detailed calculations concerning the expressions found in Sec. III B.

II. GENERAL RESULTS ON CORRELATION FUNCTIONS OF NONINTERACTING GASES

Here we recall some basic results concerning the density and first and second order correlation functions for a cloud of noninteracting bosons at thermal equilibrium. A more detailed analysis can be found in Ref. [17]. Theoretical treatments that take into account interatomic interactions can be found in Refs. [17,18,27]. We also give some approximate results for a noninteracting gas after it has expanded from a trap.

A. Definitions

Consider a cloud of N atoms at thermal equilibrium at a temperature T , confined in a trapping potential. This potential is characterized by $\{\epsilon_j, \psi_j^0(\mathbf{r})\}$ the energy and wave function of level j (here supposed nondegenerate for simplicity). In second quantization, one defines the field operators

$$\hat{\Psi}^\dagger(\mathbf{r}) = \sum_j \psi_j^*(\mathbf{r}) \hat{a}_j^\dagger, \quad \hat{\Psi}(\mathbf{r}) = \sum_j \psi_j(\mathbf{r}) \hat{a}_j.$$

The operator \hat{a}_j^\dagger creates and \hat{a}_j annihilates one particle in state $|\psi_j\rangle$ whereas $\hat{\Psi}^\dagger(\mathbf{r})$ creates and $\hat{\Psi}(\mathbf{r})$ annihilates a particle at position \mathbf{r} .

Correlation functions and the atomic density are statistical averages of such field operators. We use the Bose-Einstein distribution, $\langle \hat{a}_j^\dagger \hat{a}_k \rangle = \delta_{jk} (e^{\beta(\epsilon_j - \mu)} - 1)^{-1}$ where $\beta = 1/(k_B T)$, k_B is the Boltzmann constant and μ is the chemical potential. The value of μ ensures the normalization $\sum_j \langle \hat{a}_j^\dagger \hat{a}_j \rangle = N$. We can then define

(a) the first order correlation function $G^{(1)}(\mathbf{r}, \mathbf{r}') = \langle \hat{\Psi}^\dagger(\mathbf{r}) \hat{\Psi}(\mathbf{r}') \rangle$,

(b) the second order correlation function $G^{(2)}(\mathbf{r}, \mathbf{r}') = \langle \hat{\Psi}^\dagger(\mathbf{r}) \hat{\Psi}(\mathbf{r}) \hat{\Psi}^\dagger(\mathbf{r}') \hat{\Psi}(\mathbf{r}') \rangle$,

(c) and the density $\rho_{\text{eq}}(\mathbf{r}) = \langle \hat{\Psi}^\dagger(\mathbf{r}) \hat{\Psi}(\mathbf{r}) \rangle = G^{(1)}(\mathbf{r}, \mathbf{r})$.

Several other first and second order correlation functions can be defined (see below) but these are the most common

ones. The first order correlation function appears in interference experiments whereas second order correlation functions are related to intensity interference or density fluctuation. First and second order correlation functions are connected for thermal noninteracting atomic clouds. The $G^{(2)}$ function contains a statistical average of the type $\langle \hat{a}_j^\dagger \hat{a}_k \hat{a}_l^\dagger \hat{a}_n \rangle$ which can be calculated through the thermal averaging procedure (Wick theorem [28]). One finds $\langle \hat{a}_j^\dagger \hat{a}_k \hat{a}_l^\dagger \hat{a}_n \rangle = \langle \hat{a}_j^\dagger \hat{a}_j \rangle \langle \hat{a}_k^\dagger \hat{a}_k \rangle \times (\delta_{jl} \delta_{kn} + \delta_{jn} \delta_{kl}) + \langle \hat{a}_j^\dagger \hat{a}_j \rangle \delta_{kl} \delta_{jn}$, which leads to

$$G^{(2)}(\mathbf{r}, \mathbf{r}') = \rho_{\text{eq}}(\mathbf{r}) \rho_{\text{eq}}(\mathbf{r}') + |G^{(1)}(\mathbf{r}, \mathbf{r}')|^2 + \rho_{\text{eq}}(\mathbf{r}) \delta(\mathbf{r} - \mathbf{r}').$$

The last term is the so-called shot-noise term. It will be neglected in the following because it is proportional to N whereas the others are proportional to N^2 .

It is convenient to define a normalized second order correlation function

$$g^{(2)}(\mathbf{r}, \mathbf{r}') = \frac{G^{(2)}(\mathbf{r}, \mathbf{r}')}{\rho_{\text{eq}}(\mathbf{r}) \rho_{\text{eq}}(\mathbf{r}')}.$$

If the cloud has a finite correlation length, then for distances larger than this length the first order correlation function vanishes. Then $g^{(2)}(\mathbf{r}, \mathbf{r}) = 2$ and $g^{(2)}(\mathbf{r}, \mathbf{r}') \rightarrow 1$ when $|\mathbf{r} - \mathbf{r}'| \rightarrow \infty$. This means that the probability of finding two particles close to each other is enhanced by a factor of 2, compared to the situation where they are far apart. This is the famous bunching effect first observed by Hanbury Brown and Twiss with light [2].

The above expression of the $G^{(2)}$ function cannot be applied in the vicinity and below the Bose-Einstein transition temperature. The calculation of $\langle \hat{a}_j^\dagger \hat{a}_k \hat{a}_l^\dagger \hat{a}_n \rangle$ is performed in the grand canonical ensemble which assumes the existence of a particle reservoir that does not exist for the condensate. It is well known [29] that this gives unphysically large fluctuations of the condensate at low enough temperature. This pathology disappears at the thermodynamic limit if there is an interatomic interaction [29]. It has also been shown that it cancels for a finite number of noninteracting particles if one uses the more realistic canonical ensemble [30]. One way to keep using the grand canonical ensemble is to add the canonical result for the ground state [17]. This approach is validated by the results in Ref. [30] and will be used in the following. The largest deviation is expected to occur near the transition temperature [30]. The contribution of the ground state is $-\langle \hat{a}_0^\dagger \hat{a}_0 \rangle^2 \delta_{j0} \delta_{k0} \delta_{l0} \delta_{n0}$. Then, with ρ_0 the ground-state density, it follows that,

$$G^{(2)}(\mathbf{r}, \mathbf{r}') = \rho_{\text{eq}}(\mathbf{r}) \rho_{\text{eq}}(\mathbf{r}') + |G^{(1)}(\mathbf{r}, \mathbf{r}')|^2 - \rho_0(\mathbf{r}) \rho_0(\mathbf{r}'). \quad (1)$$

The normalized second-order then becomes

$$g^{(2)}(\mathbf{r}, \mathbf{r}') = 1 + \frac{|G^{(1)}(\mathbf{r}, \mathbf{r}')|^2}{\rho_{\text{eq}}(\mathbf{r}) \rho_{\text{eq}}(\mathbf{r}')} - \frac{\rho_0(\mathbf{r}) \rho_0(\mathbf{r}')}{\rho_{\text{eq}}(\mathbf{r}) \rho_{\text{eq}}(\mathbf{r}')}.$$

Because the ground state density is negligible for a thermal cloud, the normalized correlation function $g^{(2)}(\mathbf{r}, \mathbf{r}')$ still goes from 2 to 1 as the separation of \mathbf{r} and \mathbf{r}' increases. On the other hand, for a BEC at $T=0$, only the ground state is occupied. Then $|G^{(1)}(\mathbf{r}, \mathbf{r}')|^2 = \rho_{\text{eq}}(\mathbf{r}) \rho_{\text{eq}}(\mathbf{r}') = \rho_0(\mathbf{r}) \rho_0(\mathbf{r}')$ and

$g^{(2)}(\mathbf{r}, \mathbf{r}')=1$. The amount of particle bunching present in the second order correlation function can be quantified as $g^{(2)}(\mathbf{r}, \mathbf{r}')-1$ and this typically decays exponentially as the modulus squared of the separation between the two points increases. We define the correlation length to be the characteristic length over which the amount of particle bunching decays, that is the distance over which $g^{(2)}(\mathbf{r}, \mathbf{r}')-1$ decays to $1/e$ of its maximum value. The correlation length of a BEC is infinite. Such a system is said to exhibit bunching at high temperature over the correlation length and no bunching in the condensed phase.

B. Correlations in an expanding cloud

In most experiments, particle correlations and other characteristics are not directly measured in the atom cloud, (Ref. [16] is an exception). Rather, the cloud is released from a trap and allowed to expand during a “time of flight” before detection. For a sufficiently long time of flight, and neglecting interactions between the atoms, the positions one measures at a detector reflect the initial momenta of the particles. The results of Sec. II A concerning the correlation functions in position space all have analogs in momentum space. In fact the correlation functions in the two reciprocal spaces are closely related. At equilibrium, i.e., inside the trap, the following relationships can be easily derived:

$$\int d\mathbf{p}G^{(1)}(\mathbf{p}, \mathbf{p})e^{-i\mathbf{p}\cdot\mathbf{r}/\hbar} = \int d\mathbf{R}G^{(1)}(\mathbf{R} - \mathbf{r}/2, \mathbf{R} + \mathbf{r}/2),$$

$$\int d\mathbf{r}G^{(1)}(\mathbf{r}, \mathbf{r})e^{i\mathbf{q}\cdot\mathbf{r}/\hbar} = \int d\mathbf{P}G^{(1)}(\mathbf{P} - \mathbf{q}/2, \mathbf{P} + \mathbf{q}/2).$$

In other words, the spatial correlation length is related to the width of the momentum distribution and the momentum correlation length is related to the width of the spatial distribution, i.e., the size of the cloud. No equally simple and general relationship holds for the second order correlation functions. This is because, close to the BEC transition temperature, and at points where the ground state wave function is not negligible, the special contribution of the ground state, the last term in Eq. (1) must be included, and this contribution depends on the details of the confining potential. On the other hand, for an ideal gas far from the transition temperature one can neglect the ground state density, make the approximation that the correlation length is very short, neglect commutators such as $[\hat{\mathbf{r}}, \hat{\mathbf{p}}]$, and then write the thermal density operator as $\hat{\sigma} = e^{-\beta(\hat{\mathbf{P}}^2/2m)}e^{-\beta V(\hat{\mathbf{r}})}$. These approximations lead to

$$G^{(2)}(\mathbf{p}, \mathbf{p}') = \rho_{\text{eq}}(\mathbf{p})\rho_{\text{eq}}(\mathbf{p}') + |G^{(1)}(\mathbf{p}, \mathbf{p}')|^2$$

and

$$G^{(1)}(\mathbf{P} - \mathbf{q}/2, \mathbf{P} + \mathbf{q}/2) \sim e^{-\beta(\mathbf{P}^2/2m)} \int d\mathbf{r}e^{-\beta V(\mathbf{r})}e^{i\mathbf{q}\cdot\mathbf{r}/\hbar}.$$

One sees that in this limit, the interesting part of $G^{(2)}$ in momentum space is proportional to the square of the Fourier transform of the density distribution and independent of the

mean momentum \mathbf{P} . This result is the analog of the van Cittert-Zernike theorem [24]. For a trapped cloud of size s_α in the α direction, one has a momentum correlation “length” given by

$$l_\alpha^{(\text{coh})} = \frac{\hbar}{s_\alpha}. \quad (2)$$

If atoms are suddenly released from a trap and allowed to freely evolve for a sufficiently long time t , the positions of the particles reflect their initial momenta and the spatial correlation length at a detector is given by

$$l_\alpha^{(d)} = \frac{p_\alpha^{(\text{coh})}}{m}t = \frac{\hbar t}{ms_\alpha}. \quad (3)$$

The normalized second order correlation function is then a Gaussian of rms width $l^{(d)}/\sqrt{2}$. This result was experimentally confirmed in Ref. [15]. One wonders however, to what extent the approximations we have made are valid. The clouds used in Ref. [15] were in fact very close to the transition temperature so that effects due to the Bose nature of the density matrix may be important. Although the time of flight was very long, it is useful to quantify the extent to which identifying the momentum correlation length in the trap with the spatial correlation length at the detector is accurate. Finally, the effect of gravity on the falling atoms never appears in the above approximate treatment, and we would like to clarify the role it plays. In order to answer these questions we undertake a more careful calculation. We will confine ourselves to atoms initially confined in a harmonic trap, a good approximation to the potential used in most experiments, and happily, one for which the eigenstates and energies are known exactly.

III. DENSITY AND CORRELATION FUNCTIONS FOR A HARMONIC TRAP

A. At equilibrium in the trap

The eigenfunctions for a three-dimensional harmonic potential of oscillation frequency ω_α in the α direction, are given by

$$\psi_j^0(\mathbf{r}) = \prod_{\alpha=x,y,z} A_{j_\alpha} e^{-r_\alpha^2/2\sigma_\alpha^2} H_{j_\alpha}(r_\alpha/\sigma_\alpha).$$

Here $\sigma_\alpha = \sqrt{\hbar/m\omega_\alpha}$ is the harmonic oscillator ground-state size, H_{j_α} is the Hermite polynomial of order j_α and $A_{j_\alpha} = [\sqrt{\pi}\sigma_\alpha 2^{j_\alpha}(j_\alpha!)]^{-1/2}$. The eigenenergies are given by $\epsilon_j = \sum_{\alpha=x,y,z} \hbar\omega_\alpha(j_\alpha + 1/2)$. Then [17,29], with $\tau_\alpha = \beta\hbar\omega_\alpha$ and $\bar{\mu} = \mu - \hbar\sum\omega_\alpha/2$, one finds

$$\rho_{\text{eq}}(\mathbf{r}) = \frac{1}{\pi^{3/2}} \sum_{l=1}^{\infty} e^{\beta l \bar{\mu}} \prod_{\alpha} \frac{1}{\sigma_\alpha \sqrt{1 - e^{-2\tau_\alpha l}}} e^{-\tanh(\tau_\alpha l/2)(r_\alpha^2/\sigma_\alpha^2)}$$

and

$$G^{(1)}(\mathbf{r}, \mathbf{r}') = \frac{1}{\pi^{3/2}} \sum_{l=1}^{\infty} e^{\beta l \bar{\mu}} \prod_{\alpha} \frac{1}{\sigma_{\alpha} \sqrt{1 - e^{-2\tau_{\alpha} l}}} \exp \left[-\tanh \left(\frac{\tau_{\alpha} l}{2} \right) \times \left(\frac{r_{\alpha} + r'_{\alpha}}{2\sigma_{\alpha}} \right)^2 - \coth \left(\frac{\tau_{\alpha} l}{2} \right) \left(\frac{r_{\alpha} - r'_{\alpha}}{2\sigma_{\alpha}} \right)^2 \right].$$

The above expressions can be transformed into more familiar forms in limiting cases:

(i) For high temperature, $\mu \rightarrow -\infty$ and one recovers the Maxwell-Boltzmann distribution. The density is $\rho_{\text{eq}}(\mathbf{r}) = \frac{N}{\lambda^3} \prod_{\alpha} \tau_{\alpha} e^{-(\tau_{\alpha} l/2)(r_{\alpha}^2/\sigma_{\alpha}^2)}$ with $\lambda = \hbar \sqrt{2\pi} / \sqrt{mk_B T}$ the thermal de Broglie wavelength. The size of the cloud is $s_{\alpha} = \sigma_{\alpha} / \sqrt{\tau_{\alpha}}$ $= \sqrt{k_B T / m \omega_{\alpha}^2}$. The first order correlation function is

$$G^{(1)}(\mathbf{r}, \mathbf{r}') = \frac{N}{\lambda^3} \prod_{\alpha} \tau_{\alpha} e^{-(\tau_{\alpha} l/2)((r_{\alpha} + r'_{\alpha})/2\sigma_{\alpha})^2} e^{-\pi((r_{\alpha} - r'_{\alpha})/\lambda)^2}. \quad (4)$$

Using our definition, the correlation length is $l^{(i)} = \lambda / \sqrt{2\pi}$.

(ii) For a temperature close to but above the Bose-Einstein transition temperature, one must keep the summation over the index l . The density is $\rho_{\text{eq}}(\mathbf{r}) = \frac{1}{\lambda^3} g_{3/2}(e^{\beta \bar{\mu}} \prod_{\alpha} e^{-(\tau_{\alpha} l/2)(r_{\alpha}^2/\sigma_{\alpha}^2)})$, where $g_{\alpha}(x) = \sum_{l=1}^{\infty} x^l / l^{\alpha}$ is a Bose function. The first order correlation function is

$$G^{(1)}(\mathbf{r}, \mathbf{r}') = \frac{1}{\lambda^3} \sum_{l=1}^{\infty} \frac{e^{l\beta \bar{\mu}}}{l^{3/2}} \times \prod_{\alpha} e^{-(\tau_{\alpha} l/2)((r_{\alpha} + r'_{\alpha})/2\sigma_{\alpha})^2} e^{-(\pi l)((r_{\alpha} - r'_{\alpha})/\lambda)^2}.$$

As the temperature decreases, the number of values of l that contribute significantly to the sum increases. It is then clear from the above expression for $G^{(1)}$ that the correlation length near the center of the trap will increase and that the normalized correlation function is no longer Gaussian. Far from the center, only the $l=1$ term is important and the correlation function remains Gaussian. Thus close to degeneracy the correlation length is position dependent (for an explicit example see Sec. III B 5).

(iii) Near and below the transition temperature, the second order correlation function is given by Eq. (1) with $\rho_0(\mathbf{r}) = \frac{e^{\beta \bar{\mu}}}{1 - e^{\beta \bar{\mu}}} \prod_{\alpha} \frac{e^{-r_{\alpha}^2/\sigma_{\alpha}^2}}{(\sqrt{\pi} \sigma_{\alpha})^3}$. As the temperature decreases, the correlation at zero distance, $g^{(2)}(0, 0)$ decreases from 2 to 1 and the correlation length increases. Around the transition temperature, $g^{(2)}(0, 0)$ is already significantly different from 2 since the condensate peak density is already very large for a noninteracting harmonically trapped cloud [31]. At $T=0$, the correlation length is infinite and $g^{(2)}(\mathbf{r}, \mathbf{r}') = 1$.

B. Correlations in a harmonically trapped cloud after expansion

Here we consider the cloud after expansion. First we discuss two classes of detection methods which must be distinguished before calculating correlation functions.

1. Detection

We assume that the trapping potential is switched off instantaneously at $t=0$. The cloud expands and falls due to gravity. Two types of detection can be performed:

(a) *Snap shot*. An image is taken of the entire cloud at $t=t_0$. We have then access to

$$G_{\text{im}}^{(2)}(\mathbf{r}, t_0; \mathbf{r}', t_0) = \langle \hat{\Psi}^{\dagger}(\mathbf{r}, t_0) \hat{\Psi}(\mathbf{r}, t_0) \hat{\Psi}^{\dagger}(\mathbf{r}', t_0) \hat{\Psi}(\mathbf{r}', t_0) \rangle.$$

The usual imaging technique is absorption, and so one has access to the above correlation functions integrated along the imaging beam axis. This was used for the experiments of Refs. [12,13].

(b) *Flux measurement*. The atoms are detected when they cross a given plane. We will only consider the situation in which this plane is horizontal at $z=H$. One has access to

$$G_{\text{fl}}^{(2)}(\mathbf{r} = \{x, y, z = H\}, t; \mathbf{r}' = \{x', y', z' = H\}, t') = \langle \hat{I}(\mathbf{r}, t) \hat{I}(\mathbf{r}', t') \rangle,$$

where \hat{I} is the flux operator defined below. The detection systems required for such experiments correspond most closely to those of Refs. [10,15], in which a microchannel plate, situated below the trapped cloud, recorded the arrival times and in one case the positions of the atoms. It also corresponds closely to imaging a cloud that crosses a thin sheet of light [32], or to the experiment of Ref. [14], in which the transmission of a high finesse optical cavity records atoms as they cross the beam.

These two correlation functions are different, but if the detection is performed after a long time of flight, they are in fact nearly equivalent. This equivalence will be discussed in the following.

The flux operator is defined quantum mechanically by

$$\hat{I}(\mathbf{r}, t) = \frac{\hbar}{m} \text{Im}[\hat{\Psi}^{\dagger}(\mathbf{r}, t) \partial_z \hat{\Psi}(\mathbf{r}, t)] = \frac{\hbar}{2mi} [\hat{\Psi}^{\dagger}(\mathbf{r}, t) \partial_z \hat{\Psi}(\mathbf{r}, t) - \partial_z \hat{\Psi}^{\dagger}(\mathbf{r}, t) \hat{\Psi}(\mathbf{r}, t)].$$

The flux has thus the dimensions of a density times a velocity. We will give the explicit expression of this velocity in the Sec. III B 4. Here, the atomic field operators $\hat{\Psi}(\mathbf{r}, t)$ depend on space coordinates as well as on time. They represent the time evolution of the atomic field during the flight of the atoms, falling from the trap. The field operators for the falling cloud can be easily derived if we assume that there are no interactions between the atoms and that the occupation number in each mode is constant (as in free expansion). In this case, these operators can be defined as

$$\hat{\Psi}^{\dagger}(\mathbf{r}, t) = \sum_{\mathbf{j}} \psi_{\mathbf{j}}^*(\mathbf{r}, t) \hat{a}_{\mathbf{j}}^{\dagger}, \quad \hat{\Psi}(\mathbf{r}, t) = \sum_{\mathbf{j}} \psi_{\mathbf{j}}(\mathbf{r}, t) \hat{a}_{\mathbf{j}},$$

where the spatiotemporal dependence is carried by the wave function and the statistical occupation by the creation and annihilation operators.

2. Ballistic expansion of a harmonic oscillator stationary state

After switching off the trap, the harmonic oscillator wave functions noted $\psi_{\mathbf{j}}^0$ are no longer stationary states. There are

two ways to calculate the correlation after expansion: propagation of wave functions or propagation of the density matrix (the Schrödinger or the Heisenberg picture). In the following we will use the first approach which is physically more transparent (see Ref. [33] for the Heisenberg picture).

The ballistic expansion of a cloud is easy to calculate with the appropriate Green function. The Green function K is defined as

$$\psi_{\mathbf{j}}(\mathbf{r}, t) = \int_{-\infty}^{\infty} d\mathbf{r}_0 K(\mathbf{r}, t; \mathbf{r}_0, t_0) \psi_{\mathbf{j}}^0(\mathbf{r}_0, t_0).$$

As the $\psi_{\mathbf{j}}^0$ functions are stationary states for $t < 0$, we can take $t_0 = 0$ in the following. The Green function for particles in an arbitrarily time-varying quadratic potential is known [34]. After expansion, the potential is only due to gravity and the Green function is then

$$K(\mathbf{r}, t; \mathbf{r}_0) = \left(\frac{m}{2i\pi\hbar t} \right)^{3/2} e^{ia(\mathbf{r} - \mathbf{r}_0)^2} e^{ib(z+z_0)} e^{-ic}$$

with $a = \frac{m}{2\hbar t}$, $b = \frac{mgt}{2\hbar}$, and $c = \frac{mg^2 t^3}{24\hbar}$.

One can then derive an analytical expression of $\psi_{\mathbf{j}}(\mathbf{r}, t)$ [35,36],

$$\psi_{\mathbf{j}}(\mathbf{r}, t) = e^{i\phi(\mathbf{r}, t)} \prod_{\alpha} \frac{e^{ij_{\alpha}(\delta_{\alpha} + 3\pi/2)}}{\sqrt{\omega_{\alpha} t - i}} \psi_{\mathbf{j}}^0(\tilde{\mathbf{r}}), \quad (5)$$

where $\delta_{\alpha} = \tan^{-1}\left(\frac{1}{\omega_{\alpha} t}\right)$,

$$\phi(\mathbf{r}, t) = \frac{m}{2\hbar t} \left[(\tilde{x}\omega_x t)^2 + (\tilde{y}\omega_y t)^2 + (\tilde{z}\omega_z t)^2 + 2gt^2 \left(z - \frac{1}{8}gt^2 \right) \right] - c - \frac{3\pi}{4} \quad (6)$$

and, with $\tilde{\mathbf{r}} = \{\tilde{x}, \tilde{y}, \tilde{z}\}$,

$$\tilde{x} = \frac{x}{\sqrt{1 + \omega_x^2 t^2}}, \quad \tilde{y} = \frac{y}{\sqrt{1 + \omega_y^2 t^2}}, \quad \tilde{z} = \frac{H - \frac{1}{2}gt^2}{\sqrt{1 + \omega_z^2 t^2}}. \quad (7)$$

In the case of flux measurement, the position of the detector is fixed at $z = H$. The phase $\phi(\tilde{x}, \tilde{y}, t)$ is global as it does not depend on the index \mathbf{j} ; it will cancel in second order correlation measurements. This is in contrast to interferometric measurements where it is this phase that gives rise to fringes. The above results show that after release, the wave function is identical to that in the trap except for a phase factor and a scaling factor in the positions [37]. This scaling is obviously a property of a harmonic potential, and it considerably simplifies the expression of the correlation functions as we will see below.

3. Flux operator

Using $\partial_z H_n(z) = 2nH_{n-1}(z)$, the spatial derivative of the wave function can be written

$$\begin{aligned} \partial_z \psi_{\mathbf{j}}(\mathbf{r}, t) &= \frac{m}{\hbar} [(iv_2 - v_1) \psi_{j_z}(z, t) \\ &\quad - iv_3 \sqrt{j_z} \psi_{j_z-1}(z, t)] \psi_{j_x}(x, t) \psi_{j_y}(y, t), \end{aligned}$$

where the velocities v_1 , v_2 , and v_3 are time dependent and are given by

$$v_1(t) = \omega_z \frac{H - \frac{1}{2}gt^2}{1 + \omega_z^2 t^2}, \quad (8)$$

$$v_2(t) = \frac{1}{t} \left(H + \frac{1}{2}gt^2 - \frac{H - \frac{1}{2}gt^2}{1 + \omega_z^2 t^2} \right), \quad (9)$$

$$v_3(t) = \frac{\sqrt{2}\omega_z \sigma_z}{\sqrt{1 + \omega_z^2 t^2}} e^{i\delta_z}. \quad (10)$$

The velocity v_2 is usually much larger than the other two and will give the dominant contribution for the mean flux and the second order correlation function. An atom with zero initial velocity will acquire after a time t a velocity gt which is close to $v_2(t)$. The flux operator is

$$\hat{I}(\mathbf{r}, t) = \sum_{\mathbf{j}, \mathbf{k}} \left(v_2 \psi_{\mathbf{j}}^* \psi_{\mathbf{k}} - \frac{1}{2} (v_3 \sqrt{k} \psi_{\mathbf{j}}^* \psi_{\mathbf{k}-1_z} + v_3^* \sqrt{j} \psi_{\mathbf{j}-1_z}^* \psi_{\mathbf{k}}) \right) \hat{a}_{\mathbf{j}}^{\dagger} \hat{a}_{\mathbf{k}}, \quad (11)$$

where $\mathbf{j}-1_z$ is the vector (j_x, j_y, j_z-1) and where we write $\psi = \psi(\mathbf{r}, t)$.

4. Mean density and mean flux

We will first calculate the mean density $\rho(\mathbf{r}, t) = \langle \hat{\Psi}^{\dagger}(\mathbf{r}, t) \hat{\Psi}(\mathbf{r}, t) \rangle$. Using Eq. (5), one finds easily that $\rho(\mathbf{r}, t) = \frac{1}{\prod_{\alpha} \sqrt{1 + \omega_{\alpha}^2 t^2}} \rho_{\text{eq}}(\tilde{\mathbf{r}})$. This means that the density has the same form during expansion up to an anisotropic scale factor given by Eq. (7) [37,38]. The statistical average of Eq. (11) leads to

$$\begin{aligned} \langle \hat{I}(\mathbf{r}, t) \rangle &= \sum_{\mathbf{j}} \left(v_2 |\psi_{\mathbf{j}}|^2 - \frac{\sqrt{j_z}}{2} (v_3 \psi_{j_z}^* \psi_{j_z-1} + v_3^* \psi_{j_z} \psi_{j_z-1}^*) |\psi_{j_x} \psi_{j_y}|^2 \right) \\ &\quad \times \langle \hat{a}_{\mathbf{j}}^{\dagger} \hat{a}_{\mathbf{j}} \rangle. \end{aligned}$$

Because $v_3 \psi_{j_z}^* \psi_{j_z-1} = i \frac{|v_3|}{\sqrt{1 + \omega_z^2 t^2}} \psi_{j_z}^0(\tilde{z}) \psi_{j_z-1}^0(\tilde{z}) = -v_3^* \psi_{j_z} \psi_{j_z-1}^*$, the second term cancels out. Then, without any approximation,

$$\langle \hat{I}(\mathbf{r}, t) \rangle = \frac{v_2(t)}{\prod_{\alpha} \sqrt{1 + \omega_{\alpha}^2 t^2}} \rho_{\text{eq}}(\tilde{\mathbf{r}}) = v_2(t) \rho(\mathbf{r}, t).$$

The flux is proportional to the density of a cloud at thermal equilibrium with rescaled coordinates. This means that the mean flux of an expanding noninteracting cloud is proportional to the atomic density without any approximation. This result holds with and without gravity taken into account.

5. Second order correlation

Here we calculate the correlation functions. A discussion is given in the next section. The snap-shot correlation function is

$$G_{im}^{(2)}(\mathbf{r}, t; \mathbf{r}', t) = \sum_{\mathbf{j}, \mathbf{k}, \mathbf{l}, \mathbf{n}} \psi_{\mathbf{j}}^* \psi_{\mathbf{k}} \psi_{\mathbf{l}}^* \psi_{\mathbf{n}}' \langle \hat{a}_{\mathbf{j}}^\dagger \hat{a}_{\mathbf{k}} \hat{a}_{\mathbf{l}}^\dagger \hat{a}_{\mathbf{n}} \rangle.$$

Using Eq. (5), one finds, without any approximation (except the neglect of the shot-noise term):

$$G_{im}^{(2)}(\mathbf{r}, t; \mathbf{r}', t) = \frac{1}{\prod_{\alpha} (1 + \omega_{\alpha}^2 t^2)} \times [\rho_{\text{eq}}(\tilde{\mathbf{r}}) \rho_{\text{eq}}(\tilde{\mathbf{r}}') + |G^{(1)}(\tilde{\mathbf{r}}, \tilde{\mathbf{r}}')|^2 - \rho_0(\tilde{\mathbf{r}}) \rho_0(\tilde{\mathbf{r}}')].$$

As in the case of the mean density, the snap-shot correlation function has the same form as in the trap except for an anisotropic scale factor.

The calculation of $G_{fi}^{(2)}$ is similar,

$$\langle \hat{I}(\mathbf{r}, t) \hat{I}(\mathbf{r}', t') \rangle = - \left(\frac{\hbar}{2m} \right)^2 \sum_{\mathbf{j}, \mathbf{k}, \mathbf{l}, \mathbf{n}} [\psi_{\mathbf{j}}^* (\partial_z \psi_{\mathbf{k}}) - (\partial_z \psi_{\mathbf{j}}^*) \psi_{\mathbf{k}}] \times [\psi_{\mathbf{l}}^* (\partial_z \psi_{\mathbf{n}}) - (\partial_z \psi_{\mathbf{l}}^*) \psi_{\mathbf{n}}] \langle \hat{a}_{\mathbf{j}}^\dagger \hat{a}_{\mathbf{k}} \hat{a}_{\mathbf{l}}^\dagger \hat{a}_{\mathbf{n}} \rangle.$$

Two major differences appear compared to the mean flux calculation: the terms in v_3 and the phase factor $\delta_{\alpha} + 3\pi/2$ in Eq. (5) do not cancel. This makes the exact calculation very tedious. It is postponed to the Appendix.

Experiments are usually performed in situations satisfying two conditions: (1) the width of the cloud after expansion is much larger than that of the trapped cloud, and (2) the mean velocity acquired during free fall is much larger than the velocity spread of the trapped cloud. The first condition means that $\omega_{\alpha} t \gg 1$ and the second one that $gt \gg \sqrt{k_B T/m}$. The latter condition also means that the mean arrival time, $t_0 = \sqrt{2H/g}$, is much larger than the time width $\sqrt{k_B T/mg^2}$ of the expanding cloud. With these approximations the scale factors become quite simple. $\tilde{x} \sim \frac{x}{\omega_x t_0}$, $\tilde{y} \sim \frac{y}{\omega_y t_0}$ and $\tilde{z} \sim \frac{H - (1/2)gt^2}{\omega_z t_0} \sim \frac{g(t_0 - t)}{\omega_z}$. In particular, the coordinate \tilde{z} is proportional to the arrival time t . This means that in experiments that measure arrival times, the results have the same form when expressed as a function of vertical position.

In the correlation function of the flux, the above approximations also lead to $v_2 \approx \sqrt{2gH}$ and $|\sqrt{j_z} v_3 / v_2| \approx \sqrt{\frac{k_B T}{\hbar \omega_z} \frac{\sigma_z}{\sqrt{2}H}} = \frac{s_z}{\sqrt{2}H}$ where s_z is the width of the cloud inside the trap and where the typical value of the occupied trap level, j_z , is $\sim \frac{k_B T}{\hbar \omega_z}$. The term containing v_3 is then very small compared to the one proportional v_2 . In Ref. [15] for instance the above ratio is $\sim 10^{-5}$. We will neglect terms containing v_3 in the following. The phase factors δ_{α} in Eq. (5) are also very small since $\omega_{\alpha} t \gg 1$ and can be neglected (see the Appendix).

Under all these approximations, one finds

$$G_{fi}^{(2)}(\mathbf{r}, t; \mathbf{r}', t') = \frac{v_2 v_2'}{\prod_{\alpha} \sqrt{(1 + \omega_{\alpha}^2 t^2)(1 + \omega_{\alpha}^2 t'^2)}} [\rho_{\text{eq}}(\tilde{\mathbf{r}}) \rho_{\text{eq}}(\tilde{\mathbf{r}}') + |G^{(1)}(\tilde{\mathbf{r}}, \tilde{\mathbf{r}}')|^2 - \rho_0(\tilde{\mathbf{r}}) \rho_0(\tilde{\mathbf{r}}')].$$

We again find the same correlation function as in the trap, rescaled by a slightly different factor compared to $G_{im}^{(2)}$. This factor simply reflects the expansion of the cloud between the times t and t' .

The scaling laws for the harmonic potential result in a very simple expression for the correlation lengths at the detector,

$$l_{\alpha}^{(d)} = l^{(t)} \sqrt{1 + (\omega_{\alpha} t)^2}. \quad (12)$$

Where $l_{\alpha}^{(d)}$ is the correlation length along the α direction at the detector and $l_{\alpha}^{(t)}$ is the correlation length in the trap. If the gas is far from degeneracy $l^{(t)} = \frac{\lambda}{\sqrt{2\pi}}$, and we recover the result of Eq. (3). Close to degeneracy the correlation length is position dependent. In the case of a pulse of atoms as in Ref. [15], this formula applies along all three space axes. In addition, when making a flux measurement, one often expresses the longitudinal correlation length as a correlation time. For a pulse of atoms from a harmonic trap, with a mean velocity v at the detector, the correlation time is

$$t^{(\text{coh})} = \frac{l_z^{(d)}}{v} = l^{(t)} \frac{\omega_z}{g}. \quad (13)$$

It is independent of the propagation time as long as $\omega_z t \gg 1$.

These calculations are illustrated in the following figures. For simplicity we have used an isotropic trapping potential. As pointed out above, the normalized second-order correlation functions $g_{im}^{(2)}$ and $g_{fi}^{(2)}$ are virtually identical with typical parameters (see the Appendix) and we will use the shorter notation $g^{(2)}$. In Fig. 1 we show the normalized correlation function $g^{(2)}(\tilde{r}, 0)$ as a function of $\tilde{r} \sim r/\omega t$ for various temperatures in the vicinity the Bose-Einstein phase transition T^* . We use the saturation of the excited state population to define T^* [31]. This is the correlation function *at the center of the cloud*. One sees that at $T = T^*$ (the thick dashed line in the figure), the correlation function at zero distance is already significantly diminished compared to higher temperatures. The correlation length, on the other hand, is larger than $\lambda \omega t / \sqrt{2\pi}$. Also, one sees that the correlation function is almost flat for temperatures a few percent below T^* .

In many experiments of course, one does not measure the local correlation function, but the correlation function averaged over all points in the sample [15]. The effect of this averaging is shown in Fig. 2. We plot $g_m^{(2)}(\tilde{r}) = \frac{\int d\mathbf{R} G^{(2)}(\mathbf{R} + \tilde{r}\mathbf{e}, \mathbf{R})}{\int d\mathbf{R} G^{(1)}(\mathbf{R} + \tilde{r}\mathbf{e}, \mathbf{R} + \tilde{r}\mathbf{e}) G^{(1)}(\mathbf{R}, \mathbf{R})}$, where the vector \mathbf{e} is a unit vector in some direction. One sees that the amplitude of the correlation function decreases more slowly, and that after averaging, the correlation length hardly varies as one passes T^* .

To illustrate how local the effects which distinguish Figs. 1 and 2 are, we also plot in Fig. 3 the value of $g^{(2)}(\tilde{r}, \tilde{r})$, the zero distance correlation function as a function of \tilde{r} in the vicinity of the cloud center. One sees that even below T^* , the

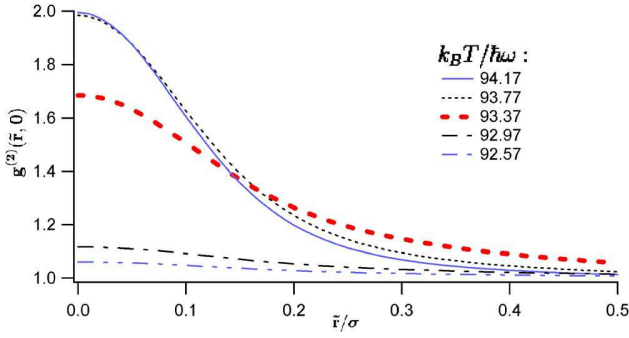


FIG. 1. (Color online) Two-body normalized correlation function at the trap center, $g^{(2)}(\tilde{r}, 0)$ for 10^6 atoms as a function of the position $\tilde{r} = r/\omega t$ for various temperatures around transition temperature. The horizontal axis is labelled in units of the size of the harmonic oscillator wave function σ . The thick dashed line corresponds to the transition temperature T^* defined in Ref. [31] and is $93.37\hbar\omega/k_B$ for 10^6 atoms. The temperature step is $0.4\hbar\omega/k_B$. The thermal de Broglie wavelength is $\sim 0.26\sigma$. The effect of the ground state population is clearly visible in the reduction of $g^{(2)}(0, 0)$, and in the rapid flattening out of the correlation function slightly below T^* .

correlator is close to 2 at a rescaled distance of a few times the harmonic oscillator length scale. We can simply interpret this effect by observing that at \tilde{r} the effective chemical potential is $\mu - V(\tilde{r})$. Away from the center, the effective chemical potential is small and this part of the cloud can be described as a Boltzmann cloud.

Before interpreting these results further, we recall some of our assumptions and their possible violation. First, we obtain Eq. (12) if we make a semiclassical approximation assuming that $k_B T$ greatly exceeds the energy spacing in the trap in each dimension of space. In an anisotropic trap, this condition can be violated in one or two dimensions and then correlation length along these directions will be larger and can become infinite for a small enough temperature. Second, we have assumed a noninteracting gas throughout.

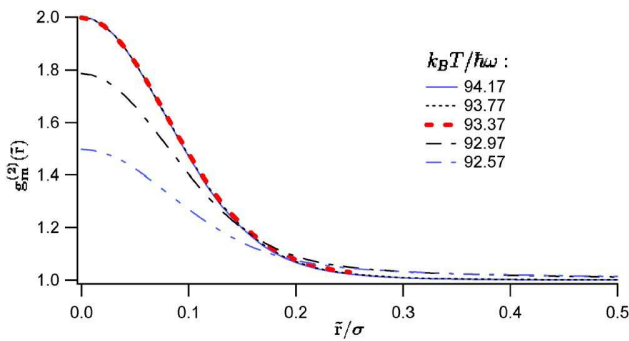


FIG. 2. (Color online) Two-body normalized correlation function $g_m^{(2)}(\tilde{r})$ for 10^6 atoms as a function of \tilde{r} . This function is an average of the two-body correlation function over the cloud. The conditions are the same conditions as for Fig. 1. Unlike Fig. 1, the shape is always almost Gaussian and converges more slowly to a flat correlation for low temperatures. This is because only a small region around $\tilde{r}=0$ is fully sensitive to the quantum atomic distribution.

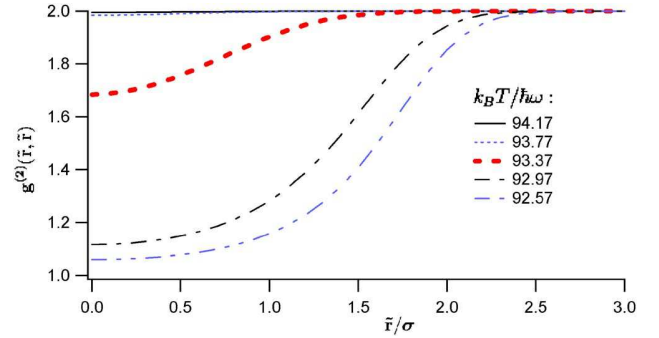


FIG. 3. (Color online) Two-body normalized correlation function $g^{(2)}(\tilde{r}, \tilde{r})$ for 10^6 atoms as a function of \tilde{r} . The conditions are the same as for Fig. 1. Even for $T < T^*$ the correlation goes to 2 far from the center. This is due to the finite spatial extent of the condensate. It can also be understood in terms of the chemical potential $\mu(\tilde{r})$ which, in a local density approximation, decreases as \tilde{r} increases and thus the correlation is equivalent to that of a hotter cloud.

Repulsive interactions inflate the trapped cloud, and thus reduce the length $l^{(d)}$ at the detector. We expect this to be the main effect for atomic clouds above the Bose-Einstein transition threshold, where the effects of atomic interactions are typically small. The reduction is typically a few percent. Even slightly below T^* , the condensate density is quite high, expelling the thermal atoms from the center of the trap. The effects of interactions inside the trap and during the cloud's expansion cannot be neglected. Taking them into account is then complex and beyond the scope of this paper.

IV. PHYSICAL INTERPRETATIONS

The main result of this paper is that in an experiment which averages over a detector in the sense of Fig. 2, even at $T=T^*$, the correlation lengths at the detector are well approximated by

$$l_\alpha^{(d)} = l^{(t)} \omega_\alpha t.$$

The correlation length increases linearly with the time of flight. A simple way to understand this result is to consider the analogy with optical speckle. Increasing the time of flight corresponds to increasing the propagation distance to the observation plane in the optical analog. The speckle size, i.e., the correlation length, obviously increases linearly with the propagation distance. Another way to understand the time dependence is to remark that after release, the atomic cloud is free and the phase space density should be constant. Since the density decreases with time as $\Pi_\alpha(\omega_\alpha t)$ and the spread of the velocity distribution is constant, the correlation volume must increase by the same factor [25].

Yet another way to look at the correlation length is to observe that, far from degeneracy, the correlation length inside the trap is the thermal de Broglie wavelength, that is, $\frac{\lambda}{\sqrt{2\pi}} = \hbar/\Delta p$ where $\Delta p = m\Delta v$ is the momentum width of the cloud. By analogy, after expansion, the correlation length is $\hbar/(\Delta p)_{\text{loc}}$, where $(\Delta p)_{\text{loc}}$ is the ‘‘local’’ width of the momen-

tum distribution. As the pulse of atoms propagates, fast and slow atoms separate, so that at a given point in space the width in momentum is reduced by a factor $\frac{s_\alpha}{\Delta v_T}$.

For a continuous beam, the formula (12) only applies in the transverse directions. In the longitudinal direction, an argument in terms of a local thermal de Broglie wavelength can be used to find the coherence length or time. If the atoms travel at velocity v without acceleration, the momentum spread and correlation length remain constant. Defining the energy width of the beam as $\Delta E = mv\Delta v$, one finds a correlation time $\lambda/v = \hbar/\Delta E$ [7]. In the presence of an acceleration such as gravity, the momentum spread of the beam decreases (the energy spread at any point ΔE is constant), which increases the correlation length. The correlation time, however, remains $\hbar/\Delta E$ [10].

The result that the coherence length of a cloud of atoms can vary with the distance of propagation, is in apparent contradiction with the results of Refs. [39,40]. Those papers give convincing reasons, both experimental and theoretical, for why the dispersion associated with the propagation of massive particles should *not* result in an increase of the coherence length. The contradiction is resolved by noting that the Mach-Zender interferometer considered in that work is sensitive to the function $f(\mathbf{r}, t) = \int d\mathbf{R} G^{(1)}(\mathbf{R}, t; \mathbf{R} + \mathbf{r}, t)$. If the Hamiltonian commutes with the momentum operator, i.e., if plane waves are stationary states, one can easily demonstrate that the function f and hence its width are independent of the time t . The experiments we analyze are sensitive to the *modulus* of $G^{(1)}$ whose width will always increase with time. Thus the coherence length can depend on the interferometer as well as the source.

The role of the acceleration of gravity in these experiments is minor. It governs the propagation time and the speed of the particles when they reach the detector. In a pulsed beam, gravity has no effect on the correlation length, although it does affect the correlation time. It also renders the rescaling of the z coordinate linear for large times so that the correlation function in position z and time have the same form. Without gravity (cancellation with a magnetic field gradient for example), a pulse of atoms would take longer to reach the detector, thereby giving the correlation length more time to dilate, and in addition they would hit the detector at a lower velocity. The correlation time would then increase with time and its order of magnitude would be $\frac{\lambda\omega t_0}{v_T} = \frac{\hbar\omega}{k_B T} t_0$ where $v_T = \sqrt{k_B T/m}$ is the thermal velocity and $t_0 = v_T/H$ is the time of flight to the detector.

V. EFFECT OF FINITE DETECTOR RESOLUTION

In the preceding sections, the detector was considered ideal, i.e., with arbitrarily good spatial and temporal resolution. Here we will consider a model of a more realistic detector, in which we suppose that the spatial resolution in the x - y plane is Gaussian. This is often the case due to smearing in pixels [13,16] and is also approximately true in Ref. [15]. To simplify the discussion we will restrict our analysis to the case $T \gg T^*$ and use a Maxwell-Boltzmann distribution rather than Bose-Einstein distribution. In this case, each direction

of space is independent and we will only consider one direction at a time in the following.

There are three different scales in the problem: the size of the cloud at the detector $s(t) \approx \sqrt{\frac{k_B T}{m}} t$, the correlation length at the detector $l^{(d)}$ and the rms width of the detector resolution function d . The definition of the resolution function is that for a density $\rho(x) = A e^{-x^2/2s(t)^2}$, the observed density is given by a convolution

$$\begin{aligned} \rho_{\text{obs}}(x) &= \int dx_0 \rho(x_0) \frac{e^{-(1/2)[(x-x_0)/d]^2}}{\sqrt{2\pi}d} \\ &= \frac{A}{\sqrt{1+d^2/s(t)^2}} e^{-x^2/2[s(t)^2+d^2]}. \end{aligned}$$

Similarly if $G^{(1)}(x, x') = A e^{i\phi} e^{-(x+x')^2/2(2s)^2} e^{-(x-x')^2/2(l^{(d)})^2}$ is the first order correlation function and $G_{\text{obs}}^{(1)}(x, x')$ the observed one, we have

$$\begin{aligned} |G_{\text{obs}}^{(1)}(x, x')|^2 &= \int dx_0 dx'_0 |G^{(1)}(x_0, x'_0)|^2 \\ &\quad \times \frac{e^{-(1/2)[(x-x_0)/d]^2}}{\sqrt{2\pi}d} \frac{e^{-(1/2)[(x'-x'_0)/d]^2}}{\sqrt{2\pi}d} \quad (14) \\ &= \frac{|A|^2}{\sqrt{[1+d^2/s^2(t)][1+4d^2/(l^{(d)})^2]}} \\ &\quad \times e^{-\{(x+x')^2/4[s(t)^2+d^2]\}} e^{-\{(x-x')^2/[l^{(d)}]^2+4d^2\}} \quad (15) \end{aligned}$$

Consequently, with $\alpha = x, y$ and z :

(i) The amplitude of the normalized correlation function becomes

$$g_{\text{obs}}^{(2)}(\mathbf{0}, \mathbf{0}) = \left(\frac{G_{\text{obs}}^{(1)}(\mathbf{0}, \mathbf{0})}{\rho_{\text{obs}}(\mathbf{0})} \right)^2 = 1 + \prod_{\alpha} \sqrt{\frac{1+d_{\alpha}^2/s_{\alpha}^2(t)}{1+4d_{\alpha}^2/(l_{\alpha}^{(d)})^2}}.$$

(ii) The observed widths of the cloud are $s_{\alpha}(t) \rightarrow \sqrt{s_{\alpha}^2(t) + d_{\alpha}^2}$.

(iii) The observed correlation lengths are $l_{\alpha}^{(d)} \rightarrow \sqrt{(l_{\alpha}^{(d)})^2 + (2d_{\alpha})^2}$. The factor 2 can be understood as $\sqrt{2} \times \sqrt{2}$ where the first term comes from the fact that d_{α} is defined for one particle and not for a pair of particles and the second one comes from the fact that the correlation length is not defined as an rms width.

In the experiment of Ref. [15] the trapped cloud had a cigar shape. At the detector the cloud was spherical but the correlation volume was anisotropic with $l_x^{(d)} \ll d \approx l_y^{(d)}/4$. In the third (vertical) direction, the resolution width was much smaller than any other length scale. The observed contrast of the correlation function was therefore approximately, $\frac{l_x^{(d)}}{2d}$.

VI. CONCLUSION

The most important conclusion of this paper is that the expansion of a noninteracting cloud from a harmonic trap in

thermal equilibrium, admits a rather simple, analytical treatment of the time variation of the density and the correlation functions. In such a pulse of atoms, correlation lengths scale in the same way as the size of the density profile. The agreement with experiment indicates that the neglect of interactions is a good approximation above the BEC transition temperature. An important next step however, is to examine interaction effects so that the next generation of experiments, which will be more precise and better resolved, can be fully interpreted.

ACKNOWLEDGMENTS

The Atom Optics group of LCFIO is member of the Institut Francilien de Recherche sur les Atomes Froids (IFRAF) and of the Fédération LUMAT of the CNRS (FR2764). This work is supported by the PESSOA Program 07988NJ, by the Atom Chips network MCRTN-CT-2003-505032, and the ANR under Contract No. 05-NANO-008-01.

APPENDIX

Explicit expression of the flux correlation function

We found in Sec. III B, the following expression for the flux operator:

$$\hat{I}(\mathbf{r}, t) = \sum_{\mathbf{j}, \mathbf{k}} \left(v_2 \psi_{\mathbf{j}}^* \psi_{\mathbf{k}} - \frac{1}{2} (v_3 \sqrt{k} \psi_{\mathbf{j}}^* \psi_{\mathbf{k}-1_z} + v_3 \sqrt{j} \psi_{\mathbf{j}-1_z}^* \psi_{\mathbf{k}}) \right) \hat{a}_{\mathbf{j}}^\dagger \hat{a}_{\mathbf{k}},$$

where $\mathbf{j}-1_z$ is the vector (j_x, j_y, j_z-1) and where we write $\psi = \psi(\mathbf{r}, t)$.

The second order correlation function for the flux is then,

$$\begin{aligned} \langle \hat{I}(\mathbf{r}, t) \hat{I}(\mathbf{r}', t') \rangle &= \sum_{\mathbf{j}, \mathbf{k}, \mathbf{l}, \mathbf{n}} \left(v_2 \psi_{\mathbf{j}}^* \psi_{\mathbf{k}} - \frac{1}{2} (v_3 \sqrt{k} \psi_{\mathbf{j}}^* \psi_{\mathbf{k}-1_z} \right. \\ &\quad \left. + v_3 \sqrt{j} \psi_{\mathbf{j}-1_z}^* \psi_{\mathbf{k}}) \right) \\ &\quad \times \left(v_2' \psi_{\mathbf{l}}^* \psi_{\mathbf{n}}' - \frac{1}{2} (v_3' \sqrt{n} \psi_{\mathbf{l}}^* \psi_{\mathbf{n}-1_z}' \right. \\ &\quad \left. + v_3' \sqrt{l} \psi_{\mathbf{l}-1_z}^* \psi_{\mathbf{n}}') \right) \\ &\quad \times \langle \hat{a}_{\mathbf{j}}^\dagger \hat{a}_{\mathbf{k}} \hat{a}_{\mathbf{l}}^\dagger \hat{a}_{\mathbf{n}} \rangle. \end{aligned}$$

Neglecting the shot-noise and ground-state contributions, this leads to

$$\langle \hat{I}(\mathbf{r}, t) \hat{I}(\mathbf{r}', t') \rangle = \langle \hat{I}(\mathbf{r}, t) \rangle \langle \hat{I}(\mathbf{r}', t') \rangle + \text{Re}(A)$$

with

$$\begin{aligned} A &= \sum_{\mathbf{j}, \mathbf{l}} \left(v_2 v_2' \psi_{\mathbf{j}}^* \psi_{\mathbf{l}}' \psi_{\mathbf{l}} \psi_{\mathbf{j}}'^* + \frac{1}{2} v_3 v_3' \sqrt{j} \sqrt{l} \psi_{\mathbf{j}}^* \psi_{\mathbf{j}-1_z}' \psi_{\mathbf{l}-1_z}' \psi_{\mathbf{l}}'^* \right. \\ &\quad \left. + \frac{1}{2} v_3 v_3' \sqrt{l} \psi_{\mathbf{j}}^* \psi_{\mathbf{j}}' \psi_{\mathbf{l}-1_z}' \psi_{\mathbf{l}}'^* - v_2 v_2' \sqrt{j} \psi_{\mathbf{j}}^* \psi_{\mathbf{j}-1_z}' \psi_{\mathbf{l}} \psi_{\mathbf{l}}'^* \right. \\ &\quad \left. - v_2' v_3 \sqrt{l} \psi_{\mathbf{j}}^* \psi_{\mathbf{j}}' \psi_{\mathbf{l}-1_z}' \psi_{\mathbf{l}}'^* \right) \langle \hat{a}_{\mathbf{j}}^\dagger \hat{a}_{\mathbf{j}} \rangle \langle \hat{a}_{\mathbf{l}}^\dagger \hat{a}_{\mathbf{l}} \rangle. \end{aligned}$$

We write $A = \sum_{i=1}^5 T_i$ where the T_i terms can be recast, using $\tan \delta_\alpha = 1/\omega_\alpha t$, $\tan \delta'_\alpha = 1/\omega'_\alpha t'$, $\Delta_\alpha = \delta'_\alpha - \delta_\alpha$, $\sum_{\alpha} j_\alpha (\delta'_\alpha - \delta_\alpha) = \mathbf{j} \cdot \mathbf{\Delta}$, $\psi_{\mathbf{j}}^0 = \psi_{\mathbf{j}}^0(\mathbf{r})$, and $\psi_{\mathbf{l}}'^0 = \psi_{\mathbf{l}}'^0(\mathbf{r}')$,

$$T_1 = v_2 v_2' \sum_{\mathbf{j}, \mathbf{l}} \psi_{\mathbf{j}}^* \psi_{\mathbf{l}}' \psi_{\mathbf{l}} \psi_{\mathbf{j}}'^* \langle \hat{a}_{\mathbf{j}}^\dagger \hat{a}_{\mathbf{j}} \rangle \langle \hat{a}_{\mathbf{l}}^\dagger \hat{a}_{\mathbf{l}} \rangle = \frac{v_2 v_2'}{\prod_{\alpha} \sqrt{(1 + \omega_\alpha^2 t^2)(1 + \omega'_\alpha{}^2 t'^2)}} \sum_{\mathbf{j}, \mathbf{l}} \psi_{\mathbf{j}}^0 \psi_{\mathbf{j}}'^0 \psi_{\mathbf{l}}^0 \psi_{\mathbf{l}}'^0 e^{i \sum_{\alpha} (j_\alpha - l_\alpha) (\delta'_\alpha - \delta_\alpha)} \langle \hat{a}_{\mathbf{j}}^\dagger \hat{a}_{\mathbf{j}} \rangle \langle \hat{a}_{\mathbf{l}}^\dagger \hat{a}_{\mathbf{l}} \rangle$$

$$= \frac{v_2 v_2'}{\prod_{\alpha} \sqrt{(1 + \omega_\alpha^2 t^2)(1 + \omega'_\alpha{}^2 t'^2)}} \left| \sum_{\mathbf{j}} \psi_{\mathbf{j}}^0 \psi_{\mathbf{j}}'^0 e^{i \mathbf{j} \cdot \mathbf{\Delta}} \langle \hat{a}_{\mathbf{j}}^\dagger \hat{a}_{\mathbf{j}} \rangle \right|^2,$$

$$T_2 = \frac{1}{2} v_3 v_3' \sum_{\mathbf{j}, \mathbf{l}} \sqrt{j} \sqrt{l} \psi_{\mathbf{j}}^* \psi_{\mathbf{j}-1_z}' \psi_{\mathbf{l}-1_z}' \psi_{\mathbf{l}}'^* \langle \hat{a}_{\mathbf{j}}^\dagger \hat{a}_{\mathbf{j}} \rangle \langle \hat{a}_{\mathbf{l}}^\dagger \hat{a}_{\mathbf{l}} \rangle =$$

$$- \frac{1}{2} \frac{|v_3 v_3'|}{\prod_{\alpha} \sqrt{(1 + \omega_\alpha^2 t^2)(1 + \omega'_\alpha{}^2 t'^2)}} \left(\sum_{\mathbf{j}} \sqrt{j} \psi_{\mathbf{j}}^0 \psi_{\mathbf{j}-1_z}'^0 e^{i \mathbf{j} \cdot \mathbf{\Delta}} \langle \hat{a}_{\mathbf{j}}^\dagger \hat{a}_{\mathbf{j}} \rangle \right) \left(\sum_{\mathbf{l}} \sqrt{l} \psi_{\mathbf{l}-1_z}'^0 \psi_{\mathbf{l}}'^0 e^{-i \mathbf{l} \cdot \mathbf{\Delta}} \langle \hat{a}_{\mathbf{l}}^\dagger \hat{a}_{\mathbf{l}} \rangle \right),$$

$$T_3 = \frac{1}{2} v_3 v_3' \sum_{\mathbf{j}, \mathbf{l}} l_z \psi_{\mathbf{j}}^* \psi_{\mathbf{j}}' \psi_{\mathbf{l}-1_z}' \psi_{\mathbf{l}}'^* \langle \hat{a}_{\mathbf{j}}^\dagger \hat{a}_{\mathbf{j}} \rangle \langle \hat{a}_{\mathbf{l}}^\dagger \hat{a}_{\mathbf{l}} \rangle = \frac{1}{2} \frac{|v_3 v_3'|}{\prod_{\alpha} \sqrt{(1 + \omega_\alpha^2 t^2)(1 + \omega'_\alpha{}^2 t'^2)}} \left(\sum_{\mathbf{j}} \psi_{\mathbf{j}}^0 \psi_{\mathbf{j}}'^0 e^{i \mathbf{j} \cdot \mathbf{\Delta}} \langle \hat{a}_{\mathbf{j}}^\dagger \hat{a}_{\mathbf{j}} \rangle \right) \left(\sum_{\mathbf{l}} l_z \psi_{\mathbf{l}-1_z}'^0 \psi_{\mathbf{l}}'^0 e^{-i \mathbf{l} \cdot \mathbf{\Delta}} \langle \hat{a}_{\mathbf{l}}^\dagger \hat{a}_{\mathbf{l}} \rangle \right),$$

$$T_4 = -v_2 v_3' \sum_{\mathbf{j}, \mathbf{l}} \sqrt{j} \psi_{\mathbf{j}}^* \psi_{\mathbf{j}-1_z}' \psi_{\mathbf{l}} \psi_{\mathbf{l}}'^* \langle \hat{a}_{\mathbf{j}}^\dagger \hat{a}_{\mathbf{j}} \rangle \langle \hat{a}_{\mathbf{l}}^\dagger \hat{a}_{\mathbf{l}} \rangle = -i \frac{v_2 |v_3'|}{\prod_{\alpha} \sqrt{(1 + \omega_\alpha^2 t^2)(1 + \omega'_\alpha{}^2 t'^2)}} \left(\sum_{\mathbf{j}} \sqrt{j} \psi_{\mathbf{j}}^0 \psi_{\mathbf{j}-1_z}'^0 e^{i \mathbf{j} \cdot \mathbf{\Delta}} \langle \hat{a}_{\mathbf{j}}^\dagger \hat{a}_{\mathbf{j}} \rangle \right) \left(\sum_{\mathbf{l}} \psi_{\mathbf{l}}^0 \psi_{\mathbf{l}}'^0 e^{-i \mathbf{l} \cdot \mathbf{\Delta}} \langle \hat{a}_{\mathbf{l}}^\dagger \hat{a}_{\mathbf{l}} \rangle \right),$$

$$T_5 = -v'_2 v_3 \sum_{j,1} \sqrt{v_z} \psi_j^* \psi_{j-1}^* \psi_{j+1}^* \langle \hat{a}_j^\dagger \hat{a}_j \rangle \langle \hat{a}_1^\dagger \hat{a}_1 \rangle = -i \frac{v'_2 |v_3|}{\prod_{\alpha} \sqrt{(1 + \omega_{\alpha}^2 t^2)(1 + \omega_{\alpha}^2 t'^2)}} \left(\sum_j \psi_j^0 \psi_j^0 e^{i\mathbf{j} \cdot \Delta} \langle \hat{a}_j^\dagger \hat{a}_j \rangle \right) \left(\sum_1 \sqrt{v_z} \psi_{1-1}^0 \psi_1^0 e^{-i\mathbf{l} \cdot \Delta} \langle \hat{a}_1^\dagger \hat{a}_1 \rangle \right).$$

The term T_1 is a real number which is not the case for T_2, T_3, T_4 , and T_5 .

Calculation for harmonic oscillator stationary states

All the above terms can be calculated analytically. All the series are identical in the direction x and y . We are then left with the calculation of three series in only one direction,

$$\begin{aligned} & \sum_{n=0}^{\infty} \sqrt{n} \psi_{n-1}^0(\tilde{z}) \psi_n^0(\tilde{z}') e^{-nu}, \\ & \sum_{n=0}^{\infty} n \psi_{n-1}^0(\tilde{z}) \psi_{n-1}^0(\tilde{z}') e^{-nu}, \\ & \sum_{n=0}^{\infty} n \psi_{n-1}^0(\tilde{z}) \psi_{n-1}^0(\tilde{z}') e^{-nu}. \end{aligned}$$

The function $g_u(\tilde{z}, \tilde{z}') = \sum_{n=0}^{\infty} \psi_{n-1}^0(\tilde{z}) \psi_n^0(\tilde{z}') e^{-nu}$ is known [17,29] and its expression is

$$g_u(\tilde{z}, \tilde{z}') = \frac{1}{\sigma \sqrt{\pi(1 - e^{-2u})}} \exp \left[-\tanh\left(\frac{u}{2}\right) \left(\frac{\tilde{z} + \tilde{z}'}{2\sigma}\right)^2 - \coth\left(\frac{u}{2}\right) \left(\frac{\tilde{z} - \tilde{z}'}{2\sigma}\right)^2 \right].$$

Using

$$\tilde{z} \psi_n^0(\tilde{z}) = \frac{\sigma}{\sqrt{2}} \langle \tilde{z} | \hat{a} + \hat{a}^\dagger | \psi_n^0 \rangle = \frac{\sigma}{\sqrt{2}} [\sqrt{n} \psi_{n-1}^0(\tilde{z}) + \sqrt{n+1} \psi_{n+1}^0(\tilde{z})],$$

one finds

$$\begin{aligned} \tilde{z} g_u(\tilde{z}, \tilde{z}') &= \frac{\sigma}{\sqrt{2}} \left(\sum \sqrt{n} \psi_{n-1}^0(\tilde{z}) \psi_n^0(\tilde{z}') e^{-nu} \right. \\ & \left. + e^u \sum \sqrt{n} \psi_n^0(\tilde{z}) \psi_{n-1}^0(\tilde{z}') e^{-nu} \right). \end{aligned}$$

It follows easily that

$$\begin{aligned} \sum_{n=0}^{\infty} \sqrt{n} \psi_{n-1}^0(\tilde{z}) \psi_n^0(\tilde{z}') e^{-nu} &= \frac{\sqrt{2}}{\sigma} \frac{\tilde{z} - e^u \tilde{z}'}{1 - e^{2u}} g_u(\tilde{z}, \tilde{z}'), \\ \sum_{n=0}^{\infty} \sqrt{n} \psi_n^0(\tilde{z}) \psi_{n-1}^0(\tilde{z}') e^{-nu} &= \frac{\sqrt{2}}{\sigma} \frac{\tilde{z}' - e^{-u} \tilde{z}}{1 - e^{2u}} g_u(\tilde{z}, \tilde{z}'). \end{aligned}$$

Moreover,

$$\sum_{n=0}^{\infty} n \psi_{n-1}^0(\tilde{z}) \psi_{n-1}^0(\tilde{z}') e^{-nu} = e^{-u} [g_u(\tilde{z}, \tilde{z}') - \partial_u g_u(\tilde{z}, \tilde{z}')].$$

Then,

$$\begin{aligned} \sum_{n=0}^{\infty} n \psi_{n-1}^0(\tilde{z}) \psi_{n-1}^0(\tilde{z}') e^{-nu} &= \left[\frac{1}{1 - e^{-2u}} + \frac{1}{2} \left(\frac{\tilde{z} + \tilde{z}'}{2\sigma \cosh \frac{u}{2}} \right)^2 \right. \\ & \left. - \frac{1}{2} \left(\frac{\tilde{z} - \tilde{z}'}{2\sigma \sinh \frac{u}{2}} \right)^2 \right] e^{-u} g_u(\tilde{z}, \tilde{z}'). \end{aligned}$$

Explicit expression of the flux correlation function—Part II

We define $G_B^{(1)}(\mathbf{r}, \mathbf{r}', \mathbf{u}) = \sum_n \psi_n^0(\mathbf{r}) \psi_n^0(\mathbf{r}') e^{-n\mathbf{u}}$. This function, the 3D equivalent of the function g_u , is connected to the one-body correlation function by $G^{(1)}(\mathbf{r}, \mathbf{r}') = \sum_{l=1}^{\infty} e^{\beta l \bar{\mu}} G_B^{(1)}(\mathbf{r}, \mathbf{r}', l\boldsymbol{\tau})$ with $\tau_{\alpha} = \beta \hbar \omega_{\alpha}$.

Then,

$$T_1 = \frac{v_2 v'_2}{\prod_{\alpha} \sqrt{(1 + \omega_{\alpha}^2 t^2)(1 + \omega_{\alpha}^2 t'^2)}} \left| \sum_l e^{\beta l \bar{\mu}} G_B^{(1)}(\tilde{\mathbf{r}}, \tilde{\mathbf{r}}', l\boldsymbol{\tau} - i\Delta) \right|^2,$$

$$\begin{aligned} T_2 &= -\frac{1}{2} \frac{|v_3 v'_3|}{\prod_{\alpha} \sqrt{(1 + \omega_{\alpha}^2 t^2)(1 + \omega_{\alpha}^2 t'^2)}} \left(\sum_l e^{\beta l \bar{\mu}} \frac{\sqrt{2}}{\sigma} \frac{\tilde{z} - e^{l\tau_z - i\Delta_z} \tilde{z}'}{1 - e^{2(l\tau_z - i\Delta_z)}} G_B^{(1)}(\tilde{\mathbf{r}}, \tilde{\mathbf{r}}', l\boldsymbol{\tau} - i\Delta) \right) \\ & \times \left(\sum_k e^{\beta k \bar{\mu}} \frac{\sqrt{2}}{\sigma} \frac{\tilde{z}' - e^{k\tau_z + i\Delta_z} \tilde{z}}{1 - e^{2(k\tau_z + i\Delta_z)}} G_B^{(1)}(\tilde{\mathbf{r}}, \tilde{\mathbf{r}}', k\boldsymbol{\tau} + i\Delta) \right), \end{aligned}$$

$$T_3 = \frac{1}{2} \frac{|v_3 v_3'|}{\prod_{\alpha} \sqrt{(1 + \omega_{\alpha}^2 t^2)(1 + \omega_{\alpha}^2 t'^2)}} \left(\sum_l e^{\beta l \bar{\mu}} G_B^{(1)}(\bar{\mathbf{r}}, \bar{\mathbf{r}}', l\tau - i\Delta) \right) \times \left\{ \sum_k e^{\beta k \bar{\mu}} \left[\frac{1}{1 - e^{-2(k\tau_z + i\Delta_z)}} + \frac{1}{2} \left(\frac{\tilde{z} + \tilde{z}'}{2\sigma \cosh \frac{k\tau_z + i\Delta_z}{2}} \right)^2 \right. \right. \\ \left. \left. - \frac{1}{2} \left(\frac{\tilde{z} - \tilde{z}'}{2\sigma \sinh \frac{k\tau_z + i\Delta_z}{2}} \right)^2 \right] e^{-(k\tau_z + i\Delta_z)} G_B^{(1)}(\bar{\mathbf{r}}, \bar{\mathbf{r}}', k\tau + i\Delta) \right\},$$

$$T_4 = -i \frac{v_2 |v_3'|}{\prod_{\alpha} \sqrt{(1 + \omega_{\alpha}^2 t^2)(1 + \omega_{\alpha}^2 t'^2)}} \left(\sum_l e^{\beta l \bar{\mu}} \frac{\sqrt{2} \tilde{z} - e^{l\tau_z - i\Delta_z} \tilde{z}'}{\sigma 1 - e^{2(l\tau_z - i\Delta_z)}} G_B^{(1)}(\bar{\mathbf{r}}, \bar{\mathbf{r}}', l\tau - i\Delta) \right) \times \left(\sum_k e^{\beta k \bar{\mu}} G_B^{(1)}(\bar{\mathbf{r}}, \bar{\mathbf{r}}', k\tau + i\Delta) \right),$$

$$T_5 = -i \frac{|v_3| v_2'}{\prod_{\alpha} \sqrt{(1 + \omega_{\alpha}^2 t^2)(1 + \omega_{\alpha}^2 t'^2)}} \left(\sum_l e^{\beta l \bar{\mu}} G_B^{(1)}(\bar{\mathbf{r}}, \bar{\mathbf{r}}', l\tau - i\Delta) \right) \times \left(\sum_k e^{\beta k \bar{\mu}} \frac{\sqrt{2} \tilde{z}' - e^{k\tau_z + i\Delta_z} \tilde{z}}{\sigma 1 - e^{2(k\tau_z + i\Delta_z)}} G_B^{(1)}(\bar{\mathbf{r}}, \bar{\mathbf{r}}', k\tau + i\Delta) \right).$$

The dominant term is T_1 and is the one used in Sec. III B 5.

Contribution of neglected terms in the correlation of the flux

Here we evaluate the neglected terms T_2 to T_5 and the shot-noise contribution. They will be evaluated in the case of clouds far above BEC threshold. Under this assumption, all the functions are separable in the variables x, y , and t and the summation over the index l in the preceding equations reduces to the single term $l=1$.

Shot-noise contribution

Using the above analysis one can show that the main term is still proportional to $v_2 v_2'$. The additional term is then,

$$\frac{v_2 v_2'}{\prod_{\alpha} \sqrt{(1 + \omega_{\alpha}^2 t^2)(1 + \omega_{\alpha}^2 t'^2)}} e^{\beta \bar{\mu}} G_B^{(1)}(\bar{\mathbf{r}}, \bar{\mathbf{r}}', \tau - i\Delta) G_B^{(1)}(\bar{\mathbf{r}}, \bar{\mathbf{r}}', i\Delta).$$

For $t=t'$, $\Delta=0$ and $G_B^{(1)}(\bar{\mathbf{r}}, \bar{\mathbf{r}}', 0) = \delta(\bar{\mathbf{r}} - \bar{\mathbf{r}}')$. The shot-noise term is then

$$\frac{v_2^2}{\prod_{\alpha} (1 + \omega_{\alpha}^2 t^2)} \rho_{\text{eq}}(\bar{\mathbf{r}}) \delta(\bar{\mathbf{r}} - \bar{\mathbf{r}}').$$

As expected, this term corresponds also to the one at equilibrium with rescaled coordinates.

T_2 - T_5 contribution

We have $G_{fl}^{(2)}(\mathbf{r}, t; \mathbf{r}', t') = \langle \hat{I}(\mathbf{r}, t) \hat{I}(\mathbf{r}', t') \rangle = \langle \hat{I}(\mathbf{r}, t) \times \langle \hat{I}(\mathbf{r}', t') \rangle \rangle + \text{Re}(A)$ where $A = \sum_{i=1}^5 T_i$.

Case $t=t'$:

$$(a) \Delta=0, \text{ then } T_1 = \frac{v_2 v_2'}{\prod_{\alpha} \sqrt{(1 + \omega_{\alpha}^2 t^2)(1 + \omega_{\alpha}^2 t'^2)}} |G^{(1)}(\bar{\mathbf{r}}, \bar{\mathbf{r}}')|^2, \quad T_2$$

and T_3 are real number and $\text{Re}(T_4) = \text{Re}(T_5) = 0$.

(b) One finds, to leading orders, $g^{(2)}(0, 0, t; 0, 0, t) - 2 \approx \frac{1}{8} \left(\frac{s_z}{H} \right)^2 \left(1 - 2 \frac{t-t_0}{t_0} \right) \left(1 - \frac{\tau_z^2}{6} \right)$ where s_z is the initial size of the cloud in the vertical direction and $t_0 = \sqrt{2H/g}$.

(c) The deviation from 2 is extremely small in the experimental conditions of Ref. [15] ($\sim 10^{-11}$) but shows that the bunching is strictly speaking not 2 at the center. This behavior is expected for any flux correlation function of dispersive waves [41].

(d) The correlation lengths at the detector are not modified by the additional terms.

Case $t \neq t'$:

(a) The correlation function can be written as

$$g^{(2)}(0, 0, t; 0, 0, t') = 1 + \frac{|G_B^{(1)}(\bar{\mathbf{r}}, \bar{\mathbf{r}}', \tau + i\Delta)|^2}{G_B^{(1)}(\bar{\mathbf{r}}, \bar{\mathbf{r}}, \tau) G_B^{(1)}(\bar{\mathbf{r}}', \bar{\mathbf{r}}', \tau)} (1 + \epsilon).$$

(b) where

$$\frac{|G_B^{(1)}(\bar{\mathbf{r}}, \bar{\mathbf{r}}', \tau + i\Delta)|^2}{G_B^{(1)}(\bar{\mathbf{r}}, \bar{\mathbf{r}}, \tau) G_B^{(1)}(\bar{\mathbf{r}}', \bar{\mathbf{r}}', \tau)} \approx e^{-[(t-t')/t^{(\text{coh})}]^2 [1 - (\tau_z^2/6) 1 - [(t+t') - 2t_0]/t_0]}$$

and

(c)

$$\epsilon \approx \frac{1}{8} \left(\frac{w_z}{H} \right)^2 \left[1 - \left(\frac{t+t' - 2t_0}{t_0} \right) \right] \left(1 - \frac{\tau_z^2}{6} \right) - \frac{3}{2(\omega_z t_0 \tau_z)^2} \left(\frac{t-t'}{t_0} \right)^2 \left(1 + \frac{\tau_z}{3} \right).$$

We have neglected terms in $\tau_z, (t-t_0)^3, (t'-t_0)^3, (t-t_0)^2(t'-t_0), (t-t_0)(t'-t_0)^2$, and higher orders.

(d) The value of ϵ is extremely small ($\sim 10^{-10}$) using Ref. [15]. The deviation from $e^{-[(t-t')/t^{(\text{coh})}]^2}$ is mainly due to the mean time $(t+t')/2$ contribution and changes the value of the correlation time in the wings of the time of flight by $\sim 3\%$. The effect of the phase factor Δ is negligible.

- [1] L. Mandel and E. Wolf, *Optical Coherence and Quantum Optics* (Cambridge University Press, Cambridge, 1995).
- [2] R. Hanbury Brown and R. Q. Twiss, *Nature (London)* **177**, 27 (1956).
- [3] G. Baym, *Acta Phys. Pol. B* **29**, 1839 (1998).
- [4] D. H. Boal, C.-K. Gelbke, and B. K. Jennings, *Rev. Mod. Phys.* **62**, 553 (1990).
- [5] U. Heinz and B. V. Jacak, *Annu. Rev. Nucl. Part. Sci.* **49**, 529 (1999).
- [6] C.-Y. Wong, *Introduction to High-Energy Heavy-Ion Collisions* (World Scientific, Singapore, 1994).
- [7] M. Iannuzzi, A. Orecchini, F. Sacchetti, P. Facchi, and S. Pascazio, *Phys. Rev. Lett.* **96**, 080402 (2006).
- [8] M. Henny, S. Oberholzer, C. Strunk, T. Heinzel, K. Ensslin, M. Holland, and C. Schonenberger, *Science* **284**, 296 (1999).
- [9] W. D. Oliver, J. Kim, R. C. Liu, and Y. Yamamoto, *Science* **284**, 299 (1999).
- [10] M. Yasuda and F. Shimizu, *Phys. Rev. Lett.* **77**, 3090 (1996).
- [11] D. Hellweg, L. Cacciapuoti, M. Kottke, T. Schulte, K. Sengstock, W. Ertmer, and J. J. Arlt, *Phys. Rev. Lett.* **91**, 010406 (2003).
- [12] M. Greiner, C. A. Regal, J. T. Stewart, and D. S. Jin, *Phys. Rev. Lett.* **94**, 110401 (2005).
- [13] S. Fölling, F. Gerbier, A. Widera, O. Mandel, T. Gericke, and I. Bloch, *Nature (London)* **434**, 481 (2005).
- [14] A. Öttl, S. Ritter, M. Köhl, and T. Esslinger, *Phys. Rev. Lett.* **95**, 090404 (2005).
- [15] M. Schellekens, R. Hoppeler, A. Perrin, J. Viana Gomes, D. Boiron, A. Aspect, and C. I. Westbrook, *Science* **310**, 648 (2005).
- [16] J. Esteve, J.-B. Trebbia, T. Schumm, A. Aspect, C. I. Westbrook, and I. Bouchoule, *Phys. Rev. Lett.* **96**, 130403 (2006).
- [17] M. Naraschewski and R. J. Glauber, *Phys. Rev. A* **59**, 4595 (1999).
- [18] M. Holzmann and Y. Castin, *Eur. Phys. J. D* **7**, 425 (1999).
- [19] K. V. Kheruntsyan, D. M. Gangardt, P. D. Drummond, and G. V. Shlyapnikov, *Phys. Rev. Lett.* **91**, 040403 (2003).
- [20] C. Mora and Y. Castin, *Phys. Rev. A* **67**, 053615 (2003).
- [21] M. A. Cazalilla, *J. Phys. B* **37**, 1 (2004).
- [22] E. Altman, E. Demler, and M. D. Lukin, *Phys. Rev. A* **70**, 013603 (2004).
- [23] C. Gies and D. A. W. Hutchinson, *Phys. Rev. A* **70**, 043606 (2004).
- [24] M. Born and E. Wolf, *Optics*, 6th ed. (Pergamon, Oxford 1980), Chap. 10.4.
- [25] D. E. Miller, J. R. Anglin, J. R. Abo-Shaer, K. Xu, J. K. Chin, and W. Ketterle, *Phys. Rev. A* **71**, 043615 (2005).
- [26] N. K. Whitlock, S. M. Barnett, and J. Jeffers, *J. Phys. B* **36**, 1273 (2003).
- [27] W. Krauth, *Phys. Rev. Lett.* **77**, 3695 (1996).
- [28] W. H. Louisell, *Quantum Statistical Properties of Radiation* (Wiley, New York, 1973).
- [29] L. D. Landau and E. M. Lifshitz, *Statistical Physics* (Butterworth, London, 1996).
- [30] H. D. Politzer, *Phys. Rev. A* **54**, 5048 (1996).
- [31] R. Hoppeler, J. C. Viana Gomes, and D. Boiron, *Eur. Phys. J. D* (to be published).
- [32] A. G. Sinclair and M. A. Kasevich, *Rev. Sci. Instrum.* **68**, 1657 (1997).
- [33] C. Cohen-Tannoudji, lecture notes at the Collège de France (1992) available at <http://www.phys.ens.fr/cours/college-de-france/1992-93/1992-93.htm>
- [34] R. P. Feynmann and A. R. Hibbs, *Quantum Mechanics and Path Integrals* (McGraw-Hill, New York, 1965).
- [35] I. S. Gradshteyn and I. M. Ryzhik, *Table of Integrals, Series, and Products* (Academic, London, 1980).
- [36] M. Naraschewski, H. Wallis, A. Schenzle, J. I. Cirac, and P. Zoller, *Phys. Rev. A* **54**, 2185 (1996).
- [37] Y. Castin and R. Dum, *Phys. Rev. Lett.* **77**, 5315 (1996).
- [38] Y. Kagan, E. L. Surkov, and G. V. Shlyapnikov, *Phys. Rev. A* **54**, R1753 (1996).
- [39] H. Kaiser, S. A. Werner, and E. A. George, *Phys. Rev. Lett.* **50**, 560 (1983).
- [40] A. G. Klein, G. I. Opat, and W. A. Hamilton, *Phys. Rev. Lett.* **50**, 563 (1983).
- [41] A. Perrin, D. Boiron, and M. Belsley (unpublished).

overexpressed oncogene by QPCR in prostate cancer, with 72.0% of cases overexpressing *ERG* (21). By using a combination of assays, we found evidence of fusion with *TMPRSS2* in 20 of 22 (>90%) cases that overexpressed *ERG* or *ETV1*, suggesting that the fusion is the most likely cause for the overexpression. FISH analysis on a set of 29 prostate cancer cases selected independently of any knowledge of *ERG* or *ETV1* expression indicates that 23 of 29 (79%) had *TMPRSS2:ETV1* fusions or *ERG* rearrangement. It is possible that this cohort is not representative of all prostate cancer samples and that this may be an overestimate of the prevalence of *TMPRSS2* fusions with ETS family members, because our split-signal approach can detect additional rearrangements involving *ERG*. However, the reported frequencies of *ERG* or *ETV1* overexpression in prostate cancer with our fusion transcript and FISH results suggest that *TMPRSS2* fusions with *ETV1* or *ERG* occur in the majority of prostate cancer cases. Coupled with the high incidence of prostate cancer [an estimated 232,090 new cases will be diagnosed in the United States in 2005 (22)], the *TMPRSS2* fusion with ETS family members is likely to be the most common rearrangement yet identified in human malignancies and the only rearrangement present in the majority of one of the most prevalent carcinomas.

Future efforts will be directed at characterizing the expressed protein products, including

the effects of N-terminal truncation of *ERG* and *ETV1*, and identifying downstream targets and the functional role of the fusions in prostate cancer development. Importantly, the existence of *TMPRSS2* fusions with ETS family members in prostate cancer suggests that causal gene rearrangements may exist in common epithelial cancers but may be masked by the multiple nonspecific chromosomal rearrangements that occur during tumor progression.

References and Notes

1. J. D. Rowley, *Nat. Rev. Cancer* **1**, 245 (2001).
2. T. H. Rabbitts, *Nature* **372**, 143 (1994).
3. J. D. Rowley, *Nature* **243**, 290 (1973).
4. A. de Klein *et al.*, *Nature* **300**, 765 (1982).
5. M. Deininger, E. Buchdunger, B. J. Druker, *Blood* **105**, 2640 (2005).
6. F. Mitelman, *Mutat. Res.* **462**, 247 (2000).
7. Materials and methods are available as supporting material on Science Online.
8. D. R. Rhodes *et al.*, *Neoplasia* **6**, 1 (2004).
9. P. A. Futreal *et al.*, *Nat. Rev. Cancer* **4**, 177 (2004).
10. Detailed results from the application of COPA to Oncomine data sets can be explored at www.oncomine.org.
11. T. Oikawa, T. Yamada, *Gene* **303**, 11 (2003).
12. T. Hsu, M. Trojanowska, D. K. Watson, *J. Cell. Biochem.* **91**, 896 (2004).
13. I. S. Jeon *et al.*, *Oncogene* **10**, 1229 (1995).
14. P. H. Sorensen *et al.*, *Nat. Genet.* **6**, 146 (1994).
15. J. Lapointe *et al.*, *Proc. Natl. Acad. Sci. U.S.A.* **101**, 811 (2004).
16. G. V. Glinsky, A. B. Glinskii, A. J. Stephenson, R. M. Hoffman, W. L. Gerald, *J. Clin. Invest.* **113**, 913 (2004).
17. R. Fonseca *et al.*, *Cancer Res.* **64**, 1546 (2004).
18. B. Lin *et al.*, *Cancer Res.* **59**, 4180 (1999).
19. D. E. Afar *et al.*, *Cancer Res.* **61**, 1686 (2001).
20. E. Jacquinet *et al.*, *Eur. J. Biochem.* **268**, 2687 (2001).
21. G. Petrovics *et al.*, *Oncogene* **24**, 3847 (2005).
22. A. Jemal *et al.*, *CA Cancer J. Clin.* **55**, 10 (2005).

23. P. J. Valk *et al.*, *N. Engl. J. Med.* **350**, 1617 (2004).
24. J. R. Vasselli *et al.*, *Proc. Natl. Acad. Sci. U.S.A.* **100**, 6958 (2003).
25. M. E. Ross *et al.*, *Blood* **102**, 2951 (2003).
26. E. Tian *et al.*, *N. Engl. J. Med.* **349**, 2483 (2003).
27. S. M. Dhanasekaran *et al.*, *FASEB J.* **19**, 243 (2005).
28. J. B. Welsh *et al.*, *Cancer Res.* **61**, 5974 (2001).
29. F. Zhan *et al.*, *Blood* **99**, 1745 (2002).
30. S. M. Dhanasekaran *et al.*, *Nature* **412**, 822 (2001).
31. E. Huang *et al.*, *Lancet* **361**, 1590 (2003).
32. C. Sotiriou *et al.*, *Proc. Natl. Acad. Sci. U.S.A.* **100**, 10393 (2003).
33. T. O. Nielsen *et al.*, *Lancet* **359**, 1301 (2002).
34. Y. P. Yu *et al.*, *J. Clin. Oncol.* **22**, 2790 (2004).
35. We thank D. Roulston and E. Fearon for helpful discussions, D. Robins and K. Burnstein for the PC3+AR cells, and R. Desphande and C. Creighton for technical assistance. Supported by the Early Detection Research Network Biomarker Developmental Lab UO1 CA111275-01 (to A.M.C.); NIH Prostate specialized program of research excellence (SPORE) P50CA69568 (to K.J.P.), RO1 CA97063 (to A.M.C.), and RO1AG21404 (to M.A.R.); American Cancer Society RSG-02-179-MGO (to A.M.C.); Department of Defense (PC040517 to R.M. and PC020322 to A.M.C.); and the Cancer Center Bioinformatics Core (support grant 5P30 CA46592). D.R.R. is supported by the Cancer Biology Training Program. K.J.P. is an American Cancer Society Clinical Research Professor. A.M.C. is a Pew Biomedical Scholar, and S.A.T. and D.R.R. are Fellows of the Medical Scientist Training Program. Nucleotide sequences for the *TMPRSS2:ETS* fusions have been deposited at GenBank with accession numbers DQ204770 to DQ04773.

Supporting Online Material

www.sciencemag.org/cgi/content/full/310/5748/644/DC1

Materials and Methods
Figs. S1 to S8
Tables S1 and S2

20 July 2005; accepted 22 September 2005
10.1126/science.1117679

REPORTS

Hanbury Brown Twiss Effect for Ultracold Quantum Gases

M. Schellekens,¹ R. Hoppeler,¹ A. Perrin,¹ J. Viana Gomes,^{1,2}
D. Boiron,¹ A. Aspect,¹ C. I. Westbrook^{1*}

We have studied two-body correlations of atoms in an expanding cloud above and below the Bose-Einstein condensation threshold. The observed correlation function for a thermal cloud shows a bunching behavior, whereas the correlation is flat for a coherent sample. These quantum correlations are the atomic analog of the Hanbury Brown Twiss effect. We observed the effect in three dimensions and studied its dependence on cloud size.

Nearly half a century ago, Hanbury Brown and Twiss (HBT) performed a landmark experiment on light from a gaseous discharge (1). The experiment demonstrated strong cor-

¹Laboratoire Charles Fabry de l'Institut d'Optique, UMR 8501 du CNRS, Centre Scientifique d'Orsay, Bâtiment 503, 91403 Orsay CEDEX, France. ²Departamento de Física, Universidade do Minho, 4710-057 Braga, Portugal.

*To whom correspondence should be addressed. E-mail: christoph.westbrook@iota.u-psud.fr

relations in the intensity fluctuations at two nearby points in space despite the random or chaotic nature of the source. Although the effect was easily understood in the context of classical statistical wave optics, the result was surprising when viewed in terms of the quantum theory. It implied that photons coming from widely separated points in a source such as a star were "bunched." On the other hand, photons in a laser were not bunched (2, 3).

The quest to understand the observations stimulated the birth of modern quantum optics (4). The HBT effect has since found applications in many other fields from particle physics (5) to fluid dynamics (6).

Atom or photon bunching can be understood as a two-particle interference effect (7). Experimentally, one measures the joint probability for two particles emitted from two separated source points, *A* and *B*, to be detected at two detection points, *C* and *D*. One must consider the quantum mechanical amplitude for the process *A*→*C* and *B*→*D* as well as that for *A*→*D* and *B*→*C*. If the two processes are indistinguishable, the amplitudes interfere. For bosons, the interference is constructive, resulting in a joint detection probability that is enhanced compared with that of two statistically independent detection events, whereas for fermions the joint probability is lowered. As the detector separation is increased, the phase difference between the two amplitudes grows large enough that an average over all possible source points *A* and *B* washes out the interference, and one recovers the sit-

uation for uncorrelated detection events. This fact was used by HBT to measure the angular size of a star (8), but another major consequence of the observation was to draw attention to the importance of two-photon amplitudes and how their interference can lead to surprising effects. These quantum amplitudes must not be confused with classical electromagnetic field amplitudes (3). Two-photon states subsequently led to many other striking examples of “quantum weirdness” (9). In contrast to a chaotic source, all photons in a single mode laser are in the same quantum state. Hence, there is only one physical process and no bunching effect. A similar effect is expected for atoms in a Bose-Einstein condensate (BEC).

Two-particle correlations have been observed both for cold neutral atoms (10–12) and for electrons (13–15), and three-particle correlations (16–18) at zero distance have also been used to study atomic gases. But the full three-dimensional effect and its dependence on the size and degeneracy of a sample has yet to be demonstrated for massive particles. Here, we demonstrate the effect for a trapped cloud of atoms close to the BEC transition temperature released onto a detector capable of individual particle detection. We extract, for varying cloud sizes, a three-dimensional picture of the correlations between identical particles produced by quantum interference. We also show that a BEC shows no such correlations. The results are in agreement with an ideal gas model and show the power of single particle detection techniques applied to the study of degenerate quantum gases.

The calculation of the phase difference of the possible two-particle detection amplitudes given in (7) can be adapted to the case of particles of mass m traveling to a detector in a time t . One can show that the correlation length observed at the detectors, that is, the typical detector separation for which interference survives, is $l_i = \frac{\hbar t}{ms_i}$, where s_i is the source size along the direction i , \hbar is the reduced Planck’s constant, and we have assumed that the size of the cloud at the detector is much larger than the initial size. The optical analog of this expression, for a source of size s and wavelength λ at a distance L from the observation plane, is $l = L\lambda/2\pi s$. This is the length scale of the associated speckle pattern. The formula can be recovered for the case of atoms traveling at constant velocity v toward a detector at distance L if one identifies \hbar/mv with the deBroglie wavelength corresponding to velocity v . The formula we give is also valid for atoms accelerated by gravity, and the interpretation of l as the atomic speckle size remains valid. A pioneering experiment on atom correlations used a continuous beam of atoms (10). For a continuous beam, the correlation time, or equivalently, the longitudinal correlation length, de-

pends on the velocity width of the source and not on the source size. Thus, the longitudinal and transverse directions are qualitatively different. By contrast, our measurements are performed on a cloud of atoms released suddenly from a magnetic trap. In this case, the three dimensions can all be treated equivalently, and the relation above applies in all three. Because the trap is anisotropic, the correlation function is as well, with an inverted ellipticity. Our sample is a magnetically trapped cloud of metastable helium atoms evaporatively cooled close to the BEC transition temperature (19) (about 0.5 μ K for our conditions). Our source is thus very small, and together with a long time of flight (308 ms) and helium’s small mass, we achieve a large speckle size or correlation volume (30 μ m by 800 μ m by 800 μ m), which simplifies the detection problem. For example, the observations are much less sensitive to the tilt of the detector than in (10).

To detect the atoms, we use an 8-cm-diameter microchannel plate detector (MCP). It is placed 47 cm below the center of the magnetic trap. A delay line anode permits position-sensitive detection of individual particles in the plane of the detector (20) (Fig. 1). Atoms are released from the trap by suddenly turning off the magnetic field. About 10% of these atoms are transferred to the magnetic field-insensitive $m = 0$ state by nonadiabatic transitions (19) and fall freely to the detector. The remaining atoms are removed by applying additional magnetic field gradients during the time of flight. For each detected atom, we record the in-plane coordinates x and y and the time of detection t . The atoms hit the detector at 3 m/s with a velocity spread below 1%, and so we convert t into a vertical position z . The observed root mean square (rms) resolution is $d \sim 250$ μ m in x and y and 2 nm in z . These

data allow us to construct a three-dimensional histogram of pair separations (Δx , Δy , and Δz) for all particles detected in a single cloud. The histograms are summed over the entire atomic distribution and over many shots, typically 1000 (21).

Because of our good resolution along z , we begin by concentrating on the correlation function along this axis. Normalized correlation functions for various experimental conditions are shown in Fig. 2A. To compute the normalized correlation function, we divide the pair separation histogram by the autoconvolution of the average single particle distribution along z . We also normalize the correlation function to unity for large separations. This amounts to dividing, for each elementary pixel of our detector, the joint detection probability by the product of the individual detection probabilities at the two pixels. This gives us the usual normalized correlation function $g^{(2)}(\Delta x = 0, \Delta y = 0, \Delta z)$. The HBT bunching effect corresponds to the bump in the top three graphs of Fig. 2A. The fourth graph shows the result for a BEC. No correlation is observed. [A detector saturation effect in the BEC data required a modified analysis procedure (21).] We have also recorded data for a cloud with a 2-mm radius and 1-mK temperature for which the correlation length is so small that the bunching effect is washed out by the in-plane detector resolution. Experimentally, the normalized correlation function in this case is indeed flat to within less than 1%.

We plot (Fig. 2B) the normalized correlation functions in the $\Delta x - \Delta y$ plane and for $\Delta z = 0$ for the same three data sets. The data in Fig. 2B show the asymmetry in the correlation function arising from the difference in the two transverse dimensions of the trapped cloud. The long axis of the correlation function is orthogonal to that of the magnetic trap.

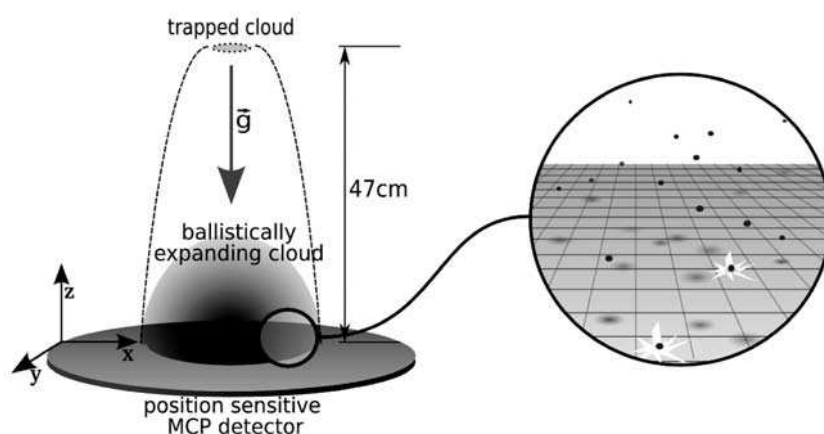


Fig. 1. Schematic of the apparatus. The trapped cloud has a cylindrical symmetry with oscillation frequencies of $\omega_x/2\pi = 47$ Hz and $\omega_y/2\pi = \omega_z/2\pi = 1150$ Hz. During its free fall toward the detector, a thermal cloud acquires a spherical shape. A 1- μ K temperature yields a cloud with an rms radius of about 3 cm at the detector. Single particle detection of the neutral atoms is possible because of each atom’s 20-eV internal energy that is released at contact with the MCP. Position sensitivity is obtained through a delay-line anode at the rear side of the MCP.

REPORTS

Fig. 2. (A) Normalized correlation functions along the vertical (z) axis for thermal gases at three different temperatures and for a BEC. For the thermal clouds, each plot corresponds to the average of a large number of clouds at the same temperature. Error bars correspond to the square root of the number of pairs. a.u., arbitrary units. (B) Normalized correlation functions in the $\Delta x - \Delta y$ plane for the three thermal gas runs. The arrows at the bottom show the 45° rotation of our coordinate system with respect to the axes of the detector. The inverted ellipticity of the correlation function relative to the trapped cloud is visible.

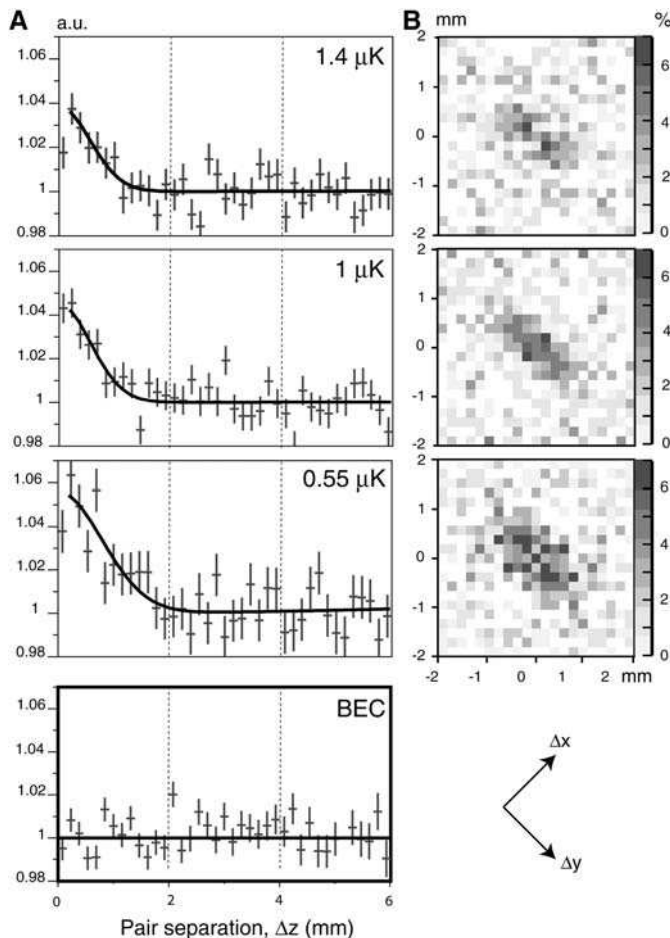
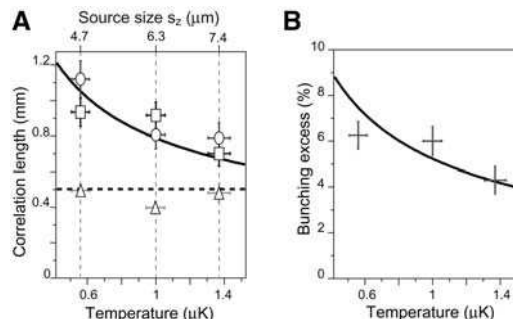


Fig. 3. Results of fits to the data in Fig. 2, A and B. (A) Fitted correlation lengths l_x , l_y , and l_z along the three axes (triangles, squares, and circles) as a function of temperature. The upper axis shows the corresponding source size s_z . Vertical error bars are from the fits. Horizontal error bars correspond to the standard deviation of the measured temperature. Along the x axis, the measurement is entirely limited by the detector resolution. The dotted horizontal line is the result of an independent estimate of the resolution. The result for the y axis has been corrected for the finite detector resolution as characterized by the fitted value of l_x . The z axis suffers from no such resolution limit. The solid curve corresponds to $\hbar t/m_s$. (B) Fitted contrast η of the correlation function for the three temperatures used. The solid line corresponds to the same non-interacting gas model as the line in (A) (27) and includes the finite detector resolution.



We expect the experimental normalized correlation function for a thermal bosonic gas to be described by

$$g_{\text{th}}^{(2)}(\Delta x, \Delta y, \Delta z) = 1 + \eta \exp\left(-\left[\left(\frac{\Delta x}{l_x}\right)^2 + \left(\frac{\Delta y}{l_y}\right)^2 + \left(\frac{\Delta z}{l_z}\right)^2\right]\right) \quad (1)$$

We have assumed here that the gas is non-interacting and that the velocity and density distribution remain roughly Gaussian even

close to the BEC transition temperature. Numerical simulations indicate that this is a good approximation when the correlation function is averaged over the entire cloud (22). As discussed above, the correlation lengths should be inversely proportional to the sizes, s_i , of the sample. In a harmonic trap with trapping frequency ω_i along the i direction, one has $s_i = \sqrt{\frac{k_B T}{m\omega_i^2}}$, where k_B is Boltzmann's constant and T is the temperature of the atoms. Because T is derived directly from the time of flight spectrum, we shall plot our data as a

function of T rather than of s . The parameter η would be unity for a detector whose resolution width d is small compared with the correlation length. Our d is smaller than l_y , but larger than l_x , and in this case the convolution by the detector resolution results in an η given roughly by $l_x/2d \sim 5\%$. We use Eq. 1 to fit the data by using η and the l_i as fit parameters and compare the results to the ideal gas model (21).

The results for l_x , l_y , and l_z for our three temperatures are plotted in Fig. 3A. The fitted values of l_x are $\sim 450 \mu\text{m}$ and are determined by the detector resolution rather than the true coherence length along x . The value of l_y has been corrected for the finite spatial resolution of the detector. The fitted value of l_z requires no correction, because in the vertical direction the resolution of the detector is much better. l_y and l_z are consistent and agree with the prediction using the known trap frequencies and temperatures. Figure 3B shows the fitted value of η versus temperature, along with the prediction of the same ideal gas model as in Fig. 3A, using the measured detector resolution. The data are in reasonable agreement with the model, although we may be seeing too little contrast at the lowest temperature. The run at $0.55 \mu\text{K}$ was above, but very close to, the BEC transition temperature. (We know this because, when taking data at $0.55 \mu\text{K}$, about one-third of the shots contained small BECs; these runs were eliminated before plotting Fig. 2.) Future work will include examining whether the effect of the repulsive interactions between atoms or finite atom number must be taken into account.

The results reported here show the power of single particle detection in the study of quantum gases. The correlations we have observed are among the simplest that should be present. Two recent experiments have shown correlations in a Mott insulator (11) as well as in atoms produced from the breakup of molecules near a Feshbach resonance (12). Improved observations of these effects may be possible with individual particle detection. Other atom pair production mechanisms, such as four-wave mixing (23, 24), can be investigated. A fermionic analog to this experiment using ^3He would also be (25) of great interest.

References and Notes

1. R. Hanbury Brown, R. Q. Twiss, *Nature* **177**, 27 (1956).
2. F. T. Arecchi, E. Gatti, A. Sona, *Phys. Lett.* **20**, 27 (1966).
3. R. J. Glauber, *Phys. Rev. Lett.* **10**, 84 (1963).
4. R. J. Glauber, *Quantum Optics and Electronics*, C. DeWitt, A. Blandin, C. Cohen-Tannoudji, Eds. (Gordon and Breach, New York, 1965), p. 63.
5. G. Baym, *Acta Phys. Pol. B* **29**, 1839 (1998).
6. B. Berne, R. Pecora, *Dynamic Light Scattering* (Dover, New York, 2000).
7. U. Fano, *Am. J. Phys.* **29**, 539 (1961).
8. R. Hanbury Brown, R. Twiss, *Nature* **178**, 1046 (1956).
9. J. S. Bell, *Speakable and Unsayable in Quantum Mechanics* (Cambridge Univ. Press, Cambridge, ed. 2, 2004).
10. M. Yasuda, F. Shimizu, *Phys. Rev. Lett.* **77**, 3090 (1996).
11. S. Fölling et al., *Nature* **434**, 481 (2005).

12. M. Greiner, C. A. Regal, J. T. Stewart, D. S. Jin, *Phys. Rev. Lett.* **94**, 110401 (2005).
13. M. Henny *et al.*, *Science* **284**, 296 (1999).
14. W. D. Oliver, J. Kim, R. C. Liu, Y. Yamamoto, *Science* **284**, 299 (1999).
15. H. Kiesel, A. Renz, F. Hasselbach, *Nature* **418**, 392 (2002).
16. Y. Kagan, B. V. Svistunov, G. V. Shlyapnikov, *Sov. Phys. JETP* **42**, 209 (1985).
17. E. A. Burt *et al.*, *Phys. Rev. Lett.* **79**, 337 (1997).
18. B. Laburthe Tolra *et al.*, *Phys. Rev. Lett.* **92**, 190401 (2004).
19. A. Robert *et al.*, *Science* **292**, 461 (2001); published online 22 March 2001 (10.1126/science.1060622).
20. O. Jagutzki *et al.*, *Nucl. Instrum. Methods Phys. Res. A* **477**, 244 (2004).
21. See supporting online materials on *Science* Online for details.
22. M. Naraschewski, R. Glauber, *Phys. Rev. A* **59**, 4595 (1999).
23. L. Deng *et al.*, *Nature* **398**, 218 (1999).
24. J. Vogels, K. Xu, W. Ketterle, *Phys. Rev. Lett.* **89**, 020401 (2002).
25. R. Stas, J. McNamara, W. Hogervorst, W. Vassen, *Phys. Rev. Lett.* **93**, 053001 (2004).
26. A. Öttl, S. Ritter, M. Köhl, T. Esslinger, *Phys. Rev. Lett.* **95**, 090404 (2005).
27. After submission of this manuscript, we became aware of a related experiment concerning atom correlations in an atom laser (26). We thank R. Sellem of the Détection Temps, Position Image Technology Division

(supported by the Mission Ressources et Compétences Technologiques–CNRS Federation FR2764 and by the Université Paris-Sud) for a decisive role in the development of the time-to-digital converter, and O. Jagutzki for advice on delay lines.

Supporting Online Material
www.sciencemag.org/cgi/content/full/1118024/DC1
SOM Text

27 July 2005; accepted 5 September 2005
Published online 15 September 2005;
10.1126/science.1118024
Include this information when citing this paper.

Quantum Coherence in an Optical Modulator

S. G. Carter,^{1*} V. Birkedal,^{1†} C. S. Wang,² L. A. Coldren,²
A. V. Maslov,³ D. S. Citrin,^{4,5} M. S. Sherwin^{1‡}

Semiconductor quantum well electroabsorption modulators are widely used to modulate near-infrared (NIR) radiation at frequencies below 0.1 terahertz (THz). Here, the NIR absorption of undoped quantum wells was modulated by strong electric fields with frequencies between 1.5 and 3.9 THz. The THz field coupled two excited states (excitons) of the quantum wells, as manifested by a new THz frequency- and power-dependent NIR absorption line. Nonperturbative theory and experiment indicate that the THz field generated a coherent quantum superposition of an absorbing and a nonabsorbing exciton. This quantum coherence may yield new applications for quantum well modulators in optical communications.

Quantum three-state systems in which two of the states are strongly coupled by an intense laser field have been widely studied in atomic and molecular systems (1). The energies of the quantum states are altered as they are “dressed” by the strong light-matter interaction. Such dressed states were first observed by Autler and Townes (AT) in a molecular system driven by a strong radio-frequency field and probed by weak microwaves (2). When a radio-frequency resonance occurred, the microwave absorption line split in two. In three-state systems with weak coupling to the environment, AT splitting can evolve into electromagnetically induced transparency (EIT), in which a strong coupling beam induces transparency at a resonance at which the undriven system is opaque (3). This transparency is due to quantum interference between the dressed states.

EIT is the basis for slow (4) and stopped light (5, 6) in atomic systems.

A variety of quantum systems similar to atomic three-state systems can be engineered in semiconductor quantum wells (QWs). A QW is a layer of one semiconductor grown between semiconductors with larger band gaps (7). The layer with the smaller gap is sufficiently thin that well-defined sets of quantized states, or subbands, are associated with electron motion parallel to the growth direction. Within each subband, there is a continuum of states associated with different momenta parallel to the plane of the QW (perpendicular to the growth direction). AT-like splitting (8), quantum interference (9, 10), and EIT (11, 12) have been reported in QWs, but their observation has been more difficult than in atoms and molecules. This is in part because of much larger absorption linewidths, which result from disorder, from stronger coupling to the environment, or from scattering between subbands.

We have fabricated a particularly simple three-level system in undoped QWs (Fig. 1). The excitation with the lowest frequency occurs at about 350 THz (wavelength 857 nm or energy 1.46 eV) when an electron is promoted from the filled valence subband of highest energy (labeled h1) to the empty conduction subband of lowest energy (labeled e1). The excited electron binds with the hole it left behind to form an exciton with a hydrogen-like wave function in the QW plane. Transitions between different in-plane states (e.g., the 1s

and 2p states) are allowed only for in-plane THz polarizations (13, 14), which are not present in the experiments discussed here. The lowest exciton state is labeled h1X. The next exciton state, h2X, consists of an electron from e1 and a hole from the second highest valence subband, h2. NIR transitions between the crystal ground state and h2X are not allowed because of quantum mechanical selection rules. However, intersubband transitions from h1X to h2X are allowed for THz radiation polarized in the growth direction. The three states analogous to those in an AT picture are the crystal ground state, the lowest exciton h1X, and the second exciton h2X (15).

This report explores the NIR absorption of undoped QWs at low temperatures (~10 K) when they are driven by strong electric fields polarized in the growth direction with frequencies between 1.5 and 3.9 THz. Because the frequency of the THz laser is about 1% of that required to create an exciton, the strong laser field does not alter the populations of the quantum states of the system. Near 3.4 THz, the drive frequency is resonant with the transition between the two lowest exciton states. The AT splitting of excitons driven by strong intersubband radiation is experimentally observed, and theoretical predictions (16, 17) are confirmed.

The sample consists of 10 In_{0.06}Ga_{0.94}As QWs (each 143 Å) separated by Al_{0.3}Ga_{0.7}As barriers (300 Å). InGaAs QWs were used instead of GaAs QWs so that the GaAs substrate was transparent for NIR light near the exciton energies. A 100-nm layer of aluminum was deposited on the surface of the sample on which the QWs were grown. The metallic boundary condition improved THz coupling and ensured that the THz field at the QWs was polarized almost perfectly in the growth direction (18). The interband absorption was probed using broadband, incoherent, NIR light from an 850-nm light-emitting diode focused onto the sample backside to a spot size ~250 μm in diameter. The NIR intensity was less than 0.3 W/cm². As illustrated in Fig. 1, the NIR beam was transmitted through the transparent substrate, interacted with the QWs, was reflected off of the Al layer, and was then collected and sent to a monochromator with an intensified charge-coupled device detector. The reflected NIR beam was measured during the 1 to 1.5 μs at the peak of the THz

¹Physics Department and Institute for Quantum and Complex Dynamics (iQCD), Broida Hall Building 572, Room 3410, ²Electrical and Computer Engineering Department, University of California, Santa Barbara, CA 93106, USA. ³Center for Nanotechnology, NASA Ames Research Center, MS 229-1, Moffett Field, CA 94035, USA. ⁴Electrical and Computer Engineering, Georgia Institute of Technology, Atlanta, GA 30332, USA. ⁵Georgia Tech Lorraine, Metz Technopole, 2-3 rue Marconi, 57070 Metz, France.

*Present address: JILA, University of Colorado, 440 UCB, Boulder, CO 80309, USA.

†née Ciulin. Present address: Department of Chemistry, University of Aarhus, Langelandsgade 140, DK-8000 Århus C, Denmark.

‡To whom correspondence should be addressed. E-mail: sherwin@physics.ucsb.edu

LETTERS

Comparison of the Hanbury Brown–Twiss effect for bosons and fermions

T. Jelte¹, J. M. McNamara¹, W. Hogervorst¹, W. Vassen¹, V. Krachmalnicoff², M. Schellekens², A. Perrin², H. Chang², D. Boiron², A. Aspect² & C. I. Westbrook²

Fifty years ago, Hanbury Brown and Twiss (HBT) discovered photon bunching in light emitted by a chaotic source¹, highlighting the importance of two-photon correlations² and stimulating the development of modern quantum optics³. The quantum interpretation of bunching relies on the constructive interference between amplitudes involving two indistinguishable photons, and its additive character is intimately linked to the Bose nature of photons. Advances in atom cooling and detection have led to the observation and full characterization of the atomic analogue of the HBT effect with bosonic atoms^{4–6}. By contrast, fermions should reveal an antibunching effect (a tendency to avoid each other). Antibunching of fermions is associated with destructive two-particle interference, and is related to the Pauli principle forbidding more than one identical fermion to occupy the same quantum state. Here we report an experimental comparison of the fermionic and bosonic HBT effects in the same apparatus, using two different isotopes of helium: ³He (a fermion) and ⁴He (a boson). Ordinary attractive or repulsive interactions between atoms are negligible; therefore, the contrasting bunching and antibunching behaviour that we observe can be fully attributed to the different quantum statistics of each atomic species. Our results show how atom–atom correlation measurements can be used to reveal details in the spatial density^{7,8} or momentum correlations⁹ in an atomic ensemble. They also enable the direct observation of phase effects linked to the quantum statistics of a many-body system, which may facilitate the study of more exotic situations¹⁰.

Two-particle correlation analysis is an increasingly important method for studying complex quantum phases of ultracold atoms^{7–13}. It goes back to the discovery, by Hanbury Brown and Twiss¹, that photons emitted by a chaotic (incoherent) light source tend to be bunched: the joint detection probability is enhanced, compared to that of statistically independent particles, when the two detectors are close together. Although the effect is easily understood in the context of classical wave optics¹⁴, it took some time to find a clear quantum interpretation^{3,15}. The explanation relies on interference between the quantum amplitude for two particles, emitted from two source points S_1 and S_2 , to be detected at two detection points D_1 and D_2 (see Fig. 1). For bosons, the two amplitudes $\langle D_1|S_1\rangle\langle D_2|S_2\rangle$ and $\langle D_1|S_2\rangle\langle D_2|S_1\rangle$ must be added, which yields a factor of 2 excess in the joint detection probability, if the two amplitudes have the same phase. The sum over all pairs (S_1, S_2) of source points washes out the interference, unless the distance between the detectors is small enough that the phase difference between the amplitudes is less than one radian, or equivalently if the two detectors are separated by a distance less than the coherence length. Study of the joint detection rates versus detector separation along the i direction then

reveals a ‘bump’ whose width l_i is the coherence length along that axis^{1,5,16–19}. For a source size s_i (defined as the half width at $e^{-1/2}$ of a gaussian density profile) along the i direction, the bump has a half width at e^{-1} of $l_i = \hbar t / (2\pi m s_i)$, where m is the mass of the particle, t the time of flight from the source to the detector, and \hbar Planck’s constant. This formula is the analogue of the formula $l_i = L\lambda / (2\pi s_i)$ for photons, if $\lambda = \hbar / (mv)$ is identified with the de Broglie wavelength for particles travelling at velocity $v = L/t$ from the source to the detector.

For indistinguishable fermions, the two-body wavefunction is antisymmetric, and the two amplitudes must be subtracted, yielding a null probability for joint detection in the same coherence volume. In the language of particles, it means that two fermions cannot have momenta and positions belonging to the same elementary cell of

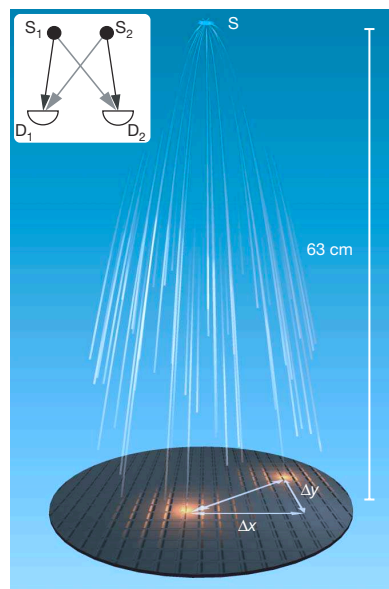


Figure 1 | The experimental set-up. A cold cloud of metastable helium atoms is released at the switch-off of a magnetic trap. The cloud expands and falls under the effect of gravity onto a time-resolved and position-sensitive detector (microchannel plate and delay-line anode) that detects single atoms. The horizontal components of the pair separation Δr are denoted Δx and Δy . The inset shows conceptually the two 2-particle amplitudes (in black or grey) that interfere to give bunching or antibunching: S_1 and S_2 refer to the initial positions of two identical atoms jointly detected at D_1 and D_2 .

¹Laser Centre Vrije Universiteit, De Boelelaan 1081, 1081 HV Amsterdam, The Netherlands. ²Laboratoire Charles Fabry de l'Institut d'Optique, CNRS, Univ. Paris-sud, Campus Polytechnique RD 128, 91127 Palaiseau Cedex, France.

phase space. As a result, for fermions the joint detection rate versus detector separation is expected to exhibit a dip around the null separation. Such a dip for a fermion ensemble must not be confused with the antibunching dip that one can observe with a single particle (boson or fermion) quantum state—for example, resonance fluorescence photons emitted by an individual quantum emitter²⁰. In contrast to the HBT effect for bosons, the fermion analogue cannot be interpreted by any classical model, either wave or particle, and extensive efforts have been directed towards an experimental demonstration. Experiments have been performed with electrons in solids^{21,22} and in a free beam²³, and with a beam of neutrons²⁴, but none has allowed a detailed study and a comparison of the pure fermionic and bosonic HBT effects for an ideal gas. A recent experiment using fermions in an optical lattice²⁵, however, does permit such a study and is closely related to our work.

Here we present an experiment in which we study the fermionic HBT effect for a sample of polarized, metastable $^3\text{He}^*$ atoms ($^3\text{He}^*$), and we compare it to the bosonic HBT effect for a sample of polarized, but not Bose condensed, metastable $^4\text{He}^*$ atoms ($^4\text{He}^*$) produced in the same apparatus at the same temperature. We have combined the position- and time-resolved detector, previously used^{15,26} for $^4\text{He}^*$, with an apparatus with which ultracold samples of $^3\text{He}^*$ or $^4\text{He}^*$ have recently been produced²⁷. Fermions or bosons at thermal equilibrium in a magnetic trap are released onto the detector, which counts individual atoms (see Fig. 1) with an efficiency of approximately 10%. The detector allows us to construct the normalized correlation function $g^{(2)}(\Delta\mathbf{r})$, that is, the probability of joint detection at two points separated by $\Delta\mathbf{r}$, divided by the product of the single detection probabilities at each point. Statistically independent detection events result in a value of 1 for $g^{(2)}(\Delta\mathbf{r})$. A value larger than 1 indicates bunching, while a value less than 1 is evidence of antibunching.

We produce gases of pure $^3\text{He}^*$ or pure $^4\text{He}^*$ by a combination of evaporative and sympathetic cooling in an anisotropic magnetic trap (see Methods). Both isotopes are in pure magnetic substates, with nearly identical magnetic moments and therefore nearly identical trapping potentials, so that trapped non-degenerate and non-interacting samples have the same size at the same temperature. The temperatures of the samples yielding the results of Fig. 2, as measured by the spectrum of flight times to the detector, are $0.53 \pm 0.03 \mu\text{K}$ and $0.52 \pm 0.05 \mu\text{K}$ for $^3\text{He}^*$ and $^4\text{He}^*$, respectively. The uncertainties correspond to the standard deviation of each ensemble. In a single realization, we typically produce 7×10^4 atoms of both $^3\text{He}^*$ and $^4\text{He}^*$. The atom number permits an estimate of the Fermi and Bose–Einstein condensation temperatures of approximately $0.9 \mu\text{K}$ and $0.4 \mu\text{K}$, respectively. Consequently, Fermi pressure in the trapped $^3\text{He}^*$ sample has a negligible (3%) effect on the trap size, and repulsive interactions in the $^4\text{He}^*$ sample have a similarly small effect. The trapped samples are therefore approximately gaussian ellipsoids elongated along the x axis with an r.m.s. size of about $110 \times 12 \times 12 \mu\text{m}^3$. To release the atoms, we turn off the current in the trapping coils and atoms fall under the influence of gravity. The detector, placed 63 cm below the trap centre (see Fig. 1), then records the x – y position and arrival time of each detected atom.

The normalized correlation functions $g^{(2)}(0,0,\Delta z)$ along the z (vertical) axis, for $^3\text{He}^*$ and $^4\text{He}^*$ gases at the same temperature, are shown in Fig. 2. Each correlation function is obtained by analysing the data from about 1,000 separate clouds for each isotope (see Methods). Results analogous to those of Fig. 2 are obtained for correlation functions along the y axis, but the resolution of the detector in the x – y plane (about $500 \mu\text{m}$ half width at e^{-1} for pair separation) broadens the signals. Along the x axis (the long axis of the trapped clouds), the expected widths of the HBT structures are one order of magnitude smaller than the resolution of the detector and are therefore not resolved.

Figure 2 shows clearly the contrasting behaviours of bosons and fermions. In both cases we observe a clear departure from statistical

independence at small separation. Around zero separation, the fermion signal is lower than unity (antibunching) while the boson signal is higher (bunching). Because the sizes of the $^3\text{He}^*$ and $^4\text{He}^*$ clouds at the same temperature are the same, as are the times of flight (pure free fall), the ratio of the correlation lengths is expected to be equal to the inverse of the mass ratio, $4/3$. The observed ratio of the correlation lengths along the z axis in the data shown is 1.3 ± 0.2 . The individual correlation lengths are also in good agreement with the formula $l_z = \hbar t / (2\pi m s_z)$, where s_z is the source size along z . Owing to the finite resolution, the contrast in the signal, which should ideally go to 0 or 2, is reduced by a factor of order ten. The amount of contrast reduction is slightly different for bosons and fermions, and the ratio should be about 1.5. The measured ratio is 2.4 ± 0.2 . This discrepancy has several possible explanations. First, the magnetic field switch-off is not sudden (timescale ~ 1 ms), and this could affect bosons and fermions differently. Second, systematic errors may be present in our estimate of the resolution function. The resolution, however, does not affect the widths of the observed correlation functions along z , and thus we place the strongest emphasis on this ratio as a test of our understanding of boson and fermion correlations in an ideal gas. More information on uncertainties and systematic errors, as well as a more complete summary of the data, are given in Supplementary Information.

Improved detector resolution would allow a more detailed study of the correlation function, and is thus highly desirable. The effect of the resolution could be circumvented by using a diverging atom lens to demagnify the source⁴. According to the formula $l = \hbar t / (2\pi m s)$, a smaller effective source size gives a larger correlation length. We have tried such a scheme by creating an atomic lens with a blue-detuned, vertically propagating, laser beam, forcing the atoms away from its axis (see Methods). The laser waist was not large compared to the cloud size, and therefore our ‘lens’ suffered from strong aberrations, but a crude estimate of the demagnification, neglecting aberrations, gives about 2 in the x – y plane. Figure 3 shows a comparison of

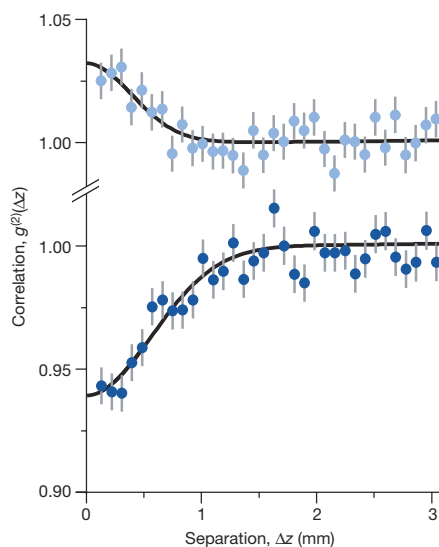


Figure 2 | Normalized correlation functions for $^4\text{He}^*$ (bosons) in the upper plot, and $^3\text{He}^*$ (fermions) in the lower plot. Both functions are measured at the same cloud temperature ($0.5 \mu\text{K}$), and with identical trap parameters. Error bars correspond to the square root of the number of pairs in each bin. The line is a fit to a gaussian function. The bosons show a bunching effect, and the fermions show antibunching. The correlation length for $^3\text{He}^*$ is expected to be 33% larger than that for $^4\text{He}^*$ owing to the smaller mass. We find $1/e$ values for the correlation lengths of 0.75 ± 0.07 mm and 0.56 ± 0.08 mm for fermions and bosons, respectively.

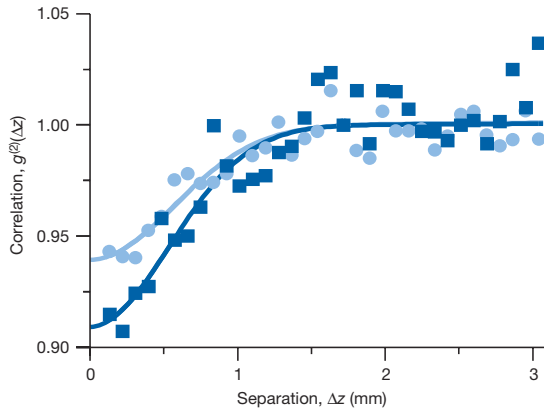


Figure 3 | Effect of demagnifying the source size. We show normalized correlation functions along the z (vertical) axis for $^3\text{He}^*$, with (dark blue squares) and without (light blue circles) a diverging atomic lens in the x - y plane. The dip is deeper with the lens, because the increase of the correlation lengths in the x - y plane leads to less reduction of contrast when convolved with the resolution function in that plane.

$g^{(2)}(\Delta z)$ for fermions with and without the defocusing lens. We clearly see a greater antibunching depth, consistent with larger correlation lengths in the x - y plane (we have checked that l_y is indeed increased) and therefore yielding a smaller reduction of the contrast when convolved with the detector resolution function. As expected, the correlation length in the z direction is unaffected by the lens in the x - y plane. Although our atomic lens was far from ideal, the experiment shows that it is possible to modify the HBT signal by optical means.

To conclude, we emphasize that we have used samples of neutral atoms at a moderate density in which interactions do not play any significant role. Care was taken to manipulate bosons and fermions in conditions as similar as possible. Thus the observed differences can be understood as a purely quantum effect associated with the exchange symmetries of wavefunctions of indistinguishable particles.

The possibility of having access to the sign of phase factors in a many-body wavefunction opens fascinating perspectives for the investigation of intriguing analogues of condensed-matter systems, which can now be realized with cold atoms. For instance, one could compare the many-body state of cold fermions and that of 'fermionized' bosons in a one-dimensional sample^{28,29}. Our successful manipulation of the HBT signal by interaction with a laser suggests that other lens configurations could allow measurements in position space (by forming an image of the cloud at the detector) or in any combination of momentum and spatial coordinates.

METHODS

Experimental sequence. Clouds of cold $^4\text{He}^*$ are produced by evaporative cooling of a pure $^4\text{He}^*$ sample, loaded into a Ioffe-Pritchard magnetic trap³⁰. The trapped state is 2^3S_1 , $m_j = 1$, and the trap frequency values are 47 Hz and 440 Hz for axial and radial confinement, respectively. The bias field is 0.75 G, corresponding to a frequency of 2.1 MHz for a transition between the $m_j = 1$ and $m_j = 0$ states at the bottom of the trap. After evaporative cooling, we keep the radio frequency evaporation field ('r.f. knife') on at constant frequency for 500 ms, then wait for 100 ms before switching off the trap. In contrast to the experiments of ref. 5, atoms are released in a magnetic-field-sensitive state.

To prepare $^3\text{He}^*$ clouds, we simultaneously load $^3\text{He}^*$ and $^4\text{He}^*$ atoms in the magnetic trap²⁷. The trapping state for $^3\text{He}^*$ is 2^3S_1 , $F = 3/2$, $m_f = 3/2$, and axial and radial trap frequencies are 54 Hz and 506 Hz—the difference compared to $^4\text{He}^*$ is only due to the mass. The two gases are in thermal equilibrium in the trap, so that $^3\text{He}^*$ is sympathetically cooled with $^4\text{He}^*$ during the evaporative cooling stage. Once the desired temperature is reached, we selectively eliminate $^4\text{He}^*$ atoms from the trap using the r.f. knife. The gyromagnetic ratios for $^4\text{He}^*$ and $^3\text{He}^*$ are 2 and $4/3$ respectively, so that the resonant frequency of the $m = 1$ to

$m = 0$ transition for $^4\text{He}^*$ is $3/2$ times larger than the $m = 3/2$ to $m = 1/2$ transition for $^3\text{He}^*$. An r.f. ramp from 3 MHz to 1.9 MHz expels all the $^4\text{He}^*$ atoms from the trap without affecting $^3\text{He}^*$. We then use the same trap switch-off procedure to release the $^3\text{He}^*$ atoms (also in a magnetic-field-sensitive state) onto the detector. We can apply magnetic field gradients to check the degree of spin polarization of either species.

Correlation function. The detailed procedure leading to this correlation is given in ref. 5. Briefly, we convert arrival times to z positions, and then use the three-dimensional positions of each atom to construct a histogram of pair separations Δr in a particular cloud. We then sum the pair distribution histograms for 1,000 successive runs at the same temperature. For separations much larger than the correlation length, this histogram reflects the gaussian spatial distribution of the cloud. To remove this large-scale shape and obtain the normalized correlation function, we divide the histogram by the autoconvolution of the sum of the 1,000 single-particle distributions.

Atom lens experiment. A 300 mW laser beam with an elliptical waist of approximately $100 \times 150 \mu\text{m}^2$ propagates vertically through the trap. The laser frequency is detuned by 300 GHz from the 2^3S_1 to 2^3P_2 transition. After turning off the magnetic trap, and waiting 500 μs for magnetic transients to die away, the defocusing laser is turned on for 500 μs .

Received 15 November; accepted 7 December 2006.

- Hanbury Brown, R. & Twiss, R. Q. Correlation between photons in two coherent beams of light. *Nature* **177**, 27–29 (1956).
- Scully, M. O. & Zubairy, M. S. *Quantum Optics* (Cambridge Univ. Press, Cambridge, UK, 1997).
- Glauber, R. J. in *Quantum Optics and Electronics* (eds DeWitt, C., Blandin, A. & Cohen-Tannoudji, C.) 63–185 (Gordon and Breach, New York, 1965).
- Yasuda, M. & Shimizu, F. Observation of two-atom correlation of an ultracold neon atomic beam. *Phys. Rev. Lett.* **77**, 3090–3093 (1996).
- Schellekens, M. *et al.* Hanbury Brown Twiss effect for ultracold quantum gases. *Science* **310**, 648–651 (2005); published online 15 September 2005 (doi:10.1126/science.1118024).
- Öttl, A., Ritter, S., Köhl, M. & Esslinger, T. Correlations and counting statistics on an atom laser. *Phys. Rev. Lett.* **95**, 090404 (2005).
- Fölling, S. *et al.* Spatial quantum noise interferometry in expanding condensates. *Nature* **434**, 481–484 (2005).
- Spielman, I. B., Phillips, W. D. & Porto, J. V. The Mott insulator transition in two dimensions. Preprint at (<http://arxiv.org/cond-mat/0606216>) (2006).
- Greiner, M., Regal, C. A., Stewart, J. T. & Jin, D. S. Probing pair-correlated fermionic atoms through correlations in atom shot noise. *Phys. Rev. Lett.* **94**, 110401 (2005).
- Altman, E., Demler, E. & Lukin, M. D. Probing many-body states of ultracold atoms via noise correlations. *Phys. Rev. A* **70**, 013603 (2004).
- Grondalski, J., Alsing, P. M. & Deutsch, I. H. Spatial correlation diagnostics for atoms in optical lattices. *Opt. Express* **5**, 249–261 (1999).
- Hellweg, D. *et al.* Measurement of the spatial correlation function of phase fluctuating Bose-Einstein condensates. *Phys. Rev. Lett.* **91**, 010406 (2003).
- Estève, J. *et al.* Observations of density fluctuations in an elongated Bose gas: ideal gas and quasicondensate regimes. *Phys. Rev. Lett.* **96**, 130403 (2006).
- Loudon, R. *The Quantum Theory of Light* 3rd edn (Oxford Univ. Press, Oxford, 2000).
- Fano, U. Quantum theory of interference effects in the mixing of light from phase independent sources. *Am. J. Phys.* **29**, 539–545 (1961).
- Hanbury Brown, R. & Twiss, R. Q. A test of a new stellar interferometer on Sirius. *Nature* **178**, 1046–1048 (1956).
- Baym, G. The physics of Hanbury Brown-Twiss intensity interferometry: From stars to nuclear collisions. *Acta Phys. Pol. B* **29**, 1839–1884 (1998).
- Boal, D. H., Gelbke, C.-K. & Jennings, B. K. Intensity interferometry in subatomic physics. *Rev. Mod. Phys.* **62**, 553–602 (1990).
- Viana Gomes, J. *et al.* Theory for a Hanbury Brown Twiss experiment with a ballistically expanding cloud of cold atoms. *Phys. Rev. A* **74**, 053607 (2006).
- Kimble, H. J., Dagenais, M. & Mandel, L. Photon antibunching in resonance fluorescence. *Phys. Rev. Lett.* **39**, 691–695 (1978).
- Henny, M. *et al.* The fermionic Hanbury Brown and Twiss experiment. *Science* **284**, 296–298 (1999).
- Oliver, W. D., Kim, J., Liu, R. C. & Yamamoto, Y. Hanbury Brown and Twiss-type experiment with electrons. *Science* **284**, 299–301 (1999).
- Kiesel, H., Renz, A. & Hasselbach, F. Observation of Hanbury Brown-Twiss anticorrelations for free electrons. *Nature* **418**, 392–394 (2002).
- Iannuzzi, M., Orecchini, A., Sacchetti, F., Facchi, P. & Pascazio, S. Direct experimental evidence of free-fermion antibunching. *Phys. Rev. Lett.* **96**, 080402 (2006).
- Rom, T. *et al.* Free fermion antibunching in a degenerate atomic Fermi gas released from an optical lattice. *Nature* **444**, 733–736 (2006).
- Jagutzki, O. *et al.* A broad-application microchannel-plate detector system for advanced particle or photon detection tasks: Large area imaging, precise multi-hit timing information and high detection rate. *Nucl. Instrum. Methods Phys. Res. A* **477**, 244–249 (2002).

27. McNamara, J. M., Jelten, T., Tychkov, A. S., Hogervorst, W. & Vassen, W. Degenerate Bose-Fermi mixture of metastable atoms. *Phys. Rev. Lett.* **97**, 080404 (2006).
28. Girardeau, M. Relationship between systems of impenetrable bosons and fermions in one dimension. *J. Math. Phys. (NY)* **1**, 516–523 (1960).
29. Olshanii, M. Atomic scattering in the presence of an external confinement and a gas of impenetrable bosons. *Phys. Rev. Lett.* **81**, 938–941 (1998).
30. Tychkov, A. S. *et al.* Metastable helium Bose-Einstein condensate with a large number of atoms. *Phys. Rev. A* **73**, 031603(R) (2006).

Supplementary Information is linked to the online version of the paper at www.nature.com/nature.

Acknowledgements This work was supported by the access programme of Laserlab Europe. The LCVU group in Amsterdam is supported by the 'Cold Atoms' programme of the Dutch Foundation for Fundamental Research on Matter (FOM) and by the Space Research Organization Netherlands (SRON). The Atom Optics group of LCFIO is a member of the IFRAF institute and of the Fédération LUMAT of the CNRS, and is supported by the French ANR and by the SCALA programme of the European Union.

Author Information Reprints and permissions information is available at www.nature.com/reprints. The authors declare no competing financial interests. Correspondence and requests for materials should be addressed to C.I.W. (christoph.westbrook@institutoptique.fr) or W.V. (w.vassen@few.vu.nl).

RÉSUMÉ

Cette thèse détaille la mesure des corrélations d'intensité quantiques dans des gaz d'hélium métastable. La mesure s'est opérée sur des gaz thermiques bosoniques ^4He et fermioniques ^3He ainsi que sur des condensats de Bose-Einstein.

En 1956, Robert Hanbury Brown et Richard Twiss ont mesuré la corrélation entre des photons provenant d'une même source thermique. Ils avaient ainsi mis en évidence que les photons émis par une telle source arrivaient préférentiellement groupés sur le détecteur. Ce groupement caractérise les bosons provenant d'une source non-cohérente. Les fermions manifestent un anti-groupement dans les mêmes conditions.

En utilisant des atomes d'hélium métastables, dont l'utilisation de galettes à micro-canaux facilite la détection individuelle, nous avons pu mettre en évidence un regroupement similaire des bosons ^4He provenant de sources thermiques de l'ordre du microkelvin. La cohérence des condensats de Bose-Einstein n'a pas permis de dégager une corrélation particulière, comme attendue. Une mesure sur des gaz thermiques des fermions ^3He a permis de mettre en évidence leur anti-groupement. Un soin particulier a été pris pour décrire le détecteur à base de galettes de microcanaux et de lignes à retard, une des clés de la réussite de la mesure.

ABSTRACT

This thesis deals with the measurement of the quantum intensity correlations in gases of metastable Helium. The measurement has been performed on thermal gases of bosonic ^4He and fermionic ^3He , as well as on Bose-Einstein condensates.

In 1956, Robert Hanbury Brown et Richard Twiss measured the correlation between photons emitted from a single thermal source. The consequently demonstrated that the photons emitted by such a source tend to arrive grouped on a detector. This bunching characterises bosons from a non-coherent source. Fermions show an anti-bunching behaviour in the same conditions.

By using metastable Helium atoms, that can be detected individually through the use of micro-channel plates, we have been able to show a similar bunching of bosons ^4He from thermal sources around the microkelvin. As expected, the coherence of the Bose-Einstein condensates did not produce a particular correlation. The measurement on thermal gases of fermionic ^3He has demonstrated the anti-bunching. Particular effort has been employed in describing the micro-channel plate based delay-line detector, the key to the experiment.